# On Microstructure and Corrosion Properties of the Laser-Powder Bed Fused (L-PBF) AlSi10Mg alloy

by

© Mehran Rafieazad

A Thesis submitted to the
School of Graduate Studies
in partial fulfillment of the requirements for the degree of

Doctor of Philosophy
Faculty of Engineering and Applied Science

Memorial University of Newfoundland
May 2021

St. John's Newfoundland

*Dedicated to*

*my beautiful wife,* ***Mona*** *and my parents*

*for their patience and faith*

# Abstract

Despite the already existing advantages of additively manufactured AlSi10Mg, there are still process-induced imperfections associated with the Laser-Powder Bed Fusion process, such as microstructural inhomogeneity and high level of porosity. This thesis aims to examine the impact of (*i*) low-temperature heat-treatment, (*ii*) recycled feedstock powder, (*iii*) the laser-powder bed fusion (L-PBF) process parameters, and (*iv*) post-printing surface treatment on the solidification defects, microstructures, and the resultant corrosion properties of L-PBF-AlSi10Mg alloy. Scanning electron microscopy and X-ray diffraction analysis confirmed that heat-treatment from 200 °C to 350 °C promotes the homogeneity of the microstructure, characterized by the uniform distribution of eutectic Si in the α-Al matrix. Moreover, the microstructural analysis confirmed that using the recycled powder in the fabrication of AlSi10Mg leads to (i) an increased volume fraction of internal porosities and solidification micro-cracks, (ii) more coarsening of interdendritic eutectic-Si network particularly along the melt pool boundaries, which were correlated to the larger size and irregular shape of the recycled powders compared to the virgin powders, leading to the reduced thermal conductivity of the recycled powders. Additionally, the implemented process parameters modifications were found to be not only effective in reducing the as-printed surface roughness of the components, but also led to the formation of cyclic small-large melt pools (MPs) in the Upskin layers of the fabricated samples. Employing friction stir processing (FSP) as a post-printing surface modification technique was shown to be effective in eliminating the process-induced porosities of the L-PBF AlSi10Mg alloy, and resulted in drastic microstructural homogenization, grain refinement, and uniform dispersion of refined Si particles. To investigate the impacts of the above-mentioned microstructural changes on the corrosion performance of the alloy, anodic polarization testing, electrochemical impedance spectroscopy in aerated and deaerated 3.5 wt.% NaCl solutions, intergranular corrosion, and Mott-Schottky tests were performed. The electrochemical measurements confirmed the improved corrosion resistance of the alloy and reduced susceptibility to penetrating selective attack at initial immersion time in the electrolyte solution by increasing the heat-treatment temperature from 200 °C to 300 °C. Moreover, the corrosion results confirmed a slight degradation of the corrosion properties of the recycled-powder fabricated samples, ascribed to further coarsening of Si-network along their melt pool boundaries. Additionally, optimization of the process parameters confirmed that the fabricated sample at the highest volumetric energy density revealed a degraded corrosion performance resulted from its extended HAZ and coarser microstructure. Moreover, improvement of the corrosion performance of the FSPed sample was confirmed by the positive shift of the pitting potential and reduction in the corrosion rate and corrosion current density as compared to the as-printed samples. This research provides solutions to the existing challenges in the industries for adopting additive manufacturing methods due to the final cost, microstructural homogeneity, high level of porosity, residual stress, and initial surface roughness.

# Acknowledgement

Firstly, I would like to express my sincere gratitude to my supervisor Dr. Ali Nasiri for the continuous support of my Ph.D. study and related research, for his patience, motivation, and immense knowledge. His guidance helped me in all the time of research and writing of the research papers and this thesis. I could not have imagined having a better supervisor, supporter, and mentor for my Ph.D. study.

Besides my supervisor, I would like to thank the rest of my supervisory committee: Dr. Susan Caines, and Dr. Lorenzo Moro, for their insightful comments and encouragement to widen my research from various perspectives.

My sincere thanks also go to Dr. Mohsen Mohammadi, who provided me with an opportunity to collaborate with his research team and gave me access to the research facilities. Without his precious support, it would not be possible to conduct this research.

I thank my fellow labmates for their help, support, and all the fun we have had in the last four years.

Last but not least, I would like to thank my family: my beloved wife, my amazing parents, my brother, and all my friends for supporting me spiritually throughout this journey. None of this would have been possible without their love, patient, and support.

TABLE OF CONTENT

# List of Tables

# List of Figures

# List of Abbreviations and Symbols

| | |
|---|---|
| $\dot{T}$ | Cooling Rate |
| $\omega''_m$ | Angular Frequency |
| $f''_m$ | Maximum Frequency |
| $\rho_\delta$ | The Resistivity at the Maximum Thickness of the Passive Layer |
| $f_{max}$ | Maximum Measured Frequency |
| $\varepsilon_r$ | Relative Dielectric Constant |
| $\theta_e$ | Intrinsic Contact Angle |
| *AF* | Acicular Ferrite |
| *AM* | Additive Manufacturing |
| *APP* | Anodic Potentiodynamic Polarization |
| *B* | Bainite |
| *BM* | Base Metal |
| *C* | Capacitance |
| *CE* | Counter Electrode |
| $C_{eff}$ | Passive Film Capacitance |
| *CMT* | Cold Metal Transfer |
| *CPE* | Constant Phase Element |
| $CPE_{cath}$ | Constant Phase Element of The Cathodic Phase |
| $CPE_{dl}$ | Constant Phase Element of The Double Layer |
| $CPE_{oxide}$ | Constant Phase Element of The Oxide Layer |
| $CPE_p$ | Constant Phase Element of The Passive Layer |
| $CPE_{pit}$ | Constant Phase Element of The Pitting |
| *CRPs* | Cu-Enriched Particles |
| $C_{SC}$ | Space Charge Capacitance |
| *D* | Particle Size |
| *d* | Grain Size |
| *DBTT* | Ductile to Brittle Transition Temperature |
| *dl* | Double Layer |
| *DLF* | Direct Laser Fabrication |
| *DMLS* | Direct Metal Laser Sintered |
| $D_{ox}$ | Steady-State Passive/Oxide Layer Thickness |
| *DRX* | Dynamic Recrystallization |
| *DSC* | Differential Scanning Calorimetry |
| *E* | Applied Potential |
| *e* | Electron Charge |
| *E.W* | Equivalent Weight |

| | |
|---|---|
| *EBSD* | Electron Backscattered Diffraction |
| $E_{corr.}$ | Corrosion Potential |
| *EDX* | Energy Dispersive X-ray |
| $E_{FB}$ | Flat Band Potential |
| *EIS* | Electrochemical Impedance Spectroscopy |
| $E_{pit}.$ | Pitting Potential |
| *F* | Polygonal Ferrite |
| *FESEM* | Field Emission Scanning Electron Microscope |
| *FIB* | Focused Ion Beam |
| *FSP* | Friction Stir Processing |
| *G* | Temperature Gradient |
| *G/R* | Solidification Rate Ratio |
| *GB* | Grain Boundary |
| *GMA* | Gas Metal Arc |
| *GMAW* | Gas Metal Arc Welding |
| *GP* | Guinier–Preston |
| *GTA* | Gas Tungsten Arc |
| *HAGB* | High Angle Grain Boundaries |
| *HAZ* | Heat Affected Zone |
| *HIP* | Hot Isostatic Pressing |
| *H-M* | Hsu And Mansfield’s Model |
| *ICHAZ* | Inter-Critical Heat Affected Zone |
| $I_{Corr.}$ | Corrosion Current Density |
| *ICP-OES* | Inductively Coupled Plasma-Optical Emission Spectrometry |
| *IGC* | Intergranular Corrosion |
| *IPF* | Inverse Pole Figure |
| *k* | Boltzmann’s Constant |
| *LAGB* | *Low Angle Grain Boundaries* |
| *LBM* | *Laser Beam Melting* |
| *LBZ* | *Localized Brittle Zones* |
| *LMD* | *Laser Metal Deposition* |
| *L-PBF* | *Laser-Powder Bed Fusion* |
| *MA* | *Martensite-Austenite* |
| *MP* | *Melt Pool* |
| *n* | *Dispersion Coefficient* |
| *NA* | *Acceptance Density* |
| *ND* | *Donor Density* |
| *NDT* | *Non-Destructive Testing* |
| *OCP* | *Open Circuit Potential* |
| *P* | *Pearlite* |
| *PDM* | *Point Defect Model* |

| | |
|---|---|
| *PF* | *Pole Figure* |
| *P-L* | *Power-Law Model* |
| *Rcath* | *Cathodic Resistance* |
| *Rct* | *Double Layer Resistance* |
| *RE* | *Reference Electrode* |
| *RE* | *Solidification Rate* |
| *Rel* | *Electrolyte Resistance* |
| *Roxide* | *Oxide Layer Resistance* |
| *Rp* | *Passive Layer Resistance* |
| *Rpit* | *Pitting Resistance* |
| *Rpol* | *Polarization Resistance* |
| *Rs* | *Ohmic Drop Resistance* |
| *SDAS* | *Secondary Dendrite Arm Spacing* |
| *SEC* | *Simplified Equivalent Circuit* |
| *SEM* | *Scanning Electron Microscopy* |
| *SLM* | *Selective Laser Melted* |
| *SLM* | *Selective Laser Melting* |
| *S-S* | *Simple Substitution Model* |
| *STEM* | *Scanning Transmission Electron Microscopy* |
| *STEM-BF* | *STEM in Bright-Field Mode* |
| *STT* | *Surface Tension Transfer* |
| *SZ* | *Stir Zone* |
| *TEM* | *Transmission Electron Microscopy* |
| *TMAZ* | *Thermo-Mechanically Affected Zone* |
| *UTS* | *Ultimate Tensile Strength* |
| *VED* | *Volumetric Energy Densities* |
| *WAAM* | *Wire Arc Additive Manufacturing* |
| *Wpit* | *Warburg Diffusion Element* |
| *XRD* | *X-Ray Diffraction* |
| *YS* | *Yield Strength* |
| $\alpha$ | *Dispersion Coefficient* |
| $\beta A$ | *Anodic Slope* |
| $\beta C$ | *Cathodic Slope* |
| $\delta$ | *Passive Layer Thickness* |
| $\varepsilon$ | *Dielectric Constant* |
| $\varepsilon 0$ | *Vacuum Permittivity* |
| $\theta$ | *Apparent Contact Angle* |
| $\lambda$ | *Dendrite Arm Spacing* |
| $\omega$ | *Angular Frequency* |

# Chapter 1

# Introduction

## 1.1. Background

During the last decades, the continuous development of advanced manufacturing components with more elaborate designs and enhanced mechanical and corrosion properties for applications in the automobile, marine, and aerospace industries has necessitated the utilization of innovative production technologies. Metal additive manufacturing as a novel and rapidly emerging fabrication technology provides promising resolutions to the existing knowledge gaps and deficiencies in design and manufacturing. This leads to a versatile technique to manufacture complicated parts with improved functionalities and performance.

As Figure 1.1 shows, the metal additive manufacturing (AM) processes can be classified based on the implemented heating source into two main categories, *i.e.*, beam-based methods, such as powder bed fusion known as selective laser melting (SLM) and electron beam melting (EBM), and arc-based technologies, such as wire arc additive manufacturing (WAAM) [1].

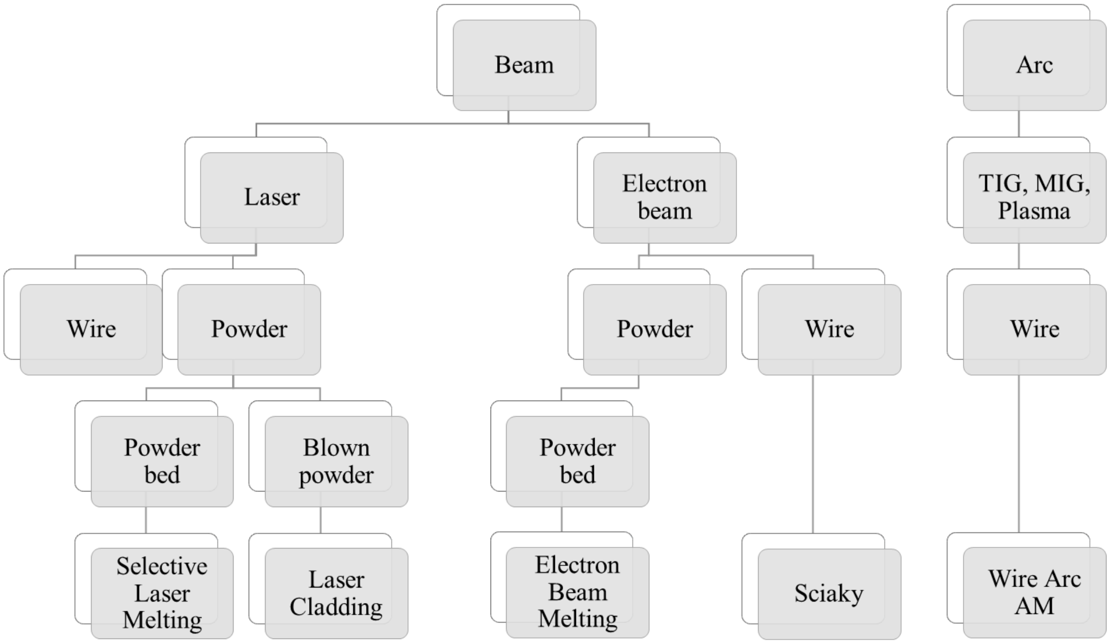

Figure 1. 1. Different Metal Additive Manufacturing processes

Laser-Powder Bed Fusion (L-PBF) is an additive manufacturing process that proposes specific advantages, such as cost- and time-effective production with the feasibility to produce near-net-shape intricate geometries without almost any material's waste and shorter time to market compared with conventional technologies. The components manufactured by Powder-bed fusion (PBF) technologies, including both laser-based and electron beam-based, are currently gaining significant interests from the academia and industry, such as biomedical, marine, automotive, and aerospace [2]. As shown in Figure 1.2, in the laser-powder bed fusion process, a laser beam with high energy is applied to beds of powders, resulting in a fully melting and metallurgical joining during each single scanning track layer-by-layer until a functional and fully dense part is fabricated. Likewise, electron beam melting (EBM) instead of a laser an electron beam as the heat source in an inert controlled- and vacuumed-atmosphere; is applied. The same technology with different terminologies has been reported in different studies to introduce this process, such as

Selective Laser Melting (SLM) [3], Direct Metal Laser Sintering (DMLS) [4], or Laser Beam Melting (LBM) [2]. So far, several types of metallic components have been successfully fabricated employing different AM technologies, including Ni alloys [5,6], stainless steel [7–9], Ti alloys [10,11], and Al-based alloys [12–16].

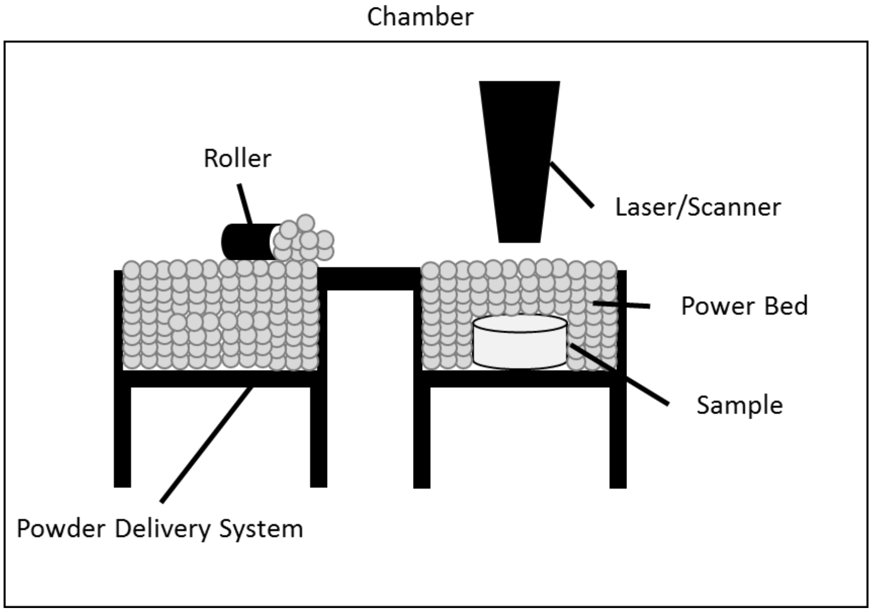

Figure 1. 2. Generic representation of an AM powder bed system.

As Figure 1. 3 shows, WAAM is an AM technology that usually benefits from a robotic arm, carrying an arc welding torch as the energy source to fabricate metallic parts additively in the form of weld beads overlaid on previously deposited layers [17,18]. Although the WAAM technology has not been completely industrialized yet, it has gained substantial attention in different industries, including aerospace, marine, and oil and gas for the fabrication of meter-scale metallic components for structural applications [1]. As compared to other AM technologies, WAAM is mainly identified by its low capital cost, unlimited build envelope, and significantly high deposition rate (3-8 kg/h), leading to substantial reduction in the fabrication time [1]. The common WAAM processes implement either a gas metal arc (GMA), gas tungsten arc (GTA), or plasma arc (PA) as the heat source [8,19,20]. Cold metal transfer (CMT) is also a new variation of GMA technology and widely adopted as the heat source to produce WAAM components [21].

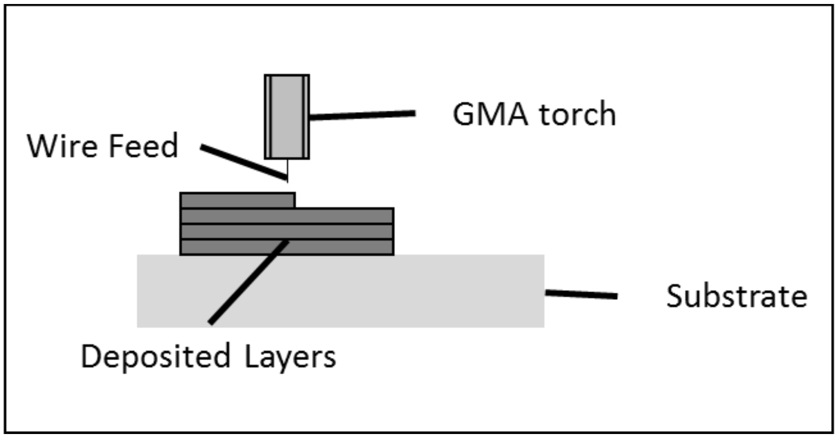

Figure 1. 3. Generic representation of an WAAM system.

## 1.2. AM methods for Al alloys

The additive manufacturing of aluminum alloys is a challenging process owning to the light-weight, high thermal conductivity, high reflectivity, and low laser absorptivity of the feedstock powders [22]. Another reason is that the Al alloys have good machinability and the costs of machined Al components are still lower than the AM fabricated parts [23]. Moreover, considering the significantly high cooling rates associated with the AM processes, the Al alloys are susceptible to solidification micro-crack during L-PBF processing, giving rise to low mechanical properties and structural integrity [24]. In addition to that, some Al alloys such as the 7xxx series contain Zn, which is a highly volatile element, resulting in melt pools turbulent, splatter, and high porosity levels [25]. Therefore, although the research in the AM of these alloys is promising, there are still struggles to adopt Al alloys by AM industries successfully such as final cost, microstructural inhomogeneity, high level of porosity, surface roughness, and residual stress [26]. However, the Al-Si alloys such as AlSi10Mg [27] and AlSi12 [28] have gained more attention from AM industries due to their great cast-ability and low solidification shrinkage resulting from the large fraction of Al-Si eutectic. Among all the Al-Si alloy family, AlSi10Mg as a traditional cast alloy has been predominantly adopted by the AM industry, particularly through L-PBF process [15]. Low solidification shrinkage and cracking susceptibility and good weldability are common characteristics of this alloy due to its near-eutectic composition [29]. Furthermore, the addition of Mg to the composition of this alloy has provided an age-hardening property through precipitation sequences of $\alpha(\mathrm{Al}) \rightarrow$ (Guinier–Preston) GP zones $\rightarrow \beta'' \rightarrow \beta' \rightarrow \beta$, where GP zones are separated clusters of Mg and Si atoms, $\beta''$ and $\beta'$ are non-stable compounds of Mg and Si atoms with different stoichiometry, and $\beta$ phase is the stable $Mg_2Si$ phase [30]. All these distinctive properties of AlSi10Mg alloy have led to a multiplicity of applications in aerospace and automotive industries [31]. However, the traditional fabrication methods, such as casting, forging, and powder metallurgy techniques, have substantially limited the accelerated adoption of the family of Al-Si-Mg alloys, particularly in harsher environments due to the required prolonged fabrication cycles for complex parts and the obtained microstructure of the alloy in as-fabricated condition. The cast AlSi10Mg alloy commonly contains a coarse eutectic silicon phase in addition to various hard and brittle intermetallic components, which can severely deteriorate its mechanical and corrosion properties [15,31,32]. In addition, implementing the L-PBF process in the fabrication of AlSi10Mg alloys has opened many new avenues for novel designs and applications for this alloy in various industries.

## 2. Motivation and Research objectives:

The unique processing characteristics of L-PBF, such as extremely rapid rate, contribute to the formation of a super fine microstructure and a great amount of residual thermal stress induced in the structure. The residual stress within the fabricated structure can cause distortion in the printed part with a dimensional inaccuracy [33]. Therefore, post-printing thermal-treatment is commonly applied to avoid any part's distortion and release the inherent residual stress [34,35]. However, previous investigations have revealed that a high-temperature thermal-treatment can extensively change the microstructure of the as-printed L-PBF-AlSi10Mg alloy and consequently cause a mechanical and corrosion performance degradation [36,37].

Moreover, as feedstock powder size and morphology are changed, many fabricated parts are expected to change [38,39]. Therefore, understanding the impacts of using different feedstock powder on the final microstructure, forming solidification imperfections, and corrosion performance of the L-PBF fabricated AlSi10Mg components is crucial for AM industries.

Furthermore, in addition to the size and morphology of the feedstock metal powder, controlling the L-PBF processing parameters, such as laser power, hatching distance, and scanning speed can also impact the internal imperfections' density, the achieved surface roughness, as well as the microstructural characteristics and consequently, the corrosion and mechanical properties of the fabricated L-PBF-AlSi10Mg parts[38–40].

Additionally, despite the well-known capabilities of the Friction Stir Processing in modifying the final microstructure and enhancing the mechanical properties of L-PBF AlSi10Mg alloy

[41,42], there is still very limited information available in the literature on implementing this unique post-printing surface treatment method to develop the performance of AM parts.

Therefore, despite all the benefits that L-PBF technologies contribute to the different manufacturing industries and similar to any other manufacturing method, it should not be considered a perfect fabrication technique with no drawback. In particular, for the L-PBF-AlSi10Mg alloy, the adopted high laser power, fast scanning speed, as well as balling and dross formation as the alloy is solidified commonly promote the formation of various imperfections, such as residual stresses within the part and microstructural inhomogeneity, high porosity level, the as-printed surface roughness, and solidification micro-defects. These process-induced imperfections are reported to be an unfavorable impact on the corrosion and mechanical characteristics of the fabricated components [13,16,40,43,44]. In order to eliminate the formation of these imperfections and consequently improve the corrosion and mechanical properties of the fabricated components, various post-printing solutions, such as post-heat treatments, using different feedstock metal powder size, tuning L-PBF process parameters, and post-printing surface treatments have been investigated. Therefore, this thesis aims to answer the following questions:

1. What is the impact of the post-printing heat-treatment on the microstructural evolution and corrosion performance of the L-PBF AlSi10Mg?

2. What is the impact of the feedstock powders, recycled powders in particular, with different size and morphology on the microstructure and corrosion properties of the L-PBF AlSi10Mg?

3. What is the true impact of the processing parameters on the microstructure and corrosion properties of the L-PBF AlSi10Mg?

4. What is the impact of the post-printing surface treatment such as Friction Stir Processing (FSP) on the microstructure and corrosion properties of the L-PBF AlSi10Mg?

Focusing on these questions, this thesis investigates the impact of four different solutions to eliminate the process-induced imperfection on the microstructure and corrosion performance of the L-PBF produced AlSi10Mg alloy.

## 3. Organization of the thesis

This thesis is written in a manuscript format (paper-based). Overall, the thesis's outcomes are published in eight peer-reviewed journal papers as a first author, four peer-reviewed journal as second or third author, three conference papers as a first author and two conference papers as second or third author, and three conference abstracts as a first author. The details of each publication are listed below.

Journal Papers:

**1)** **M. Rafieazad**, M. Mohammadi, A. Gerlich, A. Nasiri, Enhancing the Corrosion Properties of Additively Manufactured AlSi10Mg Using Friction Stir Processing, Corros. Sci. (2020) 109073. doi: https://doi.org/10.1016/j.corsci.2020.109073 **(IPF=6.720)**

2) **M. Rafieazad**, P. Fathi, M. Mohammadi, A. Nasiri, Effects of Laser-Powder Bed Fusion Process Parameters on the Microstructure and Corrosion Properties of AlSi10Mg Alloy, journal of electrochemical society (JES), 2021 https://doi.org/10.1149/1945-7111/abdfa8 **(IPF=3.721)**

3) **M. Rafieazad**, A. Chatterjee, A.M. Nasiri, Effects of Recycled Powder on Solidification Defects, Microstructure, and Corrosion Properties of DMLS Fabricated AlSi10Mg, JOM. 71 (2019). https://doi:10.1007/s11837-019-03552-2 **(IPF=2.305)**

4) **M. Rafieazad**, M. Mohammadi, A. Nasiri, On Microstructure and Early Stage Corrosion Performance of Heat Treated Direct Metal Laser Sintered AlSi10Mg, Addit. Manuf. 28 (2019) 107–119. doi: https://doi.org/10.1016/j.addma.2019.04.023 **(IPF=7.002)**

5) **M. Rafieazad**, M. Ghaffari, A. Vahedi Nemani, A. Nasiri, Microstructural evolution and mechanical properties of a low-carbon low-alloy steel produced by wire arc additive

manufacturing, Int. J. Adv. Manuf. Technol. (2019) 1–14. https://doi.org/10.1007/s00170-019-04393-8 **(IPF=2.633)**

6) **M. Rafieazad**, J.A. Jaffer, C. Cui, X. Duan, A. Nasiri, Nanosecond Laser Fabrication of Hydrophobic Stainless Steel Surfaces: The Impact on Microstructure and Corrosion Resistance, Materials (Basel). 11 (2018) 1577. https://doi.org/10.3390/ma11091577 **(IPF=3.057)**

7) **M. Rafieazad**, A. Vahedi Nemani, M. Ghaffari, A. Nasiri, On Microstructure and Mechanical Properties of a Low-Carbon Low-Alloy Steel Block Fabricated by Wire Arc Additive Manufacturing, journal of the Materials Engineering and Performance, 2020. https://doi.org/10.1007/s11665-021-05568-9 **(IPF=1.467)**

8) **M. Rafieazad**, P. Fathi, A. Nasiri, M. Haghshenas, M. Mohammadi, Isotropic Corrosion Performance of the Newly Developed L-PBF Fabricated A205 Aluminum Alloy, Materials Letter. https://doi.org/10.1016/j.matlet.2021.129541 **(IPF=3.019)**

9) M. Amiriafshar, **M. Rafieazad**, X. Duan, and A. Nasiri, "Fabrication and Coating Adhesion Study of Superhydrophobic Stainless Steel Surfaces: the Effect of Substrate Surface Roughness," Surfaces and Interfaces, p. 100526, 2020. https://doi.org/10.1016/j.surfin.2020.100526 **(IPF=3.724)**

10) P. Fathi, **M. Rafieazad**, X. Duan, M. Mohammadi, and A. M. Nasiri, "On microstructure and corrosion behaviour of AlSi10Mg alloy with low surface roughness fabricated by direct metal laser sintering," Corros. Sci., vol. 157, 2019. https://doi.org/10.1016/j.corsci.2019.05.032 **(IPF=7.002)**

11) M. Ghaffari, A. Vahedi Nemani, **M. Rafieazad**, and A. Nasiri, "Effect of Solidification Defects and HAZ Softening on the Anisotropic Mechanical Properties of a Wire Arc Additive-Manufactured Low-Carbon Low-Alloy Steel Part," JOM, vol. 71, no. 11, pp. 4215–4224, Nov. 2019. https://doi.org/10.1007/s11837-019-03773-5 **(IPF=2.305)**

12) P. Fathi, **M. Rafieazad**, …, A. Nasiri, M. Mohammadi, Corrosion Performance of Additively Manufactured Bimetallic Aluminum Alloys, *Submitted* to Journal of Electrochemical Acta **(IPF=6.215)**

Conference papers:

1) **M. Rafieazad**, M. Mohammadi, A. Gerlich, A. Nasiri, Impacts of Friction Stir Processing on Microstructure and Corrosion Properties of DMLS-AlSi10Mg, in: TMS 2020 Conf., 2020.

2) **M. Rafieazad**, A. Chatterjee, and A. M. Nasiri, Additively Manufactured DMLS-AlSi10Mg using Recycled Powder: the Impacts on Microstructure and Corrosion Properties, CSME conference, (Full Paper), Jun 2019

3) **M. Rafieazad**, P. Fathi, M. Mohammadi, and A.M. Nasiri, Low temperature heat-treatment cycle on AlSi10Mg_200C alloy fabricated by direct laser metal sintering: Microstructure evolution and corrosion resistivity, ICAA16 conference, (Full Paper), Feb2018

4) P. Fathi, **M. Rafieazad**, M. Mohammadi, X. Duan, and A.M. Nasiri, Effect of surface finishing procedures on corrosion resistance of DMLS-AlSi10Mg_200C alloy, ICAA16 conference, (Full Paper), Feb2018
5) A. Vahedi, M. Ghaffari, **M. Rafieazad**, and A. M. Nasiri, Post-Printing Heat Treatment of a Wire Arc Additively Manufactured Low Carbon Low Alloy Steel, CSME conference, (Full Paper), Jun 2019

Conference Abstracts:

1) **M. Rafieazad**, M. Mohammadi, Adrian Gerlich, and A. M. Nasiri, On Corrosion Behavior of Direct Metal Laser Sintered AlSi10Mg Alloy Before and After Friction Stir Processing, ICAA17 conference, (Full Paper), June 2020

2) **M. Rafieazad**, Mohsen Mohammadi, and A. M. Nasiri, Comprehensive Study on Microstructure, Mechanical, and Corrosion properties of DMLS AlSi10Mg, Annual research day of MUN, (Poster), May 2019

3) **M. Rafieazad**, and A. M. Nasiri, Microstructural Evolution and Mechanical Properties of a High-Strength Low Alloy Steel Produced by Wire Arc Additive Manufacturing, CANWELD Conference, (Abstract), 2018

4) J. A. Jaffer, **M. Rafieazad**, C. Cui, X. Duan, and A. M. Nasiri, Corrosion Resistance Analysis of Laser Fabricated Hydrophobic Stainless Steel Surfaces, CMSC2017, (Presentation), Jun 2017

5) M. Ghaffari, A. Vahedi, **M. Rafieazad**, and A. M. Nasiri, Anisotropy in Mechanical Properties of a Wire Arc Additive Manufactured Low Carbon Low Alloy Steel, CSME conference, (Presentation), Jun 2019

Figure 1.5 shows the structure of this Ph.D. thesis. As shown in this figure, Chapters 2 to 5 and Appendixes 1 to 3 of this thesis are prepared based on the paper submissions to peer-reviewed journals.

Chapter 2 examines the impact of low-temperature heat-treatment on the microstructure and corrosion performance of direct metal laser sintered (DMLS)-AlSi10Mg alloy.

Chapter 3 investigates the impacts of using recycled powder with different size and morphology as compared to the virgin powder on solidification defects, microstructures, and the resultant corrosion properties of direct metal laser sintered AlSi10Mg alloy.

Chapter 4 study the effects of microstructural modifications induced by tuning the laser-powder bed fusion (L-PBF) process parameters on electrochemical stability of the L-PBF-AlSi10Mg alloy.

In Chapter 5 the solid-state structural modification technique friction-stir-processing (FSP) was applied on the surface of a laser-powder-bed-fusion fabricated AlSi10Mg alloy to locally modify the microstructure and enhance the corrosion properties of the alloy.

In addition to the above chapters that cover the primary structure of this thesis, the author has been also involved with a few side projects during the course of his PhD program (presented as appendices 1 and 2 at the end of this thesis). These projects were focused on understanding the full potential of the state-of-the-art wire arc additive manufacturing (WAAM) technology to fabricate large-scale components. Owing to its significantly high deposition rate (3-8 kg/h), substantial reduction in the fabrication time, and an unlimited build envelope, WAAM technology has the potential to be one of the most significant manufacturing innovations in many industries. However, the industrial evolution and adoption of this technology are currently limited due to the current lack of a commercially available robotic WAAM platform. The presented chapters as Appendix 1 and 2 contribute critical knowledge related to the development of a versatile robotic WAAM platform and advancement of the process in fabrication of large-scale parts. Moreover, the anisotropy in mechanical properties and microstructure of the fabricated parts were investigated.

In another side project (Appendix 3), the effectiveness of hydrophobic 17-4 PH stainless steel surfaces fabricated through nanosecond fiber laser surface texturing combined with applying a hydrophobic coating and its impact on the microstructure and corrosion resistance of the surface were also investigated. Appendix 3 studies nanosecond fiber laser surface texturing capability, followed by a low energy coating in the fabrication of hydrophobic 17-4 PH stainless steel surfaces as an alternative to the ultrashort lasers previously utilized for hydrophobic surfaces production.

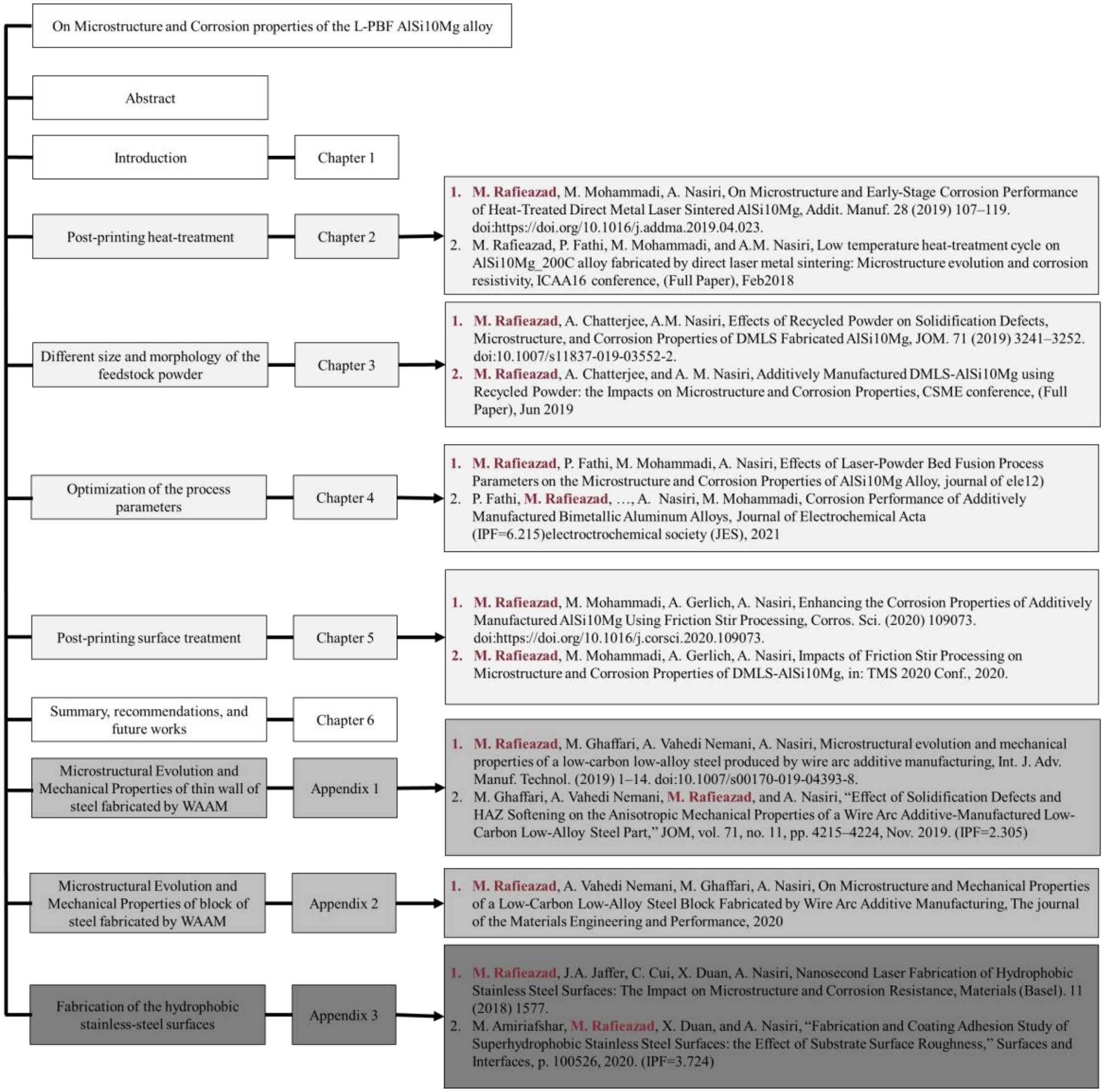

1. **M. Rafieazad**, M. Mohammadi, A. Nasiri, On Microstructure and Early-Stage Corrosion Performance of Heat-Treated Direct Metal Laser Sintered AlSi10Mg, Addit. Manuf. 28 (2019) 107–119. doi:https://doi.org/10.1016/j.addma.2019.04.023.
2. M. Rafieazad, P. Fathi, M. Mohammadi, and A.M. Nasiri, Low temperature heat-treatment cycle on AlSi10Mg_200C alloy fabricated by direct laser metal sintering: Microstructure evolution and corrosion resistivity, ICAA16 conference, (Full Paper), Feb2018

1. **M. Rafieazad**, A. Chatterjee, A.M. Nasiri, Effects of Recycled Powder on Solidification Defects, Microstructure, and Corrosion Properties of DMLS Fabricated AlSi10Mg, JOM. 71 (2019) 3241–3252. doi:10.1007/s11837-019-03552-2.
2. **M. Rafieazad**, A. Chatterjee, and A. M. Nasiri, Additively Manufactured DMLS-AlSi10Mg using Recycled Powder: the Impacts on Microstructure and Corrosion Properties, CSME conference, (Full Paper), Jun 2019

1. **M. Rafieazad**, P. Fathi, M. Mohammadi, A. Nasiri, Effects of Laser-Powder Bed Fusion Process Parameters on the Microstructure and Corrosion Properties of AlSi10Mg Alloy, journal of ele12)
2. P. Fathi, **M. Rafieazad**, …, A. Nasiri, M. Mohammadi, Corrosion Performance of Additively Manufactured Bimetallic Aluminum Alloys, Journal of Electrochemical Acta (IPF=6.215)electroctrochemical society (JES), 2021

1. **M. Rafieazad**, M. Mohammadi, A. Gerlich, A. Nasiri, Enhancing the Corrosion Properties of Additively Manufactured AlSi10Mg Using Friction Stir Processing, Corros. Sci. (2020) 109073. doi:https://doi.org/10.1016/j.corsci.2020.109073.
2. **M. Rafieazad**, M. Mohammadi, A. Gerlich, A. Nasiri, Impacts of Friction Stir Processing on Microstructure and Corrosion Properties of DMLS-AlSi10Mg, in: TMS 2020 Conf., 2020.

1. **M. Rafieazad**, M. Ghaffari, A. Vahedi Nemani, A. Nasiri, Microstructural evolution and mechanical properties of a low-carbon low-alloy steel produced by wire arc additive manufacturing, Int. J. Adv. Manuf. Technol. (2019) 1–14. doi:10.1007/s00170-019-04393-8.
2. M. Ghaffari, A. Vahedi Nemani, **M. Rafieazad**, and A. Nasiri, “Effect of Solidification Defects and HAZ Softening on the Anisotropic Mechanical Properties of a Wire Arc Additive-Manufactured Low-Carbon Low-Alloy Steel Part,” JOM, vol. 71, no. 11, pp. 4215–4224, Nov. 2019. (IPF=2.305)

1. **M. Rafieazad**, A. Vahedi Nemani, M. Ghaffari, A. Nasiri, On Microstructure and Mechanical Properties of a Low-Carbon Low-Alloy Steel Block Fabricated by Wire Arc Additive Manufacturing, The journal of the Materials Engineering and Performance, 2020

1. **M. Rafieazad**, J.A. Jaffer, C. Cui, X. Duan, A. Nasiri, Nanosecond Laser Fabrication of Hydrophobic Stainless Steel Surfaces: The Impact on Microstructure and Corrosion Resistance, Materials (Basel). 11 (2018) 1577.
2. M. Amiriafshar, **M. Rafieazad**, X. Duan, and A. Nasiri, “Fabrication and Coating Adhesion Study of Superhydrophobic Stainless Steel Surfaces: the Effect of Substrate Surface Roughness,” Surfaces and Interfaces, p. 100526, 2020. (IPF=3.724)

Figure 1. 4. Structure of the PhD thesis and related publications

## References:

[1] A. Taşdemir, S. Nohut, An overview of wire arc additive manufacturing (WAAM) in shipbuilding industry, Ships Offshore Struct. 0 (2020) 1–18. doi:10.1080/17445302.2020.1786232.

[2] S.L. Sing, J. An, W.Y. Yeong, F.E. Wiria, Laser and electron-beam powder-bed additive manufacturing of metallic implants: A review on processes, materials and designs, J. Orthop. Res. 34 (2016) 369–385. doi:10.1002/jor.23075.

[3] W.J. Sames, F.A. List, S. Pannala, R.R. Dehoff, S.S. Babu, The metallurgy and processing science of metal additive manufacturing, Int. Mater. Rev. 61 (2016) 315–360. doi:10.1080/09506608.2015.1116649.

[4] D. Herzog, V. Seyda, E. Wycisk, C. Emmelmann, Additive manufacturing of metals, Acta Mater. 117 (2016) 371–392. doi:https://doi.org/10.1016/j.actamat.2016.07.019.

[5] B.S. Amirkhiz, D. Chalasani, M. Mohammadi, TEM Study of Additively Manufactured Metallic Alloys: Nickel Aluminum Bronze, Microsc. Microanal. 25 (2019) 2588–2589. doi:10.1017/S1431927619013679.

[6] S.-H. Sun, K. Hagihara, T. Nakano, Effect of scanning strategy on texture formation in Ni-25at.%Mo alloys fabricated by selective laser melting, Mater. Des. 140 (2018) 307–316. doi:https://doi.org/10.1016/j.matdes.2017.11.060.

[7] M. Rafieazad, M. Ghaffari, A. Vahedi Nemani, A. Nasiri, Microstructural evolution and mechanical properties of a low-carbon low-alloy steel produced by wire arc additive manufacturing, Int. J. Adv. Manuf. Technol. (2019) 1–14. doi:10.1007/s00170-019-04393-8.

[8] M. Ghaffari, A. Vahedi Nemani, M. Rafieazad, A. Nasiri, Effect of Solidification Defects and HAZ Softening on the Anisotropic Mechanical Properties of a Wire Arc Additive-Manufactured Low-Carbon Low-Alloy Steel Part, JOM. 71 (2019) 4215–4224. doi:10.1007/s11837-019-03773-5.

[9] M. Kazemipour, M. Mohammadi, E. Mfoumou, A.M. Nasiri, Microstructure and Corrosion Characteristics of Selective Laser-Melted 316L Stainless Steel: The Impact of Process-Induced Porosities, JOM. 71 (2019) 3230–3240. doi:10.1007/s11837-019-03647-w.

[10] T. Ishimoto, K. Hagihara, K. Hisamoto, S.-H. Sun, T. Nakano, Crystallographic texture control of beta-type Ti–15Mo–5Zr–3Al alloy by selective laser melting for the development of novel implants with a biocompatible low Young's modulus, Scr. Mater. 132 (2017) 34–38. doi:https://doi.org/10.1016/j.scriptamat.2016.12.038.

[11] H. Attar, S. Ehtemam-Haghighi, D. Kent, X. Wu, M.S. Dargusch, Comparative study of commercially pure titanium produced by laser engineered net shaping, selective laser melting and casting processes, Mater. Sci. Eng. A. 705 (2017) 385–393. doi:https://doi.org/10.1016/j.msea.2017.08.103.

[12] P. Fathi, M. Rafieazad, X. Duan, M. Mohammadi, A. Nasiri, On Microstructure and Corrosion Behaviour of AlSi10Mg Alloy with Low Surface Roughness Fabricated by Direct Metal Laser Sintering, Corros. Sci. 157 (2019) 126–145.

[13] M. Mohammadi, H. Asgari, Achieving low surface roughness AlSi10Mg_200C parts using direct metal laser sintering, Addit. Manuf. 20 (2018) 23–32. doi:https://doi.org/10.1016/j.addma.2017.12.012.

[14] P. Fathi, M. Mohammadi, X. Duan, A. Nasiri, Effects of Surface Finishing Procedures on Corrosion Behavior of DMLS-AlSi10Mg_200C Alloy Versus Die-Cast A360.1 Aluminum, JOM. (2019) 1–12. doi:10.1007/s11837-019-03344-8.

[15] P. Fathi, M. Mohammadi, X. Duan, A.M. Nasiri, A Comparative Study on Corrosion and Microstructure of Direct Metal Laser Sintered AlSi10Mg_200C and Die Cast A360.1 Aluminum, J. Mater. Process. Technol. 259 (2018) 1–14. doi:https://doi.org/10.1016/j.jmatprotec.2018.04.013.

[16] M. Rafieazad, M. Mohammadi, A. Nasiri, On Microstructure and Early Stage Corrosion Performance of Heat Treated Direct Metal Laser Sintered AlSi10Mg, Addit. Manuf. 28 (2019) 107–119. doi:https://doi.org/10.1016/j.addma.2019.04.023.

[17] W.E. Frazier, Metal Additive Manufacturing: A Review, J. Mater. Eng. Perform. 23 (2014) 1917–1928. doi:10.1007/s11665-014-0958-z.

[18] S. Das, D.L. Bourell, S.S. Babu, Metallic materials for 3D printing, MRS Bull. 41 (2016) 729–741.

[19] J.P. Oliveira, B. Crispim, Z. Zeng, T. Omori, F.M. Braz Fernandes, R.M. Miranda, Microstructure and mechanical properties of gas tungsten arc welded Cu-Al-Mn shape memory alloy rods, J. Mater. Process. Technol. 271 (2019) 93–100. doi:https://doi.org/10.1016/j.jmatprotec.2019.03.020.

[20] F. Martina, J. Mehnen, S.W. Williams, P. Colegrove, F. Wang, Investigation of the benefits of plasma deposition for the additive layer manufacture of Ti–6Al–4V, J. Mater. Process. Technol. 212 (2012) 1377–1386. doi:https://doi.org/10.1016/j.jmatprotec.2012.02.002.

[21] P.P. Nikam, D. Arun, K.D. Ramkumar, N. Sivashanmugam, Microstructure characterization and tensile properties of CMT-based wire plus arc additive manufactured ER2594, Mater. Charact. 169 (2020) 110671. doi:https://doi.org/10.1016/j.matchar.2020.110671.

[22] M. Zavala-Arredondo, N. Boone, J. Willmott, D.T.D. Childs, P. Ivanov, K.M. Groom, K. Mumtaz, Laser diode area melting for high speed additive manufacturing of metallic components, Mater. Des. 117 (2017) 305–315. doi:https://doi.org/10.1016/j.matdes.2016.12.095.

[23] C. Brice, R. Shenoy, M. Kral, K. Buchannan, Precipitation behavior of aluminum alloy 2139 fabricated using additive manufacturing, Mater. Sci. Eng. A. 648 (2015) 9–14. doi:https://doi.org/10.1016/j.msea.2015.08.088.

[24] T. Qi, H. Zhu, H. Zhang, J. Yin, L. Ke, X. Zeng, Selective laser melting of Al7050 powder: Melting mode transition and comparison of the characteristics between the keyhole and conduction mode, Mater. Des. 135 (2017) 257–266. doi:https://doi.org/10.1016/j.matdes.2017.09.014.

[25] J.H. Martin, B.D. Yahata, J.M. Hundley, J.A. Mayer, T.A. Schaedler, T.M. Pollock, 3D printing of high-strength aluminium alloys, Nature. 549 (2017) 365–369. doi:10.1038/nature23894.

[26] K. Bartkowiak, S. Ullrich, T. Frick, M. Schmidt, New Developments of Laser Processing Aluminium Alloys via Additive Manufacturing Technique, Phys. Procedia. 12 (2011) 393–401. doi:https://doi.org/10.1016/j.phpro.2011.03.050.

[27] M. Krishnan, E. Atzeni, R. Canali, F. Calignano, D. Manfredi, E.P. Ambrosio, L. Iuliano, On the effect of process parameters on properties of AlSi10Mg parts produced by DMLS, Rapid Prototyp. J. 20 (2014) 449–458. doi:10.1108/RPJ-03-2013-0028.

[28] P. Vora, K. Mumtaz, I. Todd, N. Hopkinson, AlSi12 in-situ alloy formation and residual stress reduction using anchorless selective laser melting, Addit. Manuf. 7 (2015) 12–19. doi:https://doi.org/10.1016/j.addma.2015.06.003.

[29] H. Asgari, C. Baxter, K. Hosseinkhani, M. Mohammadi, On microstructure and mechanical properties of additi[1], Mater. Sci. Eng. A. 707 (2017) 148–158. doi:https://doi.org/10.1016/j.msea.2017.09.041.

[30] L. Zhou, A. Mehta, E. Schulz, B. McWilliams, K. Cho, Y. Sohn, Microstructure, precipitates and hardness of selectively laser melted AlSi10Mg alloy before and after heat treatment, Mater. Charact. (2018). doi:https://doi.org/10.1016/j.matchar.2018.04.022.

[31] B.A. Fulcher, D.K. Leigh, T.J. Watt, Comparison of AlSi10Mg and Al 6061 processed through DMLS, in: Proc. Solid Free. Fabr. Symp. Austin, TX, USA, 2014.

[32] A. Leon, A. Shirizly, E. Aghion, Corrosion Behavior of AlSi10Mg Alloy Produced by Additive Manufacturing (AM) vs. Its Counterpart Gravity Cast Alloy, Metals (Basel). 6 (2016). doi:10.3390/met6070148.

[33] M. Shiomi, K. Osakada, K. Nakamura, T. Yamashita, F. Abe, Residual Stress within Metallic Model Made by Selective Laser Melting Process, CIRP Ann. 53 (2004) 195–198. doi:https://doi.org/10.1016/S0007-8506(07)60677-5.

[34] D. Manfredi, E.P. Ambrosio, F. Calignano, M. Krishnan, R. Canali, S. Biamino, M. Pavese, E. Atzeni, L. Iuliano, P. Fino, C. Badini, Direct Metal Laser Sintering: an additive manufacturing technology ready to produce lightweight structural parts for robotic applications, La Metall. Ital. 105 (2013) 15–24.

[35] J. Fite, S. Eswarappa Prameela, J.A. Slotwinski, T.P. Weihs, Evolution of the microstructure and mechanical properties of additively manufactured AlSi10Mg during room temperature holds and low temperature aging, Addit. Manuf. 36 (2020) 101429. doi:https://doi.org/10.1016/j.addma.2020.101429.

[36] N.T. Aboulkhair, C. Tuck, I. Ashcroft, I. Maskery, N. Everitt, On the Precipitation Hardening of Selective Laser Melted AlSi10Mg, Metall. Mater. Trans. A. 46 (2015) 3337–3341. doi:10.1007/s11661-015-2980-7.

[37] A. Mertens, O. Dedry, D. Reuter, O. Rigo, J. Lecomte-Beckers, Thermal treatments of AlSi10Mg processed by laser beam melting, in: Proc. 26th Int. Solid Free. Fabr. Symp., 2015: pp. 1007–1016.

[38] H. Asgari, C. Baxter, K. Hosseinkhani, M. Mohammadi, On microstructure and mechanical properties of additively manufactured AlSi10Mg_200C using recycled powder, Mater. Sci. Eng. A. 707 (2017) 148–158. doi:10.1016/J.MSEA.2017.09.041.

[39] A.H. Maamoun, M. Elbestawi, G.K. Dosbaeva, S.C. Veldhuis, Thermal post-processing of AlSi10Mg parts produced by Selective Laser Melting using recycled powder, Addit. Manuf. 21 (2018) 234–247. doi:https://doi.org/10.1016/j.addma.2018.03.014.

[40] M. Rafieazad, A. Chatterjee, A.M. Nasiri, Effects of Recycled Powder on Solidification Defects, Microstructure, and Corrosion Properties of DMLS Fabricated AlSi10Mg, JOM. 71 (2019) 3241–3252. doi:10.1007/s11837-019-03552-2.

[41] M. Navaser, M. Atapour, Effect of Friction Stir Processing on Pitting Corrosion and Intergranular Attack of 7075 Aluminum Alloy, J. Mater. Sci. Technol. 33 (2017) 155–165. doi:https://doi.org/10.1016/j.jmst.2016.07.008.

[42] A.H. Maamoun, S.C. Veldhuis, M. Elbestawi, Friction stir processing of AlSi10Mg parts produced by selective laser melting, J. Mater. Process. Technol. 263 (2019) 308–320. doi:https://doi.org/10.1016/j.jmatprotec.2018.08.030.

[43] A. Leon, E. Aghion, Effect of surface roughness on corrosion fatigue performance of AlSi10Mg alloy produced by Selective Laser Melting (SLM), Mater. Charact. 131 (2017) 188–194. doi:https://doi.org/10.1016/j.matchar.2017.06.029.

[44] A. Hadadzadeh, B.S. Amirkhiz, A. Odeshi, J. Li, M. Mohammadi, Role of hierarchical microstructure of additively manufactured AlSi10Mg on dynamic loading behavior, Addit. Manuf. 28 (2019) 1–13. doi:https://doi.org/10.1016/j.addma.2019.04.012.

# Chapter 2

# On Microstructure and Early-Stage Corrosion Performance of Heat-Treated Direct Metal Laser Sintered AlSi10Mg[1] [2]

## Preface

A version of this manuscript has been published in the Additive Manufacturing Journal and ICAA16 conference proceeding. I am the first and corresponding author of thesis papers. Along with the co-authors, Parisa Fathi, Dr. Mohsen Mohammadi, and Dr. Ali Nasiri, I investigate the impact of the post-printing heat treatment on the microstructure and corrosion performance of the L-PBF AlSi10Mg alloy. I prepared methodology, experimental, formal analysis, and the first original draft of the manuscript and subsequently revised the manuscript based on the coauthors' feedback and also the peer review process. The co-authors Dr. Mohammadi and Dr. Ali Nasiri helped in conceptualization, design, project administration, and supervision, review & editing of the manuscript.

---

[1] M. Rafieazad, M. Mohammadi, and A. Nasiri, On Microstructure and Early-Stage Corrosion Performance of Heat-Treated Direct Metal Laser Sintered AlSi10Mg, Addit. Manuf., 2019, 28, p 107–119. (IPF=7.002)

[2] M. Rafieazad, P. Fathi, M. Mohammadi, and A.M. Nasiri, Low temperature heat-treatment cycle on AlSi10Mg_200C alloy fabricated by direct laser metal sintering: Microstructure evolution and corrosion resistivity, ICAA16 conference, (Full Paper), Feb2018

## Abstract

This study examines the impact of low-temperature heat-treatment on the microstructure and corrosion performance of direct metal laser sintered (DMLS)-AlSi10Mg alloy. Differential scanning calorimetry (DSC) was used to determine the phase(s) transition temperatures in the alloy. Two exothermic phenomena were detected and associated with the $Mg_2Si$ precipitation and Si phase precipitation in the as-printed alloy. Based on DSC results, thermal-treatments including below and above the active Si precipitation temperature at 200 °C and 300 °C, respectively, and 350 °C as an upper limit temperature for 3 h were applied to the as-printed samples. Scanning electron microscopy and X-ray diffraction analysis confirmed that heat-treatment from 200 °C to 350 °C promotes the homogeneity of the microstructure, characterized by uniform distribution of eutectic Si in α-Al matrix. To investigate the impact of the applied heat-treatment cycles on corrosion resistance of DMLS-AlSi10Mg at early stage of immersion, anodic polarization testing and electrochemical impedance spectroscopy were performed in aerated 3.5 wt.% NaCl solution. The results revealed more uniformly distributed pitting attack on the corroded surfaces by increasing the heat-treatment temperature up to 300 °C, attributed to the more protective nature of the spontaneously air-formed passive layer on the surface of the alloy at initial immersion time. Further increase of the heat treatment temperature to 350 °C induced severe localized corrosion attacks near the coarse Si particles, ascribed to the increased potential difference between the coalesced Si particles and aluminum matrix galvanic couple. In comparison, the corrosion of the as-printed and 200 °C heat treated samples was characterized by a penetrating selective attack along the melt pool boundaries, leading to a higher corrosion current density and an active surface at early exposure, associated with the weakness of the existing passive film on their surfaces.

***Keywords:*** *Additive Manufacturing (AM); Direct Metal Laser Sintering (DMLS); corrosion; heat treatment; microstructure.*

## 1. Introduction

The growing demand for advanced engineering components with complex designs and exceptional mechanical performances requires implementing innovative manufacturing technologies. In this vein, additive manufacturing (AM) procedures as revolutionary fabrication techniques are gaining enormous attention owing to their innovative freedom to design complicated and near-net shape functional components mostly without any geometrical constraint, saving material due to lack of scrap, and efficient product fabrication within a few hours at lower costs [1]. AM usually leads to extremely rapid cooling and solidification rates ($10^3$–$10^{11}$ K/s [2]), giving rise to the formation of unique microstructural features different from the ones obtained from conventional manufacturing techniques [3].

Aluminum alloys containing silicon and magnesium as the primary alloying elements have conceived a lightweight alloy family owning a proper mechanical performance coupled with sufficient corrosion resistance [4]. Among a wide variety of alloys in this family, AlSi10Mg as a traditional cast alloy has been predominantly adopted by the AM industry, particularly through Direct Metal Laser Sintering (DMLS) process [5]. Low solidification shrinkage and cracking susceptibility and good weldability are common characteristics of this alloy due to its near-eutectic composition [1]. Furthermore, the addition of Mg to the composition of this alloy has provided an age-hardening property through precipitation sequences of $\alpha(\mathrm{Al}) \rightarrow$ (Guinier–Preston) GP zones $\rightarrow \beta'' \rightarrow \beta' \rightarrow \beta$, where GP zones are separated clusters of Mg and Si atoms, $\beta''$ and $\beta'$ are non-stable compounds of Mg and Si atoms with different stoichiometry, and β phase is the stable Mg2Si phase [6]. All these distinctive properties of AlSi10Mg alloy have led to a multiplicity of applications in aerospace and automotive industries [7].

The unique processing conditions during DMLS, such as rapid solidification of the material associated with extremely high cooling rates of small melt pools, produce a fine microstructure and a large amount of residual thermal stresses within the structure, which can create dimensional inaccuracy or distortion in the printed part [8]. For this reason, partial annealing heat-treatment is commonly utilized to avoid part's distortion and release some of the residual stresses [9]. However, previous studies have shown that a high-temperature heat-treatment cycle extensively alters the inherent microstructure of the as-printed DMLS-AlSi10Mg alloy, and consequently leads to mechanical properties degradation [10,11]. A few previous studies reported that increasing heat-treatment temperatures for this alloy decreases the solubility of Si in supersaturated α-Al matrix, which contributes to the coarsening and coalescence of the eutectic Si particles inside the α-Al matrix, resulting in a decrease in hardness value and tensile strength, whereas the elongation was found to increase significantly [6,12,13]. From this perspective, heat-treatment can be applied to optimize and tune mechanical properties of DMLS-AlSi10Mg alloy through microstructural modifications [14].

The impact of heat treatment on corrosion resistance of DMLS-AlSi10Mg alloy has been highlighted heretofore in three previous studies [15–17]. The first study was reported by Cabrini *et al*. [15], in which the effects of two heat treatment cycles, including low temperature partial annealing at 573 K for 2 h (also known as stress relieving), and annealing for 4 h at 823 K followed by water quenching, on corrosion behavior of DMLS-AlSi10Mg alloy were investigated in aerated Harrison solution. In this work, the high-temperature annealing of DMLS-AlSi10Mg alloy at 823 K was reported to form a uniform microstructure composed of coarse Si particles within the α-Al matrix [15]. After such a drastic change of the microstructure, an active behavior and a decreased corrosion resistance of the alloy, characterized by a severe localized corrosion in the Al matrix along the periphery of the coarse Si particles, were reported [15]. On the contrary, the untreated DMLS-AlSi10Mg sample and the stress-relieved ones were reportedly exhibited a better corrosion resistance, characterized by localized and selective attacks predominantly along the melt pool boundaries. Such preferential attack on the melt pool borders were ascribed to the increased content of the Si and the breakage of its network along the heat affected zone, where Si particles separate as idiomorphic crystals [5]. Furthermore, the authors reported that stress relieving of the alloy at 573 K does not contribute to a noticeable microstructural modification [15]. Analogously, very similar corrosion properties, *i.e.* corrosion potential and pitting potential, were reported for the untreated and stress relieved DMLS-AlSi10Mg alloy [15]. Therefore, a comparable short-term and long-term corrosion performance were reported for the untreated and stress relieved DMLS-AlSi10Mg samples [15].

Contrarily, the same authors, but in another study [16] conducted intergranular corrosion tests as per ISO 11846 and highlighted a different corrosion response for the DMLS-AlSi10Mg after heat treatment at 200 °C and 300 °C for 2 h followed by air cooling. According to this study, susceptibility of the alloy to the selective corrosion attack increases from the untreated AlSi10Mg to the heat treated ones up to 300 °C, whereas higher temperature heat treatments (at 400 °C and 500 °C) were reported to change the corrosion morphology, provoking more general corrosion characteristics in the AlSi10Mg alloy [16]. Therefore, the 300 °C (573 K) heat treated AlSi10Mg samples were shown to behave differently when exposed to the Harrison solution [15] versus a more aggressive electrolyte used to perform intergranular corrosion testing (30 g/L NaCl solution with 10 mL/L HCl for 24 h) [16]. Although no quantitative corrosion properties were presented in this work, the reported findings seems to contradict the authors' first work [15], in which a similar corrosion behavior was reported for the untreated and 300 °C stress relieved AlSi10Mg. This discrepancy, albeit was not explicated, could be attributed to the differences in the type of electrolyte and testing method used in aforementioned studies.

Finally, in a recent study by Rubben *et al*. [17], the impacts of three heat treatment cycles, including artificial aging at 170 °C for 6 h, stress relieving at 300 °C for 2 h, and stress relieving at 250 °C for 2 h, on the microstructure and corrosion behavior of the selective laser melted (SLM) AlSi10Mg in a 0.1 M NaCl solution were investigated. Interestingly, no change in the microstructure of the alloy was found after the artificial aging at 170 °C, although no elucidation for the stability of the microstructure even after 6 h at 170 °C was provided [17]. Analogous to Cabrini's first work [15], the polarization behavior of all heat treated samples were reported to be very similar [17]. However, the corrosion morphology of the samples were reported to change noticeably from a superficial corrosion attack coupled with formation of micro-cracks along the melt pool boundaries for the untreated and 170 °C aged samples to a more severe penetrating corrosion attack still preferentially oriented along the melt pool borders [17]. The long-term exposure of the samples to the electrolyte seemed to cause more degradation of the 250 °C and 300 °C heat treated samples than the untreated ones [17]. However, the reported deterioration of the corrosion performance of the heat treated AlSi10Mg samples was not supported by quantitative electrochemical data in their study [17]. This observation is not consistent with the Cabrini's first work [15], where a similar corrosion performance was reported for untreated and 300 °C heat treated DMLS-AlSi10Mg alloy, requiring further investigation.

Therefore, in the context of developing and applying appropriate heat treatment cycles for additively manufactured AlSi10Mg components, there are still many unanswered questions that demand for a complementary analysis. Further investigation on the impact of low temperature heat treatment cycles on the corrosion properties of DMLS-AlSi10Mg alloy is required to be able to clarify some of the contradictions that currently exist in the literature. In addition, defining a appropriate methodology to select appropriate heat treatment temperatures with respect to the existing phase transformations in this alloy would be an efficient way to effectively tailor the desired properties in the component through heat treatment. Focusing on these gaps, this study aims for a detailed investigation of the impact of low-temperature heat-treatments on the microstructure and early stage corrosion performance of DMLS-AlSi10Mg alloy. A thorough differential scanning calorimetric analysis was conducted to be able to select the desired heat treatment temperatures deliberately.

## 2. Experimental Procedure

### 2.1. Materials

In this work, AlSi10Mg cubes with 10 mm × 10 mm × 10 mm dimensions were produced using an EOS M290 metal additive manufacturing machine equipped with a 400 W Yb-fibre laser and 100 µm spot size, where the building platform was held at 200 °C throughout the whole process. The gas atomized AlSi10Mg powder used herein had an average particle size distribution of 15-45 µm with a nominal chemical composition given in Table 1. Other processing parameters used in the fabrication process include laser power of 370 W, scanning speed of 1300 mm/s, hatching distance of 190 µm, and powder layer thickness of 30 µm. Stripe hatch strategy with 67° laser beam rotation between successive layers was used to manufacture the samples. In addition, an argon atmosphere with an oxygen content of maximum 0.1% was used in the process.

Table 2. 1 Nominal chemical composition of AlSi10Mg powder (wt.%)

| Si | Mg | Fe | Mn | Ti | Zn | Cu | Al |
|---|---|---|---|---|---|---|---|
| *9.00-11.00* | 0.20-0.45 | ≤0.55 | ≤0.45 | ≤0.15 | ≤0.10 | ≤0.05 | Bal. |

## 2.2. Differential Scanning Calorimetry

Thermal analyses were conducted using differential scanning calorimetry (Mettler-Toledo DSC1) to detect any physical transformation such as phase transformations, or precipitation phenomena that the DMLS manufactured alloy might undergo. The tests were performed on the as-printed specimens in the temperature range of 0-550 °C, utilizing different heating rates of 2 °C/min, 5 °C/min, 10 °C/min, and 20 °C/min. The consistency of the results was determined by repeating each test on at least three samples.

## 2.3. Heat-treatment of the DMLS-AlSi10Mg Specimens

The analysis of the DSC results led to the selection of three different heat-treatment temperatures, including 200 °C, 300 °C, and 350 °C. The DMLS-AlSi10Mg samples were subjected to those temperatures for 3 h in an Argon atmosphere to minimize the oxidation during heat-treatment. This was followed by water quenching of the heat-treated samples to the room temperature.

## 2.4. Microstructure Characterization

To characterize the microstructure of the samples, all DMLS-samples were sectioned along both the building plane and the building direction, followed by standard grinding and polishing procedures for Al alloys utilizing a Struers Tegramin-30 auto-grinder/polisher. The Keller's reagent (2.5 vol.% $HNO_3$, 1 vol.% HF, 1.5 vol.% HCl, and 95 vol.% $H_2O$) was used to etch and reveal the microstructure. The microstructure of all samples was characterized using an optical microscope (Nikon Eclipse 50i) and a scanning electron microscope (SEM) (FEI MLA 650F). Phase characterization of the samples after each heat-treatment was determined using a Rigaku Ultimate IV X-ray diffraction (XRD) with Cu-Kα source at 40 kV and 44 mA over a diffraction angle range of 20°-50° with a step size of 0.02°.

### 2.5. Micro-hardness Measurement

Vickers micro-hardness tests were performed on planes parallel (side view) and perpendicular (top view) to the building direction utilizing a Buehler Micromet hardness test machine at a load of 100 gf and loading time of 15 s. It is worth mentioning that the reported micro-hardness test results for each sample in this study are the average value from at least 10 different indentation points on polished surfaces.

### 2.6. Anodic Polarization Test

The electrochemical measurements of all polished DMLS-produced samples were conducted using an IVIUM CompactStat™ Potentiostat with a three-electrode cell setup based on the ASTM G5 standard for potentiodynamic polarization measurements [18], using a graphite rod as the counter electrode (CE), a saturated silver/silver chloride (Ag/AgCl) as the reference electrode (RE), and the sample as the working electrode. Previous studies have shown a lower corrosion resistivity on the side view (parallel to the building direction) of the DMLS-AlSi10Mg than that of the top view, which was reported to be associated with the higher density of the melt pool boundaries containing an increased content of Si and breakage of the Si network along the heat affected zone [15]. For this reason, in this study, the electrochemical properties of the samples were only measured on the side planes. The samples were immersed in an aerated 3.5 wt.% NaCl solution to simulate seawater corrosion conditions at 25±0.5 °C using a temperature-controlled water bath. Before the tests, the open circuit potential (OCP) was monitored for 1 h to allow for the OCP stabilization. The applied potential range for the polarization measurements was from −0.02 $V_{Ag/AgCl}$ to +0.3 $V_{Ag/AgCl}$ versus the OCP employing the scanning rate of 0.125 mV/s.

Following the polarization tests, the corrosion morphology was investigated using the SEM, after corrosion product removal using concentrated HNO3 solution (15.8 N) in an ultrasonic bath for 20 min [19]. Repeatability of the results was measured by testing at least three samples.

### 2.7. Electrochemical Impedance Spectroscopy (EIS) Test

EIS tests were also carried out on the polished samples after 1 h of immersion time at OCP in aerated 3.5 wt.% NaCl solution at 25±0.5 °C. Sinusoidal potential signals with ±0.01 V amplitude over the OCP with a frequency range between 100000 Hz and 10 mHz with ten points per decade were applied. All corrosion tests herein were carried out only on the polished surfaces to evaluate the effect of microstructure resulted from the heat-treatment on the corrosion properties.

## 3. Results and Discussion

### 3.1. DSC Results

Figure 2.1 shows the DSC scan of the as-printed sample performed at 5 °C/min, indicating two distinguishable exothermic peaks with maximum temperatures at 236.7 °C and 296.5 °C and released enthalpies of 2.57±0.13 J/g and 0.57±0.04 J/g, respectively. The DSC curves obtained from the DMLS-AlSi10Mg specimens using four different heating rates (2 °C/min, 5 °C/min, 10 °C/min, and 20 °C/min) were analyzed and the resultant peak temperature values are reported in Table 2.

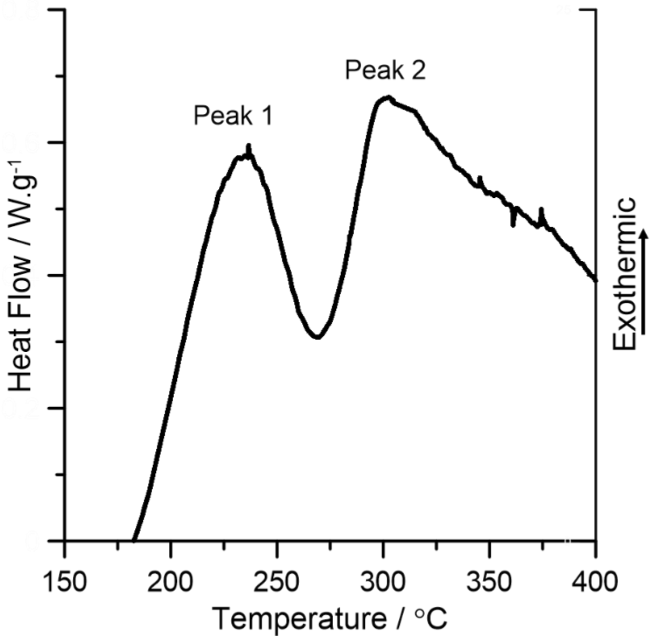

Figure 2. 1. DSC curve of the as-printed AlSi10Mg sample recorded at 5 °C/min.

Table 2. 2. Temperature values of Peak 1 and Peak 2 measured from the DSC scans of as-printed AlSi10Mg samples at various heating rates.

| Rate (°C/min) | Peak 1 (°C) | Peak 2 (°C) |
|---|---|---|
| 2 | 233.9±3.1 | 283.3±3.8 |
| 5 | 236.7±3.2 | 296.5±3.9 |
| 10 | 241.8±3.2 | 312.4±4.2 |
| 20 | 259.7±3.5 | 322.9±4.3 |

Considering the existence of two exothermic phase transformations, as shown in Figure 2.1, in order to determine proper heat-treatment cycles, the endpoint temperatures for the two distinguished transformations were determined. The peak temperature values versus the applied heating rates are plotted in Figure 2.2. To calculate the peaks' temperature values at isothermal transformation condition, the peaks' temperatures at the lowest possible heating rate value ($\varphi$ = 0 °C/min) should be calculated. Using two polynomial regressions, shown in equations (1) and (2) for the Peak 1 and Peak 2, respectively, the peaks' temperature values at $\varphi$ = 0 °C/min were calculated using the error parameter value ($R^2$) above 0.99.

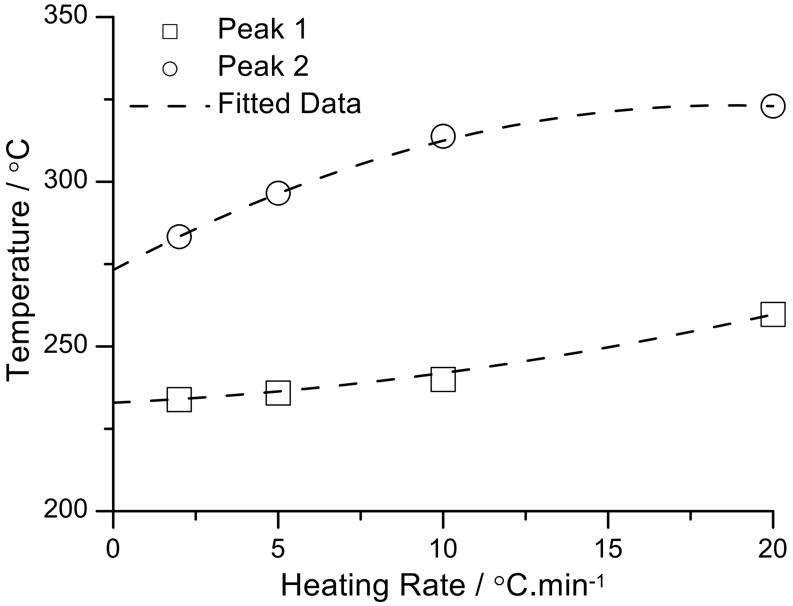

Figure 2. 2. Endpoint temperatures of peaks 1 and 2 as a function of different heating rates used in the DSC experiments.

$$T_{endpoint}^{Peak\ 1} = 0.0436\varphi^2 + 0.4673\varphi + 232.92 \qquad (R^2 = 0.9996) \qquad (1)$$

$$T_{endpoint}^{Peak\ 2} = -0.1438\varphi^2 + 5.36\varphi + 273.22 \qquad (R^2 = 1.0000) \qquad (2)$$

where $T_{endpoint}$ is the lowest possible temperature for the transformations activation, and $\varphi$ is the imposed heating rate. Therefore, by considering the lowest possible heating rate, $\varphi$ = 0 °C/min, the isothermal temperatures for the two distinguished transformations, corresponding to Peaks 1 and 2, were calculated to be 232.9 °C and 273.2 °C, respectively. The calculated endpoint temperatures can also be considered as the Y-intercepts, where the fitted graphs cross the temperature axis, as illustrated in Figure 2.2.

The temperature obtained from DSC scan for the lower temperature transformation, peak 1, is approximately the temperature reported in the previous studies [20–22] for the precipitation of $Mg_2Si$ in β" form. The temperature of the second peak is close to the temperature reported for the activation of Si interdiffusion in Al, which would typically contribute to the precipitation, coarsening, and spheroidization of Si particles in the alloy [23,24]. Therefore, such knowledge of the primary phase transformation temperatures based on the DSC analysis procedure presented herein is a great asset and a proper methodology to identify the right temperatures for the heat treatment of the alloy to obtain the desired microstructure. As an example, the DSC analysis results can rationalize the reason the aging heat treatment at 170 °C for 6 h does not lead to a profound effect on the microstructure of the DMLS-AlSi10Mg, reported in the recent work by Rubben *et al*. [17], as the selected temperature is significantly lower than the minimum required temperature for an active interdiffusion of Si in Al.

As the impact of Si network evolution resulted from applying a low temperature heat treatment on the early-stage corrosion properties of the DMLS-AlSi10Mg alloy is of particular interest herein, the heat treatment of the alloy was carried out at three temperatures with respect to the minimum required temperature for active interdiffusion of Si in Al (Si precipitation). These include a temperature below the activation of supersaturated Si precipitation from α-Al matrix (200 °C), a temperature close but higher than the Si interdiffusion activation temperature (300 °C), and a noticeably higher temperature (350 °C). The following section describes the microstructural characteristics of the alloy after applying each heat treatment cycle.

### 3.2. Microstructure Characterization

Optical and SEM micrographs of the untreated DMLS-AlSi10Mg samples in the as-printed condition are shown in Figure 2.3. The 3D representation of the optical micrographs of the DMLS-

AlSi10Mg sample in the as-printed condition (Figure 2.3a), from both side and top views (parallel and perpendicular to the building direction, respectively) confirm a proper overlapping and densification between melt pools (MP). From the side view, melt pools have a semi-circular shape, also known as a fish-scale pattern [1], which their size depends on the laser beam parameters, i.e. the beam power, hatch distance, and the scanning speed. As clearly shown on the top view of the Figure 2.3a, having columnar patterned melt pools with irregular geometries and directions is attributed to 67° rotation of the laser scan between consecutive layers [25].

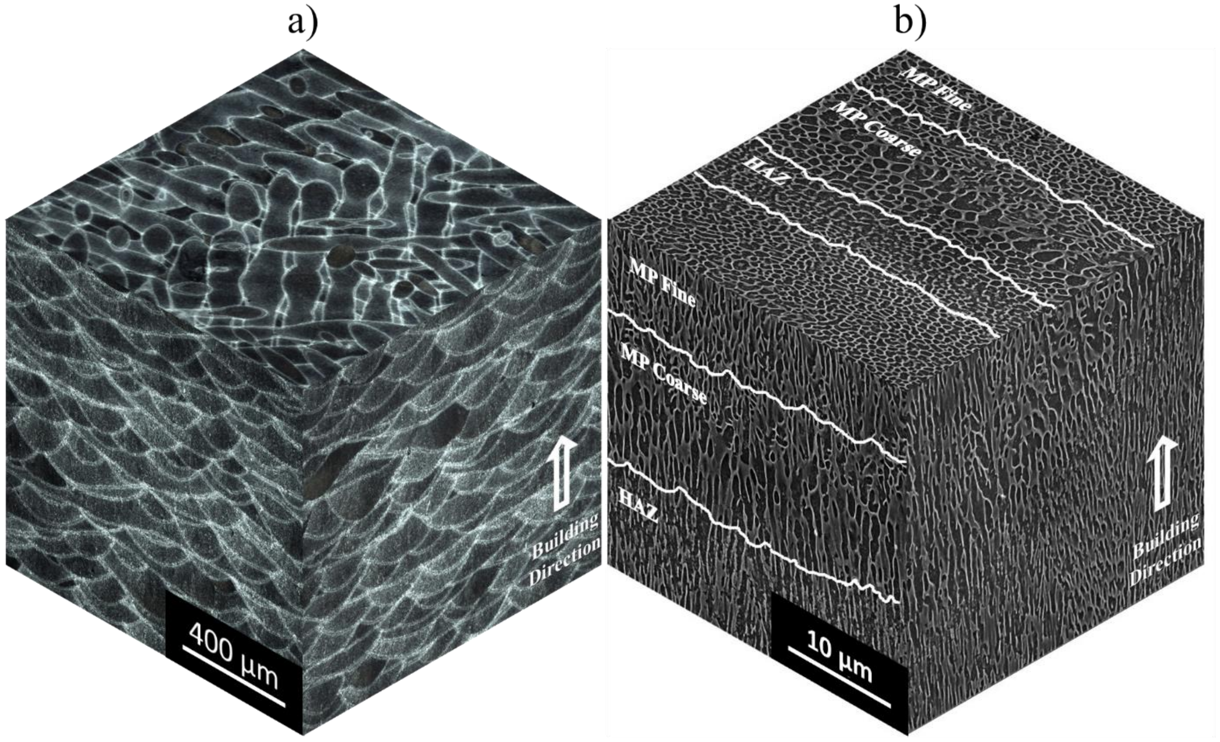

Figure 2. 3. 3D representation of (a) optical and (b) SEM micrographs of DMLS-AlSi10Mg sample, demonstrating the side view along the building direction, as well as the top view perpendicular to the building direction.

The SEM micrographs of the DMLS-AlSi10Mg from the sides and top views, presented in Figure 2.3b, demonstrate a fine cellular structure composed of an interconnected fine network of fibrous Si eutectic phase (light grey phase) distributed in a supersaturated α-Al matrix (darker phase).

Three distinguishable regions with distinct microstructures across the melt pool, including the fine cellular structure in the center (MP fine), a coarser structure from the center to the melt pool boundary (MP coarse), and a heat affected zone (HAZ) containing coarser idiomorphic Si crystals, can be clearly detected in Figure 2.3b. This transition in microstructure forms due to the overlapping scanning lines and layer-by-layer solidification of material, resulting in different thermal histories from the center of a melt pool to the boundaries of its adjacent melt pools [26]. It should be noted that, critical solidification parameters, *i.e*. temperature gradient ($G$) and solidification rate ($R$) dictate the solidified microstructure for a given composition [27]. These values vary from the melt pool borders towards its center, resulting in a fine cellular-dendritic morphology in the melt pool center, where $G$ is maximum and $R$ is minimum during solidification, and more elongated and coarser dendritic structure along the melt pool boundaries, where the melt pool experiences the lowest temperature gradient and the highest solidification rate [5]. Such transitions in the microstructure of the AlSi10Mg alloy based on the solidification behavior during the DMLS process have been modeled in a recent study [28]. The reported modeling results affirmed that the angle between the nominal growth rate and the aluminum dendrite growth direction is the dictating parameter that controls the transition of microstructure from a fine cellular-dendritic morphology to a columnar dendritic structure [28].

Figure 2.4 shows the optical micrographs taken from the side views of the DMLS-AlSi10Mg sample after heat-treatment at 200 °C, 300 °C and 350 °C. As Figure 2.4a depicts, after heat-treatment at 200 °C, the overall macrostructure remains unchanged when compared to the as-printed condition (Figure 2.3a). After heat treatment of as-printed samples at 300 °C (Figure 2.4b), the melt pool boundaries' features were still preserved and the micrograph is quite similar to that of the as-printed sample, shown in Figure 2.3a. However, the heat-treated sample at 350 °C (Figure

2.4c) shows that the melt pool boundaries have started to diminish and are no longer as sharp and clear as the lower temperatures heat treated or the as-printed ones. Heat-treatment temperatures above 400 °C have been reported to make the boundaries totally blurry and absent [12,16]. Therefore, from the low magnification view, the low-temperature heat-treatments performed on the as-printed DMLS-AlSi10Mg in this study do not interrupt the melt pools' overall macrostructure and their boundaries noticeably.

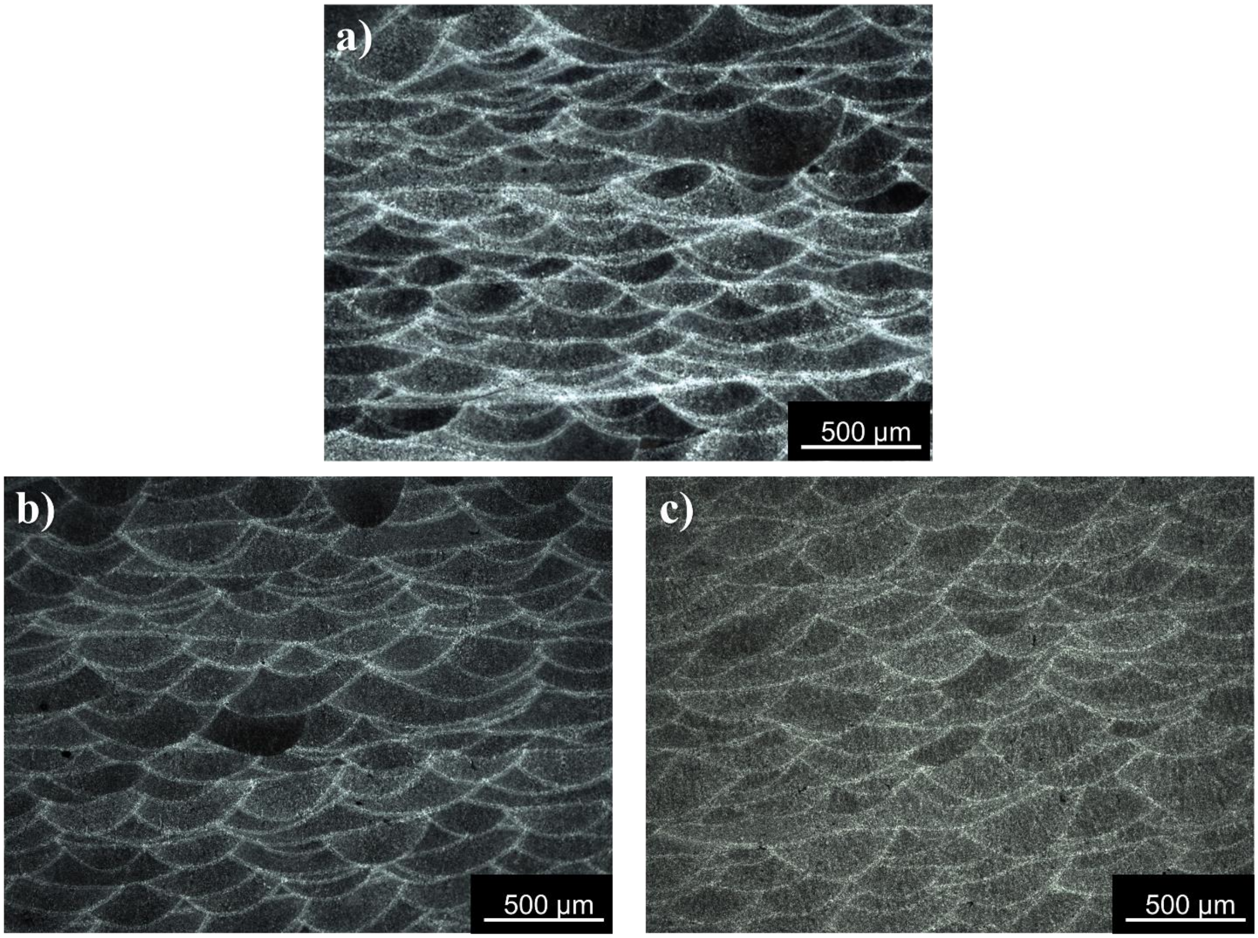

Figure 2. 4. Optical micrographs taken from side view of the DMLS-AlSi10Mg heat-treated at a) 200 °C, b) 300 °C and c) 350 °C.

Figure 2.5 shows the 3D representation of SEM images including the sides and top views of the DMLS-AlSi10Mg after heat-treatment at various temperatures, *i.e*. 200 °C, 300 °C, and 350 °C. The evolving of the Si network morphology and distribution in the DMLS-AlSi10Mg structure by increasing the heat-treatment temperature is clearly visible. The SEM micrographs revealed that by increasing the heat-treatment temperature from 200 °C to 350 °C, not only the light grey intercellular Si network is broken by the growth of silicon phase into idiomorphic particles (see Figure 2.5c), which has resulted in an obscured Si network boundary, but also the precipitation of newly formed Si particles inside the α-Al dendrites arises.

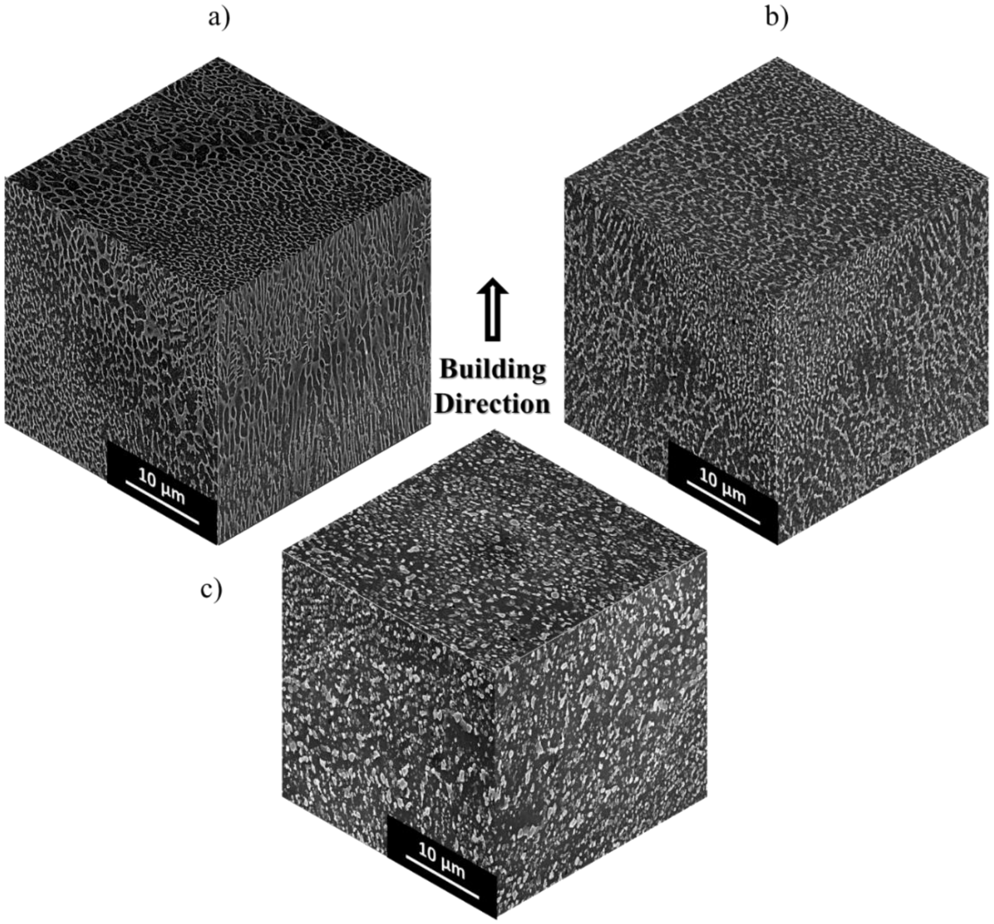

Figure 2. 5. 3D representation of the SEM micrographs taken from the DMLS-AlSi10Mg after heat-treatment at a) 200 °C, b) 300 °C, and c) 350 °C.

As shown in Figure 2.5a, the heat-treatment at 200 °C has not altered the microstructure of the as-printed sample, and as reported in previous studies, heat treatments at 200 °C or lower temperatures are primarily recommended for relieving the internal residual stresses derived from the manufacturing process of this alloy [29]. A noticeable breakage of the Si network was detected after 300 °C heat treatment (see Figure 2.5b). Some remaining features corresponding to the melt pool boundaries were still retained at 300 °C, and as reported in a previous study, the heat-treatment at 200 °C and 300 °C keeps the melt pools still visible [16]. As shown in Figure 2.5c, heat-treatment at 350 °C has resulted in a heavily precipitated microstructure (Si spheroidization and coarsening), containing a high density of Si particles (approximately 0.20-4.00 μm in size) with irregular shapes embedded in the α-Al matrix.

The heat treated microstructures of the top and the side views of the DMLS-AlSi10Mg (see Figure 2.5) confirmed a similar morphology and distribution of Si particles after the low-temperature heat treatment cycle on both cross sections. Uniform precipitation of Si particles was also detected along the intercellular boundaries with the increase in the heat-treatment temperature, which was found to be consistent with the results reported in a previous study [30], giving rise to a more uniform microstructure than that of the as-printed AlSi10Mg sample [15].

The observed microstructures after low-temperature heat treatments at different temperatures are consistent with the DSC analysis results, in which two exothermic transformations, *i.e.* precipitation of $Mg_2Si$ phase and precipitation and coarsening of Si in α-Al matrix, were predicted to occur at 232.9 °C and 273.2 °C temperatures, respectively. An active interdiffusion of Si in the aluminum matrix at $T > 273.2$ °C has contributed to the breakage of the Si network and precipitation of Si particles from the matrix by an exothermic reaction, followed by further coarsening of the existing Si particles when the heat-treatment temperature reached 350 °C.

Therefore, the cellular structure of the as-printed AlSi10Mg is ceased after heat-treatment at 350 °C, ascribed to the compositional homogenization and the Si particles' coarsening in the microstructure. It is worth noting that, although formation of $Mg_2Si$ phase was predicted by the DSC testing to occur at 232.9 °C, due to the extremely small size of this phase (< 10 nm [6,31]), it was not detected under SEM. Further microstructural characterization at higher magnifications using transmission electron microscopy (TEM) is required to investigate formation of $Mg_2Si$ phase during low temperature heat treatment of DMLS-AlSi10Mg alloy, which is the subject of a future study by the authors. Similarly, previous studies have reported the temperature range of 200 °C to 275 °C for the formation of $\beta''$-$Mg_2Si$ phase [12].

The XRD spectra of the as-printed DMLS-AlSi10Mg sample and the heat-treated ones are presented in Figure 2.6, revealing a strong texture in the (200) plane of the α-Al matrix, confirming the preferred crystal growth direction of <001> for Aluminum, indicating that z-direction (building direction) has been the main heat flow direction during solidification [28]. Also, the co-existence of both Al and Si phases in the structure was confirmed.

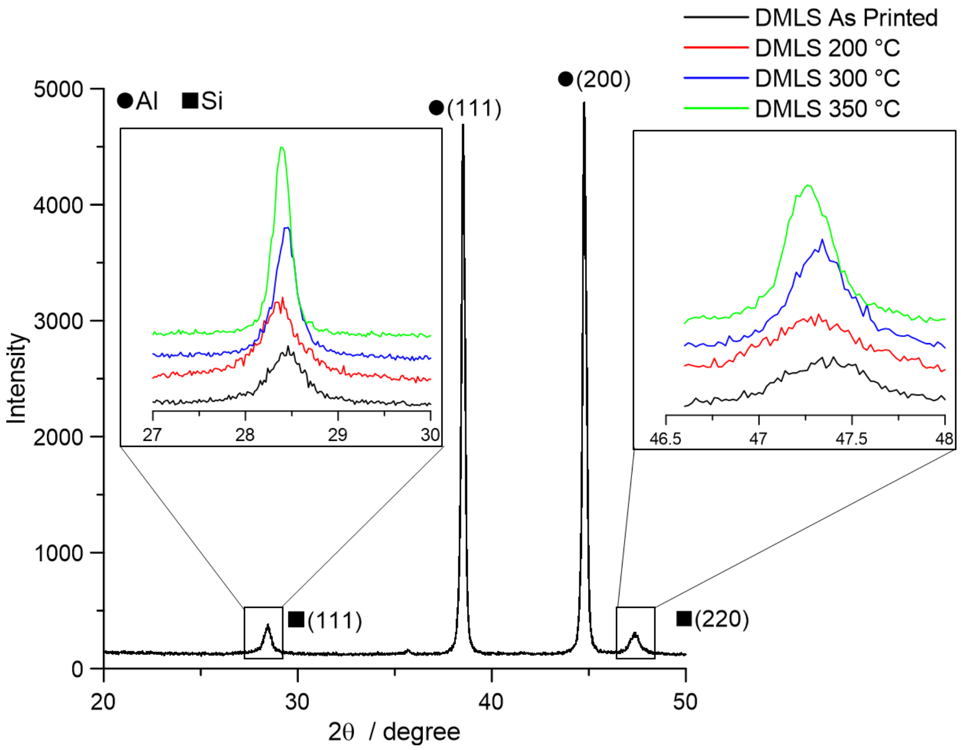

Figure 2. 6. X-ray diffraction spectra of the DMLS-AlSi10Mg samples before and after heat-treatment at different temperatures.

Based on Vegard's law, increasing the heat-treatment temperature reduces Si solid solubility in the Al matrix [14]. Accordingly, XRD patterns confirmed that increasing the heat-treatment temperature from 200 °C to 350 °C expands the Si peaks' intensity, corresponding to the increased volume fraction of the Si precipitates in the matrix. Therefore, the low-temperature heat-treatment of DMLS-AlSi10Mg at about 300 °C initiates the Si network breakage, and can result in a uniform dispersion of Si precipitates in the α-Al matrix at sufficiently long holding time.

## 3.3. Hardness Measurement Results

The trend of Vickers micro-hardness of the DMLS-AlSi10Mg samples after heat treatment at various temperatures vs the as-printed condition is presented in Figure 2.7. The hardness values of the samples were reduced by increasing the heat-treatment temperature from 200 °C to 350 °C. The as-printed sample showed the highest hardness value at 134 ± 2 HV0.1 associated with the fine grain structure and dispersion of fine eutectic Si in a supersaturated α-Al matrix, which resulted from the extremely fast solidification and cooling rate of the DMLS process ($10^3$ –$10^{11}$ K/s) [2]. The measured as-printed hardness value is very close to the reported values for the hardness of as-printed AlSi10Mg samples in previous studies [32]. As confirmed by the DSC results, heat-treatment at 232.9 °C can initiate the precipitation of the Mg2Si phase, providing precipitation hardening characteristics for this alloy. However, a continuous softening in this alloy is induced by further increasing the heat-treatment temperature from 200 ℃ to 350 ℃, resulting in a drastic decrease in the micro-hardness value from 132±2 HV0.1 to 69±2 HV0.1. This general behavior can be attributed to the breakage of Si network as well as the coarsening and coalescence of Si particles by increasing the temperature, which allows Si to diffuse at a higher extent, stimulating the growth of Si particles and reducing their number. Consequently, reinforcing Si particles become less effective in obstructing the movement of dislocations, causing softening of the alloy. Similar softening of as-printed additively manufactured AlSi10Mg alloy after applying common precipitation hardening heat treatments of Al-Si alloy, such as T6 heat treatment, were reported in a previous study [13].

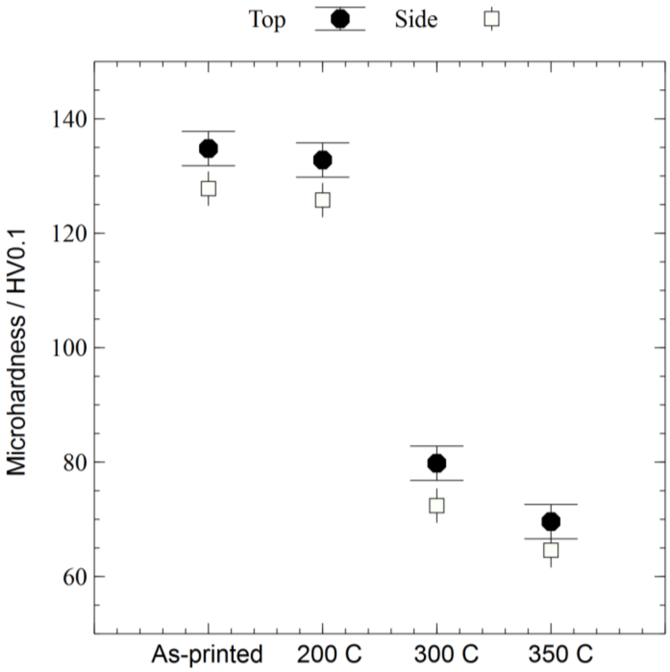

Figure 2. 7. The Vickers micro-hardness of the as-printed *vs* heat-treated DMLS-AlSi10Mg.

Comparing the micro-hardness results of the as-printed and heat-treated specimens, it is quite noticeable that the hardness values on the plane along the building direction (denoted as side in Figure 2.7) is lower than those on planes transverse to the building direction (denoted as top in Figure 2.7), confirming the existence of mechanical anisotropy even after heat treatment. A similar discrepancy in the hardness values measured from the top cross section *vs* the side cross section of a DMLS-AlSi10Mg alloy was also reported in a previous work [25], and the authors attributed that to the morphology of the melt pools, the used layer-by-layer additive method, and the non-homogeneous grain structure established through the non-uniform thermal gradient across the melt pools, resulting in the formation of more borderline porosities and defects on the side plane of the sample. Such imperfections make the side view planes softer than the top view planes [25]. Even from the electrochemical stability's perspective, Cabrini *et al*. [15] reported higher susceptibility of the side planes to selective corrosion attack in a chloride-containing environment than the top plane.

### 3.4. Anodic Polarization Results

Figure 2.8a shows the open circuit potential (OCP) evolution with time for the untreated and heat treated samples. The open circuit potential was measured over 3600 s before the anodic polarization tests in aerated 3.5 wt.% NaCl solution. The OCP values for all four samples were stabilized eventually in the range of -0.65 to -0.75 $V_{Ag/AgCl}$. The minor difference in the stable OCP values of the samples can be explained by the consistency of the entire composition on their surfaces, even though various microstructural features were formed on the heat-treated samples [17,33]. Analogously, very close OCP values were reported for the DMLS-AlSi10Mg alloy and its cast counterpart by Revilla [33], owing to their similar chemical composition and despite their significantly different microstructure. However, it should be mentioned that, by increasing the heat-treatment temperature, the OCP trend became noisier and more unstable, confirming that the applied heat-treatment can affect the degree of surface activity. The slightly higher OCP values of the 300 °C heat treated samples can also be ascribed to the uniformity of the microstructure and the reduced compositional inhomogeneity between the melt pools' center and their boundaries dominated by the extend of Si interdiffusion in $\alpha$-Al matrix.

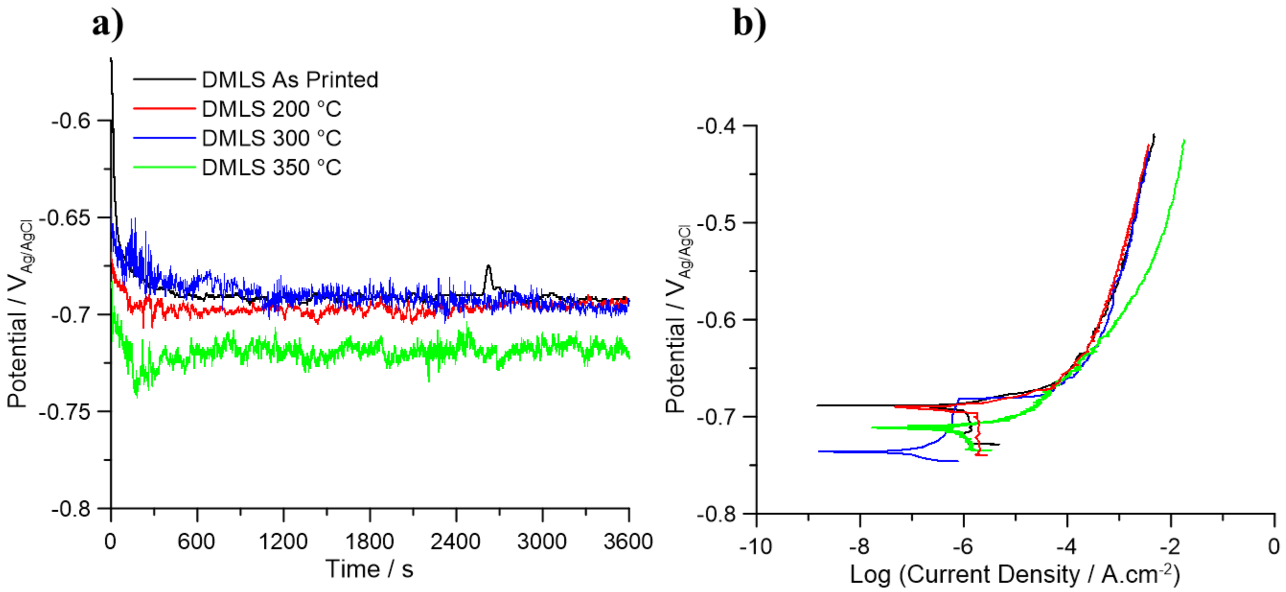

Figure 2. 8. a) Open circuit potential measurement over time, b) anodic polarization curves comparing the corrosion behavior of the as-printed DMLS-AlSi10Mg sample to the heat treated ones.

As illustrated in Figure 2.8b, all samples, except for the 300 °C heat treated DMLS-AlSi10Mg, revealed an active-like behavior at initial immersion time in the electrolyte, corresponding to the rapid increase of the current in their anodic branch by increasing the applied potential. However, after applying the heat treatment at 300 °C, a clear wide passive region ($E_{Corr.}$ + 0.06 $V_{Ag/AgCl}$) with lower corrosion current density appears on the graph, affirming a lower tendency for pit nucleation in 300 °C heat treated sample. Also, the slight shift of the corrosion potential to more active values in this sample can be plausibly attributed to the inherent microstructural inhomogeneity in a DMLS part on various planes, and was similarly detected in the previous studies [17]. However, the as-printed DMLS-AlSi10Mg and the 200 °C and 350 °C heat-treated ones exhibited approximately the same corrosion and pitting potentials (~ -0.69 $V_{Ag/AgCl}$, -0.69 $V_{Ag/AgCl}$, and -0.70 $V_{Ag/AgCl}$, respectively), meaning surface pitting can be readily triggered once the corrosion potential is reached.

Table 3 summarizes the polarization parameters derived from the anodic polarization plots shown in Figure 2.8, including the corrosion potential ($E_{Corr.}$), corrosion current density ($I_{Corr.}$), and pitting potential ($E_{pit}$) values of each of the as-printed and heat-treated DMLS samples.

Table 2. 3. Anodic polarization parameters of the heat-treated DMLS samples in aerated 3.5 wt.% NaCl solution

| | As-printed | 200 °C | 300 °C | 350 °C |
|---|---|---|---|---|
| $E_{Corr.}$ ($V_{Ag/AgCl}$) | -0.69±0.03 | -0.69±0.02 | -0.74±0.01 | -0.70±0.02 |
| $I_{Corr.}$ ($\mu A/cm^2$) | 1.90±0.38 | 1.79±0.24 | 0.19±0.45 | 3.66±0.86 |
| $E_{pit}$ ($V_{Ag/AgCl}$) | -0.69±0.03 | -0.70±0.03 | -0.68±0.01 | -0.70±0.02 |

As shown in Figure 2.5a, the low-temperature heat-treatment cycle at 200 °C has not altered the microstructure of the as-printed sample (compare Figure 2.5a with Figure 2.3b). The low-temperature heat-treatment at 200 °C is known as a recommended residual stress relieving cycle for DMLS-AlSi10Mg parts [29], derived from the manufacturing of the part as a result of Si atoms oversaturation in α-Al matrix due to extremely high cooling rates and thermal gradients inherently present in the DMLS [12]. The 200 °C heat treated sample exhibited very similar corrosion resistance to that of the as-printed sample, indicated by having approximately the same corrosion potential and corrosion current density values. The minor variation of the polarization data between the as-printed and 200 °C heat treated samples can be likely ascribed to the existing differences in terms of the density of the melt pool boundaries from sample to sample, rather than the change in the microstructure of the samples [17]. Also, the pitting potential of the as-printed and 200 °C heat treated samples remained approximately constant (around ~ -0.69 $V_{Ag/AgCl}$).

The polarization data demonstrates that the measured corrosion current density of the DMLS-AlSi10Mg samples reduces by increasing the heat-treatment temperature from 200 °C to 300 °C. This shift in the corrosion resistance of the DMLS-AlSi10Mg alloy can be attributed to the uniformity of the protective passive layer owing to the existing differences in the distribution of silicon particles on the surface affected by the heat-treatment [34]. The passive film breakdown potential values were similar for all DMLS samples and remained relatively unchanged ($E_{pit}$ ~ -0.69±0.01 $V_{Ag/AgCl}$), suggesting that the passive film composition remains almost constant, as the $E_{pit}$ value is primarily controlled by the passive film composition [34].

By further increasing the heat treatment temperature to 350 °C, the corrosion current density was found to increase drastically ($I_{Corr.}$= 3.66±0.86 μA/cm$^2$), indicating the increased intensity of corrosion attack on the surface, contributing to a significant deterioration of the corrosion performance even at initial immersion time.

To investigate the severity and morphology of the corrosion attack, the samples' surfaces were studied using SEM after corrosion products removal. Figure 2.9 shows the SEM micrographs taken from the as-printed, 200 °C, 300 °C, and 350 °C heat-treated DMLS-AlSi10Mg surfaces after the anodic polarization test. As shown in Figures 2.9a-2.9d, a penetrating selective corrosion attack was clearly detected on the untreated and 200 °C heat-treated DMLS-AlSi10Mg samples that preferentially expanded along the melt pools' borders. Very similar corrosion attack was revealed on the untreated DMLS-AlSi10Mg samples in previous studies [15–17]. The presence of coarse idiomorphic silicon crystals, which act as preferential cathodic sites relative to the α-Al matrix along the melt pool boundaries, explains the selective attack in the HAZ [33]. After heat-treatment at 300 °C, as depicted in Figures 2.9e and 2.9f, the applied heat-treatment cycle resulted in the interruption of the Si network and stimulated the precipitation of Si from supersaturated α-Al matrix (as T > 273.2 °C). However, the improved uniformity of the microstructure has suppressed penetrating selective corrosion attacks and contributed to a lower corrosion current density at initial immersion time in 3.5 wt.% NaCl electrolyte.

In addition, since the heat-treatment at 300 °C does not promote Si coarsening significantly (the average particles size < 0.20 μm), the galvanic coupling between the Si particles and the surrounding Al matrix was not provoked noticeably at initial immersion time. Therefore, as Figures 2.9e and 2.9f show, there are limited number of pits formed on the surface of 300 °C heat treated DMLS-AlSi10Mg after anodic polarization test. On the other hand, the 350 °C heat-treated sample, as shown in Figures 2.9g and 2.9h, behaved differently and showed more severe localized corrosion in the Al matrix around the periphery of the Si particles, but without a penetrating selective attack. This is ascribed to the interruption of the continuous Si network and their breakage into small Si particles, followed by their growth and coalescence with further increasing of the heat treatment temperature to 350 °C. Albeit more uniform microstructure seems to be formed, the growth of small Si particles into large Si precipitates with irregular shapes and geometries (the case of 350 °C heat treated sample), has resulted in a higher potential difference between the coarse Si precipitates and α-Al matrix, and induced a galvanic corrosion with a higher driving force. For a better interpretation of polarization results and to further investigate the protectiveness of the existing passive layer on all samples after the applied low-temperature heat-treatment, the EIS tests were conducted at initial immersion time.

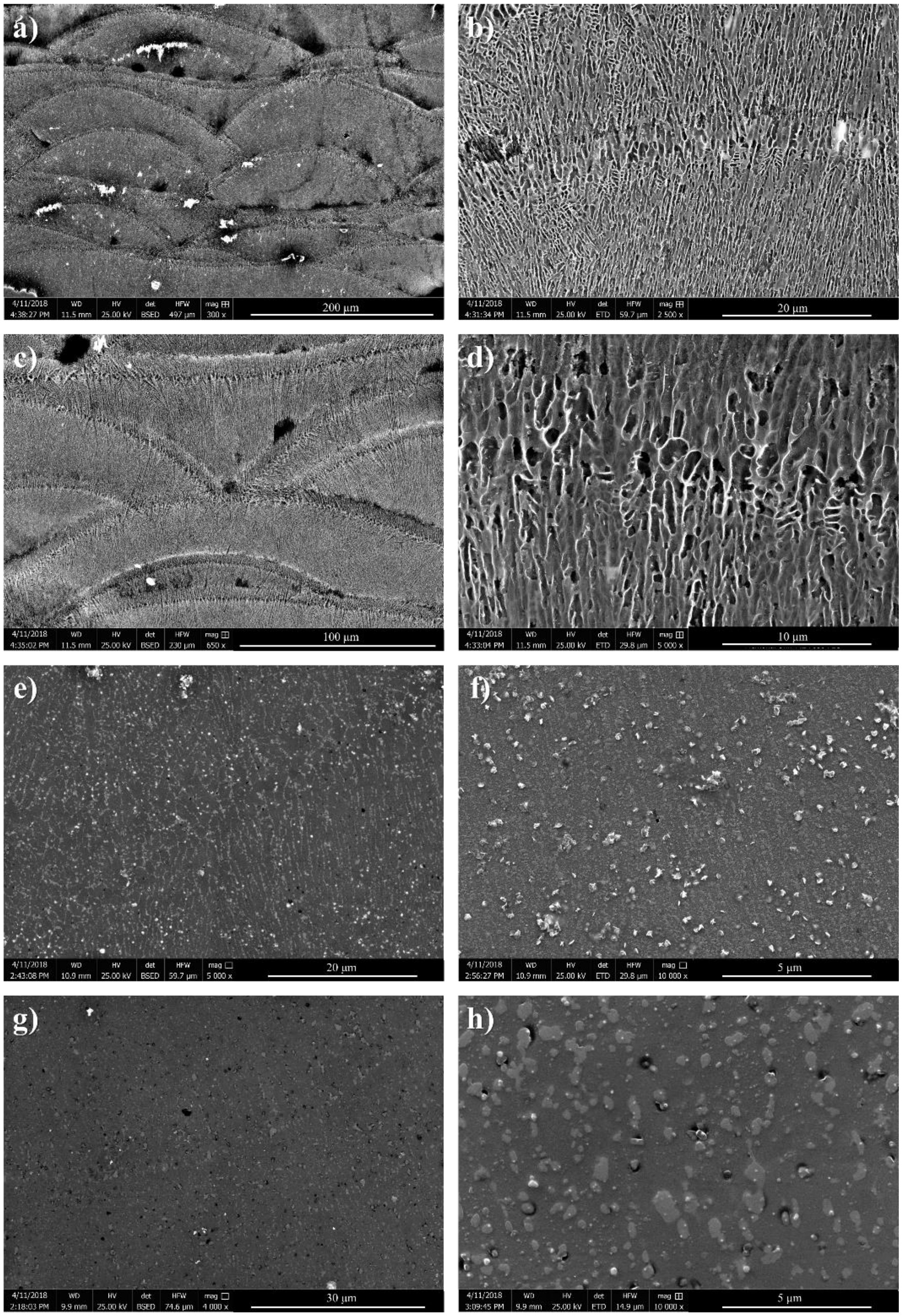

Figure 2. 9. SEM back-scattered (left column) and secondary electron (right column) images taken from the surface of the DMLS-AlSi10Mg heat treated at a) and b) As-printed, c) and d) 200 °C, e) and f) 300 °C, g) and h) 350 °C after the anodic polarization test and corrosion product removal.

### 3.5. Electrochemical Impedance Spectroscopy (EIS) Results

Figure 2.10 shows the modification of the EIS spectra in the aerated 3.5 wt.% NaCl solution after 1 h of immersion time. The constant high-frequency impedance values in the Bode plots follow the electrolyte resistance and the resultant ohmic drop in the solution. The impedance differences in the middle-low frequency ranges are more evident when changing the heat-treatment temperature. The phase angle vs frequency diagrams (shown in Figure 2.10a) of both untreated (as-printed) and the heat treated samples were characterized by two capacitive peaks with well-defined time constants one at lower frequency (30-200 mHz) and the other at higher frequency ranges (100-800 Hz). The low-frequency peak describes diffusion within corrosion products and within localized and selective attack zones, while the high-frequency peak displays the sealing of the corrosion products inside porosities [35]. It is also worth mentioning that the frequencies of the distinct peaks were approximately constant, independent from the heat-treatment temperatures. Correspondingly, two peaks were also generated on the Nyquist plots (shown in Figure 2.10b). The first Nyquist curvature corresponds to the high-frequency peak and the second one describes the low-frequency peak in the phase plot. As a general trend, the larger radius of the Nyquist curvature is an indication of improvement in the corrosion resistance of the sample.

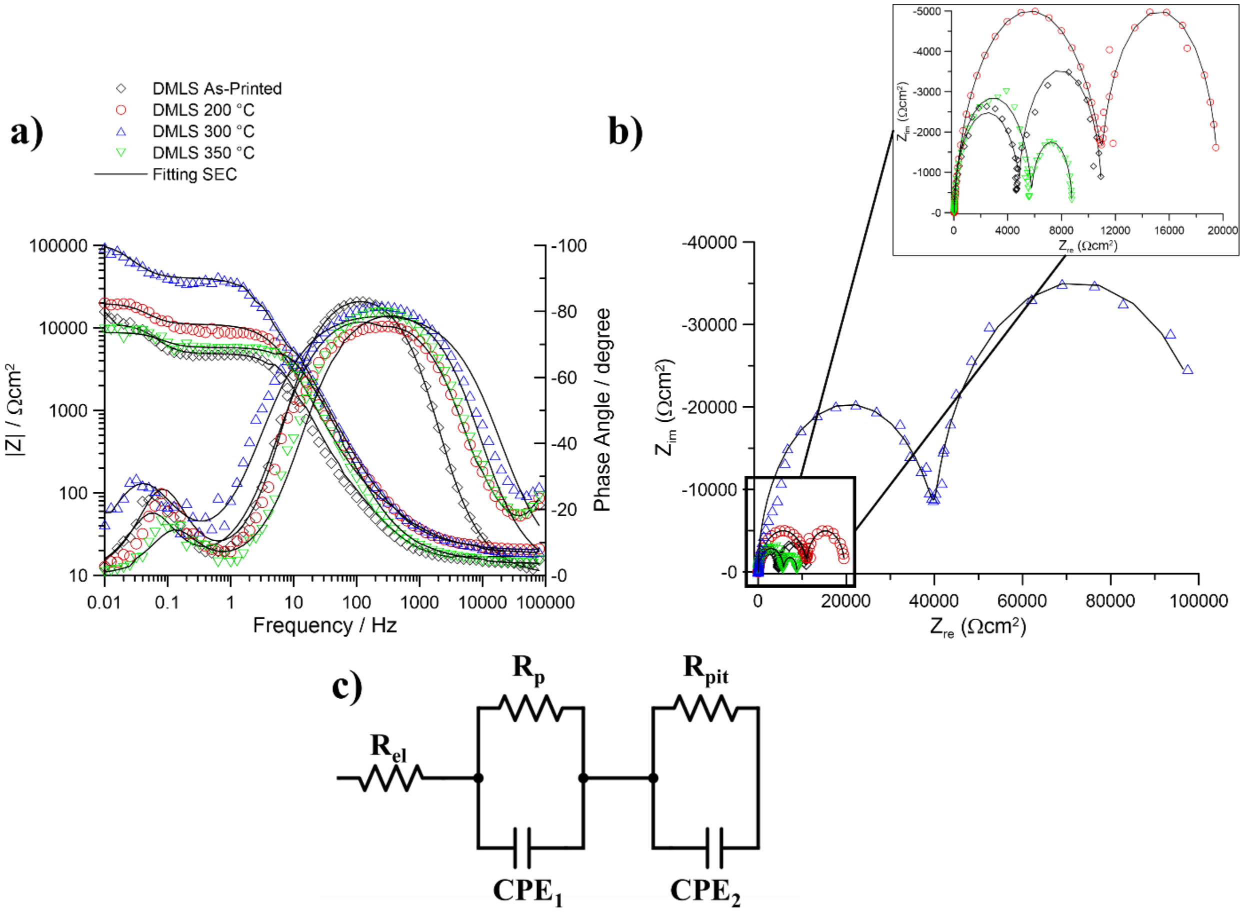

Figure 2. 10. EIS spectra and the fitting data, a) Z modulus, Bode phase angle plot, b) Nyquist spectra of the as-printed and heat treated DMLS-AlSi10Mg after heat-treatment at various temperatures, and c) the simplified equivalent circuit proposed to simulate the EIS spectra evolution.

The Bode plots show a significantly higher (approximately one order of magnitude) absolute value of impedance for the 300 °C heat treated sample than the other samples at the lower frequency range after 1 h of immersion time, which is consistent with the anodic polarization graphs shown in Figure 2.8, indicating the lowest corrosion current density for the 300 °C heat treated DMLS-AlSi10Mg sample. This confirms an improvement in the protective nature of the passive layer against corrosive environment after the low-temperature heat-treatment at optimum temperature of 300 °C. It should be noted that the reported results herein and the observed improved corrosion resistance of the 300 °C heat treated sample is limited to only the initial immersion time, representing the material's behavior at the early stage of corrosion. Studying the behavior of the material at longer immersion time or immersion in more aggressive environments, such as in Harrison solution, was not the aim of this study and has been already reported in the previous works [15–17]. Such improvement of the passive film properties on the surface of 300 °C heat treated DMLS-AlSi10Mg at the early stage of immersion was not reported in the work by Rubben [17], even though the anodic polarization results in their study revealed a slight improvement in the pitting potential of the alloy on the x-y plane with a clear passive region (~ 0.2 $V_{Ag/AgCl}$ above the pitting potential), whereas the as-printed and lower temperature heat treated surfaces, *i.e.* 170 °C and 250 °C, exhibited an active-like behavior. The authors attributed the observed differences in the polarization data of the sample to the inherent microstructural inhomogeneity of additively manufactured parts, such as having different density of the melt pool boundaries on each surface [17]. However, the anodic polarization results and the electrochemical impedance spectroscopy of the DMLS-AlSi10Mg surfaces before and after applying the heat treatment herein confirmed that low temperature heat treatment of the alloy at 300 °C can slightly enhance the protectiveness of the passive layer on its surface, leading to an improved corrosion performance at initial immersion time.

Although the heat-treatment at 300 °C promotes silicon particles precipitation followed by a slight coarsening, their size remains significantly smaller than that of the 350 °C heat-treated sample. By further increasing the heat treatment temperature to 350 °C, as Figure 2.5c shows, more active interdiffusion of Si in α-Al matrix led to a significant coarsening and coalescence of Si precipitates, particularly around the melt pool boundaries, where the existing particles were initially coarser in the as-printed condition. Therefore, the formation of lager size Si precipitates coupled with an overall higher Si concentration in the precipitation form would lead to a greater potential difference between the coarser Si particles and Al matrix, rendering a higher driving force for the galvanic corrosion [17,33]. Consequently, a deeper localized corrosion attacks on the Al matrix phase at the periphery of the coarse Si particles can be detected. An analogous observation but for a more extreme heat treatment cycle was reported by Cabrini *et al*. [15], in which a reduced corrosion resistance of the DMLS-AlSi10Mg samples after annealing for four hours at 550 °C was observed. This high-temperature heat-treatment cycle resulted in a significant coarsening of the Si particles [15], which was reported to cause a severe localized corrosion attack in the Al matrix at the periphery of the coarse Si particles, without features of penetrating selective attack.

As shown by arrows in Figure 2.11b, the severe localized corrosion of the Al matrix adjacent to the larger silicon particles of the 350 °C heat treated DMLS sample after 15 days of immersion time in the electrolyte caused the detachment and leaching of the silicon particles from the surface, leading to a localized penetrating attack. On the contrary, in the untreated or the lower temperature heat treated sample, *i.e*. 200 °C, as a result of inherent microstructural inhomogeneity of the printed part and the existing coarser Si network/particles in the MP coarse and HAZ regions along the melt pool borders than those formed in the interior of the melt pools (MP fine regions), the attack tends to follow the melt pool boundaries, leading to a selective corrosion attack along the melt pool borders, shown in Figure 2.11a by arrows.

In addition, Figure 2.11a reveals that a long exposure time to the corrosive electrolyte can contribute to the formation of micro-cracks at the border of the melt pool boundaries. Similar cracking of the melt pool boundaries was also detected on the untreated and artificially aged DMLS-AlSi10Mg samples at 170 °C in the previous work by Rubben [17] after polarization testing in 0.1 M NaCl solution, and was associated with the existing residual stress from the fabrication process in the as-printed and 170 °C artificially aged samples along with preferential dissolution of α-Al predominantly from the melt pool boundaries. Occurrence of such cracking along the melt pool boundaries even after 200 °C heat treatment herein confirms that the heat treatment of the DMLS-AlSi10Mg alloy for 3 h at 200 °C is not sufficient to entirely release the residual stresses from the structure of the printed part.

After 350 °C heat treatment for 3 h, the corroded surfaces of the samples did not reveal any superficial cracking even after a long immersion time in the electrolyte (*i.e.* 15 days, shown in Figure 2.11b), affirming that both temperature and time were high enough for a complete relief of the residual stresses.

The observed improvement in corrosion resistance of DMLS-AlSi10Mg alloy after 300 °C heat treatment of as-printed alloy is plausibly limited to only the initial immersion time, as the previous study [16] has reported that after long immersion time of the 300 °C heat treated DMLS-AlSi10Mg sample in a more corrosive electrolyte (30 g/L of NaCl with 10 mL/L of HCl), the sample's surface experienced a more severe selective corrosion attack than the untreated sample. Similar increased susceptibility of the alloy after 300 °C heat treatment for 2 h to the selective corrosion attack after immersion testing at OCP in 0.1 M NaCl solution was also reported by Rubben *et al.* [17], and was correlated to the larger Volta potential difference between the Si phase and the Al matrix after applying the heat treatment, leading to a greater driving force for galvanic coupling to initiate. Therefore, the presented results in this study do not contradict the previously reported investigations, but rather complement their observations, as it primarily describes the behavior of the heat treated DMLS-AlSi10Mg surface at initial immersion time rather than the long term behavior of the surface when exposed to a more corrosive electrolyte.

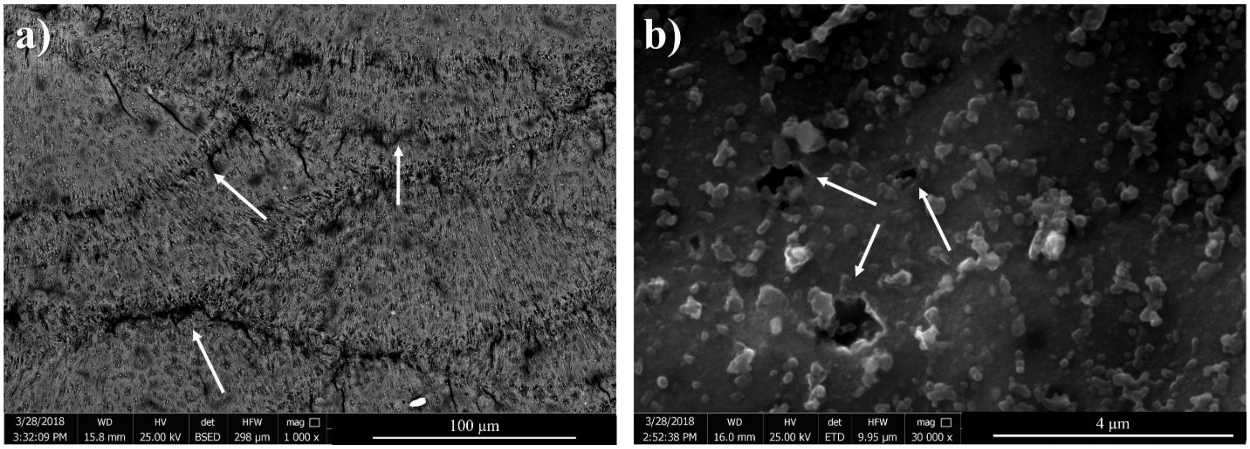

Figure 2. 11. SEM images from the surface of the DMLS-AlSi10Mg heat-treated at a) 200 °C and b) 350 °C after 15 days of immersion time in aerated 3.5 wt.% NaCl solution, followed by the corrosion product removal.

## 3.6. EIS Spectra Fitting and Modelling

For a better interpretation of the EIS data obtained in this study and to be able to describe the modification of protective passive film on the surface, the simplified equivalent circuit (SEC), shown in Figure 2.10c, was employed and fitted to the experimental EIS data. The equivalent electrical circuit model is able to physically interpret the complexity of the corrosion behavior of the DMLS samples [15].

The impedance response of all samples was described using a simplified equivalent circuit, similar to the one suggested by Cabrini *et al*. [15], which leads to a model of $R_{el}(Q_pR_p)(Q_{pit}R_{pit})$, shown in Figure 2.10c. This circuit is appropriate to explain the observed capacitive arcs on the Bode plots of the DMLS-AlSi10Mg through simulating two well-defined peaks and time constants. This circuit is composed of series of resistance, and two resistance/constant phase element parallels, where $R_{el}$ describes the ohmic drop in the solution, resulted from the resistance of the electrolyte. In this circuit, $R_p$ and $CPE_p$ correspond to the resistance and capacitive behavior of the passive layer, respectively. Similarly, $R_{pit}$ and $CPE_{pit}$ correspond to the resistance and the constant phase element of the corroding pits, respectively. The impedance of a Constant Phase Element (*CPE*) is defined as:

$$Z_{CPE} = [Q(i\omega)^n]^{-1} \quad (3)$$

where $Q$ is the *CPE* constant, $i$ is the imaginary unit ($i = \sqrt{-1}$), $\omega$ is the angular frequency, and $n$ is the dispersion coefficient and its value ranges between -1 and 1, describing inductivity, resistance, Warburg impedance, and the capacity for $n$ equal to -1, 0, 0.5, and 1, respectively [36]. In all investigated samples, the calculated values for the dispersion coefficient ($n$) was 0.89±0.01 so that the constant phase element can be replaced by the capacitor in the proposed equivalent circuit shown in Figure 2.10c. Figures 2.10a and 2.10b also show the fitting data of the EIS results collected from applying the equivalent circuit, which fitted closely with the experimental data, and include a clear description of two well-defined capacitive peaks. Considering the capacitive behavior shown in Figures 2.10a and 2.10b, the capacitive arcs at the higher frequency range display the general surface corrosion, and the low-frequency arcs are associated with the localized corrosion attacks on the surface. The computed parameters of the equivalent circuits are summarized in Table 4. Comparing the general response of the passive layer resistivity ($R_p$) and the pitting resistance ($R_{pit}$) for each sample confirms that except for the 300 °C heat treated sample, for all other samples the pitting resistance values are lower than the general passive layer resistance. This indicates that pitting corrosion is the dominant factor in controlling the corrosion behavior of the samples, which is in agreement with the observed anodic polarization curves in Figure 2.8b, showing an active-like behavior for all heat treated samples, except for the 300 °C heat treated one. Differently, the 300 °C heat treated sample revealed a higher pitting resistance than the passive layer resistance at initial immersion time, promoting the formation of a clear passive region, shown in Figure 2.8b.

Table 2. 4. EIS parameters of the equivalent circuits shown in Figure 2.10c.

| ***Sample*** | $R_{el.}$ ($\Omega cm^2$) | $R_{p.}$ ($k\Omega.cm^2$) | $R_{pit}$ ($k\Omega.cm^2$) | ***CPE, Q*** ($\mu\omega^{-1}\ s^{-n}\ cm^{-2}$) | $CPE_{pit}$, Q ($\mu\omega^{-1}\ s^{-n}\ cm^{-2}$) |
|---|---|---|---|---|---|
| ***As-printed*** | 10.69 | 5.96 | 4.93 | 518 | 4.94 |
| ***DMLS 200°C*** | 13.22 | 11.18 | 8.32 | 3.39 | 504 |
| ***DMLS 300°C*** | 18.79 | 40.38 | 64.62 | 1.46 | 1190 |
| ***DMLS 350°C*** | 11.68 | 4.81 | 2.92 | 786 | 2.55 |

As opposed to the 300 °C heat treated one that showed a noticeably high pitting resistance at the initial stage of immersion (an indication for having a passive surface), the as-printed, 200 °C, and 350 °C heat treated samples revealed relatively low $R_p$ and $R_{pit}$ values, particularly the 350 °C heat treated one, indicating characteristics of a surface that has not been fully passivated. The significantly low $R_p$ and $R_{pit}$ values of the 350 °C heat treated sample is ascribed to the existence of larger size Si particles in its structure, leading to an active behavior. However, it is known that as the corrosion progresses, either detachment of the large Si particles from the growing and coalesced pits, as the Al matrix around them oxidizes, or their coverage by the corrosion products could potentially lead to the surface's full repassivation [37]. When such state of full passivation is reached, plausibly at longer immersion time, the impedance value could potentially increase, attributed to the formation of a more stable passive film on the surface [38].

Therefore, the EIS results and the modeled data herein confirmed existence of a passive layer with a more protective nature on the 300 °C heat treated DMLS-AlSi10Mg surface at initial immersion time, leading to an improved electrochemical response. This is possibly associated with the increased uniformity of the microstructure with confined coarsening of Si particles, resulted from the heat treatment, which could potentially contribute to the spontaneous formation of a more uniform and stable passive layer in air. It should be noted that the improved corrosion response of the DMLS-AlSi10Mg surface after 300 °C heat treatment in this study was detected at the early stage of immersion. The recent studies on this alloy [15–17] are persuasive to believe that upon breakage of this pre-existing passive layer, either as a result of long exposure time or being exposed to a more corrosive electrolyte, the enhanced corrosion response of the 300 °C heat treated surface will be diminished. At that point, the Volta potential difference between the Si particles and the α-Al matrix becomes the dominant factor in controlling and dictating the corrosion properties. As the Si network breakage and slight growth of Si particles occur during the heat treatment, the Si-Al galvanic couple's potential difference arises, leading to a deeper and more intensified local penetrating attack, deteriorating the long-term corrosion performance of the DMLS-AlSi10Mg alloy as compared to that of its as-printed (untreated) counterpart.

## 4. Conclusions

In this study, the effects of low temperature heat-treatment cycles on microstructure, hardness, and electrochemical behavior of DMLS-AlSi10Mg in aerated 3.5 wt.% NaCl electrolyte at early stage of immersion were investigated. The results of this study can be summarized as follows:

- The differential scanning calorimetry analysis of the as-printed samples revealed two distinguishable exothermic transformations at 232.9 °C and 273.2 °C, which were interpreted as the $Mg_2Si$ precipitation and Si phase precipitation via solid-state diffusion, respectively.
- According to the DSC analysis results, the as-printed samples were heat-treated at 200 °C (< 273.2 °C), 300 °C (> 273.2 °C), and 350 °C (as an upper limit temperature) for 3 h followed by water quenching. Microstructural analysis results confirmed that increasing the heat-

treatment temperature from 200 °C to 350 °C resulted in the interruption of the intercellular Si network, followed by the coalescence and coarsening of the eutectic Si particles, and in general, increased content of Si precipitates in the structure. Therefore, the uniformity of the microstructure, in terms of the size and distribution of Si particles in the α-Al matrix, was promoted by the increase in the heat-treatment temperature.

- A continuous decrease in the Vickers micro-hardness values by increasing the heat-treatment temperature was found to be associated with the microstructural evolution due to the Si network interruption followed by the Si precipitates coarsening.
- The electrochemical measurements, *i.e.* anodic polarization and EIS tests, confirmed the improved corrosion resistance of the alloy and a reduced susceptibility to penetrating selective attack at initial immersion time in the electrolyte solution by increasing the heat-treatment temperature from 200 °C to 300 °C. This was evidenced by the reduced corrosion current density, and the existence of a more protective passive film on the alloy with a higher value of impedance at early stage of immersion after 300 °C heat treatment.
- Further increase of the heat treatment temperature to 350 °C was revealed to deteriorate the corrosion response significantly at early stage of immersion, inducing a severe localized corrosion attack around the coarse and coalesced Si particles. Formation of coarse Si precipitates as cathodic sites embedded in the anodic aluminum matrix provoked an active-like behavior on the surface and hindered the complete re-passivation of the surface at initial immersion time.
- The corrosion morphology was also found to change from a penetrating selective attack along the melt pool boundaries for the untreated and 200 °C heat-treated DMLS-AlSi10Mg samples to a more localized corrosion in the α-Al matrix along the border of Si particles when heat-

treated at 300 °C, ascribed to the uniformity of the microstructure achieved after 300 °C heat-treatment.

- The improved corrosion performance of the DMLS-AlSi10Mg alloy at early stage of immersion by low-temperature heat-treatment at 300 °C can be ascribed to the quality of the pre-existing passive layer attributed to the uniformity in distribution of the fine Si particles on the surface, which inhibited penetrating selective attack along the melt pool boundaries, despite localized corrosion evolved.

## Acknowledgement

The authors wish to acknowledge the support of Natural Sciences and Engineering Research Council of Canada (NSERC) [grant number RGPIN-2017-04368], for sponsoring this work. M.M. would like to specially thank New Brunswick Innovation Foundation (NBIF) [grant number RIF2017-071] for providing funding to conduct this research.

# References

[1] H. Asgari, C. Baxter, K. Hosseinkhani, M. Mohammadi, On microstructure and mechanical properties of additi[1], Mater. Sci. Eng. A. 707 (2017) 148–158. doi:https://doi.org/10.1016/j.msea.2017.09.041.

[2] S. Van Bael, G. Kerckhofs, M. Moesen, G. Pyka, J. Schrooten, J.P. Kruth, Micro-CT-based improvement of geometrical and mechanical controllability of selective laser melted Ti6Al4V porous structures, Mater. Sci. Eng. A. 528 (2011) 7423–7431.

[3] A. Leon, E. Aghion, Effect of surface roughness on corrosion fatigue performance of AlSi10Mg alloy produced by Selective Laser Melting (SLM), Mater. Charact. 131 (2017) 188–194. doi:https://doi.org/10.1016/j.matchar.2017.06.029.

[4] B. Li, H. Wang, J. Jie, Z. Wei, Effects of yttrium and heat treatment on the microstructure and tensile properties of Al–7.5Si–0.5Mg alloy, Mater. Des. 32 (2011) 1617–1622. doi:https://doi.org/10.1016/j.matdes.2010.08.040.

[5] P. Fathi, M. Mohammadi, X. Duan, A.M. Nasiri, A Comparative Study on Corrosion and Microstructure of Direct Metal Laser Sintered AlSi10Mg_200C and Die Cast A360.1 Aluminum, J. Mater. Process. Technol. 259 (2018) 1–14. doi:https://doi.org/10.1016/j.jmatprotec.2018.04.013.

[6] L. Zhou, A. Mehta, E. Schulz, B. McWilliams, K. Cho, Y. Sohn, Microstructure, precipitates and hardness of selectively laser melted AlSi10Mg alloy before and after heat treatment, Mater. Charact. (2018). doi:https://doi.org/10.1016/j.matchar.2018.04.022.

[7] B.A. Fulcher, D.K. Leigh, T.J. Watt, Comparison of AlSi10Mg and Al 6061 processed through DMLS, in: Proc. Solid Free. Fabr. Symp. Austin, TX, USA, 2014.

[8] M. Shiomi, K. Osakada, K. Nakamura, T. Yamashita, F. Abe, Residual Stress within Metallic Model Made by Selective Laser Melting Process, CIRP Ann. 53 (2004) 195–198. doi:https://doi.org/10.1016/S0007-8506(07)60677-5.

[9] D. Manfredi, E.P. Ambrosio, F. Calignano, M. Krishnan, R. Canali, S. Biamino, M. Pavese, E. Atzeni, L. Iuliano, P. Fino, C. Badini, Direct Metal Laser Sintering: an additive manufacturing technology ready to produce lightweight structural parts for robotic applications, La Metall. Ital. 105 (2013) 15–24.

[10] N.T. Aboulkhair, C. Tuck, I. Ashcroft, I. Maskery, N. Everitt, On the Precipitation Hardening of Selective Laser Melted AlSi10Mg, Metall. Mater. Trans. A. 46 (2015) 3337–3341. doi:10.1007/s11661-015-2980-7.

[11] A. Mertens, O. Dedry, D. Reuter, O. Rigo, J. Lecomte-Beckers, Thermal treatments of AlSi10Mg processed by laser beam melting, in: Proc. 26th Int. Solid Free. Fabr. Symp., 2015: pp. 1007–1016.

[12] P. Yang, M.A. Rodriguez, L.A. Deibler, B.H. Jared, J. Griego, A. Kilgo, A. Allen, D.K. Stefan, Effect of thermal annealing on microstructure evolution and mechanical behavior of an additive manufactured AlSi10Mg part, J. Mater. Res. 33 (2018) 1701–1712. doi:10.1557/jmr.2018.82.

[13] N.T. Aboulkhair, I. Maskery, C. Tuck, I. Ashcroft, N.M. Everitt, The microstructure and mechanical properties of selectively laser melted AlSi10Mg: The effect of a conventional T6-like heat treatment, Mater. Sci. Eng. A. 667 (2016) 139–146. doi:https://doi.org/10.1016/j.msea.2016.04.092.

[14] P. Ma, K.G. Prashanth, S. Scudino, Y. Jia, H. Wang, C. Zou, Z. Wei, J. Eckert, Influence of Annealing on Mechanical Properties of Al-20Si Processed by Selective Laser Melting,

Metals (Basel). 4 (2014) 28–36. doi:10.3390/met4010028.

[15] M. Cabrini, S. Lorenzi, T. Pastore, S. Pellegrini, E.P. Ambrosio, F. Calignano, D. Manfredi, M. Pavese, P. Fino, Effect of heat treatment on corrosion resistance of DMLS AlSi10Mg alloy, Electrochim. Acta. 206 (2016) 346–355. doi:https://doi.org/10.1016/j.electacta.2016.04.157.

[16] M. Cabrini, F. Calignano, P. Fino, S. Lorenzi, M. Lorusso, D. Manfredi, C. Testa, T. Pastore, Corrosion Behavior of Heat-Treated AlSi10Mg Manufactured by Laser Powder Bed Fusion, Materials (Basel). 11 (2018). doi:10.3390/ma11071051.

[17] T. Rubben, R.I. Revilla, I. De Graeve, Influence of heat treatments on the corrosion mechanism of additive manufactured AlSi10Mg, Corros. Sci. (2018). doi:https://doi.org/10.1016/j.corsci.2018.11.038.

[18] A.S. Materials, ASTM G5-14: Standard Reference Test Method for Making Potentiodynamic Anodic Polarization Measurements, ASTM, 2014. https://books.google.ca/books?id=tWpcswEACAAJ.

[19] K.S. Ferrer, R.G. Kelly, Comparison of Methods for Removal of Corrosion Product from AA2024-T3, Corrosion. 57 (2001) 110–117. doi:10.5006/1.3290336.

[20] L.C. Doan, Y. Ohmori, K. Nakai, Precipitation and Dissolution Reactions in a 6061 Aluminum Alloy, Mater. Trans. JIM. 41 (2000) 300–305. doi:10.2320/matertrans1989.41.300.

[21] J. Fiocchi, A. Tuissi, P. Bassani, C.A. Biffi, Low temperature annealing dedicated to AlSi10Mg selective laser melting products, J. Alloys Compd. 695 (2017) 3402–3409. doi:https://doi.org/10.1016/j.jallcom.2016.12.019.

[22] I. Dutta, S.M. Allen, J.L. Hafley, Effect of reinforcement on the aging response of cast 6061 Al-Al2O3 particulate composites, Metall. Trans. A. 22 (1991) 2553–2563. doi:10.1007/BF02851349.

[23] E. Ogris, A. Wahlen, H. Lüchinger, P. Uggowitzer, On the silicon spheroidization in Al-Si alloys, J. Light Met. 2 (2002) 263–269.

[24] A. Hadadzadeh, B.S. Amirkhiz, A. Odeshi, M. Mohammadi, Dynamic loading of direct metal laser sintered AlSi10Mg alloy: Strengthening behavior in different building directions, Mater. Des. 159 (2018) 201–211. doi:https://doi.org/10.1016/j.matdes.2018.08.045.

[25] L. Thijs, K. Kempen, J. Kruth, J. V. Humbeeck, Fine-structured aluminium products with controllable texture by selective laser melting of pre-alloyed AlSi10Mg powder, Acta Mater. 61 (2013) 1809–1819. doi:https://doi.org/10.1016/j.actamat.2012.11.052.

[26] X.P. Li, X.J. Wang, M. Saunders, A. Suvorova, L.C. Zhang, Y.J. Liu, M.H. Fang, Z.H. Huang, T.B. Sercombe, A selective laser melting and solution heat treatment refined Al–12Si alloy with a controllable ultrafine eutectic microstructure and 25% tensile ductility, Acta Mater. 95 (2015) 74–82. doi:https://doi.org/10.1016/j.actamat.2015.05.017.

[27] W. Kurz, D.J. Fisher, Fundamentals of solidification, trans tech publications Aedermannsdorf, Switzerland, 1986.

[28] A. Hadadzadeh, B.S. Amirkhiz, J. Li, M. Mohammadi, Columnar to equiaxed transition during direct metal laser sintering of AlSi10Mg alloy: Effect of building direction, Addit. Manuf. 23 (2018) 121–131. doi:https://doi.org/10.1016/j.addma.2018.08.001.

[29] F. Trevisan, F. Calignano, M. Lorusso, J. Pakkanen, A. Aversa, E.P. Ambrosio, M. Lombardi, P. Fino, D. Manfredi, On the Selective Laser Melting (SLM) of the AlSi10Mg Alloy: Process, Microstructure, and Mechanical Properties, Materials (Basel). 10 (2017) 1–

23.

[30] K.G. Prashanth, S. Scudino, H.J. Klauss, K.B. Surreddi, L. Löber, Z. Wang, A.K. Chaubey, U. Kühn, J. Eckert, Microstructure and mechanical properties of Al–12Si produced by selective laser melting: Effect of heat treatment, Mater. Sci. Eng. A. 590 (2014) 153–160. doi:https://doi.org/10.1016/j.msea.2013.10.023.

[31] A. Hadadzadeh, B.S. Amirkhiz, M. Mohammadi, Contribution of Mg2Si precipitates to the strength of direct metal laser sintered AlSi10Mg, Mater. Sci. Eng. A. 739 (2019) 295–300. doi:https://doi.org/10.1016/j.msea.2018.10.055.

[32] W. Li, S. Li, J. Liu, A. Zhang, Y. Zhou, Q. Wei, C. Yan, Y. Shi, Effect of heat treatment on AlSi10Mg alloy fabricated by selective laser melting: Microstructure evolution, mechanical properties and fracture mechanism, Mater. Sci. Eng. A. 663 (2016) 116–125. doi:https://doi.org/10.1016/j.msea.2016.03.088.

[33] R.I. Revilla, J. Liang, S. Godet, I. De Graeve, Local Corrosion Behavior of Additive Manufactured AlSiMg Alloy Assessed by SEM and SKPFM, J. Electrochem. Soc. . 164 (2017) C27–C35. doi:10.1149/2.0461702jes.

[34] G.S. Peng, K.H. Chen, H.C. Fang, H. Chao, S.Y. Chen, EIS study on pitting corrosion of 7150 aluminum alloy in sodium chloride and hydrochloric acid solution, Mater. Corros. 61 (n.d.) 783–789. doi:10.1002/maco.200905413.

[35] M. Cabrini, S. Lorenzi, T. Pastore, S. Pellegrini, D. Manfredi, P. Fino, S. Biamino, C. Badini, Evaluation of corrosion resistance of Al–10Si–Mg alloy obtained by means of Direct Metal Laser Sintering, J. Mater. Process. Technol. 231 (2016) 326–335. doi:https://doi.org/10.1016/j.jmatprotec.2015.12.033.

[36] S. Gudić, J. Radošević, M. Kliškić, Impedance and transient study of aluminium barrier-type oxide films, J. Appl. Electrochem. 26 (1996) 1027–1035. doi:10.1007/BF00242197.

[37] K.Jafarzadeh, T.Shahrabi, M.G.Hosseini, EIS Study on Pitting Corrosion of AA5083-H321 Aluminum-Magnesium Alloy in Stagnant 3.5% NaCl Solution, J. Mater. Sci. Technol. 24 (2008) 215. http://www.jmst.org/EN/abstract/article_8052.shtml.

[38] R. Arrabal, B. Mingo, A. Pardo, M. Mohedano, E. Matykina, I. Rodríguez, Pitting corrosion of rheocast A356 aluminium alloy in 3.5wt.% NaCl solution, Corros. Sci. 73 (2013) 342–355. doi:https://doi.org/10.1016/j.corsci.2013.04.023.

[39] H. Asgari, C. Baxter, K. Hosseinkhani, M. Mohammadi, On microstructure and mechanical properties of additively manufactured AlSi10Mg_200C using recycled powder, Mater. Sci. Eng. A. 707 (2017) 148–158. doi:10.1016/J.MSEA.2017.09.041.

[40] E.O. Olakanmi, Selective laser sintering/melting (SLS/SLM) of pure Al, Al–Mg, and Al–Si powders: Effect of processing conditions and powder properties, J. Mater. Process. Technol. 213 (2013) 1387–1405. doi:https://doi.org/10.1016/j.jmatprotec.2013.03.009.

[41] W.J. Sames, F.A. List, S. Pannala, R.R. Dehoff, S.S. Babu, The metallurgy and processing science of metal additive manufacturing, Int. Mater. Rev. 61 (2016) 315–360. doi:10.1080/09506608.2015.1116649.

[42] N.T. Aboulkhair, I. Maskery, C. Tuck, I. Ashcroft, N.M. Everitt, On the formation of AlSi10Mg single tracks and layers in selective laser melting: Microstructure and nano-mechanical properties, J. Mater. Process. Technol. 230 (2016) 88–98. doi:https://doi.org/10.1016/j.jmatprotec.2015.11.016.

[43] A.H. Maamoun, M. Elbestawi, G.K. Dosbaeva, S.C. Veldhuis, Thermal post-processing of AlSi10Mg parts produced by Selective Laser Melting using recycled powder, Addit. Manuf. 21 (2018) 234–247. doi:https://doi.org/10.1016/j.addma.2018.03.014.

[44] L.C. Ardila, F. Garciandia, J.B. González-Díaz, P. Álvarez, A. Echeverria, M.M. Petite, R. Deffley, J. Ochoa, Effect of IN718 Recycled Powder Reuse on Properties of Parts Manufactured by Means of Selective Laser Melting, Phys. Procedia. 56 (2014) 99–107. doi:https://doi.org/10.1016/j.phpro.2014.08.152.

[45] G. Nichols, S. Byard, M.J. Bloxham, J. Botterill, N.J. Dawson, A. Dennis, V. Diart, N.C. North, J.D. Sherwood, A Review of the Terms Agglomerate and Aggregate with a Recommendation for Nomenclature Used in Powder and Particle Characterization, J. Pharm. Sci. 91 (2002) 2103–2109. doi:https://doi.org/10.1002/jps.10191.

[46] A. Simchi, Direct laser sintering of metal powders: Mechanism, kinetics and microstructural features, Mater. Sci. Eng. A. 428 (2006) 148–158. doi:https://doi.org/10.1016/j.msea.2006.04.117.

[47] K. Abd-Elghany, D.L. Bourell, Property evaluation of 304L stainless steel fabricated by selective laser melting, Rapid Prototyp. J. 18 (2012) 420–428.

[48] M. Rafieazad, M. Mohammadi, A. Nasiri, On Microstructure and Early Stage Corrosion Performance of Heat Treated Direct Metal Laser Sintered AlSi10Mg, Addit. Manuf. 28 (2019) 107–119.

[49] P. Fathi, M. Mohammadi, X. Duan, A. Nasiri, Effects of Surface Finishing Procedures on Corrosion Behavior of DMLS-AlSi10Mg_200C Alloy Versus Die-Cast A360.1 Aluminum, JOM. (2019) 1–12. doi:10.1007/s11837-019-03344-8.

[50] M. Tang, P.C. Pistorius, S. Narra, J.L. Beuth, Rapid Solidification: Selective Laser Melting of AlSi10Mg, JOM. 68 (2016) 960–966. doi:10.1007/s11837-015-1763-3.

[51] B. Wu, Z. Pan, S. Li, D. Cuiuri, D. Ding, H. Li, The anisotropic corrosion behaviour of wire arc additive manufactured Ti-6Al-4V alloy in 3.5% NaCl solution, Corros. Sci. 137 (2018) 176–183. doi:https://doi.org/10.1016/j.corsci.2018.03.047.

[52] M. Cabrini, S. Lorenzi, T. Pastore, C. Testa, D. Manfredi, G. Cattano, F. Calignano, Corrosion resistance in chloride solution of the AlSi10Mg alloy obtained by means of LPBF, Surf. Interface Anal. (n.d.). doi:10.1002/sia.6601.

[53] T. Rubben, R.I. Revilla, I. De Graeve, Effect of Heat Treatments on the Anodizing Behavior of Additive Manufactured AlSi10Mg, J. Electrochem. Soc. 166 (2019) C42--C48.

[54] R.I. Revilla, D. Verkens, G. Couturiaux, L. Malet, L. Thijs, S. Godet, I. De Graeve, Galvanostatic Anodizing of Additive Manufactured Al-Si10-Mg Alloy, J. Electrochem. Soc. 164 (2017) C1027–C1034. doi:10.1149/2.1121714jes.

# Chapter 3

# Effects of Recycled Powder on Solidification Defects, Microstructure, and Corrosion Properties of DMLS Fabricated AlSi10Mg[3] [4]

## Preface

A version of this manuscript has been published in the Journal of the Minerals, Metals & Materials Society (JOM), and CSME 2019 conference proceeding. I am the first and corresponding author of these papers. Along with the co-authors, Dr. Abhijit Chatterjee, and Dr. Ali Nasiri, I investigate the impact of the recycling powders on the microstructure and corrosion performance of the L-PBF AlSi10Mg alloy. I prepared methodology, experimental, formal analysis, and the first original draft of the manuscript and subsequently revised the manuscript based on the coauthors' feedback and also the peer review process. The co-author Dr. Ali Nasiri helped in conceptualization, design, project administration, and supervision, review & editing of the manuscript.

---

[3] M. Rafieazad, A. Chatterjee, A.M. Nasiri, Effects of Recycled Powder on Solidification Defects, Microstructure, and Corrosion Properties of DMLS Fabricated AlSi10Mg, JOM. 71 (2019) 3241–3252. (IPF= 2.305)

[4] M. Rafieazad, A. Chatterjee, and A. M. Nasiri, Additively Manufactured DMLS-AlSi10Mg using Recycled Powder: the Impacts on Microstructure and Corrosion Properties, CSME conference, (Full Paper), Jun 2019

## Abstract

This study examines the impacts of using recycled powder on solidification defects, microstructures, and the resultant corrosion properties of Direct Metal Laser Sintered (DMLS) AlSi10Mg alloy. Microstructural analysis confirmed that using recycled powder in the fabrication of AlSi10Mg leads to (*i*) an increased volume fraction of internal porosities and solidification micro-cracks, (*ii*) more coarsening of interdendritic eutectic-Si network particularly along the melt pool boundaries, which were correlated to the larger size and irregular shape of the recycled powders compared to the virgin powders, leading to the reduced thermal conductivity of the recycled powders. To investigate the impacts of above-mentioned microstructural changes on the corrosion performance of the alloy, anodic polarization testing and electrochemical impedance spectroscopy in aerated 3.5 wt.% NaCl solution were performed. The results confirmed a slight degradation of the corrosion properties of the recycled-powder fabricated samples, ascribed to further coarsening of Si-network along their melt pool boundaries.

## 1. Introduction

Additive manufacturing (AM) technology is an emerging manufacturing technique, which is gaining enormous attention from industrial manufacturing sectors, owing to its malleability to design complicated, near-net-shape engineering components mostly without any geometrical constraint [1]. Regardless of the economic impacts of the AM technology on the manufacturing of intricate engineering parts, there is still a significant drawback of adopting this technology by many industries due to the cost-intensive printed components, particularly for parts having medium to simple designs [2]. To improve the affordability of the DMLS process, wasting of the feedstock metal powder is minimized by collecting and reusing ~ 90% of the feedstock powder after each building cycle [3]. However, the high temperature of the powder bed in the preheating stage and more severely the interaction between the virgin powder and the laser can cause possible microstructural and morphological changes in the virgin powder close to the parts that are being built [4].

As powder reuse cycle increases, many properties of the powder are changed [2]. This can adversely affect the build quality. To suppress all the side effects associated with implementing the used powder in fabrication of new parts without compromising on the build quality, many AM industries have incorporated a sieving process into the manufacturing cycle of the AM products. Accordingly, all collected powders after completion of each building cycle are passed through a sieving step to separate and discard partially melted or highly heated condensate powder from the remaining unmelted virgin powder, denoted as the recycled powder, and are being reused after the sieving process. Nonetheless, it has been shown that the recycled powder will not be identical to the virgin powder in terms of shape, size distribution, and the microstructure [1,5,6].

So far, a few studies have investigated the effect of using recycled powder on porosity level, density, and mechanical properties of the AM components [1,5,6]. For instance, Ardila *et al.* [6] reported comparable mechanical properties for the selective laser melting (SLM) fabricated Inconel 718 using virgin powder and the recycled powder even after 14 times of recycling. In a recent study, Asgari *et al.* [1] characterized the AlSi10Mg recycled powders after the DMLS process and reported a noticeably different particles' size, morphology, and chemical composition for the recycled powder relative to the virgin powder [7,8]. The sintering of the AlSi10Mg metal powder during the DMLS process and the subsequent agglomeration was reported to cause approximately 12% increase in the average size of the particles [1]. Furthermore, it was shown that the recycled AlSi10Mg powder is slightly deformed and elongated as compared to the spherical shape of the virgin powder [1], which can potentially contribute to a lower apparent density as compared to that of the spherical virgin powder [5].

The change in the morphology and the size of metal powder has been also reported to impact the density and volume fraction of the internal defects in the AM fabricated parts. Abd-Elghany and Bourell [9] have reported that an increase in 304L stainless steel particle size used in the powder layer thickness range of 30-70 μm can lead to a 6% decrease in the density of manufactured parts due to a reduction in the contact area of each powder layer. It is also known that the densification process has a significant impact on the formation of pores in the samples. As Maamoun *et al*. [5] reported, two types of pores have been commonly detected in the DMLS-AlSi10Mg samples fabricated using the recycle powders, *i.e*., spherical pores and keyhole pores. Small spherical pores (diameter<10 μm) form due to the large interparticle spacing in the powder during the laser-melting process. Such interparticle voids can potentially act as gas entrapment sites, contributing to the formation of the spherical pores [5]. On the other hand, large keyhole pores mainly form due to the improper melting of the powders, ascribed to the lack of thermal conduction between the powders during the laser melting process [5].

In the context of corrosion properties, although Revilla *et al.* [10] reported no significant influence of the recycled powder on the corrosion potential of SLM-AlSi10Mg using anodic polarization testing, the observed slight corrosion performance difference between the recycled powder fabricated samples and the virgin ones were not adequately correlated to the microstructural variations between the samples. Furthermore, although the increased size of the recycled powder were detected in the previous studies [1,5,10], the effect of the powder size on the final microstructure of the samples were not clearly discussed, and no elucidation for the slight microstructural variations between the recycled powder and the virgin powder fabricated samples has been provided.

Therefore, despite the existing few studies on the microstructure and mechanical properties of the DMLS fabricated AlSi10Mg alloy using the recycled powders [1,5], the impacts of using recycled powder on the formation of solidification defects and corrosion properties of the fabricated parts are still unknown. This knowledge is crucial for AM fabricated AlSi10Mg parts since one of the major concerns with using DMLS-AlSi10Mg components in marine or aerospace applications is their corrosion performance [11]. This study aims to investigate the impact of using recycled powder on solidification-induced defects, the microstructural evolution, and the resulting corrosion properties of the DMLS-AlSi10Mg parts.

## 2. Materials and Methods

### 2.1. Material

DMLS-AlSi10Mg cubic samples with a dimension of 15×15×15 mm were fabricated employing an EOS-M290 machine at AMM Company in Concord, Canada, using the processing parameters of 30 µm powder layer thickness, the platform temperature of 200 °C, laser power of 360 W with the spot size of 100 µm, scanning speed of 1000 mm/s, hatching distance of 0.21 mm, and 67° laser beam rotation between the consecutive layers. Three types of AlSi10Mg feedstock powders with chemical composition of 9.0-11.0 wt.% Si, 0.2-0.4 wt.% Mg, Fe and Mn $\leq$ 0.55 wt.%, and balance Al [12,13] were utilized for fabrication, including a virgin powder and two types of recycled powders, one after four times and the other after five times of reuse cycles. These fabricated samples were denoted as Virgin, 4X and 5X-samples, respectively. For the case of the recycled powders, after each building cycle, the collected powder was sieved prior to the next building cycle. Therefore, the 4X-samples were built using a recycled powder that was passed through 4 building cycles along with 4 subsequent sieving steps before being used for fabrication of 4X-samples, whereas the used recycled powder for fabrication of 5X-sample was passed through one additional building and its subsequent sieving cycle as compared to the 4X-sample. Albeit the samples of used feedstock powders were not provided to the research team by the manufacturer for further chemical and morphological analyses, the particle size distribution analysis of all feedstock metal powders used herein was conducted by the manufacturer and the data (plotted in Figure 3.1) were shared with the research team. Accordingly, the average particle size of the Virgin, 4X, and 5X-recycled powders were measured to be 8.8±7 µm, 12.4±7 µm, and 13.7±9 µm, respectively.

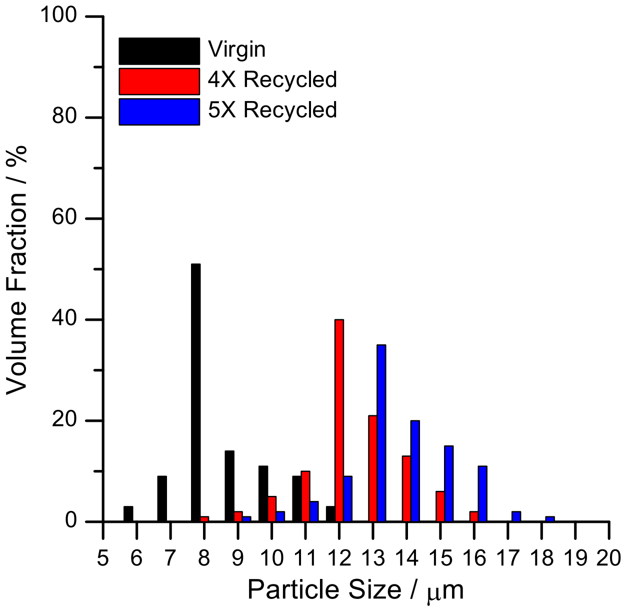

Figure 3. 1. Particle size distribution for the Virgin and recycled powders used in this study

## 2.2. Microstructure Characterization

To characterize the microstructures of the samples, all DMLS-samples were sectioned along both the building plane and the building direction and prepared following the standard grinding and polishing procedures for aluminum alloys. The polished surfaces were then chemically etched using Keller's reagent [14] to reveal the microstructure. The microstructures of all samples were characterized using an optical microscope and a FEI-MLA-650F field emission scanning electron microscope (FESEM). Phase characterization of different samples was carried out using X-ray diffraction (XRD) with Cu-$K_\alpha$ source at the diffraction angle range of 20°-70° with a step size of 0.02°.

## 2.3. Anodic Polarization Testing

The anodic potentiodynamic polarization (APP) testing was conducted using an IVIUM-CompactStat$^{TM}$ Potentiostat computer-controlled instrument with a three-electrode cell setup according to the ASTM-G5 standard. All electrochemical corrosion tests were performed in an aerated 3.5wt.% NaCl solution at 25±0.5°C in a temperature-controlled water bath. Prior to each polarization test, the open circuit potential (OCP) was monitored for 1h to ensure that samples attained the electrochemical stability before the test was run. The APP tests were conducted in the potential range of -0.02V to +0.3V with respect to the OCP value and with a scanning rate of 0.15mV/s.

## 2.4. Electrochemical Impedance Spectroscopy (EIS) Testing

Additionally, the EIS tests were carried out on polished samples after 1h and 120h of immersion times in an aerated 3.5wt.% NaCl solution at 25±0.5°C. Signals with 0.01V amplitude were applied over the OCP with a frequency range between $10^{5}$-$10^{-2}$Hz. All corrosion tests were conducted on the polished surfaces to eliminate the effects of surface roughness on corrosion properties.

## 2.5. Intergranular Corrosion Testing

The intergranular corrosion testing was performed on the polished surfaces of the side view of different samples as per ISO-11846 standard, where samples were immersed in 30g/L of NaCl solution containing 10mL/L of HCl at 25°C for 24h. After one day of immersion, samples were rinsed with distilled water and investigated using FESEM. Repeatability of the corrosion results was measured by testing at least three samples.

## 3. Results and Discussion

### 3.1. Microstructure Characterization

The optical micrographs taken from the Virgin, 4X, and 5X DMLS-AlSi10Mg samples are shown in Figure 3.2. The 3D representation of the optical micrographs of DMLS-AlSi10Mg samples from both side and top views confirmed a proper overlapping and densification between melt pools. The morphology of the melt pools from the side view of the fabricated samples revealed a semi-circle shape, which its size is primarily dependent on the volumetric energy density used in the manufacturing of the samples. The top view of all three fabricated samples shows irregular melt pool geometries and directions, attributed to the 67° rotation of the laser scan between the consecutive layers [1]. The optical microscopy investigation also confirmed that employing recycled powders does not alter the overall macrostructure and morphology of the melt pools noticeably in the fabricated samples. This was found to be in agreement with the results reported in previous studies [1,5,10], confirming a consistent overall macrostructure for both virgin powders and recycled powders fabricated samples.

A critical difference between the Virgin sample and the recycled ones to note is the volume of the formed internal porosities in the samples. A closer look at the optical microscopic images of the built samples both in as-polished (Figures 3.2(b), (e), and (h)) or etched condition (Figures 3.2(c), (f), and (i)) reveals that using recycled powders in the fabrication of DMLS-AlSi10Mg has resulted in the formation of larger and higher quantities of spherical and keyhole porosities in the 4X and 5X-samples compared to the Virgin sample. The average porosity percentage in the Virgin sample was calculated to be 0.54±0.16%, which can be considered a low porosity level compared to the available values in the literature [1]. However, by increasing the re-use/recycling times, the porosity percentage was increased to 1.10±0.76% and 1.56±0.84% for the 4X and 5X-samples, respectively. The higher volume fraction of internal porosities in both 4X and 5X-samples can be correlated to the reduced effective thermal conductivity of the recycled powders, as it depends on the size, shape, and void fraction between the powders. The increased size and the distorted shapes of the recycled powders [5] relative to the virgin powders would increase the volume fraction of internal voids between the powder particles, leading to a lower thermal conductivity between them [8]. In other words, in the case of virgin powders, the sintering kinetics are more accelerated than that of the recycled powders, ascribed to the higher active contact surface area of small particles along with smaller gaseous pockets in the inter-particle spacing of the virgin powder.

It has been shown by Olakanmi [2] that the irregular shapes of the metal powders as a result of the agglomeration can intensify the formation of voids and porosities in the SLM fabricated Al-Mg, and Al-Si parts. In addition, the substantial impact of the particle size on the increased porosity level of the iron parts manufactured by direct laser sintering method has been reported [8]. Thus, the irregular shape [5] and the larger particle size [1] of the recycled powders contribute to the entrapment of larger gaseous pores between the powder layers and even inside the powders [15], leading to a reduced thermal conductivity between the particles. Consequently, the sintering kinetics during the fabrication process are lowered, promoting the formation of internal porosities. Furthermore, the larger size of the porosities in the recycled powder fabricated samples than the Virgin sample was attributed to the decreased packing density of the recycled powders as a result of their agglomeration.

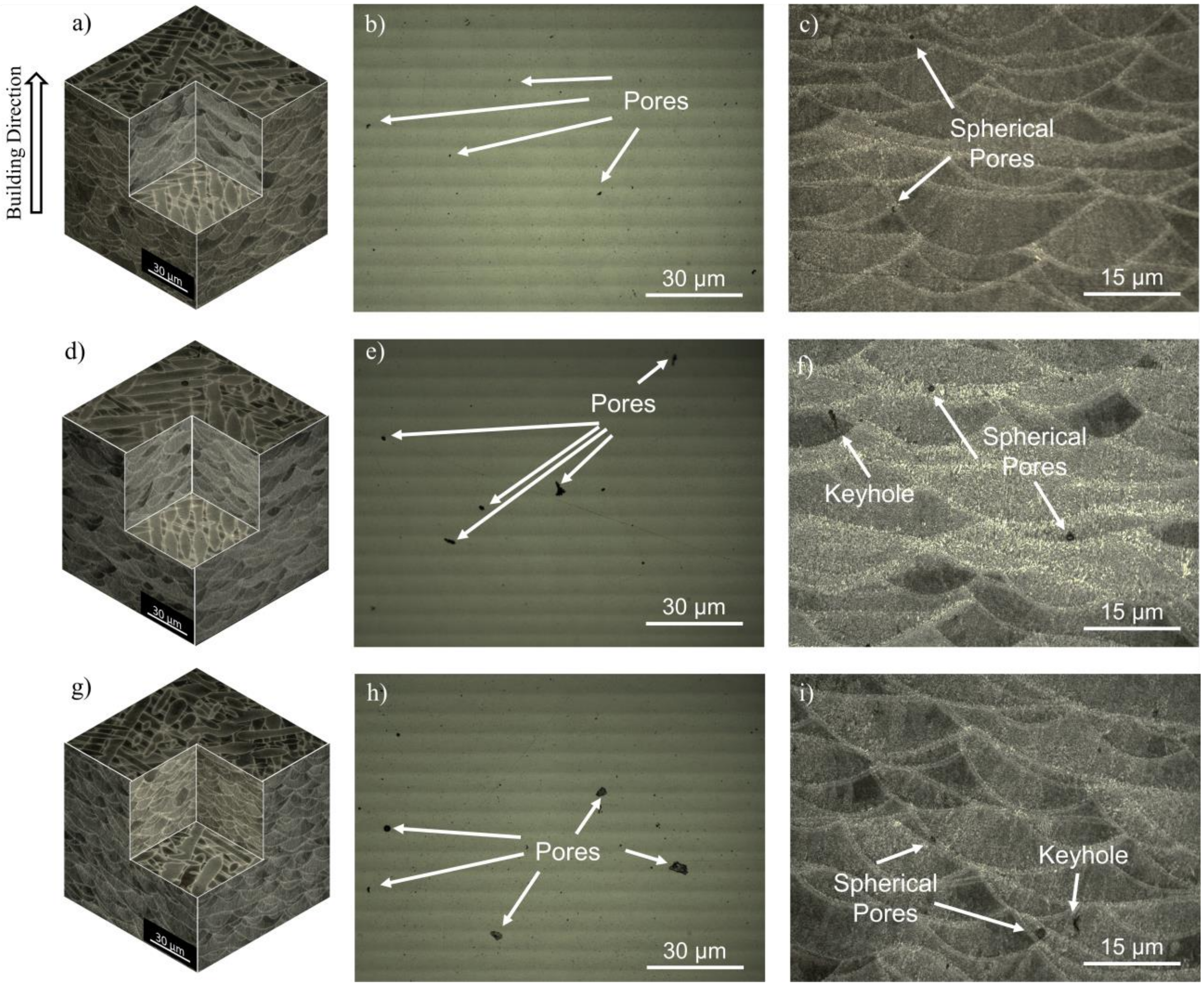

Figure 3. 2. Optical micrographs of the DMLS-AlSi10Mg samples fabricated from the a), b) and c) Virgin, d), e) and f) 4X-recycled, g), h) and i) 5X-recycled powders.

To further investigate the microstructure of the fabricated DMLS-AlSi10Mg samples, FESEM analysis was employed. FESEM micrograph of the Virgin sample (Figure 3.3a) revealed the formation of an extremely fine cellular dendritic structure of aluminum containing a continuous network of eutectic-Si phase (Figure 3.3b) primarily formed along the interdendritic regions. This microstructure is commonly reported for the additively manufactured AlSi10Mg alloy [12,14]. Over a melt pool area, three distinguishable regions with well-defined microstructures were formed, *i.e.*, a region with fine cellular structure (MP-Fine), followed by a confined region with coarse cellular structure (MP-coarse), and a narrow heat affected zone (HAZ) that forms on the edge of the melt pools in the previously solidified track due to the overlapping scanning lines and layer-by-layer solidification of the material [16]. It should be noted that the essential solidification parameters, *i.e.*, temperature gradient ($G$) and solidification rate ($R$), control the variation of microstructure across the melt pool [21]. Along the melt pool boundaries, where $G$ is the lowest and $R$ is the highest, more elongated and coarser dendritic structure forms.

Comparing the microstructure along the melt pool boundaries in the vicinity of the HAZ in Virgin, 4X, and 5X-samples revealed a noticeably coarser Si-network along the melt pool boundary of the recycled samples (Figures 3.3 (c–f)), particularly in the 5X-sample. As schematically shown in Figures 3.4a and 4b, the increased average particle size in the recycled powder (Figure 3.4b) reduces the packing factor and the density of the powder bed as compared to that of the virgin powder bed (Figure 3.4a). Simchi [8] reported that the effective thermal conductivity of the particles varies with their size, void space between them, arrangement, and active surface contact. Therefore, the recycled powders, having a larger size [1] and elongated shapes [5], form a greater void space and smaller contact areas, leading to a lower thermal conductivity between them. Thus, a smaller portion of laser's volumetric energy density is dissipated by conduction through the metal powders into the previously solidified tracks. Consequently, a larger portion of laser beam energy is consumed for melting of the metal powders, and plausibly resulting in the formation of higher temperature melt pools. This can potentially cause a slower cooling rate of the melt pool, leading to further coarsening of the solidified structure and excessive solute segregation (eutectic-Si) from the liquid during solidification. The observed coarser Si-network along the interdendritic regions and further precipitation of this phase at the interior of the dendrites confirmed the slower cooling rate of the melt pools during solidification in the case of 4X and more noticeably 5X-sample.

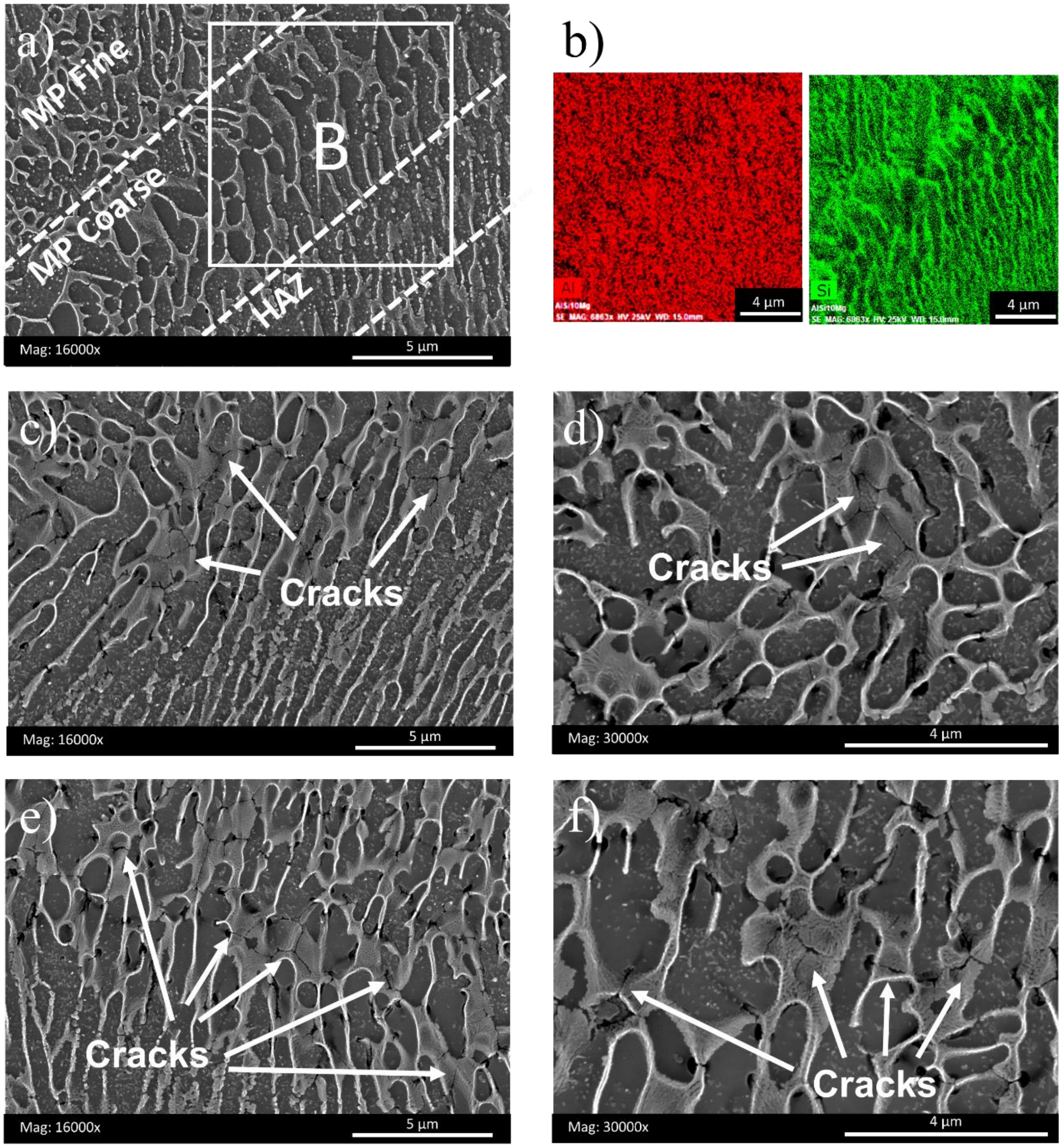

Figure 3. 3. SEM micrographs from the side view of the a) Virgin sample, b) EDX concentration maps of the enclosed are in (a) shown by B, c) and d) 4X-sample, e) and f) 5X-sample.

In addition to the increased solute segregation in the recycled samples, a closer look at the microstructure of the samples in Figure 3.3 confirms that by increasing the particle size from the virgin powder to the 4X and 5X-recycled ones, the α-Al dendrite arm spacing (cell size) has been expanded. For aluminum alloys that undergo a rapid cooling during solidification, Equation 3.1 has been proposed showing the inverse relationship between the cooling rate ($\dot{T}$ (K/s)) and the size of dendrite arm spacing (λ (μm)) [15].

$$\lambda = 43.2\dot{T}^{-0.324} \qquad \text{Eq. 3.1}$$

Accordingly, considering the coarser cells of α-Al in recycled samples, it can be interpreted that the recycled powders fabricated samples experienced a slower cooling rate during solidification compared to the Virgin samples. This observation is also consistent with the relationship suggested by Tang *et al.* [15], showing the proportionality between the secondary dendrite arm spacing (SDAS (μm)) and the particle size (D (μm)) in SLM-AlSi10Mg alloy as follows:

$$\mathrm{SDAS} = 0.14\mathrm{D}^{0.61} \qquad \text{Eq. 3.2}$$

Therefore, when the recycled powders are used as the feedstock material instead of virgin powders, the change in the particle size and the resulting change in the convective heat transfer coefficient would primarily affect the cooling rate during solidification and the resultant microstructure.

Interestingly, in the coarse region of the recycled samples along the melt pool boundary, especially in the 5X-sample, the formation of the solidification micro-cracks primarily in the areas where interdendritic Al-Si lamellar eutectic structure had formed, was detected (shown in Figures 3.3(c – f) and 4f by arrows). It is well established that in materials with high coefficient of thermal expansion, such as aluminum alloys, excessive solute segregation during solidification, *e.g.* Si phase in the case of AlSi10Mg alloy, in the presence of high degree of residual stresses (common to the DMLS fabricated parts, as material experiences extremely high cooling rates) can enhance the solidification cracking susceptibility of the material.

Figures 3.4c and 4d schematically illustrate the solidification of α-Al dendrites and interdendritic Al-Si eutectic phase in AlSi10Mg alloy. In the Virgin sample (Figure 3.4c), a finer α-Al dendrite surrounded by a lower volume fraction of eutectic-Si has formed, ascribed to the higher cooling rate associated with the smaller particle size of the metal powder as compared to the recycled samples. On the other hand, the slower solidification/cooling rates of the melt pools in the recycled samples (Figure 3.4d) has provided a longer time at high temperature, promoted not only further growth of α-Al dendrites, but also rejection of more Si solute atoms from the α-Al solid solution (indicated by the red arrows in Figure 3.4d), leading to formation of coarser lamellae of eutectic-Si. Therefore, as shown in Figure 3.4d, in the recycled samples, a coarser α-Al dendrite with excessive solute segregation has formed along the melt pool boundaries as compared to the Virgin sample. Consequently, the samples fabricated using the recycled powders seem to be more susceptible to solidification cracking than the virgin powder fabricated ones (compare the FESEM micrographs in Figures 3.4e and 3.4f).

Although, comparable mechanical properties were reported for the DMLS-AlSi10Mg parts fabricated using virgin and recycled powders [1], their investigated recycled powder was only one time re-used, implying that their recycled powders could not have experienced a significant change in their shape, size distribution, and morphology, only after one building cycle. Accordingly, the formation of solidification cracks was not detected in that study [1]. However, the presented results herein confirmed that after four or five times of powder re-use cycles, a noticeable number of solidification micro-cracks formed in the as-printed samples, which can potentially deteriorate the mechanical properties of the fabricated part. Despite the vital importance of the mechanical properties in the build quality, the current study is mainly focused on the microstructure and corrosion properties of the parts, and the study of mechanical properties of the fabricated samples is subjected to a future work by the authors.

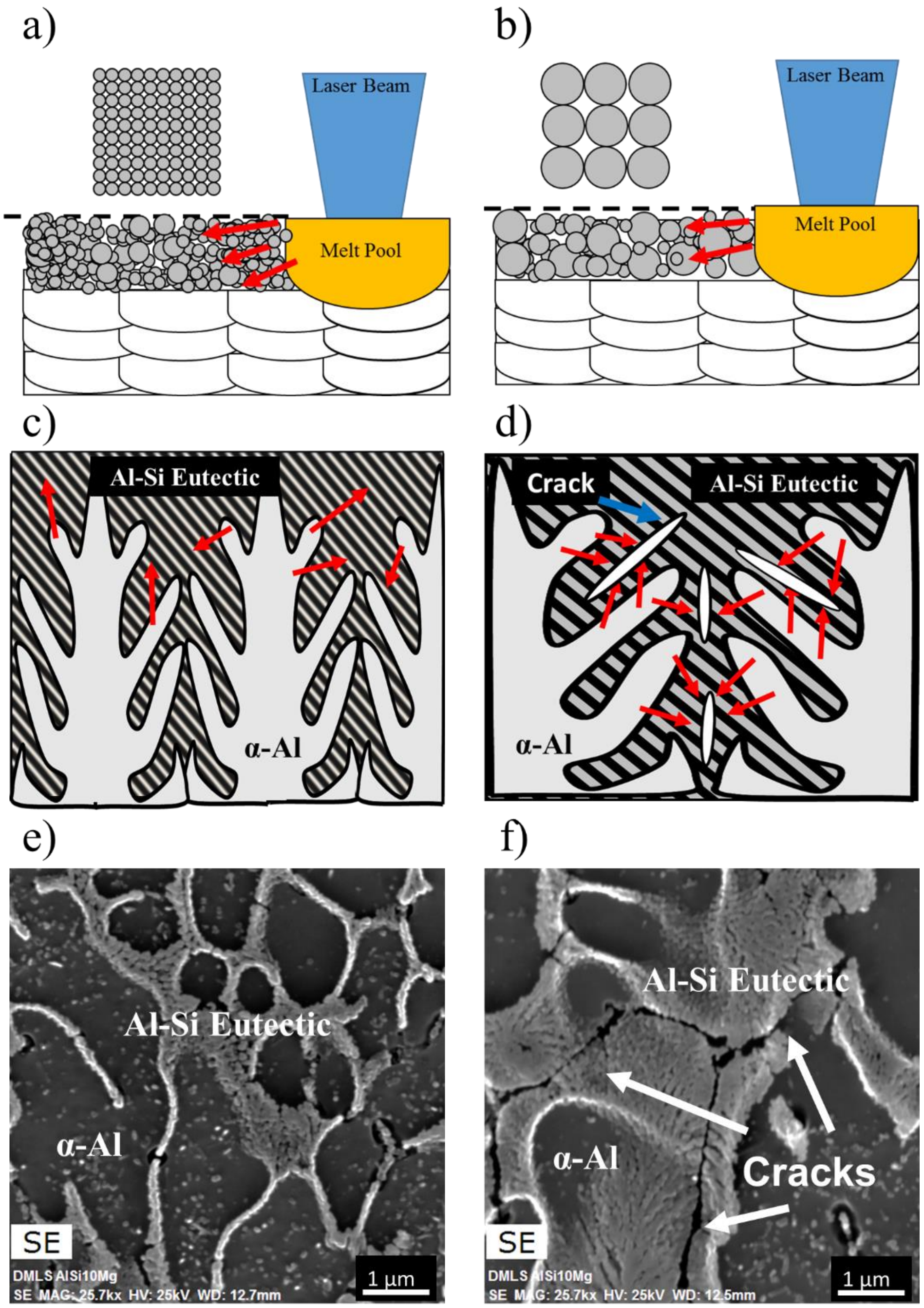

Figure 3. 4. Schematic of the DMLS process using the (a) virgin and (b) recycled powders. Schematic of solidification features in the c) Virgin and d) 4X/5X-samples. FESEM image of the coarse Al-Si eutectic phase in the e) Virgin and f) 5X-samples.

The XRD spectra of the DMLS-AlSi10Mg samples are presented in Figure 3.5, revealing the co-existence of both Al and Si phases for all three different samples. Noticeably, the Si peaks at 28°, 47°, and 56° in the XRD patterns of the samples intensify from the Virgin to 4X, and 5X-recycled samples, corresponding to the increased content of Si in precipitation/eutectic form from the Virgin to 4X and 5X-samples. This is consistent with the microstructural observations results presented in Figure 3.3, revealing the coarsening of interdendritic Si-network in the recycled samples compared to that of the Virgin sample.

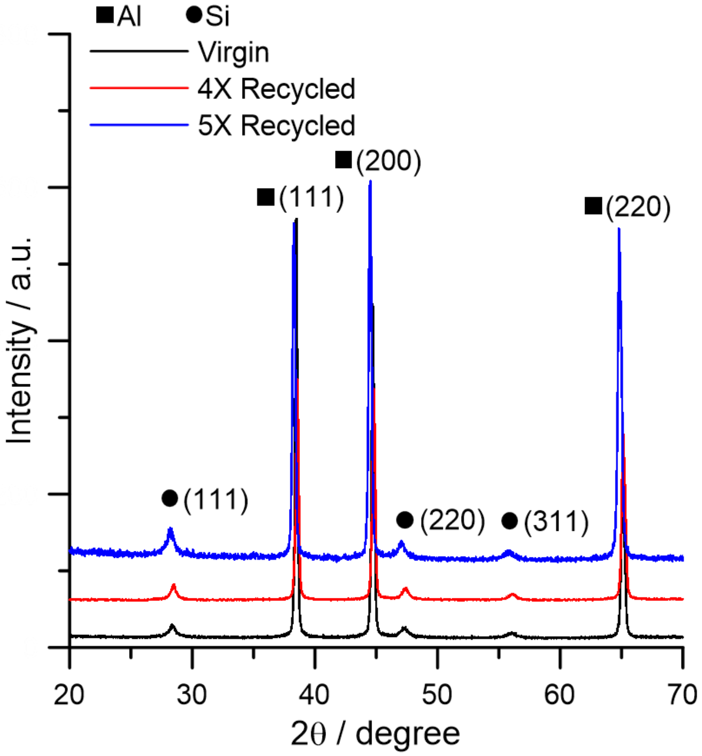

Figure 3. 5. XRD spectra of the DMLS-AlSi10Mg samples fabricated using virgin and recycled powders.

## 3.2. Corrosion Properties

Figure 3.6a shows the evolution of the OCP for all samples over 3600s in an aerated 3.5wt.% NaCl solution. Since the entire composition of all samples was approximately the same, the OCP values for all fabricated samples using different powders were stabilized around -0.70±0.01 $V_{Ag/AgCl}$, which was found to be consistent with previous studies [10]. However, the 5X-recycled sample revealed a slightly lower and more unstable corrosion potential, as compared to the other samples. The fluctuations of the OCP value have been ascribed to simultaneous localized dissolution and re-formation of the passive film on the surface of alloys with self-passivating properties, causing the electrochemical instability of the surface [17]. Meanwhile, the more negative $E_{OCP}$ value of the 5X-recycled sample indicates the higher activity and less electrochemical stability of its surface. This can be associated with the impact of using the recycled powders on the microstructure, and the resulted higher volume fraction of porosities in the fabricated samples, in addition to further coarsening and breakage of Si-network into idiomorphic crystals in the HAZ of 4X and 5X-recycled samples, as compared to those in the Virgin sample [10].

Figure 3.6b shows anodic polarization curves of the virgin and recycled powders fabricated samples with polished surfaces. Previous studies have shown a lower corrosion resistance on the side plane of the DMLS-AlSi10Mg than the top view plane, associated to the higher density of the melt pool boundaries on the side view plane, where an increased content of Si and the breakage of the Si-network and their growth have been detected [10,18]. For this reason, all electrochemical properties of the samples were measured on the side view planes. As depicted in Figure 3.6b, for all samples, the anodic current was rapidly increased by increasing the applied potential, resulting in the metal dissolution at an elevated rate [19]. This represents an active-like behavior for all polished surfaces herein, which is in agreement with the results reported in previous studies

[10,19,20]. Therefore, regardless of the type of the employed metal powder, formation of a passive region was not detected on the polarization graphs of all samples, confirming that surface pitting can immediately happen once the corrosion potential is reached.

As a general trend, a higher corrosion potential and a lower corrosion current density represent greater corrosion properties and higher electrochemical stability [12]. The corrosion potential of all three samples was approximately in the same range (-0.672±0.02, -0.679±0.01, and -0.690±0.03$V_{Ag/AgCl}$ for the Virgin, 4X, and 5X-recycled samples, respectively), which is likely ascribed to the uniformity of the chemical composition on the surface of all samples. However, when the corrosion current density ($I_{Corr.}$) values are compared, a noticeably higher (~2 times) corrosion current density was measured for the 5X-recycled sample (1.262±0.02μA/cm$^2$) versus the Virgin sample (0.642±0.01μA/cm$^2$), and the 4X-recycled sample showed an intermediate value (0.828±0.02μA/cm$^2$). This indicates increased severity of corrosion attack on the surface of the samples in the order of Virgin<4X<5X samples, confirming the deterioration, although not significant, of the corrosion performance when the recycled powders are used as the feedstock material.

The degraded corrosion properties of the recycled powder samples were attributed to the coarser microstructure along the melt pool borders of the recycled samples containing a higher content of eutectic-Si phase and lower content of solute Si in α-Al solid solution. This consequently results in an increased potential difference between the cathodic Si precipitates and anodic α-Al matrix, leading to a greater susceptibility of melt pool boundaries of the recycled samples to galvanic selective attack [10,21,22]

To further investigate the stability and protectiveness of the passive layer formed on the fabricated samples over time, EIS tests in aerated 3.5wt.% NaCl solution were carried out at different immersion times. Figures 3.6c and 6d show the modification of the Nyquist spectra for all samples over two different immersion times, *i.e.*, 1h and 120h. The radius of Nyquist curvature characterizes the stability of the protective passive film on the surface of the samples. The first and the second curvatures in the Nyquist plots correspond to the high-frequency ($10^2$-$10^3$Hz) and low-frequency (0.01-0.1Hz) responses, respectively [12–14]. As a general trend, the larger curvature of Nyquist arcs for the Virgin sample confirms a slower kinetic for the corrosion reactions (Figure 3.6c). This is in agreement with the anodic polarization results (shown in Figure 3.6b), corroborating the lowest corrosion current density ($I_{Corr.}$) for the Virgin sample. The Nyquist plots in just immersed condition (after 1h) for both 4X and 5X-recycled samples confirmed the lower resistance of the protective passive film on their surfaces as compared to the Virgin sample. The Nyquist plot of the Virgin sample showed one broad capacitive arc at the early stage of immersion (shown in Figure 3.6c). However, a closer look at the Nyquist plots of the recycled samples (in Figure 3.6c) reveals that the broad arc is comprised of two different arcs, one in low frequencies and the other in intermediate frequencies, with non-evident time constants [11], which is typical behavior of passive aluminum.

After a longer immersion time (120h), the Nyquist diagram (Figure 3.6d) revealed two distinct capacitive arcs with well-defined time constants in the range of low to intermediate frequencies. The first peak (at the intermediate frequency) corresponds to the sealing effect of the corrosion products inside the surface porosities or other active areas, such as α-Al/Si interface, while second peak (at low-frequency) is assigned to the diffusion within the passive layer and through localized corroded zones [18]. Analogous to the initial immersion time, even after 120h of immersion time, the Nyquist responses of all three samples (shown in Figure 3.6d) revealed a larger capacitive arc for the Virgin sample, confirming the higher stability of the protective passive film on its surface, leading to its greater corrosion resistance compared to the 4X and 5X-recycled samples.

Therefore, although the microstructural variations resulted from applying recycled powders in fabrication of DMLS-AlSi10Mg were not significant, the corrosion testing results presented herein confirmed that even a slight coarsening of interdendritic Si-network along the melt pool boundaries can affect the corrosion performance of the part, leading to a deterioration of its electrochemical stability in chloride containing environments.

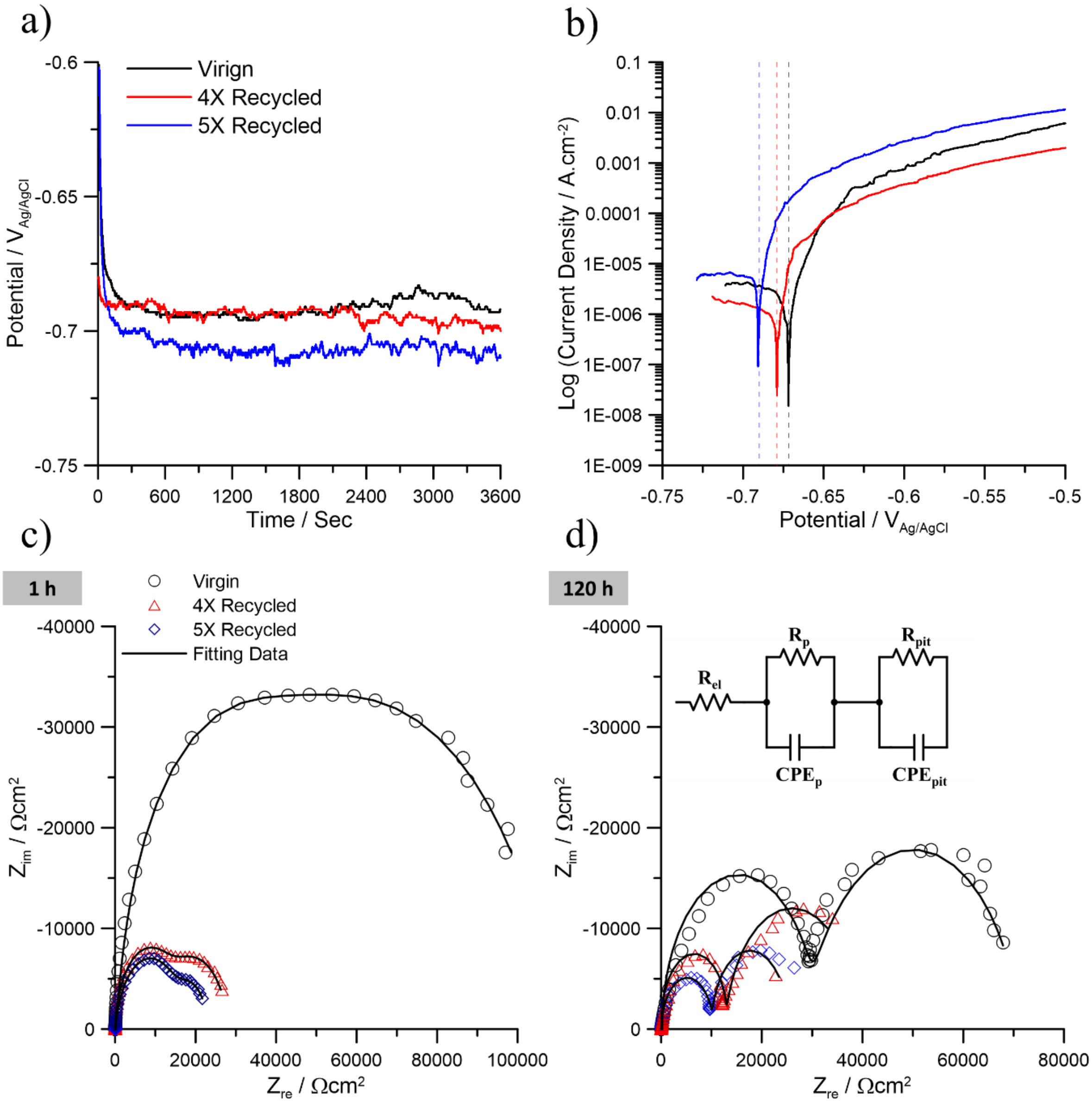

Figure 3. 6. a) OCP measurements over time, b) anodic polarization curves comparing the corrosion behavior of the Virgin, 4X, and 5X-samples. Nyquist spectra and the fitting data after c) 1h and d) 120h of immersion times.

To further explain and interpret the EIS data obtained in this study and describe the modification of protective passive film on the surface over time, a simplified equivalent circuit (SEC), shown in Figure 3.6d, was fitted to the experimental EIS data to physically interpret the complexity of the corrosion behavior of DMLS samples [11–14]. In the simplified equivalent circuit, $R_{el}$ describes the resistance of the electrolyte, $R_p$ and $CPE_p$ correspond to the resistance and constant phase element of the passive layer, and similarly, $R_{pit}$ and $CPE_{pit}$ correspond to the resistance and the constant phase element of the corroding pits, respectively.

The SEC fitted data are shown in Figures 3.6c and 3.6d, and the simulated parameters of the equivalent circuit are summarized in Table I. The higher values of the passive layer resistance ($R_p$) than the pitting resistance ($R_{pit}$) for all samples indicates that the pitting corrosion of the surface dominates over the general uniform corrosion attack, which is in agreement with the active-like behavior of all surfaces observed on the polarization graphs. Furthermore, at both immersion times, the $R_p$ and $R_{pit}$ values of the Virgin sample were found to be higher than those in the 4X and 5X-recycled samples, confirming the existence of a less protective passive film on the surface of the recycled powder fabricated samples compared to their virgin powder fabricated counterpart. Comparing the $R_p$ and $R_{pit}$ values of the 4X to the 5X-recycled one also indicates a slight degradation of passive layer resistance against both general corrosion and pitting corrosion attacks in the 5X-sample, which is consistent with the polarization results (Figure 3.6b).

Table 3. 1. The EIS parameters of the equivalent circuit shown in Figure 3.6d.

| ***Sample*** | **$R_{p.}$ ($k\Omega.cm^2$)** | **$CPE_p(Q_p)$ ($\mu\omega^{-1}s^{-n}cm^{-2}$)** | **$R_{pit}$ ($k\Omega.cm^2$)** | **$CPE_{pit}(Q_{pit})$ ($\mu\omega^{-1}s^{-n}cm^{-2}$)** |
|---|---|---|---|---|
| *1 h* | | | | |
| ***Virgin*** | 62.04 | 12.12 | 47.45 | 57.04 |
| ***4x*** | 14.70 | 227.80 | 13.50 | 23.80 |
| ***5x*** | 13.13 | 213.10 | 10.98 | 2.62 |
| *120 h* | | | | |
| ***Virgin*** | 36.3 | 79.60 | 31.92 | 0.92 |
| ***4x*** | 30.95 | 275.00 | 14.54 | 2.26 |
| ***5x*** | 20.85 | 3.93 | 13.14 | 413.80 |

The intergranular corrosion test was also conducted to investigate the corrosion morphology of the recycled samples compared to the Virgin sample. Figure 3.7 shows the FESEM images from the exposed surfaces of the Virgin, 4X, and 5X-samples after the intergranular corrosion testing. As shown in Figures 3.7a and 3.7b, a selective corrosion attack preferably along the melt pools borders was detected on the Virgin sample. The selective corrosion attack along the melt pool boundaries of DMLS/SLM-AlSi10Mg is commonly reported in previous studies [12,14], and is attributed to the enrichment of Si phase in that region, stimulating the micro-galvanic corrosion of the anodic Al matrix along the melt pool boundaries and in particular in the HAZ, where coarsening and breakage of Si-network into idiomorphic crystals were observed.

On the other hand, the surfaces of the recycled samples (Figures 3.7 (c – f)) revealed a more severe selective corrosion attack accompanied by formation of several superficial cracks on the Al matrix along the melt pool boundaries, particularly in the HAZ, after the intergranular corrosion testing. Formation of these corrosion mediated surface cracks in DMLS-AlSi10Mg products was also reported in a recent study and was ascribed to the existence of high level of residual stresses in the as-printed part provoking the adverse effect of the microstructural evolutions near the melt pool boundaries [20,23]. Therefore, further coarsening of Si-network along the melt pool regions in the recycled samples relative to the Virgin sample and the resulted accelerated dissolution of the anodic α-Al matrix from those regions have contributed to the surface cracking of the 4X and 5X-recycled samples after intergranular corrosion testing.

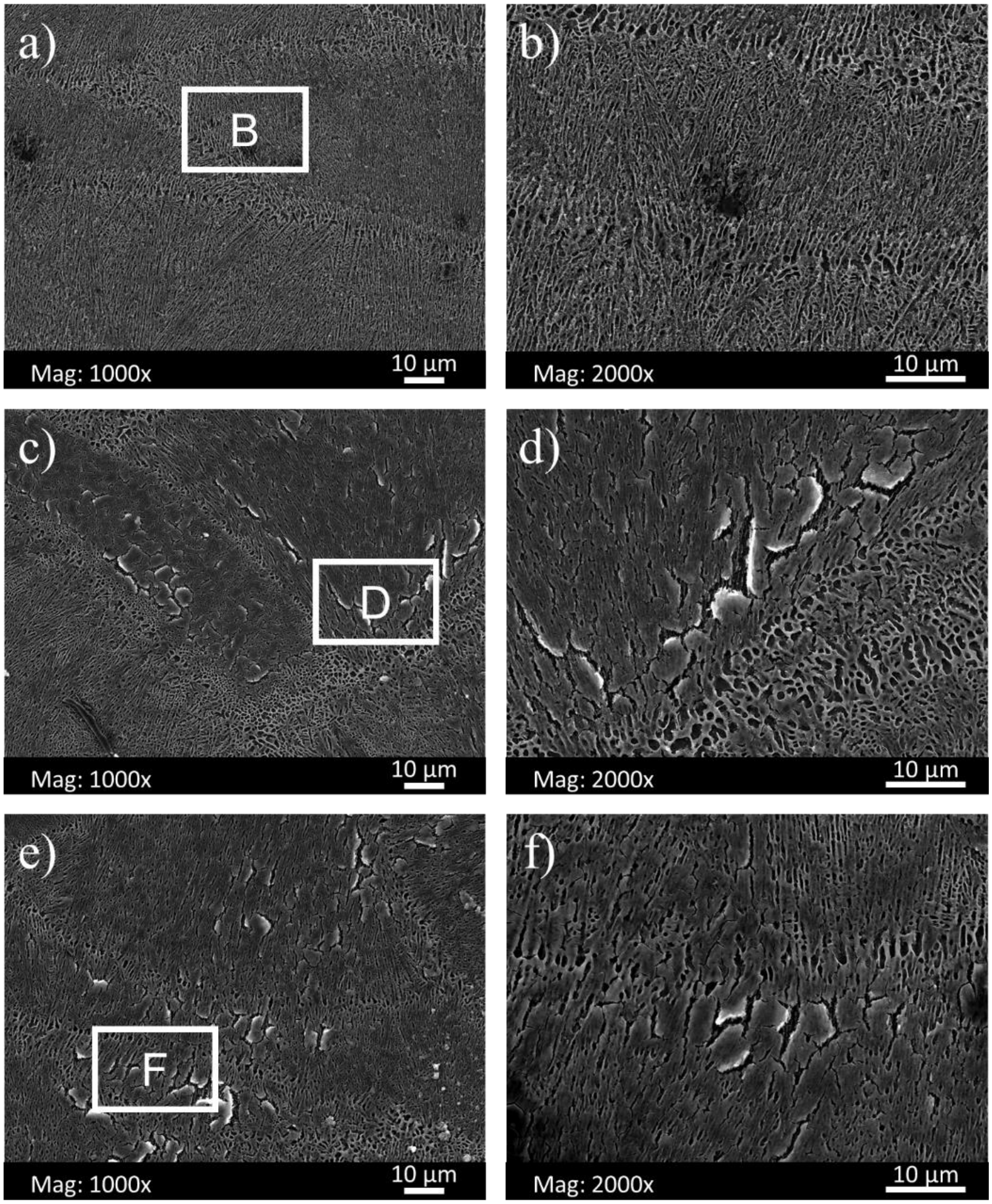

Figure 3. 7. SE-SEM micrographs of the DMLS-AlSi10Mg fabricated from the a) virgin powder, b) enclosed area in (a), c) 4X-recycled powder, d) enclosed area in (c), e) 5X-recycled powder, and f) enclosed area in (e), after the intergranular corrosion test.

## 4. Conclusions

In this work, the effects of using AlSi10Mg recycled powder after 4 times (4X) and 5 times (5X) of re-use cycles on the solidification defects, microstructure, and electrochemical properties of the DMLS-produced AlSi10Mg parts were investigated. The following conclusions can be drawn from this study:

1. Microstructural analysis results confirmed that using the recycled powder in the fabrication of the alloy leads to the formation of a higher density of internal discontinuities and defects, including porosities and solidification micro-cracks, accompanied by an increased content of eutectic-Si and coarsening of the interdendritic Si-network in the structure, mostly along the melt pool boundaries.
2. Such microstructural variations in the recycled samples were correlated to the larger size and irregular shape of the recycled powders compared to the virgin powders, leading to a reduced thermal conductivity for the recycled powders. The reduced thermal conductivity associated with the recycled powders was found to lessen the cooling rate of the melt pools during fabrication, causing excessive Si solute segregation during solidification, which was found to increase the solidification cracking susceptibility of the alloy.
3. The electrochemical measurements, *i.e.*, anodic polarization and EIS tests, confirmed that the increased eutectic-Si content along the melt pool boundaries in the 4X and 5X-samples deteriorated the corrosion resistance in the recycled powder fabricated samples.
4. The intergranular corrosion test confirmed an accelerated preferential corrosion attack combined with the formation of superficial micro-cracks along the melt pool boundaries in the 4X and 5X-recycled samples dominated by the microstructural evolutions and in particular coarsening of the Si phase in the recycled samples. Therefore, the slight microstructural

variations in the recycled samples were found to play a key role in dictating the material's corrosion behavior.

## Acknowledgment

The authors wish to acknowledge the support of Natural Sciences and Engineering Research Council of Canada (NSERC) [grant number RGPIN-2017-04368] for sponsoring this work.

## References

[1] H. Asgari, C. Baxter, K. Hosseinkhani, M. Mohammadi, On microstructure and mechanical properties of additively manufactured AlSi10Mg_200C using recycled powder, Mater. Sci. Eng. A. 707 (2017) 148–158. doi:10.1016/J.MSEA.2017.09.041.

[2] E.O. Olakanmi, Selective laser sintering/melting (SLS/SLM) of pure Al, Al–Mg, and Al–Si powders: Effect of processing conditions and powder properties, J. Mater. Process. Technol. 213 (2013) 1387–1405. doi:https://doi.org/10.1016/j.jmatprotec.2013.03.009.

[3] W.J. Sames, F.A. List, S. Pannala, R.R. Dehoff, S.S. Babu, The metallurgy and processing science of metal additive manufacturing, Int. Mater. Rev. 61 (2016) 315–360. doi:10.1080/09506608.2015.1116649.

[4] N.T. Aboulkhair, I. Maskery, C. Tuck, I. Ashcroft, N.M. Everitt, On the formation of AlSi10Mg single tracks and layers in selective laser melting: Microstructure and nano-mechanical properties, J. Mater. Process. Technol. 230 (2016) 88–98. doi:https://doi.org/10.1016/j.jmatprotec.2015.11.016.

[5] A.H. Maamoun, M. Elbestawi, G.K. Dosbaeva, S.C. Veldhuis, Thermal post-processing of AlSi10Mg parts produced by Selective Laser Melting using recycled powder, Addit. Manuf. 21 (2018) 234–247. doi:https://doi.org/10.1016/j.addma.2018.03.014.

[6] L.C. Ardila, F. Garciandia, J.B. González-Díaz, P. Álvarez, A. Echeverria, M.M. Petite, R. Deffley, J. Ochoa, Effect of IN718 Recycled Powder Reuse on Properties of Parts Manufactured by Means of Selective Laser Melting, Phys. Procedia. 56 (2014) 99–107. doi:https://doi.org/10.1016/j.phpro.2014.08.152.

[7] G. Nichols, S. Byard, M.J. Bloxham, J. Botterill, N.J. Dawson, A. Dennis, V. Diart, N.C. North, J.D. Sherwood, A Review of the Terms Agglomerate and Aggregate with a Recommendation for Nomenclature Used in Powder and Particle Characterization, J. Pharm. Sci. 91 (2002) 2103–2109. doi:https://doi.org/10.1002/jps.10191.

[8] A. Simchi, Direct laser sintering of metal powders: Mechanism, kinetics and microstructural features, Mater. Sci. Eng. A. 428 (2006) 148–158. doi:https://doi.org/10.1016/j.msea.2006.04.117.

[9] K. Abd-Elghany, D.L. Bourell, Property evaluation of 304L stainless steel fabricated by selective laser melting, Rapid Prototyp. J. 18 (2012) 420–428.

[10] R.I. Revilla, J. Liang, S. Godet, I. De Graeve, Local Corrosion Behavior of Additive Manufactured AlSiMg Alloy Assessed by SEM and SKPFM, J. Electrochem. Soc. . 164 (2017) C27–C35. doi:10.1149/2.0461702jes.

[11] M. Cabrini, S. Lorenzi, T. Pastore, S. Pellegrini, E.P. Ambrosio, F. Calignano, D. Manfredi, M. Pavese, P. Fino, Effect of heat treatment on corrosion resistance of DMLS AlSi10Mg alloy, Electrochim. Acta. 206 (2016) 346–355. doi:https://doi.org/10.1016/j.electacta.2016.04.157.

[12] P. Fathi, M. Mohammadi, X. Duan, A.M. Nasiri, A Comparative Study on Corrosion and Microstructure of Direct Metal Laser Sintered AlSi10Mg_200C and Die Cast A360.1 Aluminum, J. Mater. Process. Technol. 259 (2018) 1–14. doi:https://doi.org/10.1016/j.jmatprotec.2018.04.013.

[13] M. Rafieazad, M. Mohammadi, A. Nasiri, On Microstructure and Early Stage Corrosion Performance of Heat Treated Direct Metal Laser Sintered AlSi10Mg, Addit. Manuf. 28 (2019) 107–119.

[14] P. Fathi, M. Mohammadi, X. Duan, A. Nasiri, Effects of Surface Finishing Procedures on

Corrosion Behavior of DMLS-AlSi10Mg_200C Alloy Versus Die-Cast A360.1 Aluminum, JOM. (2019) 1–12. doi:10.1007/s11837-019-03344-8.

[15] M. Tang, P.C. Pistorius, S. Narra, J.L. Beuth, Rapid Solidification: Selective Laser Melting of AlSi10Mg, JOM. 68 (2016) 960–966. doi:10.1007/s11837-015-1763-3.

[16] X.P. Li, X.J. Wang, M. Saunders, A. Suvorova, L.C. Zhang, Y.J. Liu, M.H. Fang, Z.H. Huang, T.B. Sercombe, A selective laser melting and solution heat treatment refined Al–12Si alloy with a controllable ultrafine eutectic microstructure and 25% tensile ductility, Acta Mater. 95 (2015) 74–82. doi:https://doi.org/10.1016/j.actamat.2015.05.017.

[17] B. Wu, Z. Pan, S. Li, D. Cuiuri, D. Ding, H. Li, The anisotropic corrosion behaviour of wire arc additive manufactured Ti-6Al-4V alloy in 3.5% NaCl solution, Corros. Sci. 137 (2018) 176–183. doi:https://doi.org/10.1016/j.corsci.2018.03.047.

[18] M. Cabrini, S. Lorenzi, T. Pastore, S. Pellegrini, D. Manfredi, P. Fino, S. Biamino, C. Badini, Evaluation of corrosion resistance of Al–10Si–Mg alloy obtained by means of Direct Metal Laser Sintering, J. Mater. Process. Technol. 231 (2016) 326–335. doi:https://doi.org/10.1016/j.jmatprotec.2015.12.033.

[19] M. Cabrini, S. Lorenzi, T. Pastore, C. Testa, D. Manfredi, G. Cattano, F. Calignano, Corrosion resistance in chloride solution of the AlSi10Mg alloy obtained by means of LPBF, Surf. Interface Anal. (n.d.). doi:10.1002/sia.6601.

[20] T. Rubben, R.I. Revilla, I. De Graeve, Influence of heat treatments on the corrosion mechanism of additive manufactured AlSi10Mg, Corros. Sci. (2018). doi:https://doi.org/10.1016/j.corsci.2018.11.038.

[21] T. Rubben, R.I. Revilla, I. De Graeve, Effect of Heat Treatments on the Anodizing Behavior of Additive Manufactured AlSi10Mg, J. Electrochem. Soc. 166 (2019) C42--C48.

[22] R.I. Revilla, D. Verkens, G. Couturiaux, L. Malet, L. Thijs, S. Godet, I. De Graeve, Galvanostatic Anodizing of Additive Manufactured Al-Si10-Mg Alloy, J. Electrochem. Soc. 164 (2017) C1027–C1034. doi:10.1149/2.1121714jes.

[23] M. Cabrini, F. Calignano, P. Fino, S. Lorenzi, M. Lorusso, D. Manfredi, C. Testa, T. Pastore, Corrosion Behavior of Heat-Treated AlSi10Mg Manufactured by Laser Powder Bed Fusion, Materials (Basel). 11 (2018). doi:10.3390/ma11071051.

# Chapter 4

# Effects of Laser-Powder Bed Fusion Process Parameters on the Microstructure and Corrosion Properties of AlSi10Mg Alloy[5]

## Preface

A version of this manuscript has been accepted in the Journal of Electrochemical Society, 2021 (JES). I am the first and corresponding author of these papers. Along with the co-authors, Parisa Fathi, Dr. Mohsen Mohammadi, and Dr. Ali Nasiri, I investigate the effects of microstructural modifications induced by tuning the laser-powder bed fusion (L-PBD) process parameters on the electrochemical stability of the L-PBF-AlSi10Mg alloy are investigated. I prepared methodology, experimental, formal analysis, and the first original draft of the manuscript and subsequently revised the manuscript based on the coauthors' feedback and also the peer review process. The co-authors Dr. Mohsen Mohammadi and Dr. Ali Nasiri helped in conceptualization, design, project administration, and supervision, review & editing of the manuscript.

---

[5] M. Rafieazad, P. Fathi, M. Mohammadi, A. Nasiri, Effects of Laser-Powder Bed Fusion Process Parameters on the Microstructure and Corrosion Properties of AlSi10Mg Alloy, Journal of Electrochemical Society (JES). 2021. https://doi.org/10.1149/1945-7111/abdfa8 (IPF= 3.721)

## Abstract

In this study, the effects of microstructural modifications induced by tuning the laser-powder bed fusion (L-PBD) process parameters on electrochemical stability of the L-PBF-AlSi10Mg alloy are investigated. Three groups of L-PBF-AlSi10Mg samples were fabricated utilizing combinations of L-PBF process parameters for their Upskin layers. The implemented process parameters modifications were found to be not only effective in reducing the as-printed surface roughness of the components, but also led to the formation of cyclic small-large melt pools (MPs) in Upskin layers of the fabricated samples. Such consecutive modification in the size of MPs led to the increased inhomogeneity of the microstructure, contributing to the formation of a coarser intercellular eutectic-Si network, larger grain size, and lower density of low angle grain boundaries. Among all fabricated samples, the sample that experienced the fastest cooling during solidification was found to reveal the highest corrosion resistance and the best passive film stability on its Upskin surface both in naturally-aerated and deaerated 3.5 wt.% NaCl electrolyte, owing to the finer Al-Si eutectic structure that forms along its large MP-boundaries. The as-printed microstructure of the L-PBF-AlSi10Mg was found a dominant factor in determining the necessity of applying post-printing surface polishing procedures to attain better corrosion properties.

**Keywords:** Additive manufacturing (AM); laser-powder bed fusion (L-PBF); AlSi10Mg; microstructure; corrosion.

## 1. Introduction

Over the past decades, the continuously growing attention to advanced engineering components with more intricate designs and improved mechanical and corrosion performance for applications in harsher environments has demanded the implementation of innovative manufacturing technologies [1]. Metal-based additive manufacturing, or three-dimensional (3D) printing, as a novel and rapidly evolving fabrication technology, offers a variety of solutions to the existing gaps and deficiencies both in design and manufacturing and introduces a versatile method to fabricate intricate parts with improved performance and functionalities. Laser-powder bed fusion is an additive manufacturing process that offers distinct advantages, such as cost-effective manufacturing with the feasibility to create near net shape complex geometries without almost any loss of material, and shorter time to market compared with traditional technologies. Different terminologies have been used in different studies to refer to this process, such as Selective Laser Melting (SLM) [1], Direct Metal Laser Sintering (DMLS) [2], or Laser Beam Melting (LBM) [2].

Heretofore, various types of metals have been successfully fabricated using different AM technologies, including Ti alloys [3,4], Ni alloys [5,6], stainless steel [7–9], and Al-based alloys [10–14]. From the large family of aluminum alloys, AlSi10Mg alloy has been primarily implemented as the feedstock material by the additive manufacturing industry, and in particular, through the laser-powder bed fusion (L-PBF) process. The hypo-eutectic AlSi10Mg alloy has many applications in different industries, including aerospace, marine, and automotive due to its low thermal expansion, lightweight, and decent corrosion, and mechanical performance [14–16]. However, the traditional fabrication methods, such as casting, forging, and powder metallurgy techniques, have substantially limited the accelerated adoption of the family of Al-Si-Mg alloys, particularly in harsher environments due to the required prolonged fabrication cycles for complex parts and the obtained microstructure of the alloy in as-fabricated condition. AlSi10Mg commonly contains a coarse eutectic silicon phase in addition to various hard and brittle intermetallic components, which can severely deteriorate its mechanical and corrosion properties [13,15,17]. In addition, implementing the L-PBF process in the fabrication of AlSi10Mg alloys has opened many new avenues for novel designs and applications for this alloy in various industries.

Regardless of all the advantages that L-PBF technology is able to offer to the manufacturing industry, analogous to any other manufacturing process, it should not be considered as a flawless fabrication technique. In particular, for the L-PBF-AlSi10Mg alloy, the implemented high laser power, fast scanning rate, and balling and dross formation during solidification of the alloy commonly lead to the formation of various imperfections, such as microstructural inhomogeneity, high level of porosity, solidification micro-defects, residual stresses within the part, and the as-printed surface roughness. Such process-induced imperfections can adversely impact the corrosion and mechanical properties of the fabricated components [11,14,18–20]. In order to diminish the formation of these defects and subsequently improve the corrosion and mechanical performance of the parts, various post-printing solutions, such as post-heat treatments [14,21,22], using different feedstock metal powder size [16,19], tuning L-PBF process parameters [10,11,23], hot isostatic pressing (HIP) [24], and post-printing surface treatments [25,26] have been implemented.

It was reported that solution heat treatment improves the ductility of L-PBF-AlSi10Mg alloy at the expense of the tensile strength reduction [27–29]. Other post-printing heat treatment cycles have been introduced as an effective way to improve the microstructural homogeneity in L-PBF-AlSi10Mg alloy [14,30]. It has been shown that by elevating the post-printing thermal-treatment temperature of the L-PBF-AlSi10Mg alloy from 200 °C to 350 °C, the breakage of the continuous Si network occurs, followed by the coarsening and growth of Si phase into idiomorphic particles, resulted in an ulterior Si network boundaries and a more homogenous microstructure as compared to the as-printed condition [14]. Therefore, any heat treatment cycle at temperatures higher than 250 °C ultimately disturbs the as-printed cellular microstructure of L-PBF-AlSi10Mg alloy and consequently deteriorates the corrosion performance of the alloy [22,30–32].

Controlling the L-PBF processing parameters, such as size and morphology of the feedstock metal powder, laser power, hatching distance, and scanning speed can also impact the internal defects' density, the achieved surface roughness, as well as the microstructure and consequently, the corrosion performance of the fabricated L-PBF-AlSi10Mg parts [16,19,33]. Microstructural analysis of the L-PBF-AlSi10Mg alloy using a feedstock powder with a larger size (13.7±9 μm) as compared to the smaller powders (8.8±7 μm) revealed that the size and morphology of the powders primarily impact the degree of Si networks coarsening, level of porosity, and solidification micro-cracks, giving rise to the deterioration of the corrosion performance of this alloy [19]. Other studies also reported the impact of tuning the L-PBF process parameters on the initial surface roughness of L-PBF-AlSi10Mg samples in the as-printed condition [10,11,23]. It has been reported that changing the laser power, beam offset, hatching distance, and scanning speed can drastically alter the final surface roughness of the samples [10,11,23]. For instance, the previous study by the authors showed that by reducing the hatch distance from 0.21 mm to 0.12 mm, scanning speed from 1000 mm/s to 775 mm/s, and beam offset from 0.2 mm to 0.1 mm, the surface roughness of the fabricated L-PBF-AlSi10Mg can be noticeably improved from $R_a$ = 5.1 ± 1.5 μm to 1.1 ± 0.2 μm [10]. The reported adjusted process parameters also resulted in a low level of porosity in the fabricated parts as compared to the published data in the literature for L-PBF-AlSi10Mg [11]. It is also reported that the modification of the process parameters not only can impact the achieved as-printed surface roughness of the part, but also it can modify the microstructure, and consequently, the corrosion property of the printed sample [10].

In the recent study by the authors [10], the corrosion response of the fabricated samples was investigated in the as-printed surface finish. However, it is known that the corrosion properties of the as-printed L-PBF-AlSi10Mg sample can be significantly affected and even controlled by the heavily oxidized partially melted particles that shroud the as-printed surfaces [10,13]. Therefore, to be able to accurately identify the exclusive impacts of the microstructural modifications in L-PBF-AlSi10Mg on its corrosion properties and electrochemical stability, the as-printed surface roughness and the pre-existing partially melted powder particles should be eliminated from the surface of the alloy through polishing. Focusing on this gap, this research, as a supplementary study to the previous works by the authors [10,11], aims to investigate the effect of the applied microstructural modifications by tuning the printing process parameters, independent from the resultant surface roughness, on the corrosion properties of the L-PBF-AlSi10Mg alloy. The impact of dissolved oxygen in naturally-aerated 3.5 wt.% NaCl electrolyte on the corrosion response of the L-PBF AlSi10Mg alloy is also investigated. Furthermore, comparisons are made between the corrosion response of the fabricated samples with the as-printed surface finish reported in the authors' previous study [10] and their polished counterparts to further clarify the necessity of implementing a post-printing surface modification method, such as polishing, on the L-PBF fabricated AlSi10Mg components.

## 2. Experimental Procedure

### 2.1. Material and Fabrication Process

In this study, three AlSi10Mg cubes with 15 × 15 × 15 mm dimensions were fabricated using an EOS M290 metal 3D printer machine equipped with a 400 W Ytterbium-fiber laser with 100 µm spot size at platform temperature of 165 °C. The used gas atomized AlSi10Mg powders in this study had the particle size distribution of 15-45 µm. The chemical composition of the used feedstock metal powder is summarized in Table 1. Other processing parameters, such as 30 µm thickness of the powder layer and stripe hatch rotation of the laser beam by 67° between successive layers, were kept constant in the fabrication of all samples [10].

Table 4. 1. Nominal chemical compositions of AlSi10Mg_200C powder (wt. %)

| ***Si*** | ***Mg*** | ***Fe*** | ***Mn*** | ***Ti*** | ***Zn*** | ***Cu*** | ***Al*** |
|---|---|---|---|---|---|---|---|
| 9.00-11.00 | 0.20- 0.45 | ≤0.55 | ≤0.45 | ≤0.15 | ≤0.10 | ≤0.05 | Bal. |

To investigate the effect of the fabrication process parameters on the modification of the microstructure, solidification behavior, and corrosion properties of the L-PBF-AlSi10Mg samples, three groups of samples, *i.e*. Surface I, Surface II, and Regular, having the same processing parameters for their core but different fabrication parameters for their last three to seven printed layers (so-called Upskin layer), were fabricated [10]. The detailed L-PBF process parameters used for the manufacturing of the Upskin layers in different samples are summarized in Table 2, whereas the employed process parameters for the core of these three samples can be found in the previous study by the authors [10]. The process parameters employed for the printing of the Surface I and Surface II samples are the same except that the hatch distance and beam offset used for the Upskin layer of Surface II sample were slightly lower than those in the Surface I sample.

Table 4. 2. Process parameters for the deposition of the Upskin layers of each samples.

| ***Process Parameters*** | ***Surface I*** | ***Surface II*** | ***Regular*** |
|---|---|---|---|
| Hatch Distance / mm | 0.13 | 0.12 | 0.21 |
| Speed / mm.s$^{-1}$ | 775 | 775 | 1000 |
| Power / W | 370 | 370 | 360 |
| Beam Offset / mm | 0.15 | 0.10 | 0.20 |
| VED* / J.mm$^{-3}$ | 122.42 | 132.62 | 57.14 |

*Volumetric Energy Density of the laser

## 2.2. Microstructure Characterization

To be able to assess the applied microstructural modifications on the Upskin layer of each sample, the Upskin surfaces were delicately polished perpendicular to the building direction, using Tegramin-30 Struers auto-grinder/polisher to a mirror-like finish surface using a 0.02 µm alumina suspension. Keller’s reagent (2.5 vol.% $HNO_3$, 1.5 vol.% HCl, 1 vol.% HF, and 95 vol.% $H_2O$) were used to expose the microstructural features. The microstructural analysis of the samples was carried out using scanning electron microscopy (SEM-FEI MLA 650F) with an energy dispersive X-ray (EDX from Bruker) detector and an HKL Electron backscattered diffraction (EBSD) system. The grains size, crystallographic orientations, and grain boundary evolutions were also examined by EBSD analysis using Nordlys II HKL EBSD detector over two different scanning areas of 300×300 µm and 150×150 µm at the step size of 0.7 µm and 0.35 µm, respectively. An EBSD post-processing software (Channel 5) was used to post-process and analyze the EBSD results.

## 2.3. Electrochemical Measurements

The corrosion analyses were conducted on the top surface of the polished Upskin layers of the L-PBF fabricated samples using an IVIUM CompactStat™ Potentiostat with a three-electrode cell setup according to the ASTM G5 standard for anodic polarization measurements [34]. A graphite rod as the counter electrode (CE) and a saturated silver/silver chloride (Ag/AgCl) electrode as the reference electrode (RE) were used. For all electrochemical testing, aerated 3.5 wt.% NaCl solution at 25 °C was used as the electrolyte. Prior to the corrosion tests, the open circuit potentials (OCP) were monitored for 1 h for stabilization. The potential range for the anodic curve measurements was applied from −0.02 V to +0.3 V *vs*. OCP, employing a scanning rate of 0.125 mV/s. To easily observe the pitting potential ($E_{pit}$) of the samples, the anodic polarization tests were also performed using the same parameters in deaerated condition, prepared by bubbling argon gas at the rate of 150 $cm^3$/min for an hour in the electrolyte [35]. The electrochemical impedance spectroscopy (EIS) tests were also performed on the polished Upskin surfaces of each sample from 1 h up to 96 h of immersion time in aerated 3.5 wt. % NaCl solution. Signals with 0.01 V amplitude over the OCP with a sinusoidal frequency range between 100 kHz and 10 mHz were applied. To confirm the repeatability of the obtained corrosion data, at least three samples were tested for each condition. The corrosion morphology of the samples was also studied after polarization testing in both aerated and deaerated solutions as well as after EIS testing at 1 h and 96 h of immersion times using the SEM. Prior to the corrosion morphology analysis, the formed corrosion products were removed from the samples' surfaces by immersing the corroded samples in concentrated $HNO_3$ (15.8 N) solution for 15 min [36].

## 3. Results and Discussion

### 3.1. Microstructural Characterization

Since the effects of adopted variations in the process parameters can only be detected in the last three to seven deposited layers, the top surface of the fabricated samples was the main focus of the conducted microstructural and corrosion studies herein. The SEM micrographs taken from different Upskin layers (shown in Figure 4.1) clearly depict the morphologies of the MPs from both the top and side views of the Surface I, Surface II, and Regular samples. The polished surfaces were delicately prepared aligned with the building plane (top view) and building direction (side view) to ensure the observed MPs on the top view are perfectly parallel to the direction of the laser scan and on the side view are perpendicular to the scanning plane (x-y plane).

Figures 4.1a-4.1c show the SEM micrographs taken from the side view of all samples, confirming the cyclic formation of the small-large MPs in the Upskin layer of Surface I and Surface II samples. On the other hand, a relatively consistent MP size in the Upskin layer of the Regular sample was detected (Figure 4.1c). It has been reported that by enhancing the overlap between two subsequent passes resulted from decreasing the hatch distance during fabrication, the heat transfer intensity through the previously solidified MP increases, giving rise to a more notable difference in the size of MPs between the two successive passes [10].

As can be seen in Figures 4.1d-4.1f, the observed MPs on the top view of the fabricated samples do not exhibit a tear-dropped morphology with irregular geometries and directions similar to what commonly reported in the previous studies [12–14]. Differently, the MP boundaries are side by side parallel with the direction of the laser scan, confirming the 67° rotation between different layers. However, the microstructure of the core of all three samples, *i.e.*, the microstructural features of the MPs and their boundaries, was found to be very comparable to common L-PBF-AlSi10Mg microstructure reported earlier in the literature [10–14].

Comparing the geometrical characteristics of the MPs of the top and side views of different samples, shown in Figures 4.1a-4.1f, confirmed the variation of the MPs’ width in a periodic manner in Surface I, and more noticeably, in Surface II. The slight change in the hatch distance and beam offset from the Regular sample to Surface II led to the formation of such bi-layer MP structure, leading to the formation of almost two times more compacted MPs per unit area in the Surface I and Surface II's Upskin layers as compared to that of Regular sample.

The detailed microstructural features taken from the Upskin layer of the fabricated samples are presented in Figure 4.1g-4.1l. All samples similarly revealed the formation of a notably fine cellular network of eutectic Si along the interdendritic regions of the primary Al phase, commonly reported as the dominant microstructure in all powder bed fusion fabricated AlSi10Mg parts (shown in Figure 4.1g) [10,14,19]. Across each MP, there are three distinct regions with different microstructures formed as a result of different thermal histories, *i.e.*, fine cellular structure (MP-fine), coarse cellular structure (MP-coarse), and transition heat-affected zone (HAZ) structure. It is worth noting that two solidification parameters, *i.e.*, solidification rate ($R$) and temperature gradient ($G$), contribute to such microstructural variations for a given composition. During the solidification in the MP center, $R$ is minimum, and $G$ is maximum, resulting in the formation of the fine cellular-dendritic morphology. On the other hand, along the MP boundaries, the more elongated and coarser dendritic structure is formed due to the highest solidification rate and the lowest temperature gradient that material undergoes [14].

The SEM micrographs of both small and large MPs of different samples revealed different shape and size distribution of the eutectic Si network parallel to the extension of each region, resulting from different solidification behavior. Figure 4.1g and 4.1j confirmed that the microstructure of the two neighboring MPs and their MP-coarse region's average size (extension towards the MP fine region) of the Surface I sample are almost comparable. However, the MP boundaries of the Surface II sample (Figures 4.1h-4.1k) revealed two different MP microstructure, including the smaller MPs (Figure 4.1h) with a narrow MP-coarse region and larger MPs (Figure 4.1k) containing a broader MP-coarse region. The SEM images shown in Figures 4.1i and 4.1l confirmed that the MPs of the Regular sample possess almost the same size, distribution, and morphology of the intercellular Si network along their boundaries. However, due to the lower volumetric energy densities (VED) employed in the printing of the Regular sample, a slightly smaller average size of the eutectic Si network was found in the Regular sample compared with the Surface I sample. A more comprehensive microstructural analysis of the fabricated samples is presented in the authors' previous study [10].

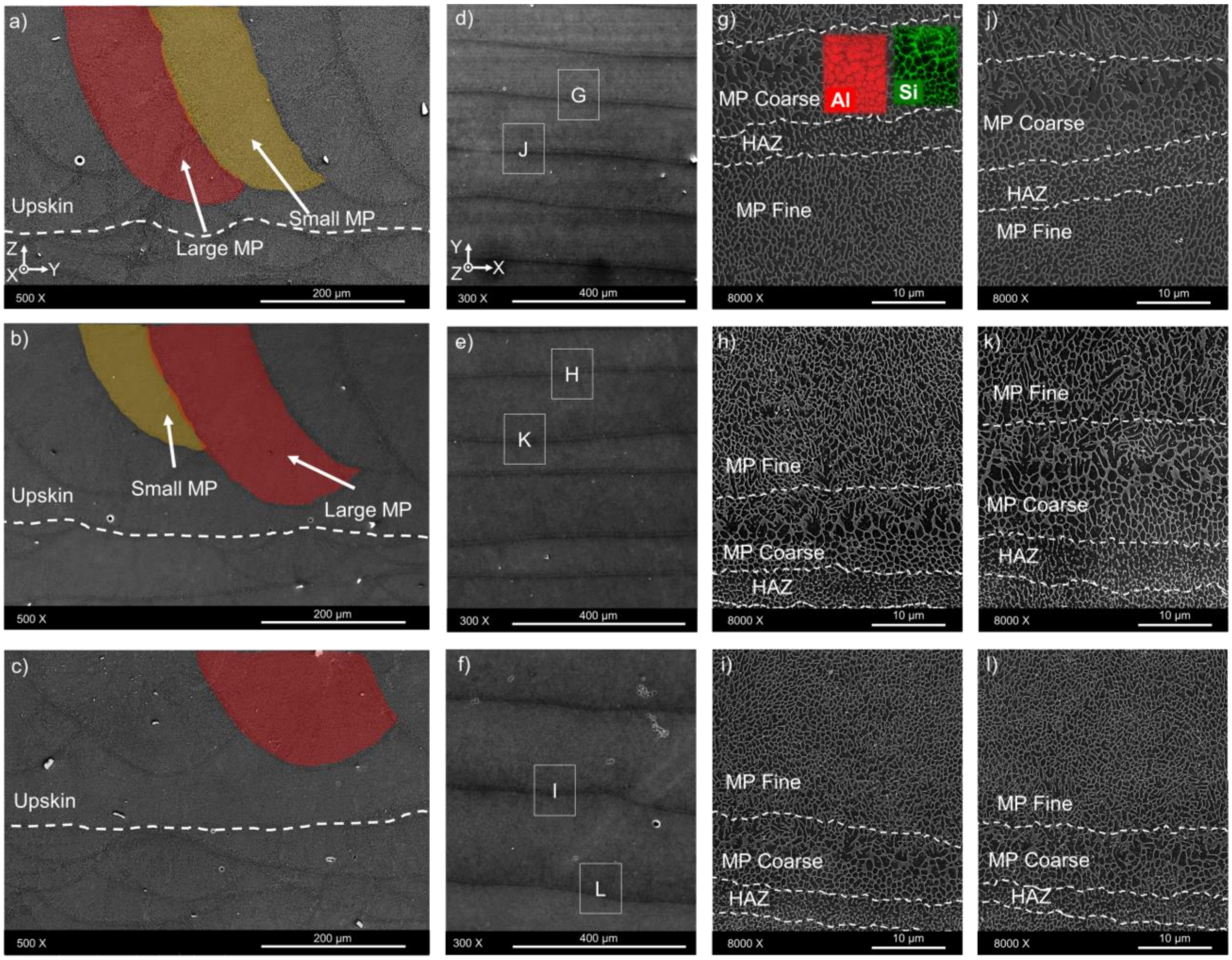

Figure 4. 1. SEM micrographs taken from the side (y-z plane) and top (x-y plane) view of the (a) and (d) Surface I, (b) and (e) Surface II, (c) and (f) Regular samples, (g) higher magnification image from the small MP boundary, the enclosed are in (d) indicated by G, (j) large MP boundary, the enclosed are in (d) indicated by J, (h) higher magnification image from the small MP boundary, the enclosed are in (e) indicated by H, (k) larger MP boundary, the enclosed are in (e) indicated by K, (i) higher magnification image from the small MP boundary, the enclosed are in (f) indicated by I, and (l) large MP boundary, the enclosed are in (f) indicated by L.

In a complementary analysis to the SEM microstructural investigation on three Upskin layers herein, EBSD analysis was carried out. The obtained inverse pole figure (IPF-z) maps, where the z-axis is parallel to the building direction of the Upskin layer, are shown in Figure 4.2a-c. A combination of equiaxed and columnar grains with varying volume fractions within each MP can be detected in the IPF maps of all samples, ascribed to the gradual variations of the temperature gradient (*G*) and solidification rate (*R*) from the center of the MP towards its boundary. It is well-known that in the L-PBF process, the heat is mainly dissipated through the previously solidified layers [10,20,37]. Therefore, the detected variation in the MP size in each sample and also from one sample to another would affect the heat flux intensity and direction (cooling rate), and consequently, the resultant microstructures.

The grains size distribution and grains aspect ratio of the Upskin layers of all samples in both large and small MPs were extracted from the IPF maps and are presented in Figure 4.3. The grain size distributions of the large MPs shown in Figures 4.2a-c were calculated to be 0.79 ± 0.90, 0.95 ± 1.44, and 0.89 ± 1.27 μm for the Surface I, and Surface II, and Regular samples, respectively. The finer and more randomly orientated equiaxed grains (grains with aspect ratio < 3) in the larger MP of Surface I sample (shown in Figure 4.2a) are associated with the fastest solidification/cooling rate of the large MPs in this sample. On the other hand, the coarser microstructure with more columnar grains (grains with aspect ratio > 3) of the Surface II in its large MPs, is attributed to the highest *VED* used in the fabrication of this sample along with the smaller size of the previously solidified MP adjacent to each large MP (see Figure 4.1b), causing a smaller overlap between the small and large MPs, which leads to solidification of the large MPs in Surface II sample at slower cooling rates as compared to that of the Surface I sample. The average grain size of the Regular sample is also slightly higher than the grain size of the Surface I sample, which is ascribed to the larger hatch distance used in printing of this sample, causing the reduced heat dissipation intensity from the MPs of this sample during solidification, even though its MPs sizes are significantly smaller than the Surface I and II samples (due to the lower *VED* used for the fabrication of the Regular sample). Therefore, the largest grain structure was measured for the large MPs of the Surface II sample, resulting from the lowest *R* for its large MPs as compared to the Surface I and Regular samples.

Regarding the small MPs in the Upskin layers of the additively manufactured samples, the grain size distributions of the small MPs of the Upskin layers shown in IPFs (Figures 4.2a-c) were measured to be 0.64 ± 0.40, 0.55 ± 0.23, and 0.81 ± 0.27 μm for the Surface I, Surface II, and Regular samples, respectively. Comparing the small MPs of all samples reveals that the finest and more randomly orientated grain structure with aspect ratio < 3 has been formed in the Surface II sample ascribed to the fastest solidification rate of its small MPs abutting to the large MPs in this sample, leading to the formation of a higher density of equiaxed grains compared with the small MPs of the other two samples.

To further elaborate on the microstructural variations between the fabricated samples and establish a correlation between the grain boundary migration and particular boundary formation during solidification of each MP, the grain boundary analysis of the MPs in the Upskin layers of the samples was also carried out. Figures 4.2d-i depict the grain boundary (GB) maps taken from the fabricated samples. In these maps, the low angle grain boundaries (LAGBs), possessing misorientation angles less than 15° (subgrains), and the high angle grain boundaries (HAGBs) with misorientation angles higher than 15° (typically correspond to fully recrystallized grains [20,38]), are shown by red and black lines, respectively. The measured areas were focused on a region that contained at least two adjacent MPs, including their MP-fine and MP-coarse regions, and the HAZ of the large MPs. The MP-coarse region was particularly important to be characterized (depicted in the enclosed areas in Figures 4.2d-f indicated by G, H, and I, respectively) since this area has been reported to be more vulnerable to selective corrosion attack [10,19]. As a general trend, the density of the LAGBs close to the MP boundaries is higher than the MP's center. The formation of this non-uniform LAGBs distribution is ascribed to the moving heat source-induced temperature gradient during the L-PBF process. In the large MP boundaries of the Surface I (Figure 4.2g), a higher density of cellular LAGBs, as subgrains, confined inside the HAGBs were found. The fastest solidification rate in the large MP of the Surface I sample acts as an impediment to grain boundaries' migration, promoting the formation of more LAGBs [39,40]. Differently, during the fabrication of the Regular sample, the MPs stay at the high temperature for a longer time as compared to the Surface I sample, contributing to merging each subgrain boundaries with its neighboring subgrains and forming more expanded subgrains, while still surrounded by the HAGBs (Figure 4.2i). In Surface II sample, on the other hand, upon exposure of the large MPs to a high temperature for a more extended period of time during the solidification (in comparison with Surface I and Regular samples), the cellular LAGBs greatly merge with their adjacent subgrain boundaries, causing the annihilation of LAGBs. Therefore, the observed refined grains and subgrains in Surface I sample are associated with the rapid solidification rate of the MPs in this sample, as the mobility of the grain boundaries is primarily the temperature and time-dependent [41]. However, by decreasing the solidification rate and exposing the MPs to a higher temperature for a longer time (the case of large MPs of Surface II), those LAGBs are gradually disappeared and transformed into the HAGBs.

It is worth mentioning that the non-coherent HAGBs that possess a higher grain boundary energy are more susceptible to localized corrosion attack, while coherent LAGBs with lower grain boundary energy are more resistant to corrosion [42–44]. The detailed analysis of the electrochemical response of all samples is presented in the following section.

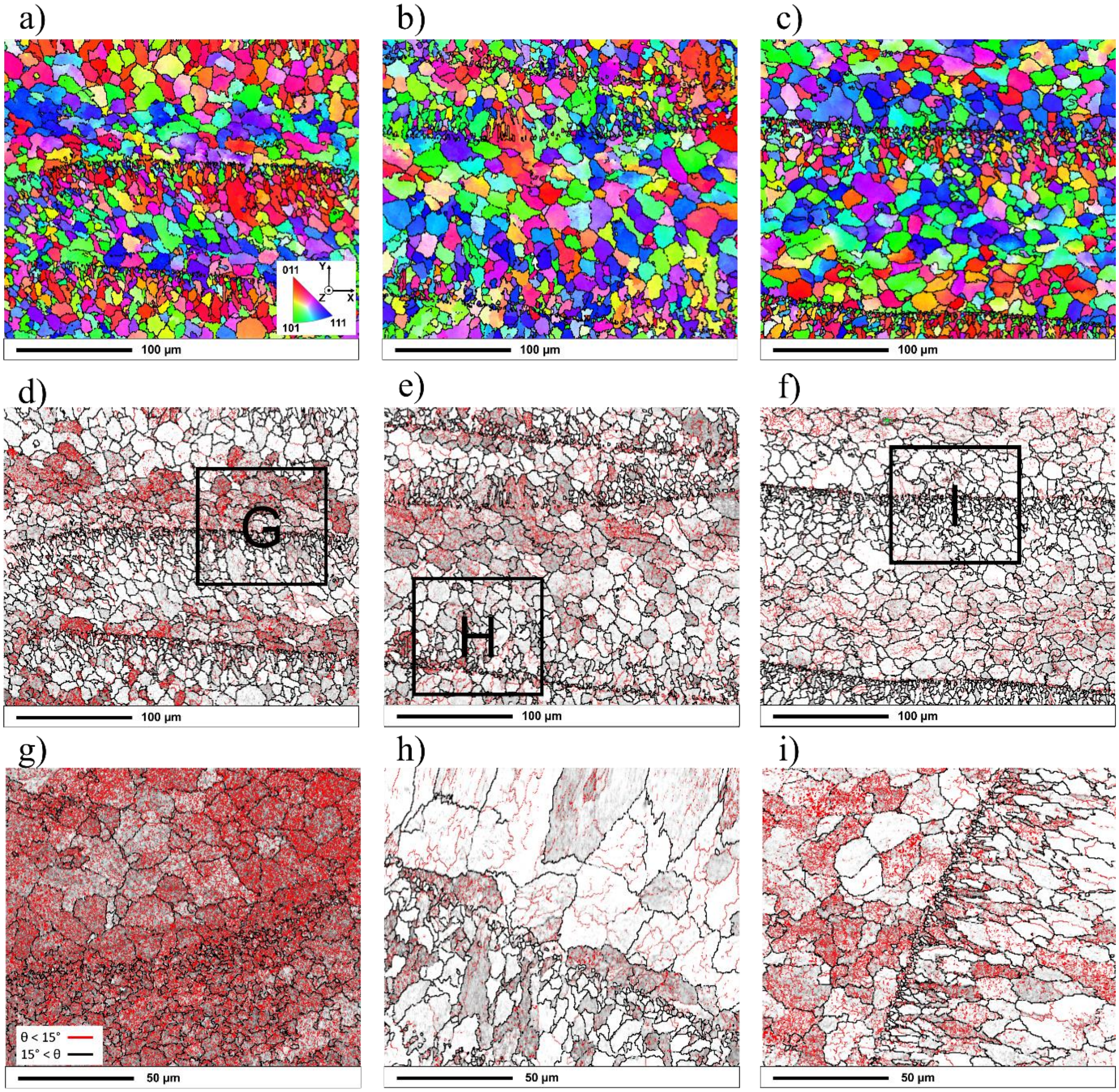

Figure 4. 2. EBSD inversed pole figure (IPF-z) maps taken from the Upskin layer of the (a) Surface I, (b) Surface II, and (c) Regular samples. The grain boundary maps taken from the (d) Surface I, (e) Surface II, and (f) Regular samples, (g) higher magnification image from the large MP boundary of Surface I, the enclosed area in (d) indicated by G, (h) higher magnification image from the large MP boundary of Surface II, the enclosed area in (e) indicated by H, and (i) higher magnification image from the large MP boundary of Regular sample, the enclosed area in (f) indicated by I.

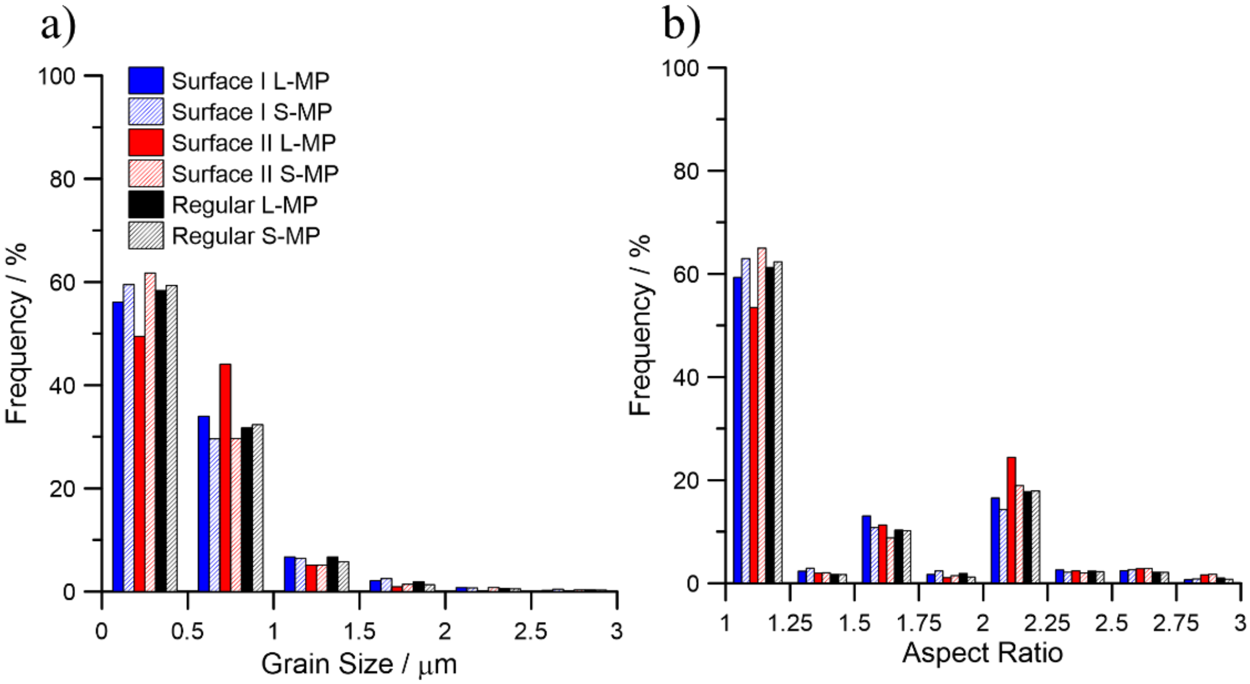

Figure 4. 3. The statistical distribution plots showing the distribution of (a) grain size, and (b) grains' shape aspect ratio at different regions across both the large melt pool (L-MP) and small melt pool (S-MP) for the Surface I, Surface II, and Regular samples.

The pole figures (PF) of the MPs' microstructure were calculated from the EBSD maps to investigate the micro-texture distribution resulted from the different processing parameters and solidification behavior of the Upskin layers in all three samples. Figure 4.4 demonstrates {100}, {110}, and {111} PFs for both small and large MPs of each sample shown in Figures 4.2 (a-c), in which z-axis is normal to plane of the {100} pole figure. The {001}<100> cube texture appeared in the PFs are commonly reported for the epitaxial growth in the solidification of the Al alloys [41,45]. The <001> direction is the easy growth and heat dissipation direction for cubic structures during solidification [10]. Comparing the large and small MPs of the studied samples revealed that the large MPs of Surface I and Surface II samples (Figures 4.4a and 4c) indicated the highest texture intensity of 8.77 and 11.12, respectively. This is correlated to the slower solidification rate of these MPs that has resulted in the formation of a higher fraction of columnar grains, promoting the strong texture in the {100} PFs along the large MP boundaries. The displayed overview of the MPs' cross-section in Figure 4.1 (a-c) clearly shows a more notable size difference between two successive MPs in the Surface II sample, resulting in a comparably slower solidification rate in its large MPs relative to those in Surface I and Regular samples. On the other hand, comparing the PFs taken from the small MPs of the Surface I and Surface II samples confirmed that the weaker texture intensity is corresponding to the small MP of the Surface II sample (5.86), conforming well with their expected cooling rates during solidification.

Figure 4.4 also shows a more noticeable difference between the intensity regions in the PFs of the Surface I and Surface II samples, corresponding to the noticeable difference between the solidification behavior of their large and small MPs, especially for the Surface II sample, whereas the texture difference between the consecutive MPs of the Regular sample was not that significant, ascribing to the consistency of the MPs' size and geometry over the entire Upskin layer of the Regular sample.

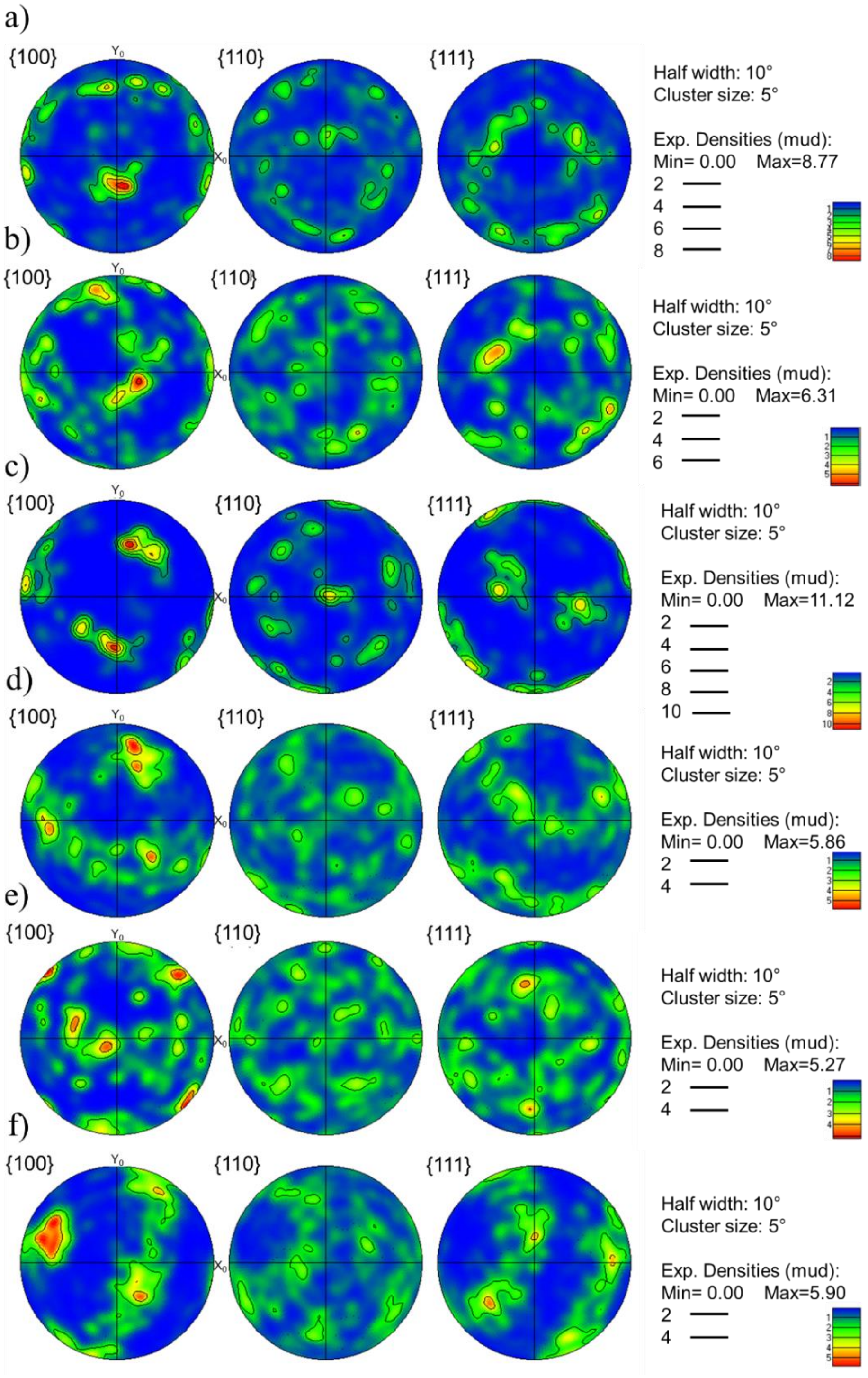

Figure 4. 4. Pole figures (PFs) taken from the Upskin layer of the (a) large and (b) small MPs of Surface I, (c) large and (d) small MPs of Surface II, (e) large and (f) small MPs of Regular samples.

## 3.2. Corrosion Properties

Figure 4.5a illustrates the open circuit potential (OCP) measurements on the as-polished surfaces over 3600 s prior to the anodic polarization tests in both naturally-aerated and deaerated 3.5 wt.% NaCl electrolyte. In the aerated solution, the OCP values independent from different Upskin layers were stabilized eventually around ~ −0.70 $V_{Ag/AgCl}$. Expectedly, removing the oxygen content from the used electrolyte was found to shift the OCP values to less noble potentials and led to the stabilization of the OCP values at different potentials in the order of Surface II < Regular < Surface I samples.

Figure 4.5b shows the anodic polarization plots of the studied samples obtained from testing in both aerated and deaerated electrolyte in polished condition. Revealing a very similar polarization behavior in aerated condition, all three samples showed a rapid increase of the anodic current by applying potential, plausibly due to occurrence of localized corrosion attacks on the surface at an elevated rate. Such active-like behavior of the polished L-PBF-AlSi10Mg surfaces is consistent with the previously reported results in the literature [14,19,46]. Moreover, no passive region was observed to appear, confirming that approximately the same values of pitting potential and corrosion potential resulted in an instantaneous localized attack on the surface once the corrosion potential is attained. Since the formation of the passive region was not detected for the samples, the electrolyte was deaerated to shift the corrosion potentials to less noble values than the $E_{pit}$ by diminishing the oxygen reduction reaction.

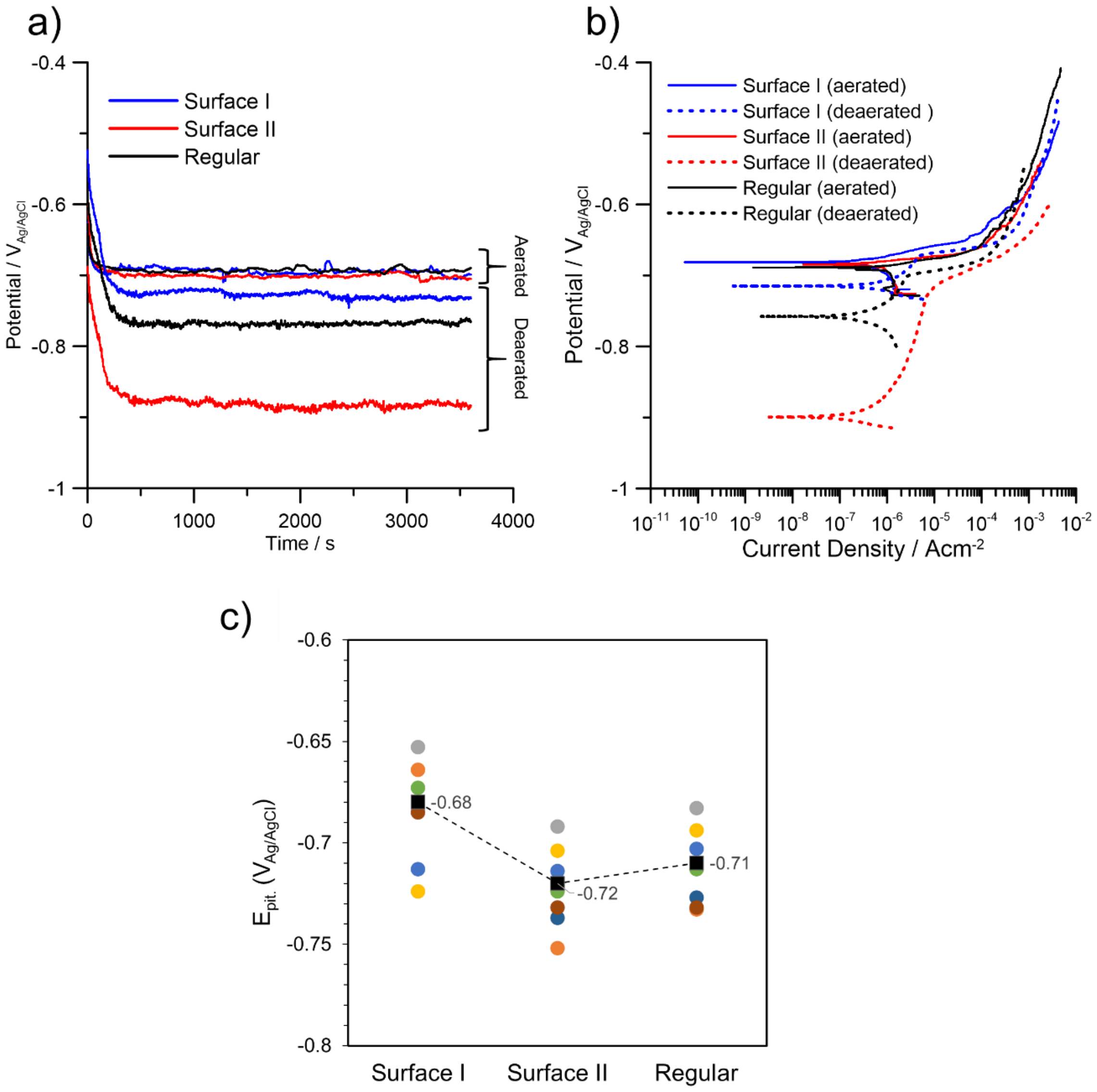

Figure 4. 5. a) The OCP measurements over time, (b) the anodic polarization curves comparing the corrosion behavior of the Surface I, Surface II, and Regular samples in aerated and deaerated 3.5 wt.% NaCl solution, (c) the $E_{pit.}$ distribution graph.

Table 4. 3 shows the results extracted from the anodic polarization curves demonstrated in Figure 4.5b, *i.e*. the corrosion potential ($E_{corr.}$) and the pitting potential ($E_{pit}$) values of each of the fabricated samples. It is worth mentioning that the quantitative $E_{corr.}$ values extracted from the anodic polarization plots can only be used qualitatively to compare the polarization response of

different samples due to the anticipated localized nature of corrosion attack on Al-Si-Mg alloys [47]. Figure 4.5b shows that the pitting potentials of all three samples in aerated condition are approximately the same, which is plausibly associated with the severity of the environment that has dominated over the impact of microstructural variations between the samples in controlling the polarization response of the samples. For the same reason, the corrosion potential was also hard to distinguish in all three samples. However, in the deaerated condition, the corrosion potentials were shifted to less noble values than the pitting potentials. Also, a distinct passive region was detected for all three samples. Despite the significant variation of the passive window's range between the samples, the distribution of pitting potential values in deaerated solution (Figure 4.5c) did not reflect a drastic change between the samples (-0.68±0.03 $V_{Ag/AgCl}$, -0.71±0.02, and -0.72±0.03 $V_{Ag/AgCl}$ for the Surface I, Regular, and Surface II samples, respectively). However, a slight reduction (~ 40 mV) in the average value of the pitting potential for the Surface II sample as compared to the Surface I sample is notable. The similarity between the measured $E_{pit}$ values in deaerated solution and the $E_{corr.}$ values in aerated solution for all three samples confirms that in presence of oxygen in the testing electrolyte, the pitting is initiated even at $E_{corr.}$ during the equilibration time.

Therefore, the observed initial response of the anodic polarization of the studied samples in aerated electrolyte did not capture a clear difference between the corrosion properties of the samples. However, the significant variation of the OCP value and $E_{corr.}$ for the Surface II sample and the slight change of its pitting potential towards less noble potentials in deaerated electrolyte as compared to other samples can be ascribed to the coarser microstructure and more extended MP coarse region along the large MP borders of the Surface II sample. The extended microstructure is possessing a higher content of interdendritic Si phase with a greater potential difference as compared to the α-Al matrix.

Table 4. 3. Anodic polarization parameters of the as-polished Upskin layer of the Surface I, Surface II, and Regular samples in aerated and deaerated 3.5 wt.% NaCl solution.

| *Sample* | $E_{corr.}(V_{Ag/AgCl})$ | $E_{pit.}(V_{Ag/AgCl})$ |
|---|---|---|
| **Surface I (aerated)** | -0.69±0.02 | - |
| **Surface I (deaerated)** | -0.71±0.02 | -0.68±0.03 |
| **Surface II (aerated)** | -0.68±0.03 | - |
| **Surface II (deaerated)** | -0.92±0.03 | -0.72±0.03 |
| **Regular (aerated)** | -0.69±0.01 | - |
| **Regular (deaerated)** | -0.77±0.03 | -0.71±0.02 |

In order to study the morphology and severity of the corrosion attack, the Upskin surfaces of the samples were investigated using SEM after removing corrosion products. Figure 4.6 and 4.7 show the corrosion morphology of the Surface I, Surface II, and Regular samples after anodic polarization testing in aerated and deaerated conditions, respectively. As shown in Figures 4.6a-4.6c, in all samples tested in aerated electrolyte the corrosion has initiated preferentially in the form of localized selective attack along the melt pool boundaries. As a result of the greater concentration of coarser silicon particles along the melt pool borders than those formed in the interior of the melt pools, the attack tends to follow the melt pool boundaries, leading to the selective corrosion attack shown at a higher magnification in Figures 4.6d-4.6f by arrows. The coarser Si network along the melt pool boundaries of the L-PBF-AlSi10Mg alloy has been proven to create a larger Volta potential difference between the Si phase and the Al matrix than that in the interior of the melt pools, giving rise to a greater driving force for galvanic corrosion to occur [46,48,49]. Similar corrosion morphology around the melt pool boundaries of L-PBF-AlSi10Mg alloy was also reported in the literature [31,50]. Despite the similarity of the corrosion morphology between the studied samples herein, the detected selective attack on the Surface II sample was noticeably more severe (Figures 4.6b and 4.6e), ascribed to the coarser Si network and more extended MP-coarse region formed in the Upskin layer of Surface II sample.

A similar corrosion morphology in the form of selective corrosion attack along the melt pool boundaries (shown by arrows in Figures 4.7a-4.7c) was observed for the tested samples in deaerated electrolyte. Despite the existing literature has confirmed that generally the corrosion rate of metals increases by increasing the concentration of dissolved oxygen in an aqueous medium through expediting the cathodic reduction reaction [51], the corrosion attacks on the samples exposed to the deaerated solution were found to be more severe than those immersed in aerated solution. Such discrepancy can be ascribed to the lower corrosion potentials, and consequently longer polarization duration of the samples in deaerated electrolyte before the tests were interrupted at a constant current threshold, leading to higher anodic charge of the samples and the formation of deeper attacks. Consistent with the results obtained from testing in aerated solution, the detected selective corrosion attacks for the Surface II sample in deaerated condition were more severe than the Regular and Surface I samples, conforming to the corrosion results shown in Table 3.

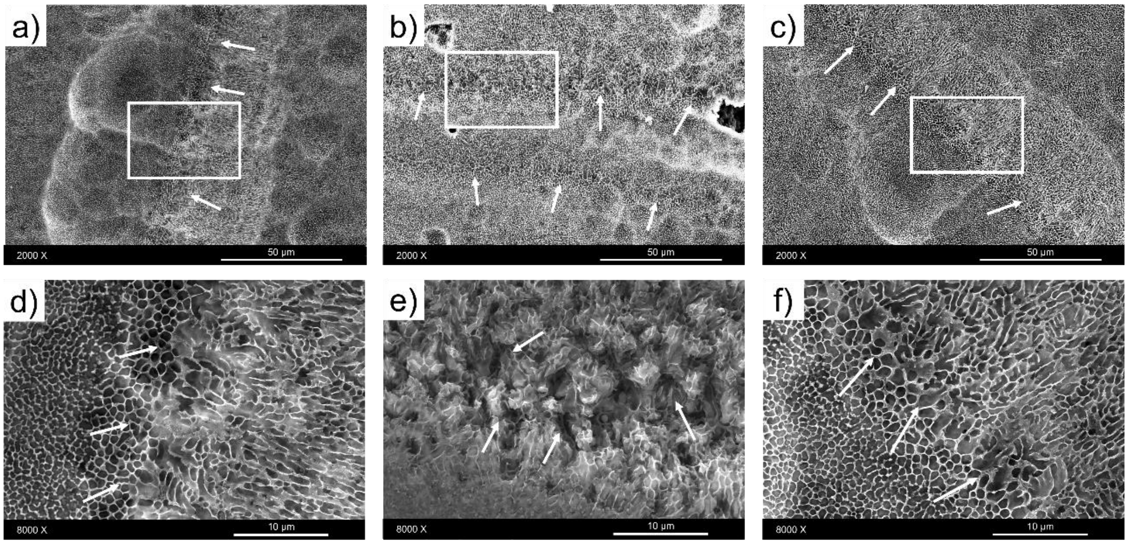

Figure 4. 6. SEM micrographs taken from the L-PBF AlSi10Mg after anodic polarization testing in aerated 3.5 wt.% NaCl solution: a) Surface I (aerated), d) higher magnification of the enclosed area in (a), b) Surface II (aerated), e) higher magnification of the enclosed area in (b), c) Regular sample (aerated), f) higher magnification of the enclosed area in (c).

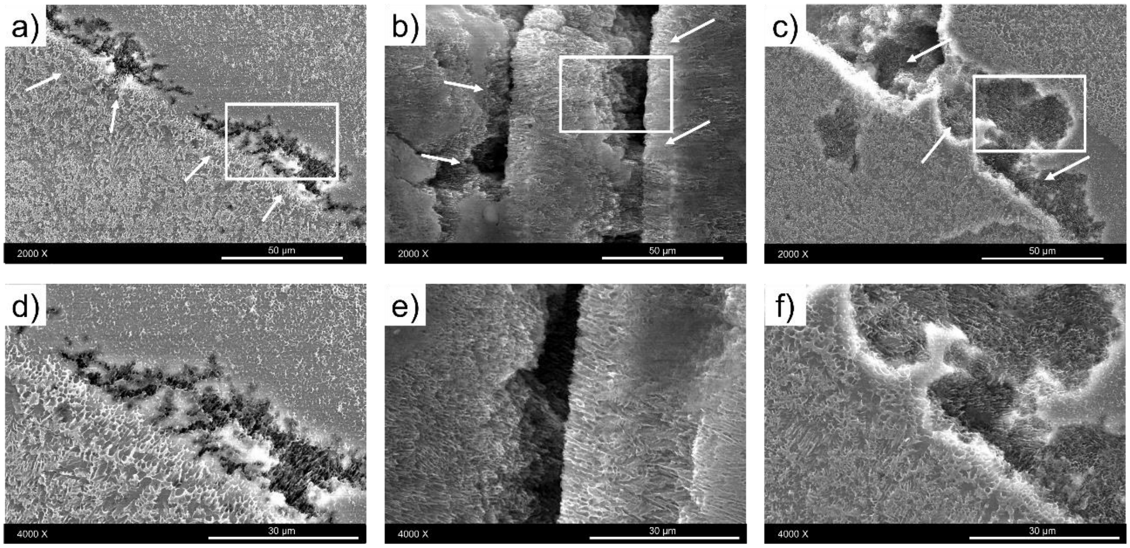

Figure 4. 7. SEM micrographs taken from the L-PBF AlSi10Mg after anodic polarization testing in deaerated 3.5 wt.% NaCl solution: a) Surface I (deaerated), d) higher magnification of the enclosed area in (a), b) Surface II (deaerated), e) higher magnification of the enclosed area in (b), c) Regular sample (deaerated), f) higher magnification of the enclosed area in (c).

To investigate the protectiveness and integrity of the passive film that formed on the Upskin layer of different samples, EIS tests were performed in aerated 3.5 wt.% NaCl electrolyte. The obtained Bode diagrams for all samples after 1 h and 96 h of immersion times at room temperature are shown in Figures 4.8a and 4.8b, respectively. The impedance values at the high frequency range in the Bode plots correspond to the electrolyte resistance and the resultant ohmic drop in the solution, while the low to middle frequency range impedance values represent the passive film stability on the Upskin surface of three different samples. The Bode plots after 1 h of immersion exhibit a noticeably higher absolute value of impedance for the Surface I sample than the Surface II and Regular samples at the lower frequency range. After 96 h of immersion times, the Surface I sample showed more than one order of magnitude higher impedance at the lower frequency range than the Surface II or the Regular samples (see Figure 4.8c). This indicates a slower kinetic rate for all possible corrosion reactions on Surface I sample, confirming the presence of a more protective and stable passive layer against the diffusion of aggressive species on the Upskin layer of the Surface I sample after 96 h of immersion time.

After 1 h of immersion time, the phase angle *vs* frequency diagrams of all three samples (Figure 4.8a) revealed an inductive behavior at very low frequencies, as evidenced by the shift of the phase angle to positive values. Although the interpretation of the inductive loop for Al alloys has been discussed in several corrosion studies [50,52,53], it is still controversial. Arrabal *et al.* [50] stated that the inductive behavior of a cast Al-Si-Mg alloy is associated with active nucleation of pits at the periphery of the intermetallic particles, while in others studies, it was indicated that inductive behavior is more likely promoted by decreasing the protectiveness of the aluminum oxide layer [53,54]. Considering the noisy impedance and phase angle responses at the low frequency range detected in this study (shown in Figure 4.8a), it was concluded that the observed inductive behavior of the studied surfaces after 1 h of immersion time was also associated with the frequent change of the active surface area (melt pool boundaries), resulted from the adsorption and subsequent separation of hydrogen bubbles. The deformed peaks in the low-frequency range are also reported to be ascribed to the diffusion processes inside the developing pits [50]. To better reveal the presence of constant phase element at higher frequencies, corresponding to the formation of oxide layer on Al alloys, the phase angle and modulus diagrams were corrected ($\varphi_{adj}$ and $|Z|_{adj}$, respectively) according to the electrolyte ohmic resistance [55–57]. The modified Bode representations for ohmic resistance are expressed as:

$$\varphi_{adj} = tan^{-1}(Z_{img}/Z_{rel} - R_{el,est.}) \qquad \text{Eq. 4.1}$$

$$|Z|_{adj} = \sqrt{{Z_{img}}^2 + (Z_{rel} - R_{el,est.})^2} \qquad \text{Eq. 4.2}$$

where $R_{el,est.}$ is the electrolyte resistance estimation, which is the average value of the measured electrolyte resistance among different samples ($R_{el,\ est.}$ = 7.70 $\Omega cm^2$ herein). The modified Bode plots after 1 h of immersion time is shown in Figure 4.8b. The modified phase angle ($\varphi_{adj}$) after 1 h of immersion time clearly presents the constant value of 80° for Surface I and Regular samples and 60° for Surface II sample at frequencies higher than 158 Hz, representing constant phase element (CPE) behavior.

The impedance of a constant phase element (*CPE*) is determined by $Z_{CPE} = [Q(i\omega)^n]^{-1}$, in which $Q$ is considered as the *CPE* constant, $i$ is the imaginary unit ($j = \sqrt{-1}$), $\omega$ describes the angular frequency (rad/s), and $n$ is known as the dispersion coefficient of the constant phase element, and its value changes within -1 and 1 range, representing inductivity, resistance, Warburg impedance, and the capacitance for the $n$ value equals to -1, 0, 0.5, or 1, respectively. The determined values for the dispersion coefficient ($n$) were 0.92±0.02 for all different samples; therefore, the CPE constants can be substituted by capacitors in the equivalent circuits shown in Figures 4.8g and 4.8h. The calculated parameters of the SECs are given in Table 4.

The Bode diagrams of the samples after 96 h of immersion time (Figure 4.8c) revealed a drastic change by showing three capacitive arcs with well-defined time constants, *i.e.* one at low frequencies, one at intermediate frequencies, and the other at higher frequencies. The low-frequency peak defines localized and selective attack zones resulted from anodic dissolution of Al, creating a charge transfer resistance, as well as diffusion within corrosion products, while the mid-frequency peak corresponds to the formation of the passive layer and sealing effect of the corrosion products within the porosities and other active areas [52]. The capacitive peak at high-frequency range for this alloy has been reported to be ascribed to the formation of an exterior layer of corrosion products between the sample's surface and the electrolyte [10]. The observed transition of the surfaces from active with inductive behavior at 1 h of immersion time to passive after 96 h of immersion time can be attributed to (*i*) repassivation of the growing pits or localized attack regions resulted from detachment of cathodic Si particles from the exposed surface to the electrolyte due to the anodic dissolution of Al matrix at their periphery, and (*ii*) the formation and accumulation of corrosion products on the surface. The ohmic resistance corrected Bode diagrams after 96 h of immersion time are also shown in Figure 4.8d. The corrected phase angle plots after 96 h of immersion time show distinct constant values of 86°, 59°, and 68° for Surface I, Surface II, and Regular samples, respectively, at frequencies higher than 4 kHz, confirming the CPE response of all three samples in the high frequency range.

Figures 4.8e and 4.8f show the OCP trends before running the EIS testing at 1 h and 96 h of immersion times, respectively. Similar to the OCP trend before the anodic polarization testing (Figure 4.5a), the OCP values after 1 h of immersion time were stabilized around $\sim -0.70$ $V_{Ag/AgCl}$, confirming the spontaneous pitting of all surfaces at the OCP at the initial immersion time. Analogous to the observed state of full repassivation for all samples from EIS data after 96 h of immersion time, the OCP values (Figure 4.8f) were also found to shift to less noble potentials than the samples' pitting potentials after 96 h and led to the stabilization of the OCP values at distinct potentials in the order of Surface II < Regular < Surface I samples.

The deterioration of the corrosion performance in the Surface II sample can be explained by the formation of the expanded HAZ and MP coarse region in the Surface II sample (resulted from the slower cooling rate for its larger MPs), leading to a greater driving force for micro-galvanic corrosion of aluminum matrix as the anodic site along the MP boundaries [48,58]. Furthermore, the positive impact of the higher density of LAGBs in the Surface I sample as compared to the other two samples (shown in Figures 4.2d-i), although not as a controlling factor but rather as a contributing factor to its electrochemical stability should be considered. Previous studies have reported a direct correlation between the density of LAGBs and the improved corrosion resistance of various grades of aluminum alloys [42–44].

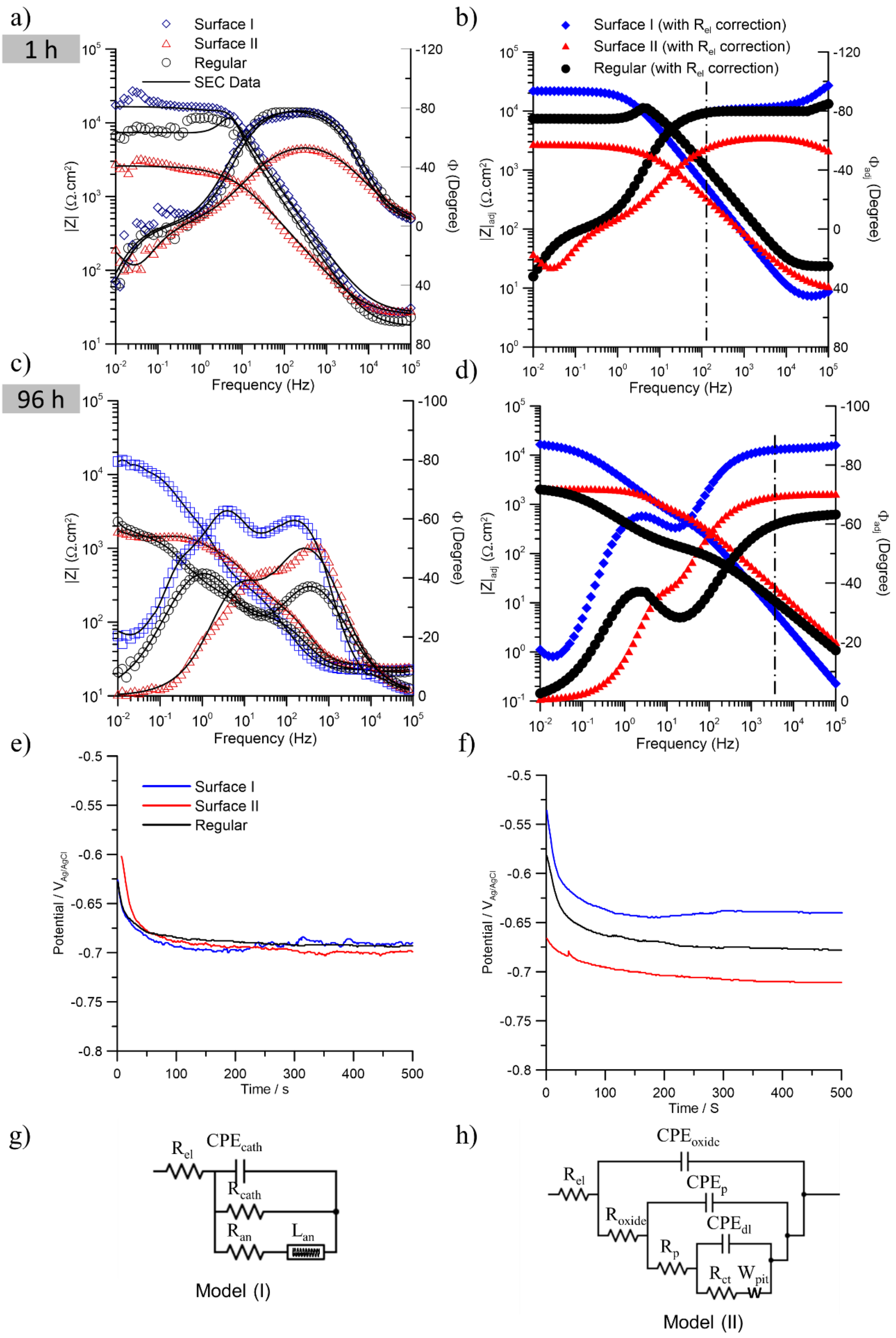
a)
1 h
Surface I
Surface II
Regular
SEC Data
|Z| (Ω.cm²)
Φ (Degree)
Frequency (Hz)
b)
Surface I (with $R_{el}$ correction)
Surface II (with $R_{el}$ correction)
Regular (with $R_{el}$ correction)
$|Z|_{adj}$ (Ω.cm²)
$\Phi_{adj}$ (Degree)
Frequency (Hz)
c)
96 h
|Z| (Ω.cm²)
Φ (Degree)
Frequency (Hz)
d)
$|Z|_{adj}$ (Ω.cm²)
$\Phi_{adj}$ (Degree)
Frequency (Hz)
e)
Surface I
Surface II
Regular
Potential / $V_{Ag/AgCl}$
Time / s
f)
Potential / $V_{Ag/AgCl}$
Time / S
g)
$R_{el}$
$CPE_{cath}$
$R_{cath}$
$R_{an}$
$L_{an}$
Model (I)
h)
$CPE_{oxidc}$
$R_{el}$
$CPE_{p}$
$R_{oxide}$
$CPE_{dl}$
$R_{p}$
$R_{ct}$
$W_{pit}$
Model (II)

Figure 4. 8. (a) The Bode spectra, the fitting data, and (b) electrolyte resistance corrected Bode spectra after 1 h, (c) the Bode spectra, the fitting data, and (d) electrolyte resistance corrected Bode spectra after 96 h of immersion time. The OCP measurements after (e) 1 h and (f) 96 h of immersion time. The equivalent electric circuits suggested to interpret the EIS data after (g) 1 h, and (h) 96 h of immersion time.

For a better interpretation of the characteristics of the passive layer that formed on all polished Upskin layers of the printed samples and to describe its modification over time, two simplified equivalent circuits (SEC), demonstrated in Figures 4.8g and 4.8h, was applied and fitted to the obtained EIS spectra. For the EIS spectra after 1 h of immersion time with inductive behavior, an equivalent circuit, shown in Figure 4.8g, similar to the one proposed by Arrabal *et al.*[50] was used to describe the active-like behavior of the surface. In this circuit, $R_{el}$ is the electrolyte resistance, $CPE_{cath}$ and $R_{cath}$ represent the capacitive behavior and resistance of the cathodic Si particles (*vs* the anodic Al matrix), $R_a$ and $L_a$ refer to the resistance of the corrosion products at the periphery of the Si particles and the inductance of protons created by hydrolysis of $Al^{3+}$ species [50]. The impedance response of the samples after 96 h of immersion time with three capacitive arcs was described using a simplified equivalent circuit, similar to the one suggested by Fathi *et al.*[10], shown in Figure 4.8h. In this equivalent circuit, $R_{el}$ explains the ohmic drop in the electrolyte, derived from the resistance of the solution. The constant phase element and the resistor corresponding to the newly formed layer of corrosion products (oxide layer) on the surface after 96 h are shown by $CPE_{oxide}$ and $R_{oxide}$, respectively. The $CPE_p$ and its parallel $R_p$ correspond to the capacitive and resistance response of the passive layer, respectively. Likewise, $CPE_{dl}$ and its parallel $R_{ct}$ correspond to the constant phase element and resistance of the double layer (*dl*) charging-discharging at the Upskin's surface, respectively. Finally, the Warburg diffusion element ($W_{pit}$) describes the ionic diffusion of corrosive ions within the passive film and inside the localized corrosion areas (pits). The protective oxide layer formed on aluminum alloys is known to be composed of two different layers, *i.e.* an inner and an outer layer [59]. The inner layer adjacent to the metal surface with the maximum thickness of 4 nm is characterized by having a compact and amorphous nature, and is formed spontaneously in air [60–62]. Differently, the outer oxide layer is reported to be a thicker and more porous layer of hydrated oxide with the thickness of hundreds of nanometers, promoted by the reactions between the metal and its environment [59].

The significantly higher $R_{ct}$ value of the Surface I sample after 96 h of immersion time as compared to its $R_{an}$ value at 1 h confirms that the full repassivation of its surface has occurred after 96 h. A similar trend, although to a lesser extent, can be detected for the Regular and Surface II samples. After 96 h of immersion time, when the state of full repassivation is reached, the impedance value is increased, attributed to the formation of a stable passive film on the surface. Moreover, all samples showed a third time constant at high frequencies, characterizing the formation of an outer oxide layer in contact with the electrolyte. The calculated low $R_{oxide}$ values in Table 4 revealed a minor contribution for the outer oxide layer in providing protection for the underlying substrates. After 96 h of immersion time, the Surface I sample exhibited the highest passive resistance ($R_p$=12.3±1.24 kΩcm$^2$) and charge transfer resistance ($R_{ct}$=8.7±0.45 kΩcm$^2$) and the Surface II sample showed the lowest passive layer resistance ($R_p$=5.33±0.34 kΩcm$^2$) as well as charge transfer resistance ($R_{ct}$=4.27±0.05 kΩcm$^2$). Therefore, the EIS data confirmed the formation of a passive layer with better stability and quality on the Upskin layer of the Surface I sample, resulting in its improved corrosion performance as compared to the Surface II and Regular samples.

Table 4. 4. The fitting parameters of the EIS measurements including the elements of the SEC shown in Figure 4.8g and 4.8h.

| | ***R*** ***($\Omega cm^2$)*** | ***$R_{cath}$*** ***($k\Omega.cm^2$)*** | ***$R_{an}$*** ***($k\Omega.cm^2$)*** | ***$R_{oxide}$*** ***($k\Omega.cm^2$)*** | ***$R_{p.}$*** ***($k\Omega.cm^2$)*** | ***$R_{ct}$*** ***($k\Omega.cm^2$)*** | ***Chi-square*** ***($10^{-3}$)*** |
|---|---|---|---|---|---|---|---|
| *Surface I* | | | | | | | |
| ***1 h*** | 7.47±0.34 | 0.42±0.04 | 0.71±0.02 | - | - | - | 0.83 |
| ***96 h*** | 8.23±0.27 | - | - | 0.13±0.02 | 12.3±1.24 | 8.7±0.45 | 0.14 |
| *Surface II* | | | | | | | |
| ***1 h*** | 6.43±0.22 | 0.56±0.07 | 0.33±0.05 | - | - | - | 0.85 |
| ***96 h*** | 8.67±0.87 | - | - | 0.6±0.01 | 5.33±0.34 | 4.27±0.05 | 0.14 |
| *Regular* | | | | | | | |
| ***1 h*** | 7.44±0.35 | 0.33±0.01 | 0.54±0.04 | - | - | - | 0.80 |
| ***96 h*** | 7.98±0.54 | - | - | 0.08±0.01 | 6.24±0.56 | 5.67±0.04 | 0.15 |
| | ***$CPE_{cath}$,Q*** ***($\mu\omega^{-1}$ $s^{-n}$ $cm^{-2}$)*** | ***$CPE_{oxide}$, Q*** ***($\mu\omega^{-1}$ $s^{-n}$ $cm^{-2}$)*** | ***$CPE_{p}$, Q*** ***($\mu\omega^{-1}$ $s^{-n}$ $cm^{-2}$)*** | ***$CPE_{dl}$, Q*** ***($\mu\omega^{-1}$ $s^{-n}$ $cm^{-2}$)*** | ***$L_{an}$*** ***($k\Omega.s$)*** | ***$W_{pit}$*** ***($k\Omega.cm^2$)*** | |
| *Surface I* | | | | | | | |
| ***1 h*** | 5.42±0.11 | - | - | - | 2.5±0.15 | | |
| ***96 h*** | - | 18.23±1.34 | 13.25±0.45 | 8.36±0.64 | - | 0.45±0.03 | |
| *Surface II* | | | | | | | |
| ***1 h*** | 3.23±0.34 | - | - | - | 0.56±0.04 | | |
| ***96 h*** | - | 3.11±1.06 | 89.44±0.77 | 65.76±2.04 | - | 0.56±0.02 | |
| *Regular* | | | | | | | |
| ***1 h*** | 4.36±0.73 | - | - | - | 0.58±0.06 | | |
| ***96 h*** | - | 12.65±1.55 | 45.44±0.35 | 34.41±1.25 | - | 0.48±0.05 | |

To further investigate the corrosion morphology after the EIS testing, the Upskin surfaces of the three samples were studied using the SEM after 1 h and 96 h of immersion time in the electrolyte followed by removing corrosion products. As shown in Figures 4.9a-4.9f, after 1 h of immersion time, a slight corrosion attack was detected on all the samples. The severity of localized attack on Surface II sample was found to be slightly more noticeable along its melt pool boundaries as compared to the other two samples (shown by arrows). Analogously, after 96 h of immersion time (Figures 4.10a-4.10f), the onset of corrosion attack was detected preferentially along the melt pool boundaries resulted from the selective dissolution of aluminum matrix adjacent to the coarse Si particles at the melt pool boundaries [14]. The detrimental effect of increased Si content on the oxide layer's structure and stability formed on additively manufactured Al-Si alloys has been reported in a recent study, where increased Si content from 7 to 12 wt.% was reported to cause the formation of less uniform and locally thinner anodic oxide layer containing wider pores with a greater inter-pore distance with a lower density [63]. Similar to the corrosion morphology after anodic polarization testing, the Surface II sample revealed a more severe attack along its melt pool borders, while the Surface I sample was found to be affected the least.

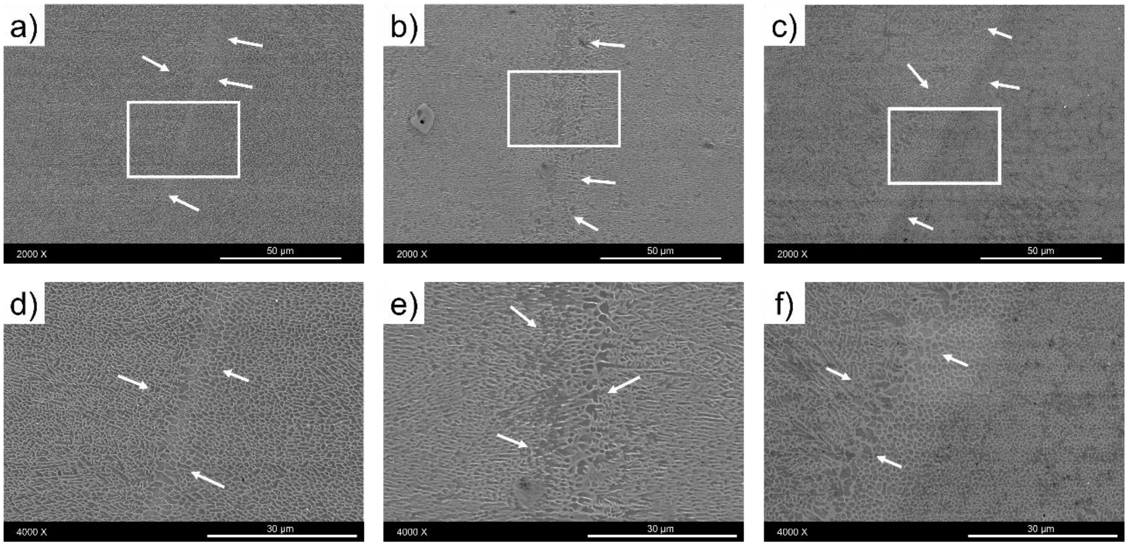

Figure 4. 9. SEM micrographs taken from the L-PBF AlSi10Mg after EIS testing at 1 h of immersion time, showing the surface of the a) Surface I , d) higher magnification of the enclosed area in (a), b) Surface II, e) higher magnification of the enclosed area in (b), c) Regular sample, and f) higher magnification of the enclosed area in (c).

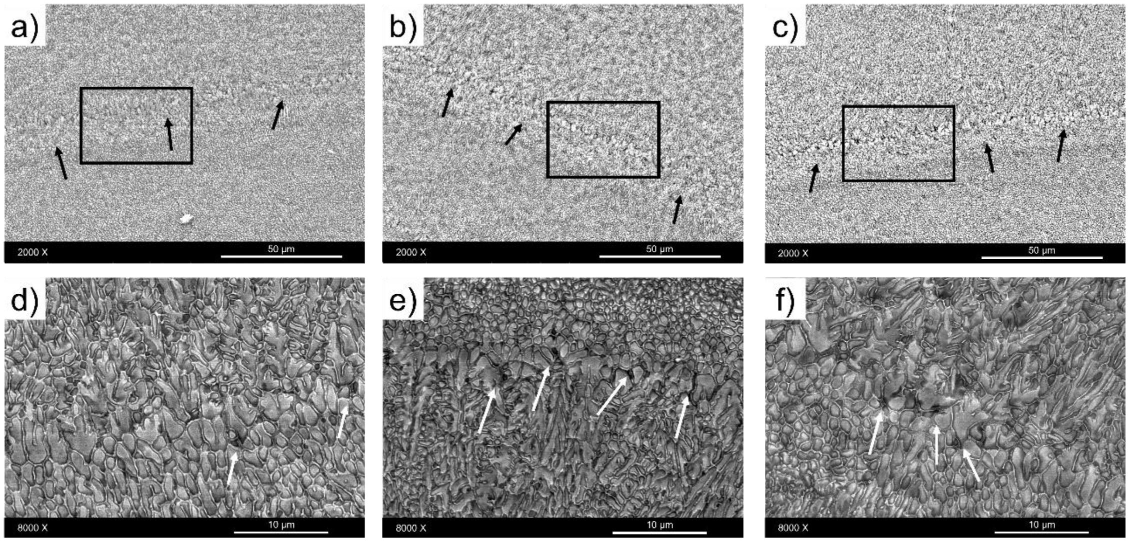

Figure 4. 10. SEM micrographs taken from the L-PBF AlSi10Mg after EIS testing at 96 h of immersion time, showing the surface of the a) Surface I , d) higher magnification of the enclosed area in (a), b) Surface II, e) higher magnification of the enclosed area in (b), c) Regular sample, and f) higher magnification of the enclosed area in (c).

### *3.3. Comparisons with the As-printed Surfaces: the Inconsistent Role of Polishing*

To better understand the impact of polishing as a post-printing surface modification procedure on the electrochemical properties of the fabricated samples, comparisons were made between the corrosion properties of the fully polished samples studied herein and their as-printed counterparts studied in the authors' previous work [10].

The previous study revealed a significant difference between the OCP values of the fabricated samples with as-printed surface finish. The $E_{OCP}$ values of the as-printed Surface I, Surface II, and Regular samples were reported to be stabilized around −0.52 ± 0.02 $V_{Ag/AgCl}$, −0.73 ± 0.03 $V_{Ag/AgCl}$, and −0.62 ± 0.05 $V_{Ag/AgCl}$, respectively [10]. The trend and values of all samples' $E_{OCP}$ with as-printed surface finish indicate that the Surface I possess the highest passive film stability, and the Surface II has the lowest stability of the passive film. The attachment of partially melted oxidized powder particles to the as-printed surfaces is believed to have a contribution to the formation of a passive film with improved stability on the as-printed surfaces as compared to that of the polished ones [13].

Different from the active-like response of the polished surfaces in aerated solution, as reported in the previous study [10], the as-printed surfaces were reported to reveal a clear passive window for all the samples and a pitting potential higher than the corrosion potential occurring at $E_{pit}$= -0.38 ± 0.10 $V_{Ag/AgCl}$, -0.62 ± 0.08 $V_{Ag/AgCl}$, and -0.14 ± 0.06 $V_{Ag/AgCl}$ for Surface I, Surface II, and Regular samples, respectively [10]. This indicates a lower tendency for pitting formation; also, a favorable condition for the repassivation of the surface in the samples with the initial as-printed surface roughness as compared to their polished counterparts. The detected active-like behavior of the polished surfaces in aerated solution was found to diminish upon removing the oxygen content of the electrolyte, leading to the formation of a clear passive window for all samples with stable pitting occurring at -0.68±0.03$V_{Ag/AgCl}$, -0.72±0.03 $V_{Ag/AgCl}$, and -0.71±0.02 $V_{Ag/AgCl}$ for Surface I, Surface II, and Regular samples, respectively.

Comparing the anodic polarization curves of the as-polished surfaces in aerated solution (shown in Figure 4.5b) to those of the as-printed ones reported in [10] reveals a clear change of the corrosion potentials towards more negative values for the as-polished surfaces. The order of corrosion potential for the as-printed surfaces were reported to be Surface II ($E_{corr.}$=−0.68 ± 0.08 $V_{Ag/AgCl}$) < Regular ($E_{corr.}$= -0.58 ± 0.05 $V_{Ag/AgCl}$) < Surface I ($E_{corr.}$= -0.51 ± 0.04 $V_{Ag/AgCl}$). Therefore, the polished surfaces seem to have a higher tendency for corrosion reactions to begin as compared to the as-printed surfaces. Removing the oxygen content of the electrolyte further contributed to lowering the corrosion potentials to less noble values.

Moreover, comparing the protectiveness and integrity of the passive layer that formed on the polished Upskin surfaces (Figure 4.8c) to those of the as-printed surfaces after 96 h of immersion time reported in [10] also confirms a clearly different electrochemical response between the as-polished and the as-printed samples, correlated to the impact of heavily oxidized and partially melted powder particles that cover the surface of the as-printed samples and act as a preserving barrier facing the corrosion attacks on the surface, eliminating a direct exposure of the surface with the corrosive environment [12,13]. Surface polishing completely removes the partially melted powder particles and eliminates the pre-existing thick and stable surface layers from the samples. For the case of the Regular and Surface II samples with coarser microstructure along their large MPs boundaries, polishing of the samples exposes their coarse as-printed microstructure (particularly the case of Surface II sample) to the corrosive medium, causing the deterioration of their corrosion properties. Therefore, to attain a better corrosion response from the Regular and Surface II samples in a chloride-containing environment, such as in marine, the post-printing polishing of the samples should be avoided. On the other hand, for the Surface I sample, comparing the impedance response of the sample with as-polished and the as-printed surface finishes after 96 h of immersion time revealed an improved corrosion response, possessing a higher impedance values in a wide range of frequencies, for the as-polished surface. This observation suggests that the finer microstructure of the Surface I sample, particularly along its large MP boundaries, has better electrochemical stability at longer immersion time as compared to the as-printed surface finish, confirming the positive impact of post-printing polishing on the corrosion response of the Surface I sample.

Furthermore, the general response of the passive layer resistance ($R_p$) and charge transfer resistance ($R_{ct}$) of each sample in the polished condition was found to be different from those with as-printed surface finish reported in [10], revealing a general uniform corrosion of the surface than a stable pitting attack for all L-PBF-AlSi10Mg samples with as-printed surface finish, as evidenced by their higher $R_{ct}$ than their general passive layer resistance [10]. This was similarly ascribed to the presence of the partially oxidized particles on the as-printed surfaces, which can eliminate the active nucleation of pits adjacent to the Si phases [13]. Post-printing polishing of the surface completely removes the partially melted powder and exposes the MP boundaries to the active corrosive species.

Comparing the obtained results in this study with the existing literature on the impact of as-printed surface roughness on the corrosion properties of L-PBF-AlSi10Mg alloy reveals both similarities and inconsistencies. Analogous to the results obtained for the Surface I sample, Cabrini *et al*. [52] and Leon *et al*. [18] also reported an improved corrosion response for the L-PBF-AlSi10Mg after polishing and removing the as-printed surface roughness of the alloy. However, the improved corrosion response of as-polished samples in their study was primarily correlated to the reduced surface roughness of the alloy after polishing. Differently, the enhanced corrosion performance of polished Surface I sample studied herein is mainly due to the better quality of the passive film that reforms after polishing on Surface I sample at longer immersion times as compared to the native oxide layer on the as-printed sample.

Contrary to the reported results by Cabrini *et al*. [52] and Leon *et al*. [18], the presented results herein confirmed the corrosion properties degradation of the Regular and Surface II samples after polishing. To elucidate such discrepancy, a close attention should be paid to the reported as-printed surface roughness of the samples in previous studies as compared to the obtained surface roughness values in this study. The reported L-PBF-AlSi10Mg arithmetic surface roughness ($R_a$) by Cabrini *et al*. [52] and Leon *et al*. [18] were approximately 18 µm and 3.2-12.5 µm, respectively, which are significantly higher than the Surface II roughness (~ 1.1 µm). Therefore, regardless of the microstructural features induced by the process parameters, the high roughness of fabricated parts in previous studies has a dominant impact on controlling the electrochemical properties of the surfaces, leading to appearance of localized corrosion attacks preferentially at the roughness sites [18]. Accordingly, it is expected that removing the superficial roughness of as-printed surfaces by polishing in their studies would contribute to a better electrochemical stability of the surfaces. Differently, the obtained as-printed surface roughness in current study (1.1 µm for Surface II) is comparable to the reported roughness of as-polished surfaces in previous studies (~ 0.8 µm [18]). Consequently, the adverse effect of surface roughness on the corrosion properties of the samples studied herein has been diminished, and instead the positive effect of the native passive film formed during the fabrication process for the as-printed samples has dominated over the negative impact of the obtained non-homogenous microstructure for the as-polished surfaces (the case of Surface II and Regular samples). This has resulted in relatively better corrosion performance of the as-printed Surface II and Regular samples than their as-polished counterparts.

It should be also mentioned that the significantly higher volumetric energy density of the laser used in this study to fabricate the samples (122.4 J/mm$^3$ and 132.6 J/mm$^3$ for the Surface I and II samples, respectively) as compared to the previous works (47.8 J/mm$^3$ [52] and 66.6 J/mm$^3$ [18]) enhances the interlayer connection and improves the wettability of molten metal, leading to flatten melt pools and drastically lower surface roughness in as-printed condition.

Therefore, to be able to decide on the best post-printing surface finishing practices for improved corrosion response of the L-PBF-AlSi10Mg, a careful assessment of the as-printed microstructure of the fabricated part is required. Although a meticulous tuning of the L-PBF process parameters used in the fabrication of the AlSi10Mg components has been shown herein to be an effective method to tailor a desired microstructure with an improved corrosion response on the surface of the component (the case of Surface I sample), to be able to fully benefit from such improvement, a careful polishing of the surface is recommended. Differently, if such microstructural refinement is not being considered in the fabrication process, tuning of the process parameters can still contribute to a significant reduction of the surface roughness (the case of Surface II sample), and meanwhile, in order to diminish any possible degradation in the corrosion performance of the fabricated parts due to the coarsening of the microstructure, polishing of the as-printed surface finish should be avoided.

## 4. Conclusions

In this work, the effects of L-PBF process parameters on the microstructure and the resultant corrosion properties of the L-PBF-produced AlSi10Mg in both naturally-aerated and deaerated 3.5 wt.% NaCl solution were studied. Reducing the hatch distance used in the manufacturing process of the L-PBF-AlSi10Mg was found to contribute to the formation of a bimodal structure, comprised of small and large MPs in a cyclic manner. For the fabricated sample with the lowest hatch distance, the variation in the MPs' size was found to create a non-homogenous microstructure by forming a coarser eutectic Si network with a stronger {100}<100> cubic texture and a lower density of low angle grain boundaries along the large MPs' boundaries, attributed to the reduced cooling rate during solidification of such large MPs. On the other hand, the sample that experienced the fastest cooling rate during the solidification revealed a finer eutectic Si phase, more uniformly distributed grains, a high density of LAGBs bounded by HAGBs, and a weaker texture along its large MP boundaries.

Anodic polarization testing at the initial immersion time in naturally-aerated electrolyte did not reveal a noticeable difference between the fabricated samples and all samples unveiled spontaneous localized corrosion along their melt pool boundaries when their corrosion potentials were reached. Differently, testing in deaerated electrolyte separated the corrosion potentials from their corresponding pitting potentials by shifting the corrosion potentials to less noble values, and revealed a clear passive region for all samples. The fabricated sample at the highest volumetric energy density (leading to its lowest cooling rate during solidification) showed significantly lower OCP and $E_{corr.}$ values and a slightly lower breakdown potential in deaerated solution at compared to the other samples. Contrarily, the nobler $E_{corr.}$ value for the sample that underwent a faster cooling/solidification rate was attributed to the reduced driving force for galvanic corrosion between Al and Si phases due to the formation of a finer Al-Si eutectic structure along its large MPs boundaries.

EIS results in aerated solution confirmed that although the state of full repassivation for all samples was achieved at longer immersion times (96 h), the fabricated sample at the highest volumetric energy density revealed a degraded corrosion performance resulted from its extended HAZ and coarser microstructure.

The comparisons between the as-printed L-PBF-AlSi10Mg surfaces versus their polished counterparts revealed that the presence of the accumulated partially melted powder particles on the as-printed samples can be beneficial towards the improved corrosion performance of the part, only if the as-printed microstructure of the alloy contains a coarse Al-Si structure along the MP boundaries. However, if the fabrication process has led to the formation of a fine eutectic structure along the MP boundaries, polishing of the as-printed surfaces is recommended to be able to fully benefit from the enhanced electrochemical stability of the formed microstructure.

## Acknowledgement

The authors are grateful to the support of Natural Sciences and Engineering Research Council of Canada (NSERC) [grant number RGPIN-2017-04368] and the Memorial University of Newfoundland for providing funding to conduct this research.

# References

[1] W.J. Sames, F.A. List, S. Pannala, R.R. Dehoff, S.S. Babu, The metallurgy and processing science of metal additive manufacturing, Int. Mater. Rev. 61 (2016) 315–360. doi:10.1080/09506608.2015.1116649.

[2] D. Herzog, V. Seyda, E. Wycisk, C. Emmelmann, Additive manufacturing of metals, Acta Mater. 117 (2016) 371–392. doi:https://doi.org/10.1016/j.actamat.2016.07.019.

[3] T. Ishimoto, K. Hagihara, K. Hisamoto, S.-H. Sun, T. Nakano, Crystallographic texture control of beta-type Ti–15Mo–5Zr–3Al alloy by selective laser melting for the development of novel implants with a biocompatible low Young's modulus, Scr. Mater. 132 (2017) 34–38. doi:https://doi.org/10.1016/j.scriptamat.2016.12.038.

[4] H. Attar, S. Ehtemam-Haghighi, D. Kent, X. Wu, M.S. Dargusch, Comparative study of commercially pure titanium produced by laser engineered net shaping, selective laser melting and casting processes, Mater. Sci. Eng. A. 705 (2017) 385–393. doi:https://doi.org/10.1016/j.msea.2017.08.103.

[5] B.S. Amirkhiz, D. Chalasani, M. Mohammadi, TEM Study of Additively Manufactured Metallic Alloys: Nickel Aluminum Bronze, Microsc. Microanal. 25 (2019) 2588–2589. doi:10.1017/S1431927619013679.

[6] S.-H. Sun, K. Hagihara, T. Nakano, Effect of scanning strategy on texture formation in Ni-25at.%Mo alloys fabricated by selective laser melting, Mater. Des. 140 (2018) 307–316. doi:https://doi.org/10.1016/j.matdes.2017.11.060.

[7] M. Rafieazad, M. Ghaffari, A. Vahedi Nemani, A. Nasiri, Microstructural evolution and mechanical properties of a low-carbon low-alloy steel produced by wire arc additive manufacturing, Int. J. Adv. Manuf. Technol. (2019) 1–14. doi:10.1007/s00170-019-04393-8.

[8] M. Ghaffari, A. Vahedi Nemani, M. Rafieazad, A. Nasiri, Effect of Solidification Defects and HAZ Softening on the Anisotropic Mechanical Properties of a Wire Arc Additive-Manufactured Low-Carbon Low-Alloy Steel Part, JOM. 71 (2019) 4215–4224. doi:10.1007/s11837-019-03773-5.

[9] M. Kazemipour, M. Mohammadi, E. Mfoumou, A.M. Nasiri, Microstructure and Corrosion Characteristics of Selective Laser-Melted 316L Stainless Steel: The Impact of Process-Induced Porosities, JOM. 71 (2019) 3230–3240. doi:10.1007/s11837-019-03647-w.

[10] P. Fathi, M. Rafieazad, X. Duan, M. Mohammadi, A. Nasiri, On Microstructure and Corrosion Behaviour of AlSi10Mg Alloy with Low Surface Roughness Fabricated by Direct Metal Laser Sintering, Corros. Sci. 157 (2019) 126–145.

[11] M. Mohammadi, H. Asgari, Achieving low surface roughness AlSi10Mg_200C parts using direct metal laser sintering, Addit. Manuf. 20 (2018) 23–32. doi:https://doi.org/10.1016/j.addma.2017.12.012.

[12] P. Fathi, M. Mohammadi, X. Duan, A. Nasiri, Effects of Surface Finishing Procedures on Corrosion Behavior of DMLS-AlSi10Mg_200C Alloy Versus Die-Cast A360.1 Aluminum, JOM. (2019) 1–12. doi:10.1007/s11837-019-03344-8.

[13] P. Fathi, M. Mohammadi, X. Duan, A.M. Nasiri, A Comparative Study on Corrosion and Microstructure of Direct Metal Laser Sintered AlSi10Mg_200C and Die Cast A360.1 Aluminum, J. Mater. Process. Technol. 259 (2018) 1–14. doi:https://doi.org/10.1016/j.jmatprotec.2018.04.013.

[14] M. Rafieazad, M. Mohammadi, A. Nasiri, On Microstructure and Early Stage Corrosion

Performance of Heat Treated Direct Metal Laser Sintered AlSi10Mg, Addit. Manuf. 28 (2019) 107–119. doi:https://doi.org/10.1016/j.addma.2019.04.023.

[15] B.A. Fulcher, D.K. Leigh, T.J. Watt, Comparison of AlSi10Mg and Al 6061 processed through DMLS, in: Proc. Solid Free. Fabr. Symp. Austin, TX, USA, 2014.

[16] H. Asgari, C. Baxter, K. Hosseinkhani, M. Mohammadi, On microstructure and mechanical properties of additively manufactured AlSi10Mg_200C using recycled powder, Mater. Sci. Eng. A. 707 (2017) 148–158. doi:10.1016/J.MSEA.2017.09.041.

[17] A. Leon, A. Shirizly, E. Aghion, Corrosion Behavior of AlSi10Mg Alloy Produced by Additive Manufacturing (AM) vs. Its Counterpart Gravity Cast Alloy, Metals (Basel). 6 (2016). doi:10.3390/met6070148.

[18] A. Leon, E. Aghion, Effect of surface roughness on corrosion fatigue performance of AlSi10Mg alloy produced by Selective Laser Melting (SLM), Mater. Charact. 131 (2017) 188–194. doi:https://doi.org/10.1016/j.matchar.2017.06.029.

[19] M. Rafieazad, A. Chatterjee, A.M. Nasiri, Effects of Recycled Powder on Solidification Defects, Microstructure, and Corrosion Properties of DMLS Fabricated AlSi10Mg, JOM. 71 (2019) 3241–3252. doi:10.1007/s11837-019-03552-2.

[20] A. Hadadzadeh, B.S. Amirkhiz, A. Odeshi, J. Li, M. Mohammadi, Role of hierarchical microstructure of additively manufactured AlSi10Mg on dynamic loading behavior, Addit. Manuf. 28 (2019) 1–13. doi:https://doi.org/10.1016/j.addma.2019.04.012.

[21] T. Rubben, R.I. Revilla, I. De Graeve, Influence of heat treatments on the corrosion mechanism of additive manufactured AlSi10Mg, Corros Sci. 147 (2019) 406–415. doi:10.1016/j.corsci.2018.11.038.

[22] M. Cabrini, S. Lorenzi, T. Pastore, C. Testa, D. Manfredi, G. Cattano, F. Calignano, Corrosion resistance in chloride solution of the AlSi10Mg alloy obtained by means of LPBF, Surf. Interface Anal. (n.d.). doi:10.1002/sia.6601.

[23] F. Calignano, D. Manfredi, E.P. Ambrosio, L. Iuliano, P. Fino, Influence of process parameters on surface roughness of aluminum parts produced by DMLS, Int. J. Adv. Manuf. Technol. 67 (2013) 2743–2751. doi:10.1007/s00170-012-4688-9.

[24] U. Tradowsky, J. White, R.M. Ward, N. Read, W. Reimers, M.M. Attallah, Selective laser melting of AlSi10Mg: Influence of post-processing on the microstructural and tensile properties development, Mater. Des. 105 (2016) 212–222. doi:https://doi.org/10.1016/j.matdes.2016.05.066.

[25] T. Yang, K. Wang, W. Wang, P. Peng, L. Huang, K. Qiao, Y. Jin, Effect of Friction Stir Processing on Microstructure and Mechanical Properties of AlSi10Mg Aluminum Alloy Produced by Selective Laser Melting, JOM. 71 (2019). doi:10.1007/s11837-019-03343-9.

[26] M. Rafieazad, M. Mohammadi, A. Gerlich, A. Nasiri, Impacts of Friction Stir Processing on Microstructure and Corrosion Properties of DMLS-AlSi10Mg, in: TMS 2020 Conf., 2020. doi:http://doi-org-443.webvpn.fjmu.edu.cn/10.1007/978-3-030-36296-6_22.

[27] W. Li, S. Li, J. Liu, A. Zhang, Y. Zhou, Q. Wei, C. Yan, Y. Shi, Effect of heat treatment on AlSi10Mg alloy fabricated by selective laser melting: Microstructure evolution, mechanical properties and fracture mechanism, Mater. Sci. Eng. A. 663 (2016) 116–125. doi:https://doi.org/10.1016/j.msea.2016.03.088.

[28] N.T. Aboulkhair, A. Stephens, I. Maskery, C. Tuck, I. Ashcroft, N.M. Everitt, Mechanical properties of selective laser melted AlSi10Mg: nano, micro, and macro properties, in: Proc. Solid Free. Fabr. Symp., 2015: pp. 1–30.

[29] J. Fiocchi, A. Tuissi, P. Bassani, C.A. Biffi, Low temperature annealing dedicated to

AlSi10Mg selective laser melting products, J. Alloys Compd. 695 (2017) 3402–3409. doi:https://doi.org/10.1016/j.jallcom.2016.12.019.

[30] M. Cabrini, F. Calignano, P. Fino, S. Lorenzi, M. Lorusso, D. Manfredi, C. Testa, T. Pastore, Corrosion Behavior of Heat-Treated AlSi10Mg Manufactured by Laser Powder Bed Fusion, Materials (Basel). 11 (2018). doi:10.3390/ma11071051.

[31] M. Cabrini, S. Lorenzi, T. Pastore, S. Pellegrini, E.P. Ambrosio, F. Calignano, D. Manfredi, M. Pavese, P. Fino, Effect of heat treatment on corrosion resistance of DMLS AlSi10Mg alloy, Electrochim. Acta. 206 (2016) 346–355. doi:https://doi.org/10.1016/j.electacta.2016.04.157.

[32] T. Rubben, R.I. Revilla, I. De Graeve, Effect of Heat Treatments on the Anodizing Behavior of Additive Manufactured AlSi10Mg, J. Electrochem. Soc. 166 (2019) C42--C48.

[33] A.H. Maamoun, M. Elbestawi, G.K. Dosbaeva, S.C. Veldhuis, Thermal post-processing of AlSi10Mg parts produced by Selective Laser Melting using recycled powder, Addit. Manuf. 21 (2018) 234–247. doi:https://doi.org/10.1016/j.addma.2018.03.014.

[34] A.S. Materials, ASTM G5-14: Standard Reference Test Method for Making Potentiodynamic Anodic Polarization Measurements, ASTM, 2014. https://books.google.ca/books?id=tWpcswEACAAJ.

[35] ASTM G5-14e1, Standard Reference Test Method for Making Potentiodynamic Anodic Polarization Measurements, West Conshohocken, PA, 2014, 2020. www.astm.org.

[36] K.S. Ferrer, R.G. Kelly, Comparison of Methods for Removal of Corrosion Product from AA2024-T3, Corrosion. 57 (2001) 110–117. doi:10.5006/1.3290336.

[37] L. Thijs, K. Kempen, J. Kruth, J. V. Humbeeck, Fine-structured aluminium products with controllable texture by selective laser melting of pre-alloyed AlSi10Mg powder, Acta Mater. 61 (2013) 1809–1819. doi:https://doi.org/10.1016/j.actamat.2012.11.052.

[38] K. Saeidi, F. Akhtar, Subgrain-controlled grain growth in the laser-melted 316L promoting strength at high temperatures, R. Soc. Open Sci. 5 (2018) 172394. doi:10.1098/rsos.172394.

[39] M. Huo, L. Liu, W. Yang, Y. Li, S. Hu, H. Su, J. Zhang, H. Fu, Formation of low-angle grain boundaries under different solidification conditions in the rejoined platforms of Ni-based single crystal superalloys, J. Mater. Res. 34 (2019) 251–260. doi:10.1557/jmr.2018.408.

[40] Y. Huang, F.J. Humphreys, Subgrain growth and low angle boundary mobility in aluminium crystals of orientation {110}〈001〉, Acta Mater. 48 (2000) 2017–2030. doi:https://doi.org/10.1016/S1359-6454(99)00418-8.

[41] A. Hadadzadeh, C. Baxter, B.S. Amirkhiz, M. Mohammadi, Strengthening mechanisms in direct metal laser sintered AlSi10Mg: Comparison between virgin and recycled powders, Addit. Manuf. 23 (2018) 108–120. doi:https://doi.org/10.1016/j.addma.2018.07.014.

[42] L. Tan, T.R. Allen, Effect of thermomechanical treatment on the corrosion of AA5083, Corros. Sci. 52 (2010) 548–554. doi:https://doi.org/10.1016/j.corsci.2009.10.013.

[43] D.S. D'Antuono, J. Gaies, W. Golumbfskie, M.L. Taheri, Grain boundary misorientation dependence of β phase precipitation in an Al–Mg alloy, Scr. Mater. 76 (2014) 81–84. doi:https://doi.org/10.1016/j.scriptamat.2014.01.003.

[44] T. Minoda, H. Yoshida, Effect of grain boundary characteristics on intergranular corrosion resistance of 6061 aluminum alloy extrusion, Metall. Mater. Trans. A. 33 (2002) 2891–2898. doi:10.1007/s11661-002-0274-3.

[45] A. Hadadzadeh, B.S. Amirkhiz, J. Li, M. Mohammadi, Columnar to equiaxed transition during direct metal laser sintering of AlSi10Mg alloy: Effect of building direction, Addit.

Manuf. 23 (2018) 121–131. doi:https://doi.org/10.1016/j.addma.2018.08.001.

[46] M. Cabrini, S. Lorenzi, T. Pastore, C. Testa, D. Manfredi, M. Lorusso, F. Calignano, M. Pavese, F. Andreatta, Corrosion behavior of AlSi10Mg alloy produced by laser powder bed fusion under chloride exposure, Corros. Sci. (2019). doi:10.1016/j.corsci.2019.03.010.

[47] B.G. Prakashaiah, D. Vinaya Kumara, A. Anup Pandith, A. Nityananda Shetty, B.E. Amitha Rani, Corrosion inhibition of 2024-T3 aluminum alloy in 3.5% NaCl by thiosemicarbazone derivatives, Corros. Sci. 136 (2018) 326–338. doi:https://doi.org/10.1016/j.corsci.2018.03.021.

[48] R.I. Revilla, J. Liang, S. Godet, I. De Graeve, Local Corrosion Behavior of Additive Manufactured AlSiMg Alloy Assessed by SEM and SKPFM, J. Electrochem. Soc. . 164 (2017) C27–C35. doi:10.1149/2.0461702jes.

[49] P. Fathi, M. Mohammadi, A.M. Nasiri, Low Surface Roughness Additively Manufactured AlSi10Mg: The Impacts on Corrosion and Water Repellency Properties, in: TMS 2020 149th Annu. Meet. Exhib. Suppl. Proc., Springer International Publishing, Cham, 2020: pp. 309–320.

[50] R. Arrabal, B. Mingo, A. Pardo, M. Mohedano, E. Matykina, I. Rodríguez, Pitting corrosion of rheocast A356 aluminium alloy in 3.5wt.% NaCl solution, Corros. Sci. 73 (2013) 342–355. doi:https://doi.org/10.1016/j.corsci.2013.04.023.

[51] M.V. Rendón, C. Jorge Andrés, P. Fernández, Evaluation of the corrosion behavior of the al-356 alloy in NaCl solutions, Quim. Nova. 34 (2011) 1163–1166. http://www.scielo.br/scielo.php?script=sci_arttext&pid=S0100-40422011000700011&nrm=iso.

[52] M. Cabrini, S. Lorenzi, T. Pastore, S. Pellegrini, D. Manfredi, P. Fino, S. Biamino, C. Badini, Evaluation of corrosion resistance of Al–10Si–Mg alloy obtained by means of Direct Metal Laser Sintering, J. Mater. Process. Technol. 231 (2016) 326–335. doi:https://doi.org/10.1016/j.jmatprotec.2015.12.033.

[53] G.S. Peng, K.H. Chen, H.C. Fang, H. Chao, S.Y. Chen, EIS study on pitting corrosion of 7150 aluminum alloy in sodium chloride and hydrochloric acid solution, Mater. Corros. 61 (n.d.) 783–789. doi:10.1002/maco.200905413.

[54] M. Keddam, C. Kuntz, H. Takenouti, D. Schustert, D. Zuili, Exfoliation corrosion of aluminium alloys examined by electrode impedance, Electrochim. Acta. 42 (1997) 87–97. doi:https://doi.org/10.1016/0013-4686(96)00170-3.

[55] M.E. Orazem, B. Tribollet, Electrochemical impedance spectroscopy, New Jersey. (2008).

[56] M.E. Orazem, N. Pe\'be\`re, B. Tribollet, Enhanced Graphical Representation of Electrochemical Impedance Data, J. Electrochem. Soc. 153 (2006) B129. doi:10.1149/1.2168377.

[57] T.T.M. Tran, B. Tribollet, E.M.M. Sutter, New insights into the cathodic dissolution of aluminium using electrochemical methods, Electrochim. Acta. 216 (2016) 58–67. doi:https://doi.org/10.1016/j.electacta.2016.09.011.

[58] R.I. Revilla, D. Verkens, G. Couturiaux, L. Malet, L. Thijs, S. Godet, I. De Graeve, Galvanostatic Anodizing of Additive Manufactured Al-Si10-Mg Alloy, J. Electrochem. Soc. 164 (2017) C1027–C1034. doi:10.1149/2.1121714jes.

[59] G. Šekularac, I. Milošev, Corrosion of aluminium alloy AlSi7Mg0.3 in artificial sea water with added sodium sulphide, Corros. Sci. 144 (2018) 54–73. doi:https://doi.org/10.1016/j.corsci.2018.08.038.

[60] P.M. Natishan, W.E. O'Grady, Chloride Ion Interactions with Oxide-Covered Aluminum

Leading to Pitting Corrosion: A Review, J. Electrochem. Soc. 161 (2014) C421--C432. doi:10.1149/2.1011409jes.

[61] A. Kolics, A.S. Besing, P. Baradlai, R. Haasch, A. Wieckowski, Effect of pH on Thickness and Ion Content of the Oxide Film on Aluminum in NaCl Media, J. Electrochem. Soc. 148 (2001) B251–B259. doi:10.1149/1.1376118.

[62] S.Y. Yu, W.E. O’Grady, D.E. Ramaker, P.M. Natishan, Chloride ingress into aluminum prior to pitting corrosion. An investigation by XANES and XPS, J. Electrochem. Soc. 147 (2000) 2952–2958. doi:10.1149/1.1393630.

[63] R.I. Revilla, Y. Rojas, I. De Graeve, On the Impact of Si Content and Porosity Artifacts on the Anodizing Behavior of Additive Manufactured Al-Si Alloys, J. Electrochem. Soc. . 166 (2019) C530–C537. http://jes.ecsdl.org/content/166/14/C530.abstract.

# Chapter 5

# Enhancing the Corrosion Properties of Additively Manufactured AlSi10Mg Using Friction Stir Processing [6] [7]

## Preface

A version of this manuscript has been published in the Journal of Corrosion Science. I am the first and corresponding author of these papers. Along with the co-authors, Dr. Mohsen Mohammadi, Dr. Adrian Gerlich, and Dr. Ali Nasiri, I investigate the effects of FSP on the microstructural modification and electrochemical stability of the L-PBF-AlSi10Mg alloy. I prepared methodology, experimental, formal analysis, and the first original draft of the manuscript and subsequently revised the manuscript based on the coauthors' feedback and also the peer review process. The co-authors Dr. Mohsen Mohammadi, Dr. Adrian Gerlich, and Dr. Ali Nasiri helped in conceptualization, design, project administration, and supervision, review & editing of the manuscript.

---

[6] M. Rafieazad, M. Mohammadi, A. Gerlich, A. Nasiri, Enhancing the Corrosion Properties of Additively Manufactured AlSi10Mg Using Friction Stir Processing, Corros. Sci. (2020) 109073. doi:https://doi.org/10.1016/j.corsci.2020.109073. (IPF=6.720)

[7] M. Rafieazad, M. Mohammadi, A. Gerlich, A. Nasiri, Impacts of Friction Stir Processing on Microstructure and Corrosion Properties of DMLS-AlSi10Mg, in: TMS 2020 Conf., 2020. doi:http://doi-org-443.webvpn.fjmu.edu.cn/10.1007/978-3-030-36296-6_22

## Abstract

The solid-state structural modification technique friction-stir-processing (FSP) was applied on the surface of a laser-powder-bed-fusion fabricated AlSi10Mg alloy to locally modify the microstructure and enhance the corrosion properties of the alloy. A uniform microstructure was formed after FSP, comprised of a homogenous distribution of the Si-particles embedded in an Al-matrix with an ultrafine-grained structure containing a low fraction of subgrains, and reduced porosity level. This structure offers improved corrosion properties, ascribed to the formation of a thicker passive layer with a lower donor density on the FSPed regions as compared to the as-fabricated metal.

**Keywords:** Additive manufacturing (AM), Laser-powder bed fusion (L-PBF), Friction Stir Processing (FSP), AlSi10Mg, Microstructure, Corrosion.

## 1. Introduction

Among various types of Al alloys, the hypo-eutectic AlSi10Mg alloy has excellent castability and weldability due to a high fluidity and narrow solidification range associated with a eutectic Al-Si composition (Al-11.7 wt.% Si). It also offers age hardening response through $Mg_2Si$ precipitation, and has been widely used in a variety of applications in the aerospace, aeronautics, automotive, and marine industries [1–3]. However, the as-cast AlSi10Mg alloy is characterized by a coarse dendritic microstructure containing acicular Si phase, where second phase particles and intermetallic constituents can lead to mediocre corrosion resistance and mechanical performance for this alloy [4–6]. In recent years, to exploit the full potential of this alloy particularly for more intricate components with integrated functionality, state-of-the-art additive manufacturing (AM) technology has been adopted.

Various AM methods, such as Laser-Powder Bed Fusion (L-PBF), also known as Selective Laser Melting (SLM), Laser Beam Melting (LBM), Direct Metal Laser Sintering (DMLS), or Direct Laser Fabrication (DLF) have been developed so far to produce a broad range of metallic components [7], such as Ti-based alloys [8,9], Ni-based alloys [10–12], Cu-based alloys [13,14], steels [15–17], stainless steels [18,19], and Al-based alloys [3,4,7,20,21]. Compared to the traditional manufacturing methods, the unique processing conditions associated with the L-PBF technology, involving a high volumetric energy density and rapid scanning strategy, lead to drastically high solidification and cooling rates of small melt pools ($10^3$–$10^{11}$ $K/s^2$) [3], which induces a high-temperature gradient and a large amount of residual stresses within the fabricated components [22,23]. Therefore, the AM fabricated parts are potentially susceptible to the formation of different solidification defects, such as microstructural inhomogeneities, high porosity levels, inclusions, and solidification micro-cracks, adversely impacting the mechanical and corrosion properties of the printed components [3,21,24,25]. To eliminate such process-induced imperfections, a variety of post-printing methods have been attempted by the AM manufacturing industries and researchers, including post-printing thermal processing [3,26–31] and surface [7,25] treatments, using feedstock powders with different sizes and morphologies [21,24,32,33], and optimization of the printing processing parameters [7,34,35].

Previous studies reported that applying post-printing heat-treatment cycles above 200 °C ultimately improves the microstructural homogeneity of L-PBF-AlSi10Mg alloy by disturbing the continuous network of the Si phase, followed by the diffusion and agglomeration of the Si phase into idiomorphic particles [3]. Consequently, the corrosion performance of the alloy is reported to be deteriorated [3,29–31,36]. Even though a post-printing heat-treatment cycle can be applied to tailor the microstructure of the L-PBF AlSi10Mg alloy, it cannot reduce the level of internal porosities [37]. Hot isostatic pressing (HIP) is capable of reducing the process-induced pores present in the as-printed sample [38,39], which has been shown to improve the elongation of L-PBF processed AlSi10Mg alloy by almost 20%, while the tensile strength was reported to decrease by around 60%.

So far, a few studies have examined the impact of processing parameters optimization, such as the size of the feedstock powder, laser power, hatching distance, and scanning speed on the size and distribution of the Si particles, grain refinement, density of the printed part, level of internal porosities, corrosion and mechanical performance of the L-PBF-AlSi10Mg components [4,25,35,40]. In a recent study by the authors, the microstructure of the L-PBF AlSi10Mg alloy, fabricated using a feedstock powder with a larger size (13.7±9 µm), revealed a coarser microstructure with a higher level of porosity and solidification micro-cracks as compared to the regular powders size (8.8±7 µm) [21]. This consequently led to deterioration of the corrosion properties of the alloy [21], although its mechanical performance was not significantly affected [24]. It has been also reported that the presence of porosities in L-PBF AlSi10Mg samples can negatively impact the corrosion performance of the alloy in chloride-containing environments [21,40]. Furthermore, the process-induced porosities on the surface of the L-PBF AlSi10Mg alloy were shown to deteriorate the stability of the anodized layer, ascribed to the cracking of the anodic oxide film inside the pores [40]. A recent study also showed that by reducing the content and size of the porosities of L-PBF AlSi10Mg from 1.56 ± 0.84% to 0.54 ± 0.16%, the corrosion current density noticeably decreased from 1.262 ± 0.02 $\mu A/cm^2$ to 0.642 ± 0.01 $\mu A/cm^2$, indicating a significant improvement in the corrosion performance [21]. Other studies also investigated the effect of tuning the L-PBF process parameters on the initial surface roughness, level of porosity, and microstructural modification of the as-printed L-PBF-AlSi10Mg samples [7,25]. It has been reported that by reducing the hatch distance from 0.21 mm to 0.13 mm, scanning speed from 1000 mm/s to 775 mm/s, and beam offset from 0.2 mm to 0.15 mm, the surface roughness of the fabricated L-PBF-AlSi10Mg can be noticeably improved from $R_a = 5.1 \pm 1.5$ µm to 1.1 ± 0.2 µm [7]. Such modifications of the processing parameters were reported to create a finer grain structure in the fabricated part possessing a uniform distribution of Si particles, lower level of porosity, and better resistance to pitting and general corrosion attacks [7]. Analogous to the post-printing heat-treatment and HIP, optimization of the printing process parameters does not entirely eliminate the process-induced porosities from the structure of the as-printed alloy, despite promoting microstructural uniformity. Consequently, it is necessary to establish a new post-printing method to improve the microstructural homogeneity and corrosion performance of the L-PBF-AlSi10Mg alloy simultaneously.

Only a few recent studies have reported the impact of applying friction stir processing (FSP), as a solid-state technique, on the microstructure of the L-PBF AlSi10Mg [41–43]. Yang *et al.* [41] reported that FSP is capable of eliminating the porosity of the L-PBF-AlSi10Mg alloy and refining the grain structure from 13.6 μm to 2.3 μm. In another study [42], it was demonstrated that the level of porosity is decreased from 0.13% in the as-printed condition to below 0.03% after FSP of L-PBF-AlSi10Mg. The positive impact of the FSP on the corrosion performance of the as-cast Al–30Si alloy has been reported by Rao *et al.* [44], correlating such improvement to both grains size and the Si particles size reduction after FSP. The refined grains and uniform distribution of Si particles in the FSPed Al-30Si alloy were reported to cause the formation of a thicker and denser passive layer as compared to the as-cast condition [44]. Furthermore, it has been reported that increasing grain size from 40 μm to 290 μm can potentially promote the intergranular cracking susceptibility in 7075-T6 aluminum alloy immersed in deaerated 0.5 M NaCl solution [45]. In another study, Pang *et al.* [46] also showed that the FSP of the AA7075 Al alloy resulted in a uniform distribution of the cathodic constituent phase with a smaller distance from each other, giving rise to the improved resistance of the alloy against the intergranular corrosion.

Regardless of the reported promising capabilities of the FSP in modifying the microstructure and improving the mechanical performance of L-PBF AlSi10Mg alloy, there is still very limited information available in the open literature on adopting this new post-printing surface treatment technique to modify the performance of AM components. Also, the impacts of the FSP-induced microstructural modifications on the electrochemical stability and corrosion resistance of the L-PBF-AlSi10Mg alloy are hitherto unreported. Focusing on these gaps, the present study aims to better understand the microstructural evolution during FSP of L-PBF-AlSi10Mg alloy and the resultant corrosion performance of the processed alloy as compared to the non-processed as-printed L-PBF-AlSi10Mg.

## 2. Experimental Methods

### 2.1. Material and FSP Process Parameters

In this study, 25×10×45 mm cuboid samples of L-PBF AlSi10Mg were fabricated utilizing an EOS M290 metal 3D printer machine (EOS, Germany) with a 400 W Yb-fibre laser and spot size of 100 μm. Fabrication was performed using standard optimized parameters, including a laser power of 370 W, powder layer thickness of 30 μm, hatch spacing of 0.19 mm, scanning speed of 1300 mm/s, and the stripe scanning strategy with the rotation angle of 67° between consecutive layers. The laser's volumetric energy density (*VED*) [7] used for fabrication of the samples was calculated to be 49.93 J/mm$^3$. To abate the process-induced residual stresses in the fabricated samples, the specimens were printed while maintaining the platform temperature at 200 °C in an argon atmosphere. Gas atomized AlSi10Mg feedstock powder was used with a particle size distribution of 8.8±7 μm and the measured chemical composition listed in Table 1. Inductively coupled plasma-optical emission spectrometry (ICP-OES) was employed to precisely measure the chemical composition of the feedstock powder employing an Agilent ICAP (Model 725) ICP-OES machine located at Cambridge Materials Testing Limited (Cambridge, ON) [47].

Table 5. 1. The measured chemical composition of AlSi10Mg powder used in this study (wt. %)

| ***Si*** | ***Mg*** | ***Fe*** | ***Ni*** | ***Cu*** | ***Al*** |
|---|---|---|---|---|---|
| 10.8 | 0.35 | 0.55 | - | - | Bal. |

The applied post-printing friction stir processing of the L-PBF AlSi10Mg specimen and the position and geometries of the used FSP tool are shown in Figure 5.1a schematically. The surface of the L-PBF AlSi10Mg sample was cleaned with acetone prior to the FSP. A single-pass FSP was conducted along the building direction (Z-axis) of the L-PBF sample, using a tool made of H13 steel, with a shoulder diameter of 15 mm and a 4.5 mm pin length, respectively. The tilt angle of the tool from the normal direction was 3°, and the plunge depth was 0.2 mm. The tool's travel and rotation speeds were 63 mm.min$^{-1}$ and 1120 rpm, respectively. The final processed L-PBF-AlSi10Mg sample is shown in Figure 5.1b.

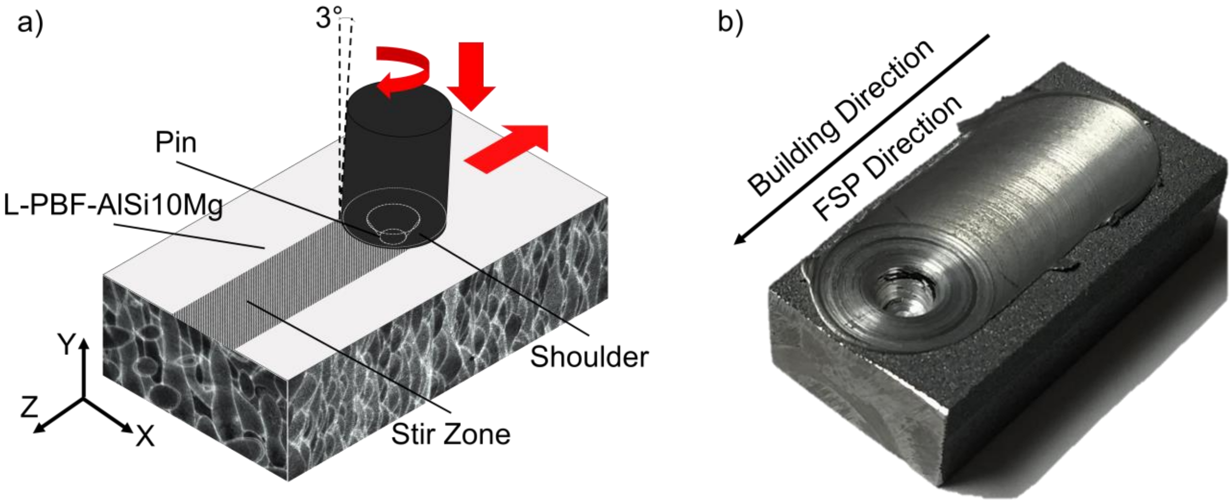

Figure 5. 1. (a) Schematic demonstration of conducting the FSP on the L-PBF-AlSi10Mg, and (b) the FSPed L-PBF-AlSi10Mg sample.

## 2.2. Microstructure Characterization

For the microstructural characterization of the FSPed specimen, the fabricated sample was sectioned perpendicular and parallel to the FSP direction, followed by cold-mounting in an epoxy resin (EpoFix, Struers, Denmark). Following the standard sample preparation procedures for Al alloys, employing a Struers' Tegramin-30 grinder/polisher (Struers, Denmark), the FSPed cross-section of the sample (X-Y plane) was polished to obtain a mirror-like finish using a 0.02 μm alumina suspension in the final polishing step. In order to reveal the microstructural features, the polished surfaces were etched using Keller's reagent [7] for 20 s. Macro- and microstructural characteristics of the FSPed sample were investigated using a Nikon Eclipse 50i optical microscope (Nikon Instruments, Melville, NY) and field emission scanning electron microscope (FESEM, FEI MLA 650 F, Hillsboro, Oregon) equipped with a QUANTAX Energy Dispersive X-Ray Spectroscopy (EDS) detector (Bruker, Billerica, Massachusetts) and an HKL Electron Backscatter Diffraction (EBSD) system (Oxford Instruments, Abingdon, UK). In order to compare the porosity contents before and after the FSP in the L-PBF-AlSi10Mg sample, the porosity size and distribution on the polished surfaces of the samples at different cross-sections were measured using the ImageJ software. For detailed microstructural analysis of the FSPed region, transmission electron microscopy (TEM) in the scanning mode (STEM) was conducted using an FEI Tecnai Osiris TEM equipped with a Super-EDS X-ray detection system operated at 200 kV. A sub-nanometer electron probe was used for the STEM-EDS elemental mapping analysis to obtain spatial resolutions in the order of 1 nm. To prepare TEM foils from the center of the FSPed region, an in situ lift-out technique [48] using a focused ion beam (FIB)-field emission SEM (Zeiss NVision 40 [Carl Zeiss, Chicago, IL] was adopted. The grains size and their morphology were also investigated using EBSD analysis (Nordlys II HKL EBSD detector) over scanning areas of 150 μm×150 μm and 300 μm×300 μm at a step size of 0.35 μm and 0.70 μm, respectively. The post-processing of the raw EBSD data was performed using Channel 5 software (HKL Inc., Hobro, Denmark).

### 2.3. Corrosion Properties Analysis

All electrochemical testing were performed on 5 mm×5 mm polished surfaces prepared from the X–Y plane of the FSPed area, as well as the side view (Y–Z plane) and the top view (X–Y plane) of the non-processed base metal (BM), denoted as the Side and the Top samples, respectively. A standard three-electrode corrosion cell setup [49], connected to a computer-controlled IVIUM CompactStat™ Potentiostat (IVIUM Technologies, Eindhoven, The Netherlands) was used in this study. The L-PBF-AlSi10Mg sample, a saturated silver/silver chloride (Ag/AgCl) electrode, and a graphite rod were employed as the working electrode, the reference electrode (RE), and the counter electrode (CE), respectively. The samples were tested in 1000 ml aerated 3.5 wt.% NaCl electrolyte to mimic the corrosion conditions in seawater environment. The temperature of the electrolyte during each test was kept constant at room temperature (25±0.1 °C) using a temperature-controlled water bath. For each electrochemical characterization measurement, the polished surface of the samples was ultrasonically cleaned in ethanol for 5 min and then washed with distilled water and dried under cold air. Before each electrochemical testing, the open circuit potential (OCP) was monitored for 3600 s for stabilization. The anodic polarization measurements were conducted in the potential range of −0.02 V to +0.3 V *vs* OCP, using a potential sweep rate of 0.125 mV/s.

The electrochemical impedance spectroscopy (EIS) tests were also performed in aerated 3.5 wt.% NaCl electrolyte at 25 °C for immersion times of 1 h, 72 h, and 120 h, using the AC signal with 0.01 V amplitude over the OCP in the frequency range of 100 kHz to 10 mHz. The impedance data and the corrosion parameters were evaluated employing the IviumSoft electrochemical optimization software (IVIUM Technologies, Eindhoven, The Netherlands).

The intergranular corrosion (IGC) measurement was conducted on the polished surfaces of the BM samples, including the top and side views as well as the FSPed samples according to the ISO 11846 standard [29], in which each sample was immersed in a solution containing 30 g/L of sodium chloride and 10 mL/L of HCl at room temperature (25°C) for 1 day [50]. After 24 h of immersion, the corrosion products were mechanically removed by ultra-soft brushing followed by rinsing with water [29], and then investigated via FESEM.

To investigate the semiconducting property of the oxide/passive layer formed on the surface of the FSPed and the BM samples, Mott–Schottky analyses were performed by monitoring the frequency response at 1 kHz and 10 kHz during a 25 mV/s negative potential scan between -1.5 V to 0.0 V *vs* OCP. The repeatability of the results obtained from all corrosion tests was measured by testing at least three samples.

## 3. Results and Discussion

### 3.1. Microstructure Characterization

Figure 5.2a shows a low-magnification view from the entire transverse cross-section (X-Y plane) of the FSPed L-PBF-AlSi10Mg sample, showing the processed zone, including the stir zone (SZ), thermo-mechanically affected zone (TMAZ), and the base metal (BM) (see Figure 5.2d). Despite the presence of a heat affected zone (HAZ) between the TMAZ and the BM, the fine microstructural features associated with this region could not be captured using the optical microscope. Figure 5.2b shows the microstructural characteristic of the L-PBF AlSi10Mg, in which the plane of view is perpendicular to the building direction (top view), revealing a tear-drop morphology for the melt pools, similar to what has been commonly reported in previous studies [4,7,20]. The used hatching strategy with a 67° laser beam rotation between the consecutive layers during the L-PBF process resulted in the formation of the irregular melt pool directions and geometries in the top view of the BM. The long axis of each single oval-shaped melt pool indicates the laser scanning direction. Figure 5.2c shows the optical micrograph from the as-printed L-PBF-AlSi10Mg sample parallel to the building direction (side view), revealing a fish-scale morphology for the melt pools' cross sectional overview with a width in the range of 100-150 μm.

Figure 5.2d shows a higher magnification image taken from the SZ-BM interface (corresponding to the enclosed area in Figure 5.2a indicated by D). The TMAZ region is quite narrow, about 75–100 µm wide, leading to a sharp microstructural transition from the BM to the SZ. The optical microscopy investigation of the SZ (shown in Figure 5.2e) revealed that the observed melt pools characteristics in the BM (Figures 5.2b and 5.2c) were absent and entirely annihilated in the stir zone, which was attributed to the severe plastic deformation combined with the generated frictional heat during the FSP in this region. As compared to the SZ, TMAZ experiences a significantly lower level of deformation during the FSP and is mostly affected by the generated high temperature during the process.

The level of L-PBF process-induced porosity was measured on the polished surfaces using the ImageJ software before and after performing FSP on different cross-sections. The Top and Side samples from the BM showed almost the same porosity content with average porosity percentage of 0.664±0.14% (indicated by small arrows in Figure 5.2f), which can be considered a low porosity level as compared to what has been reported in the literature [24]. Interestingly, the polished surface of the SZ (Figure 5.2g) clearly indicates that applying the FSP has eliminated the nearly all of the porosity, causing a significant reduction of the porosity level in the SZ. It is generally accepted that porosity and solidification micro-cracks in the L-PBF AlSi10Mg alloy are susceptible regions to pitting corrosion attacks [44,46]. Therefore, the reduction of internal pores in the FSPed L-PBF sample can plausibly contribute to the corrosion properties of the alloy positively.

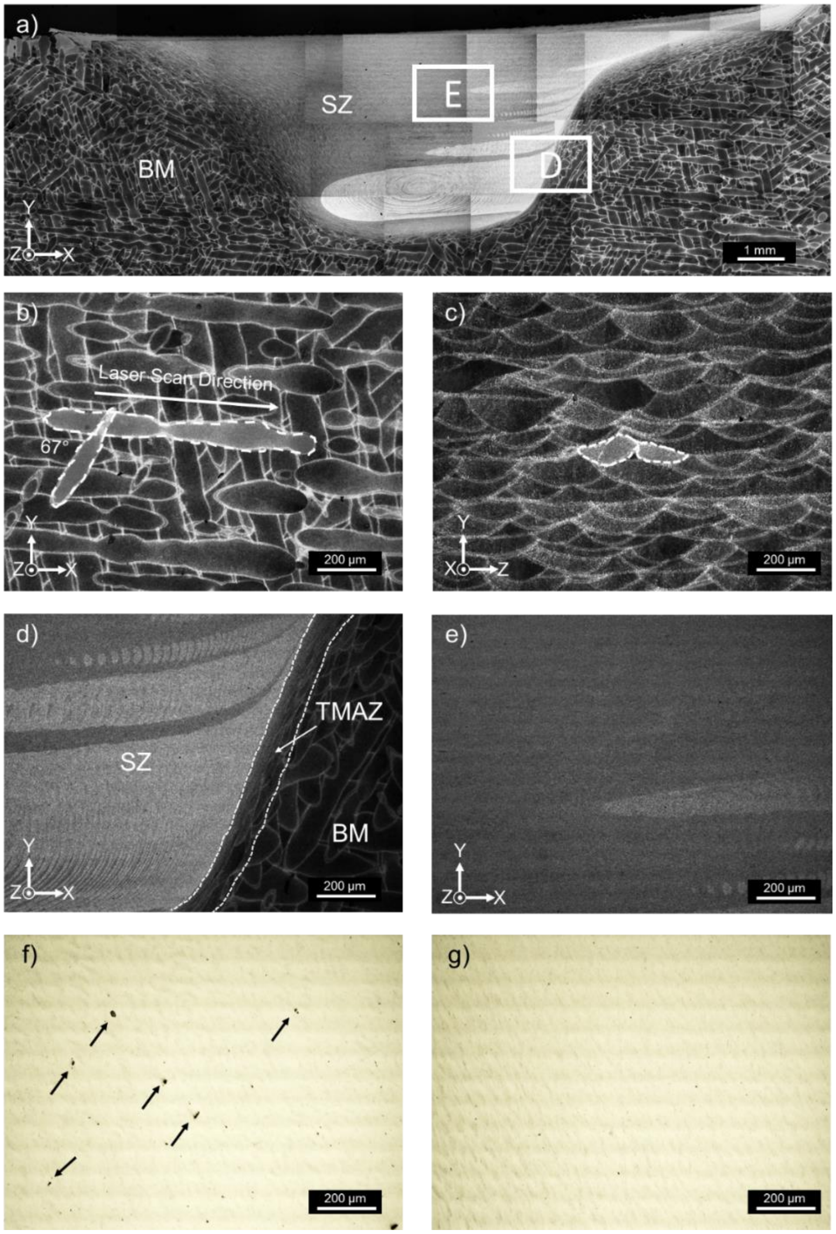

Figure 5. 2. Optical micrographs taken from (a) the entire cross-sectional overview of the FSPed L-PBF-AlSi10Mg sample, (b) the top view, perpendicular to the building direction (X-Y plane), (c) the side view, along the building direction (Y-Z plane), (d) the enclosed area in (a) indicated by D, (e) the enclosed area in (a) indicated by E, and the polished surface of (f) BM, (g) SZ.

Figures 5.3a and 5.3b show the characteristics of the microstructural features for the L-PBF AlSi10Mg alloy, perpendicular (X-Y plane) and parallel (Y-Z plane) to the building direction, respectively, consisting of a remarkably fine dendritic structure (~ 0.5-2 μm) within the aluminum matrix (dark grey), and a continuous network of Si phase (light grey) formed along the interdendritic regions (shown in Figure 5.3a). The as-printed microstructure of the L-PBF AlSi10Mg revealed a nonhomogeneous microstructure with a non-uniform distribution of Si particles with different morphologies. In the vicinity of the melt pool boundaries, three distinct regions with different microstructures were formed due to the variation of solidification behavior and thermal history along the centerline of the melt pool. These microstructures consist of the coarse melt pool (MP) and fine MP regions, both having a cellular structure inside the melt pool, and a narrow HAZ in the previously solidified track containing broken idiomorphic Si crystals. The directional solidification features of the side view's microstructure in Figure 5.3b indicate the cellular growth towards the melt pool’s center. Such directional solidification features were absent in the top view microstructure, confirming the asymmetric microstructure of the as-printed sample in terms of size and morphology of Si, and possibly the density of the grain boundaries.

Figures 5.3c-5.3f show the modifications of the intercellular Si phase in the stir zone and TMAZ. Comparing the microstructure of the SZ with that of the top and side views clearly indicates that the severe plastic deformation and the high temperature associated with the FSP have completely disrupted the continuous network of Si and resulted in a slight growth of the silicon phase into a more globular particle. Therefore, the FSP has completely eliminated the observed inhomogeneity and irregularities in the as-printed microstructure of the L-PBF-AlSi10Mg alloy and formed a uniform distribution of discontinuous Si phase in the Al matrix (Figure 5.3e).

The EDX chemical composition maps for Si element shown in Figure 5.3f were taken from the as-printed BM and the SZ (Figure 5.3$f_1$ and 5.3$f_2$, respectively), illustrating the distribution of the Si phase in the Al matrix. The more uniform distribution of the Si phase in the SZ (Fig 3$f_2$) as compared to that in the side view sample (Fig 3$f_1$) was also accompanied with an increase in the area fraction of this phase from 30% in the side sample to almost 36% in the SZ. A similar observation was reported by Rao *et al*. [44] after applying 3 FSP passes on the hypereutectic Al-30Si alloy, causing the increase of the Si phase volume fraction from 35% to 61%.

It is well known that the shape, size, and distribution of Si particles play an essential role in the corrosion performance of the L-PBF-AlSi10Mg alloy [3,21]. It was observed that the SZ and TMAZ showed finer and uniformly distributed idiomorphic Si particles in comparison with the BM (Figure 5.3d). Similar to the SZ, the TMAZ experienced plastic deformation (even though at much lower level as compared to the SZ) and heating during the FSP, so the light grey intercellular Si network has also completely disrupted. However, due to the lower temperature that the TMAZ is exposed to during the FSP as compared to the SZ, the Si particles in the TMAZ were finer than those in the SZ (see Figure 5.3d).

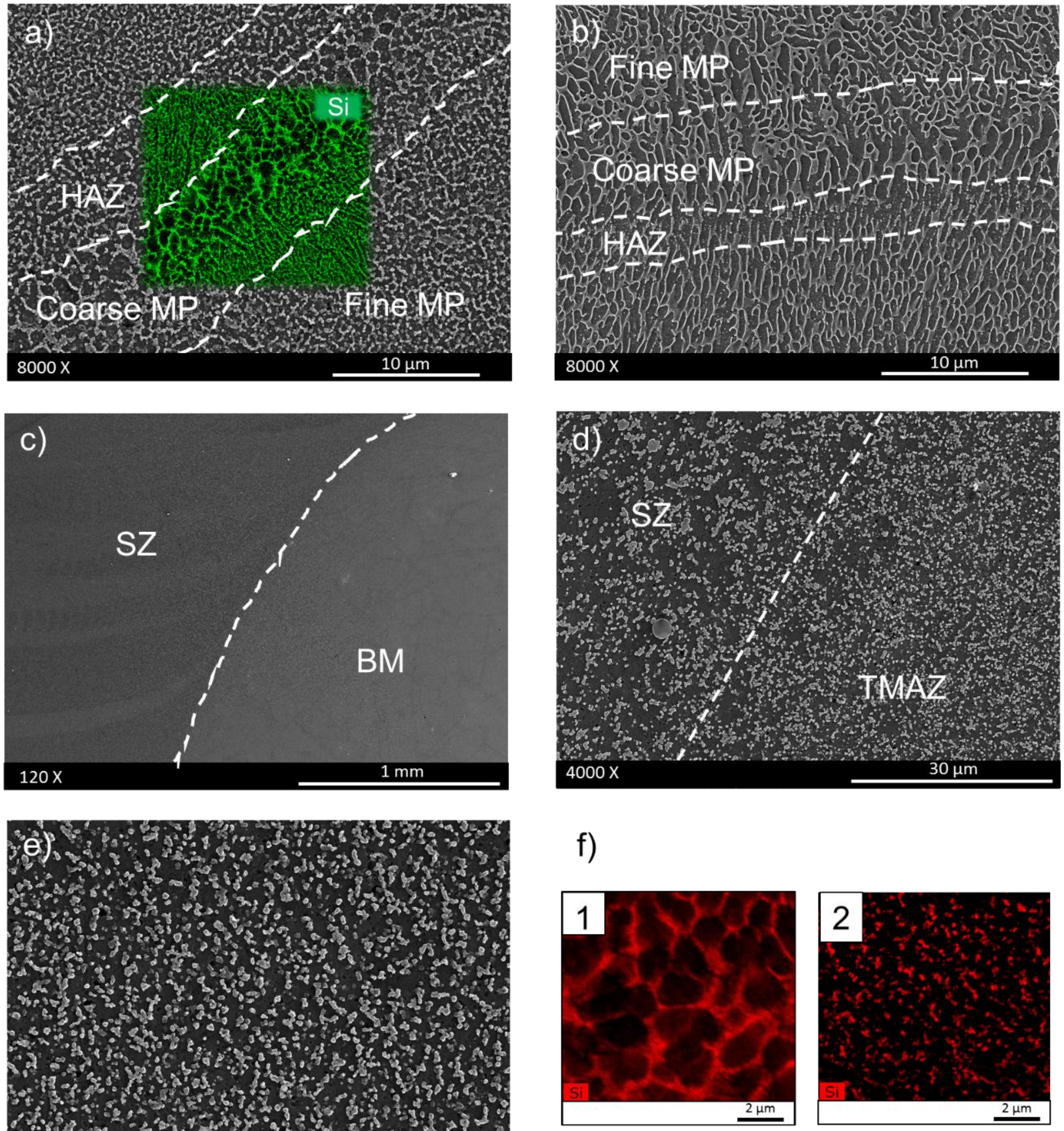

Figure 5. 3. SEM micrographs taken from (a) the top (X-Y plane) view, (b) the side (Y-Z plane) view, and (c) FSPed cross-section of the L-PBF-AlSi10Mg, the distribution of the Si particles in the (d) TMAZ and e) SZ, (f) EDX-Si maps taken from the side view ($f_1$) and the SZ ($f_2$),

The STEM in bright-field mode (STEM-BF) combined with Energy dispersive X-Ray spectroscopy (EDS) were employed to investigate the positions of the Si particles in the stir zone of the FSPed L-PBF AlSi10Mg with respect to the grains of the α-Al matrix. Figure 5.4 shows the STEM-BF image from the SZ of the FSPed L-PBF AlSi10Mg sample and its corresponding EDS elemental maps, confirming uniform distribution of very fine Si particles throughout the SZ. As clearly revealed from Figure 5.4b, despite the formation of Si precipitates in the interior of each Al grain, the majority of detected Si particles were found to be accommodated along the α-Al grain boundaries. These intergranular Si particles correspond to the disrupted eutectic Si phase that were formed in the as-printed sample with a continuous network morphology primarily along the grain boundaries of cell-like α-Aluminum matrix [32][47]. Furthermore, Figure 5.4a revealed a substantial grain refinement in the processed region, characterized by the formation of fine equiaxed grains uniformly distributed throughout the SZ. The observed grain refinement in the SZ has been thoroughly investigated using EBSD analysis in the following section.

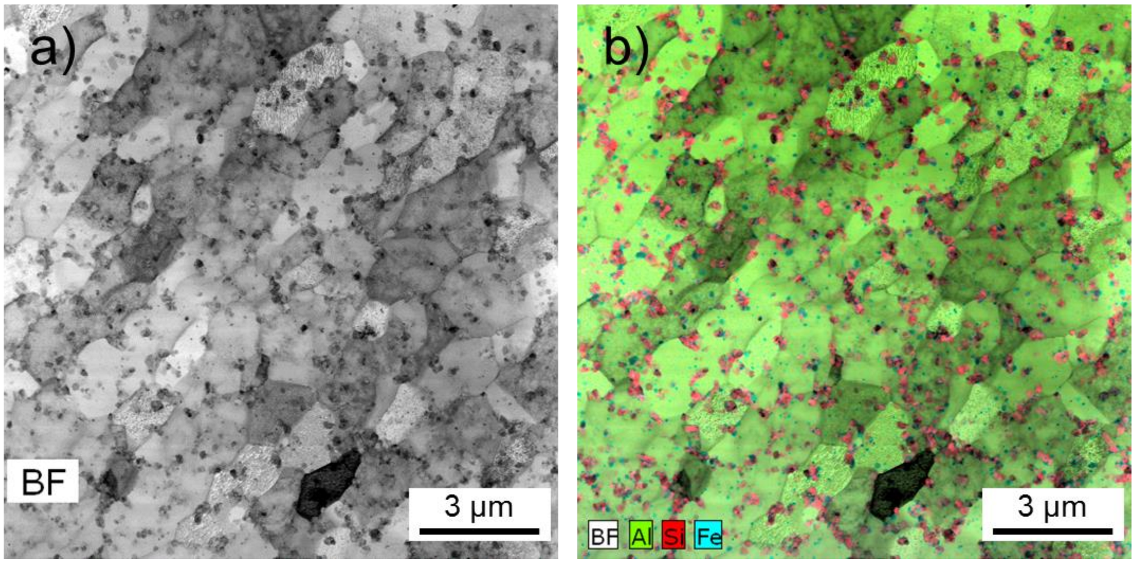

Figure 5. 4. (a) STEM-BF image from the microstructure of FSPed L-PBF AlSi10Mg in the SZ and (b) EDS elemental maps of Al (green), Si (red), and Fe (blue) superimposed on the STEM-BF image shown in (a).

In addition to all existing secondary phases/micro-constituents, the grain size and grain boundaries density are known to be critical factors in controlling the corrosion performance of the metallic components [44,46,51]. Therefore, EBSD analysis was conducted before and after FSP to study the grain size/morphology in detail. The obtained EBSD inverse pole figures (IPF) maps along the Z-direction, where the Z-axis is parallel to the building direction, for three different samples studied herein are demonstrated in Figure 5.5.

Figure 5.5a indicates the formation of equiaxed and ultrafine recrystallized grains that were uniformly distributed across the SZ. Such refinement in the grain structure of SZ is known to be governed by dynamic recrystallization (DRX) during FSP [52]. Therefore, the dual action of the severe plastic deformation and friction-induced heat during stirring has triggered DRX, leading to the evolution of ultrafine grain structure in the SZ. In contrast to the non-uniform microstructure of the as-printed L-PBF AlSi10Mg sample, the FSPed region revealed a refined and homogenous structure comprised of uniformly distributed broken Si phase embedded in a matrix of ultra-fine Al grains.

Figures 5.5b and 5.5c show the grain structure of the Top and Side samples, respectively. As a general observation, the Top and Side samples have significantly coarser and non-uniform grain structures as compared to the SZ. The IPF map of the Top sample (Figure 5.5b) revealed primarily equiaxed grains with a random grain orientation (similar to the SZ), but significantly larger grain size than that of the SZ sample. The positions of the melt pool boundaries can also be traced along the paths that contain highly accumulated smaller equiaxed grains, as shown by the dashed lines in Figure 5.5b.

The IPF map of the Side sample (Figure 5.5c) revealed the formation of mostly columnar grains (dominantly presented with red color (<100>)), which are aligned with the easy growth direction of the crystal (<100> direction for cubic structures) during solidification. Analogous to the Top sample, the positions of highly accumulated small grains correspond to the melt pool boundaries. Therefore, as-printed L-PBF AlSi10Mg has a non-uniform grain structure with the combination of columnar and equiaxed grains. In general, during solidification, by decreasing the value of the temperature gradient over the solidification rate ratio (G/R) at the solidification front, the grain morphology is changed from columnar to equiaxed [53]. Therefore, the equiaxed grains are expected to form at the melt pool boundaries with the lowest temperature gradient and highest solidification rates. Moving from the melt pool boundaries towards the melt pool's center, the grains become dominantly columnar (especially on the Side sample), due to the reduced solidification rate and increased temperature gradient [7].

Figures 5.5d-5.5f show the grain boundary (GB) misorientation maps from the SZ, Top, and Side samples, respectively, where the low angle grain boundaries (LAGBs) with misorientation angle less than 15° and the high angle grain boundaries (HAGBs) having misorientation angles higher than 15° [54] were differentiated using red and black lines, respectively. As Figure 5.5d shows, the SZ has the lowest density of the LAGBs as compared to the Top and Side samples, confirming that during FSP, the occurrence of continuous dynamic recrystallization causes the subgrains boundaries (LAGBs) to migrate into high angle grain boundaries resulted from severe plastic straining of the material at high temperature associated with the FSP [55]. On the other hand, the Top and Side samples show approximately a similar distribution of LAGBs (Figures 5.5e and 5.5f).

The grain size distribution of the SZ, Top, and Side samples is shown in Figure 5.5g. The occurrence of DRX in the SZ has resulted in a significant grain refinement (~ 90% of the grains with a size <2 μm) as compared to that of the as-printed BM samples. The Top and Side samples revealed significantly coarser grain structure with the average grain size of 12±0.40 μm and 23±0.7 μm, respectively. Therefore, considering all the detected microstructural variations between the FSPed region and the non-processed BM, including the shape, size, and distribution of Si phase and the grain size and the grains morphology, it is reasonable to expect different electrochemical performance for the FSPed sample. The electrochemical properties of all studied samples herein are presented and compared in the following section.

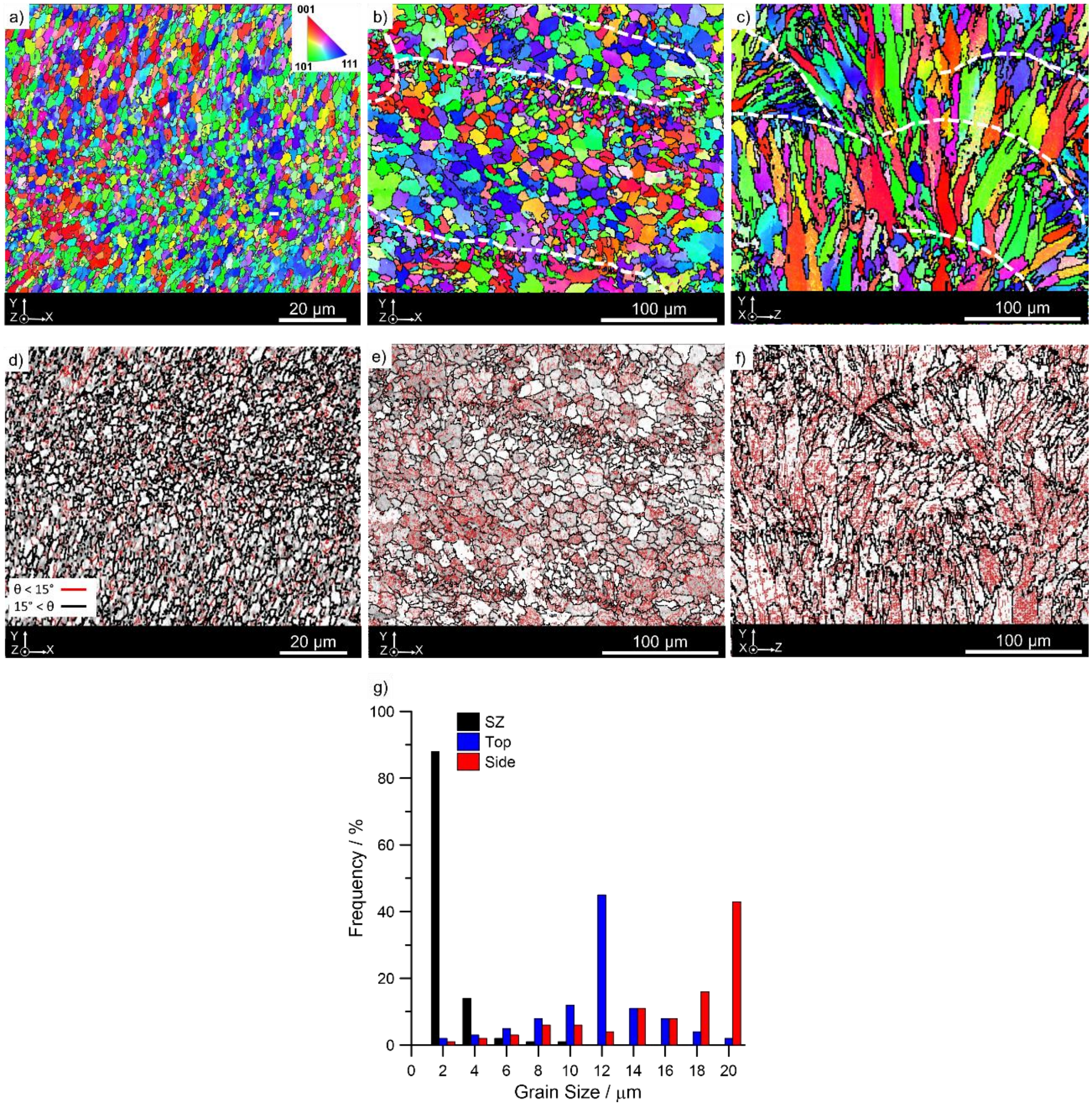

Figure 5. 5. The EBSD inverse pole figure maps taken from the (a) SZ, (b) Top view (X-Y plane), and (c) Side view (Y-Z plane) of the L-PBF AlSi10Mg. The grain boundary maps taken from the (d) SZ, (e) Top, and (f) Side samples, (g) statistical distribution plots showing the mean grain size distribution in all studied samples.

## 3.2. Corrosion Properties Analysis

### *3.2.1. OCP and anodic polarization results*

The steady-state open-circuit potential (OCP) evolution over 3600 s of immersion time in aerated 3.5% NaCl solution for the SZ, Top, and Side samples are presented in Figure 5.6a. The OCP values for all samples were stabilized at about the same value, around -0.73±0.06 $V_{Ag/AgCl}$, and no considerable difference resulted from variations in the microstructural features between the samples was detected. The measured proximity in the OCP values of different samples is plausibly attributed to the chemical composition uniformity on the surface of three samples, suggesting the formation of native oxide layers with similar nature on all samples [21,56]. However, the SZ sample revealed a slightly higher (more positive), although not significant, OCP values than the Top and Side samples. The nobler $E_{OCP}$ value of the SZ sample indicates marginally higher electrochemical stability and lower activity of its surface. This can possibly be ascribed to the uniformity of the microstructure and the lower volume fraction of porosities in the SZ after FSP.

The anodic polarization plots of the SZ, Top, and Side samples in polished condition are illustrated in Figure 5.6b and Table 2 lists all anodic polarization parameters for all samples. The pitting potential ($E_{pit}$), corrosion potential ($E_{corr.}$), corrosion rate, and corrosion current density ($I_{corr.}$) values for each sample were obtained from their respective polarization plots. The reported mean values of $E_{corr.}$, $E_{pit}$, and $I_{corr.}$ in Table 2 were calculated from independent measurements from different samples.

The polarization curve obtained from the Side sample reveals that the anodic current density increased rapidly at approximately the corrosion potential, confirming an instantaneous pitting on the Side surface once the corrosion potential is attained. Such active-like behavior with almost no passivity has been also reported in previous studies for the side view of the L-PBF AlSi10Mg [3,21]. The higher density of melt pool boundaries exposed to the corrosive environment on the Side sample than those on the Top sample leads to the active-like behavior of the Side surface [40,57]. However, during the FSP, the entire Si network of the L-PBF AlSi10Mg was eliminated, resulting in a significant change of its corrosion performance. As Figure 5.6b shows, a wide passivity range was detected on the polarization curve of the SZ sample, leading to a nobler pitting potential for this sample as compared to the Top and Side samples (+0.16 V higher than the Side sample). Analogously, Rao *et al.* [44] reported +0.27 V increase in the breakdown potential of the cast Al-30Si alloy after applying one FSP pass to this alloy. The Top surface sample showed an intermediate behavior, suggesting an asymmetric corrosion response for the L-PBF AlSi10Mg BM, which is also consistent with the previous studies [40,57]. The lower density of the melt pool boundaries and also finer grain structure on the Top view (X-Y plane) as compared to the Side view (Y-Z plane) contributed to the higher pitting potential of the Top sample, and ultimately the better resistance of the top plane against localized pitting attack compared with the side plane in as-printed sample [40,57].

It can be clearly noted that the pitting potential and the overall corrosion performance of the L-PBF AlSi10Mg improved as the Si morphology changed from the Side sample, to the Top and SZ sample. The lower pitting potential of the Top and Side samples as compared to the SZ can be attributed to the presence of the continuous network of large eutectic silicon phase, particularly along the melt pool boundaries (see Figure 5.3b) with a non-uniform distribution, provoking the susceptibility of the interface between the coarse silicon and the surrounding Al matrix to the penetration of the corrosive chloride ions in addition to the existence of the L-PBF produced porosities on the as-printed BM, leading to the easier breakdown of the passive layer [40]. Similar observations have been previously reported for an FSPed Al-30Si alloy and ECAPed pure Al [44,51,58]. Rao *et al.* [44] showed that during FSP of the as-cast hypereutectic Al-30Si alloy, the average grains size and the size of the Si particles are reduced from the 20.00 µm and 188.00 µm to 0.74 µm and 2.10 µm, respectively, resulting in the improved corrosion performance of the alloy, indicated by the decreased corrosion current density from 4.15±0.35 µA/cm$^2$ to

2.49±0.2 μA/cm$^2$ and increased pitting potential from -0.709±0.002 $V_{Ag/AgCl}$ to 0.435±0.003 $V_{Ag/AgCl}$. Analogous to the results obtained herein, Rao *et al.* [44] also reported that FSP transforms the LAGBs in the as-cast structure to the HAGBs, positively contributing to the improved corrosion performance of the alloy through increasing the passive layer thickness from 14±0.06 nm to 52±0.56 nm.

Previous studies [44,51] have reported a Hall-Petch type relationship (a linear regression) between the corrosion current density (or corrosion rate) and the grain size ($d$) for materials that are able to form protective passive layer on them, such as aluminum alloys, as follows:

$$Corrosion\ current\ density = A + Bd^{-0.5} \qquad \text{Eq. (1)}$$

where $A$ is a corrosion environment constant and $B$ is a material-dependent constant (varies with chemical composition and level of impurity) [51]. Therefore, if a passive layer is formed on the surface, the grain size reduction of the base material decreases the corrosion rate or corrosion current density. Thus, the formed ultra-fine grain structure in the SZ sample is expected to positively contribute to the improved corrosion performance of the alloy. Figures 5.6c and 5.6d display the correlation between the corrosion current density ($I_{corr.}$) and pitting potential ($E_{pit.}$) *vs* the grain size raised to the power of -0.5, respectively, measured for the SZ, Top, and Side samples. Applying the FSP was found to drastically reduce the corrosion current density value (Figure 5.6c) and shifted the pitting potential to more positive values (Figure 5.6d). The obtained linear regression trend, with the $R^2$ value (the square of correlation coefficient) higher than 0.94, clearly indicates that the corrosion performance of the L-PBF AlSi10Mg alloy is improved by decreasing the average grain size of the alloy.

In addition to the impact of the refined grain structure of the Al matrix, the FSP has also resulted in breaking up the Si network and their uniform distribution, giving rise to the increased area fraction of cathodic Si and decreased area of the anodic Al. Therefore, the increased area fraction of cathodic sites (Figure 5.3f$_2$), decreased area fraction of anodic sites, and the increased density of grain boundaries as fast diffusion paths, promoting the oxygen diffusion, all contributed to the reduced dissolution of the Al matrix. However, it is worth mentioning that in the absence of the passive layer, the grain size reduction, and consequently the increased density of the grain boundaries, will likely increase the overall reactivity on the surface and deteriorate the corrosion performance [59,60].

It is also evident that the FSP-induced microstructural modifications have mostly impacted the anodic reaction as well as the pitting potential of the alloy and only a small change in the cathodic reactions was detected. This can be ascribed to diverse natures of the cathodic and anodic reactions. It is known that the anodic reaction relies more on ionic conduction than electronic conduction, and the fast diffusion paths along the grain boundaries can accelerate the ionic conduction in metallic components [44]. Lee *et al*. [61] studied the impact of the grain size and the grain boundary density on the corrosion response of aluminum by comparing the single crystal and polycrystalline Al, and reported an increase in the passive film ion conduction in the polycrystalline aluminum sample as compared to the single-crystal Al, attributed to the existence of the grain boundaries [61].

Equation (1) can also be applied to yield a correlation between the grain size and the measured pitting potentials of the samples (see Figure 5.6d). The anodic polarization data also confirmed that after applying FSP, the $E_{pit}$ value shifted to a more positive value (see Table 2 and Figure 5.6d), suggesting that decreasing the grain size and uniform distribution of the Si particles lead to the improved pitting resistance of the alloy as well. The overall conclusion from the anodic polarization results was that applying the FSP on the as-printed L-PBF AlSi10Mg alloy is beneficial as it improved the pitting potential and decreased the corrosion current density, and subsequently the corrosion rate of the alloy.

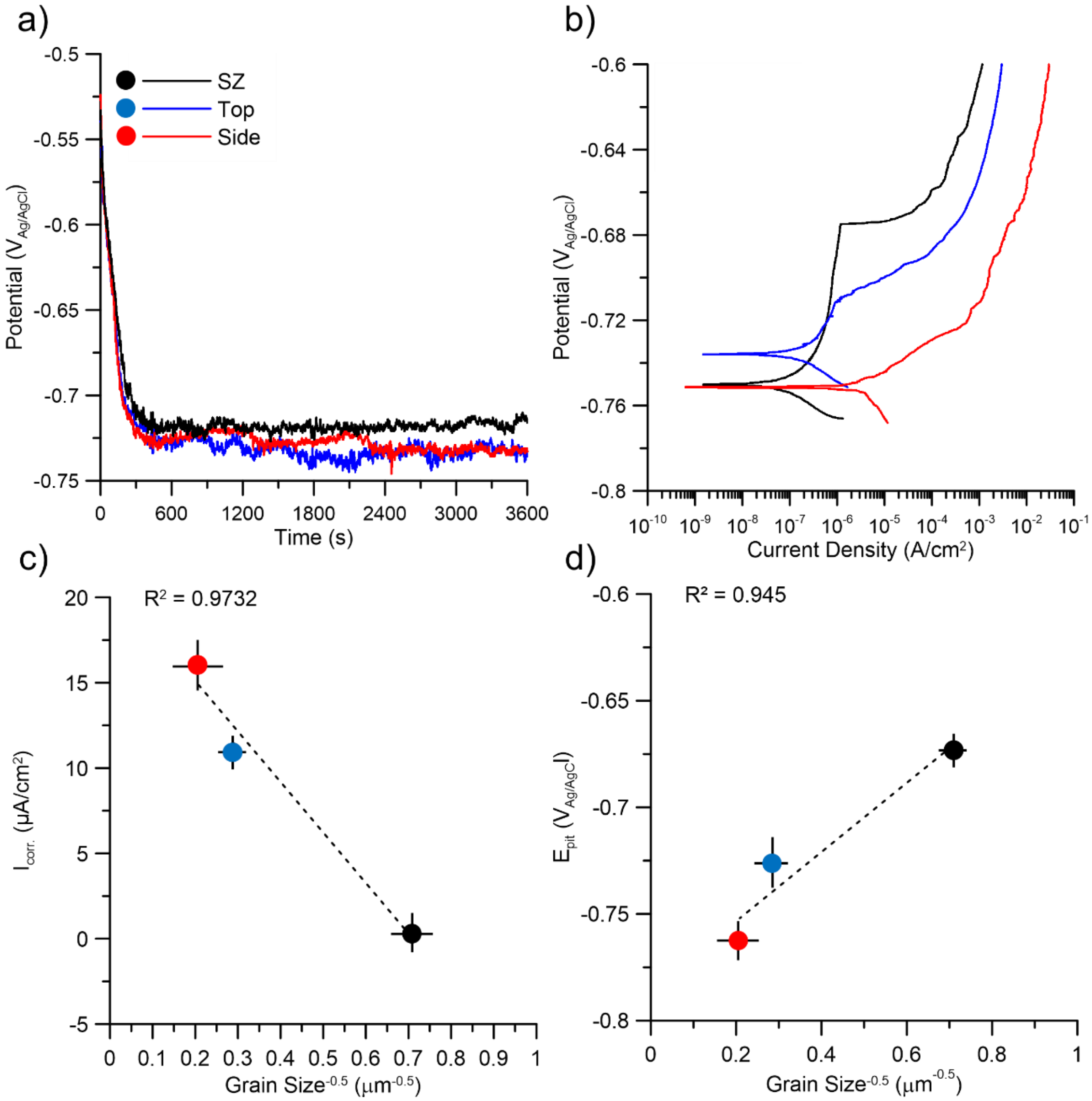

Figure 5. 6. (a) The OCP measurements over 3600 s, (b) the anodic polarization graphs comparing the polarization response of the SZ, Top, and Side samples, Hall–Petch type relationship between (c) corrosion current density ($I_{corr}$) and (d) pitting potential ($E_{pit.}$) *vs* aluminum matrix grain size.

Table 5. 2. Electrochemical parameters extracted from anodic polarization graphs (Figure 5.6b) of the SZ, Top, and Side samples.

| Sample | $E_{corr.}$ ($V_{Ag/AgCl}$) | $I_{corr.}$ (µA/cm$^2$) | $E_{pit.}$ ($V_{Ag/AgCl}$) | Corrosion rate (µm/year) |
|---|---|---|---|---|
| SZ | -0.77±0.05 | 0.32±0.20 | -0.68±0.02 | 12±1 |
| Top | -0.76±0.02 | 11.07±1.40 | -0.72±0.02 | 28±3 |
| Side | -0.77±0.03 | 16.04±0.90 | -0.77±0.09 | 580±12 |

### *3.2.2. Electrochemical impedance spectroscopy results*

To further analyze and compare the protectiveness and stability of the formed passive layer on the surface of the SZ, Top, and Side samples, impedance spectroscopy in aerated 3.5 wt.% NaCl electrolyte was conducted. Figure 5.7 shows the obtained Nyquist diagrams from the SZ, Top, and Side samples for different immersion times, *i.e.* 1 h, 72 h, and 120 h. At the initial immersion time (Figure 5.7a), the Nyquist plots of all samples showed one broad and well-defined capacitive arc. The formation of such broad capacitive peak in Al alloys is commonly attributed to the superposition of two individual peaks with non-discriminating time constants [30]. At longer exposure times (72 h and 120 h), the Nyquist diagrams have more complex behavior and revealed two distinct and partially overlapped capacitive peaks, one at low and the other at high-frequency ranges. The low-frequency capacitive loop (the second Nyquist peak) corresponds to the diffusion and charge transfer within the interface of the metal surface and the solution, while the capacitive semicircle at the high-frequency range (the first Nyquist peak) is attributed to the interface between the passive layer and the solution (representing the general surface corrosion) [3,7,44]. The Nyquist curvature radius describes the protectiveness and stability of the passive layer on the surface of the samples, such that the larger curvature radius of the Nyquist response indicates slower kinetics of corrosion reactions [21]. The largest semicircle was obtained for the SZ sample and the smallest semicircles for the Side sample, which is consistent with the anodic polarization results (shown in Figure 5.6b), confirming the lowest current density and the corrosion rate as well as the highest pitting potential for the SZ sample. Therefore, after 1 h of immersion time, a passive film with a more protective nature was formed on the SZ sample than that of the Top and Side samples. After longer immersion times of 72 h and 120 h, similar to the just immersed condition, the Nyquist responses (shown in Figures 5.7b and 5.7c) exhibited a larger capacitive loop for the SZ sample, indicating the formation of a passive layer with higher electrochemical stability on its surface, resulting in better corrosion performance of the SZ sample as compared to the Top and Side samples.

The grain structure is a critical factor affecting the passivation ability and the formation of a stable and protective passive/oxide layer on the metal surfaces [61–63]. Correlating the Nyquist plots with the formed microstructure in the studied samples reveals that even though the similarity in the shape of Nyquist plots indicated a comparable nature for the corrosion reactions on all samples, the electrochemical stability of the passive layer can noticeably vary by the modification in the microstructure. As previously reported, high density of the melt pool boundaries on the surface of L-PBF AlSi10Mg alloy adversely impacts the uniformity of the passive/oxide layer [40]. A thinner passive/oxide layer is reported to form along the melt pool boundaries of the L-PBF AlSi10Mg alloy [40]. Also, the transformation of the LAGB to HAGB and reducing the level of porosities after FSP of the L-PBF AlSi10Mg alloys should be considered as contributing factors to the stability of the passive layer [44]. Therefore, the FSP-induced microstructural modifications, *i.e*. the grain refinement, uniform distribution of the interdendritic Si particles, and the reduced porosity level, can significantly influence the corrosion properties of the L-PBF AlSi10Mg part, leading to the improved electrochemical stability of the alloy in chloride-containing environments.

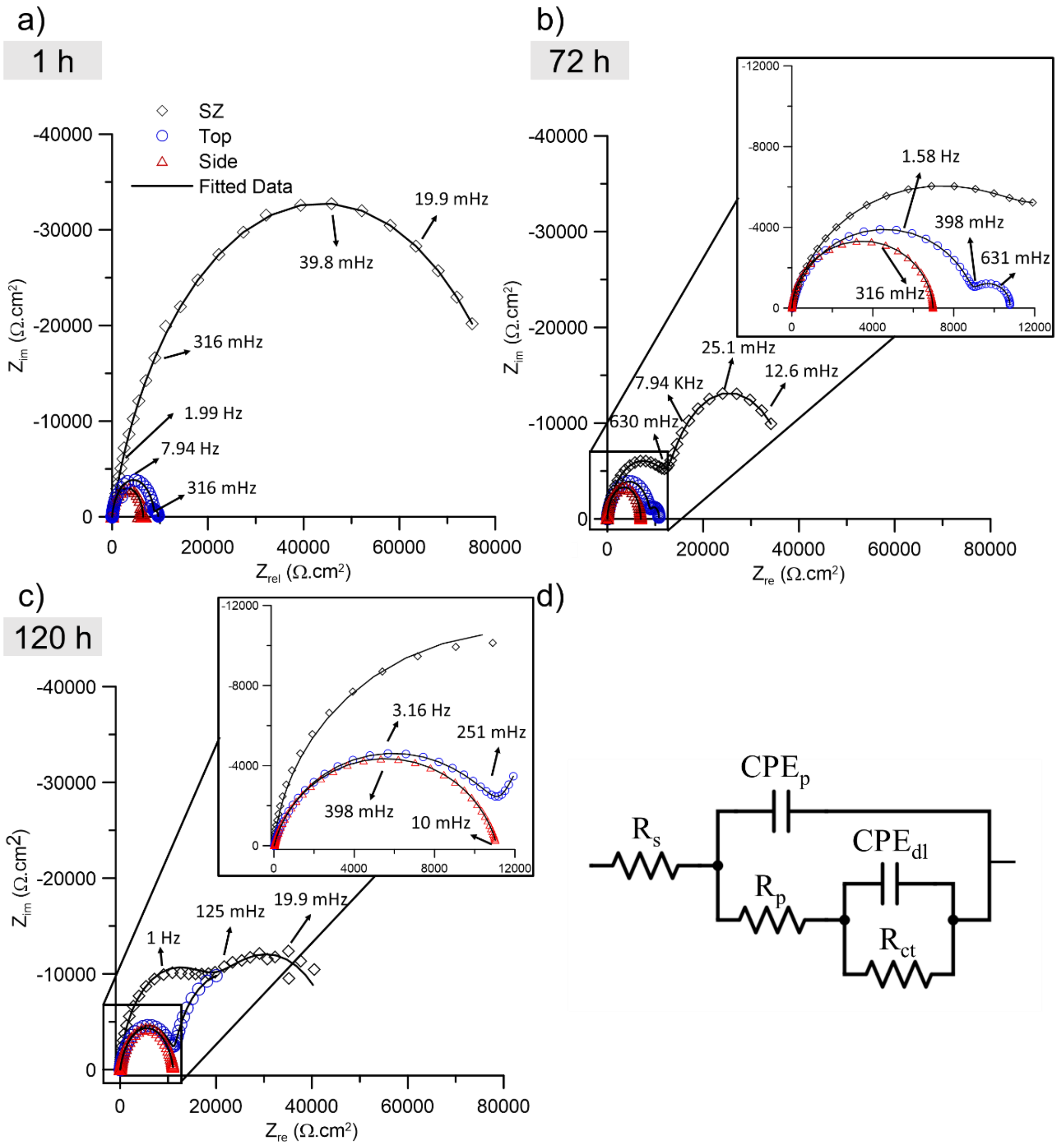

Figure 5. 7. Nyquist spectra and the fitted data after a) 1 h, b) 72 h, and c) 120 h of immersion time, d) the simplified equivalent circuit used to interpret the evolution of the EIS spectra.

To gain a better understanding of the passive film evolution on all samples over immersion time, the simplified equivalent circuit (SEC) of $R_s+(Q_p[R_p+(Q_{dl}R_{ct})])$ (shown in Figure 5.7d) was fitted to the measured impedance spectra. The obtained fitted data are also included on the Nyquist plots in Figure 5.7.

In the SEC model used here (Figure 5.7d), $R_s$ represents the ohmic drop in the electrolyte, $R_p$ *and* $CPE_p$ correspond to the resistance and the capacitance of the passive layer, respectively, $R_{ct}$ and $CPE_{dl}$ *represent the* charge transfer resistance and its corresponding double layer (*dl*) constant phase element, respectively, at the interface of the substrate and the passive layer. The impedance of a Constant Phase Element (*CPE*) is defined as $Z_{CPE} = [Q(j\omega)^{\alpha}]^{-1}$, where $Q$ is the *CPE* constant, $j$ is the imaginary unit ( $j = \sqrt{-1}$), $\omega$ is the angular frequency (rad/s), and $\alpha$ is the dispersion coefficient of the *CPE*, and its value changes from -1 (for a pure inductor) to 1 (for a pure capacitor) [7]. It has been reported that even when the measured values for the dispersion coefficient ($\alpha$) were higher than 0.90±0.02, the used *CPE* constants cannot be considered as accurate pure capacitors in the adopted SEC presented in Figure 5.7d [64]. Considering the uneven nature of the formed oxide layer, the constant phase elements are employed to represent its overall capacitance [65]. Although, in some studies, $Q$ is reported as the capacitance, it should be noted that $Q$ has the dimension of $s^n/\Omega$, while the capacitance ($C$) unit is $s/\Omega$ or F [66]. In this regard, Orazem *et al.* [64] showed that $Q$ does not represent the actual and pure capacitance properties of the oxide film. Therefore, converting $Q$ into $C$ is critical when experimental capacitance data are employed to calculate the thickness of the oxide layer on Al alloys quantitatively. There are a number of models developed by different researchers to determine the passive film capacitance ($C_{eff}$) by using *CPE* parameters, such as Simple Substitution (S-S model) method, which directly converts $C_{eff}$ to $Q$ for $\alpha$~1 [64], Hsu and Mansfeld’s model [66], and Brug’s model [67].

According to the Hsu and Mansfeld's model (H-M model), the correlation between $Q$ and $C_{eff}$ is defined as [66]:

$$C_{eff} = Q(\omega_m^{"})^{\alpha-1} = Q(2\pi f_m^{"})^{\alpha-1} \qquad \text{Eq. (2)}$$

where $C_{eff}$ is the passive film capacitance, $\omega_m^{"}$ and $f_m^{"}$ are the angular frequency and the frequency at which the imaginary component of the impedance has the maximum value, respectively. The $f_m^{"}$ values can be extracted from the EIS spectra shown in Figure 5.7. Hamadou *et al*. [68] reported a different correlation between $C_{eff}$ and $Q$ as follows:

$$C_{eff} = Q^{1/\alpha} R_p^{(1-\alpha)/\alpha} \qquad \text{Eq. (3)}$$

where $R_p$ describes the resistance of the passive film.

Brug *et al.* [67] also introduced a model to describe the behavior of constant phase elements based on the concept of a double-layer capacitance distribution on the surface and electrolyte interface resulted from the inhomogeneity of the surface. Their proposed equation for $C_{eff}$ is shown below:

$$C_{eff} = Q^{1/\alpha} \left(\frac{R_s R_{pol}}{R_s + R_{pol}}\right)^{(1-\alpha)/\alpha} \qquad \text{Eq. (4)}$$

where $R_s$ represents the ohmic drop in the solution and $R_{pol}$ corresponds to the polarization resistance.

The alternative power-law (P-L) model, developed by Hirschorn *et al.* [69], described the CPE parameters using a normal resistivity distribution of time constants. The P-L model presents an effective method for the interpretation of CPE parameters in terms of resistivity, film thickness, and dielectric constant. According to this model, the $C_{eff}$ is represented as [69]:

$$C_{eff} = gQ(\rho_{\delta}\varepsilon\varepsilon_0)^{1-\alpha} \qquad \text{Eq. (5)}$$

where $g$ is a function of $\alpha$ ($g = 1 + 2.88(1 - \alpha)^{2.375}$), $\varepsilon$ and $\varepsilon_0$ are the dielectric constant and vacuum permittivity ($8.85 \times 10^{-14}$ Fcm$^{-1}$), respectively. The $\rho_{\delta}$ represents the resistivity at the maximum thickness of the passive layer ($x=\delta$). The value for the parameter $\rho_{\delta}$ is usually uncertain. However, its maximum value can be calculated using the following equation [64]:

$$\rho_{\delta,max} = \frac{1}{2\pi f_{max}\varepsilon\varepsilon_0} \qquad \text{Eq. (6)}$$

Therefore the maximum value of the $C_{eff}$ can be measured to be:

$$C_{eff,max} = gQ(2\pi f_{max})^{\alpha-1} \qquad \text{Eq. (7)}$$

Therefore, the $\rho_{\delta,max}$ at the maximum measured frequency ($f_{max}$) of 100 kHz and dielectric constant of 8.5 for $Al_2O_3$ [44] was calculated to be $2.12\times10^6$ Ωcm.

The fitting parameters extracted from the Nyquist plots of different samples are listed in Table 3, while the calculated capacitance of the passive layer ($C_{eff}$) at different immersion times using S-S model, H-M model, Brug's, and P-L models are presented in Table 4.

Comparing the passive layer resistance values ($R_p$) with the charge transfer resistance values ($R_{ct}$) of the SZ and the Top samples at different immersion times reveals that the $R_{ct}$ values are always higher than their corresponding $R_p$ values, indicating that general corrosion is the dominant corrosion attack on their surfaces. However, the Side sample behaved differently and showed lower charge transfer resistance than passive layer resistance, revealing the pitting corrosion as the predominant corrosion on its surface. This observation is in agreement with the anodic polarization results (Figure 5.6b), exhibiting a clear passive region for the Top and, more obviously, the SZ sample, and an active-like behavior for the Side sample.

After 1 h of immersion, the SZ sample showed a significantly higher passive layer and charge transfer resistance (34.21±1.80 KΩ.cm$^2$ and 42.12±2.80 KΩ.cm$^2$, respectively), indicating better corrosion performance of the SZ sample as compared to the Top and Side samples. The lowest passive layer and charge transfer resistance (6.24±1.40 KΩ.cm$^2$ and 8.35±2.00 KΩ.cm$^2$, respectively) were measured for the Side sample, indicating the lowest stability of the protective oxide layer on its surface, consistent with the trend of anodic polarization graphs (Figure 5.6b).

After longer immersion times, *i.e.* 72 h and 120 h, the electrochemical stability of the SZ sample is slightly reduced, as evidenced by the moderate decrease in the $R_p$ and $R_{ct}$ values after 120 h of immersion time (18.23±1.50 KΩ.cm$^2$ and 22.65±4.60 KΩ.cm$^2$, respectively) as compared to the just immersed condition (1 h). However, the Top and Side samples showed a drastic reduction in their $R_p$ and $R_{ct}$ values after 72 h and more significantly after 120 h of immersion time, indicating more accelerated dissolution and removal of the passive layer at longer immersion times.

Table 5. 3. The fitting parameters of the EIS spectra including the elements of the *SEC* shown in Figure 5.7d.

| | $R_s$ ($\Omega cm^2$) | $R_p$ ($k\Omega cm^2$) | $CPE_p$, $Q$ ($\mu S\ Sec^n\ cm^{-2}$) | $\alpha_p$ | $R_{ct}$ ($k\Omega cm^2$) | $CPE_{dl}$, $Q$ ($\mu S\ Sec^n\ cm^{-2}$) | $\alpha_{dl}$ |
|---|---|---|---|---|---|---|---|
| **SZ** | | | | | | | |
| *1 h* | 8.32±0.70 | 34.21±1.80 | 5.54±0.70 | 0.90±0.02 | 42.12±2.80 | 5.24±1.30 | 0.95±0.03 |
| *72 h* | 7.25±0.40 | 22.18±2.20 | 7.12±1.10 | 0.97±0.01 | 32.01±3.20 | 6.67±2.40 | 0.96±0.01 |
| *120 h* | 4.10±0.60 | 18.23±1.50 | 20.34±2.50 | 0.91±0.03 | 22.65±4.60 | 15.35±3.70 | 0.94±0.01 |
| **Top** | | | | | | | |
| *1 h* | 5.39±0.20 | 16.23±1.30 | 15.43±1.30 | 0.99±0.02 | 18.25±3.20 | 15.12±2.20 | 0.96±0.10 |
| *72 h* | 5.15±0.80 | 2.95±0.90 | 22.23±1.80 | 0.97±0.02 | 5.07±1.20 | 18.75±2.40 | 0.98±0.03 |
| *120 h* | 4.23±0.30 | 1.42±0.60 | 62.23±1.80 | 0.92±0.04 | 4.11±1.40 | 45.37±5.40 | 0.94±0.01 |
| **Side** | | | | | | | |
| *1 h* | 9.23±0.50 | 8.35±2.00 | 17.33±4.20 | 0.93±0.01 | 6.24±1.40 | 18.48±1.20 | 0.97±0.03 |
| *72 h* | 8.95±0.6 | 2.14±1.30 | 32.24±1.30 | 0.99±0.02 | 1.98±0.90 | 25.45±4.10 | 0.96±0.02 |
| *120 h* | 6.76±0.20 | 1.45±0.40 | 84.54±1.40 | 0.95±0.01 | 1.02±0.40 | 65.22±7.50 | 0.95±0.03 |

The passive layer of the Al alloys is primarily composed of aluminum oxide ($Al_2O_3$) and aluminum hydroxide $Al(OH)_3$, and is known to be an electrical insulator having a bandgap of 3 eV with a higher charge transfer than the Al matrix [70]. The electrochemical cathodic and anodic reactions occurring on the surface of the L-PBF AlSi10Mg in an aerated and aqueous electrolyte are the reduction of oxygen and oxidation of aluminum, respectively, as follows [71]:

$$2Al+3H_2O \rightarrow Al_2O_3+6H^++6e^- \qquad \text{Eq. (8)}$$

$$O_2+2H_2O+4e^- \rightarrow 4OH^- \qquad \text{Eq. (9)}$$

The dissolved oxygen in the aqueous electrolyte diffuses into the Al alloy-electrolyte interface to initiate the reduction reaction, resulting in producing hydroxide ions (Eq. 9), which in turn participate in the oxidation reaction of Al, causing the formation of aluminum oxide or aluminum hydroxide:

$$Al+3OH^- \rightarrow Al(OH)_3+3e^- \qquad \text{Eq. (10)}$$

$$2Al+6OH^- \rightarrow Al_2O_3+3H_2O+6e^- \qquad \text{Eq. (11)}$$

The formation of aluminum oxide ($Al_2O_3$) or aluminum hydroxide ($Al(OH)_3$) with a higher charge transfer than the substrate Aluminum results in interruption of the anodic reactions by abating the diffusion in the anodic Al part of the alloy [44]. On the other hand, the high level of strains and dynamic recrystallization induced by the FSP process can increase the potential sites for nucleation of the oxide layer [44], and plausibly contribute to the formation of a thicker oxide layer. Table 4 summarizes the oxide film capacitances ($C_{eff}$) calculated from the S-S, H-M, Brug's, and P-L models. The thickness of the steady-state passive/oxide layer ($D_{ox}$) can be determined based on the obtained EIS data and using the plate capacitor relationship [44]:

$$D_{ox} = \frac{\varepsilon \varepsilon_0 A}{C_{eff}} \qquad \text{Eq. (12)}$$

where $\varepsilon$ is the dielectric constant of the passive/oxide layer, assumed to be equal to 8.5 for $Al_2O_3$ [44], $\varepsilon_0$ is the vacuum permittivity ($8.854 \times 10^{-14}$ F cm$^{-1}$), $C_{eff}$ is the pure passive film capacitance, and $A$ is the geometric surface area of the corroded sample.

The calculated thicknesses ($D_{ox}$) of the passive layer for all three samples after different immersion times using three adopted models are also given in Table 4 [72]. The predicted values for the oxide layer thickness using the S-S and H-M models were found to be comparable and in the range of 10.18-10.6 Å for the Side sample, 12.44-12.79 Å for the Top sample, and significantly higher (35.91-37.68 Å) for the SZ sample after 1 h of immersion time. The estimated $D_{ox}$ values from the Brug's model for different samples were almost 1.5-1.7 order of magnitude higher than the predictions from the S-S and H-M models (14.42 Å, 18.61 Å, and 68.13 Å for the Side, Top, and SZ samples, respectively, after 1 h). The P-L model also predicted a similar trend for the oxide layer thickness after 1 h of immersion time (16.64 Å, 23.95 Å, and 81.35 Å for the Side, Top, and SZ samples, respectively). Consistent with the observed trends in the EIS data ($R_p$ and $R_{ct}$ trends), the thickness of the oxide layer was found to reduce at longer immersion times, ascribed to the anodic dissolution of the oxide film into the electrolyte over time.

The aforementioned calculations, regardless of the adopted model, confirm that the FSP-induced microstructural modifications can cause the formation of a thicker passive layer on the L-PBF AlSi10Mg alloy, thereby improving the corrosion performance of the alloy. As reported in a previous study, the increased Si content in the melt pool boundaries of L-PBF AlSi10Mg alloy provokes the formation of a thinner passive/oxide layer along the melt pool boundaries [40]. Furthermore, reducing the thickness of oxide layer after longer immersion time is ascribed to the higher rate of dissolution of the passive layer from the interface of the sample and the electrolyte than the formation rate of the passive layer [73]. Therefore, the EIS results in support of anodic polarization data confirmed that a thicker, more protective, and stable passive layer is formed over the SZ sample, giving rise to its better corrosion performance as compared to the Top and Side samples.

Table 5. 4. The calculated capacitance and the thickness of the oxide layer using S-S, H-M, Brug's, and P-L models.

| | $C_{eff}$ ($\mu F\ cm^{-2}$) | $C_{eff}$ ($\mu F\ cm^{-2}$) | $C_{eff}$ ($\mu F\ cm^{-2}$) | $C_{eff}$ ($\mu F\ cm^{-2}$) | $D_{ox}$ (Å) | $D_{ox}$ (Å) | $D_{ox}$ (Å) | $D_{ox}$ (Å) |
|---|---|---|---|---|---|---|---|---|
| | *S-S* | *H-M* | *Brug* | *P-L* | *S-S* | *H-M* | *Brug* | *P-L* |
| **SZ** | | | | | | | | |
| *1 h* | 5.24±0.50 | 4.99±0.10 | 2.76±0.20 | 2.31±0.30 | 35.91±1.30 | 37.68±2.40 | 68.13±3.20 | 81.35±4.10 |
| *72 h* | 6.67±0.70 | 6.39±0.60 | 4.18±0.30 | 3.46±0.20 | 28.21±2.20 | 29.43±2.00 | 45.04±3.60 | 54.29±3.00 |
| *120 h* | 15.35±0.80 | 14.90±0.80 | 8.12±0.50 | 5.76±0.40 | 12.26±0.90 | 12.63±1.20 | 23.16±2.10 | 32.68±1.20 |
| **Top** | | | | | | | | |
| *1 h* | 15.12±0.50 | 14.72±0.50 | 10.11±0.40 | 7.86±0.30 | 12.44±1.20 | 12.79±1.30 | 18.61±2.20 | 23.95±3.10 |
| *72 h* | 18.75±0.60 | 18.04±1.00 | 16.58±0.60 | 13.51±0.30 | 10.03±0.70 | 10.43±0.80 | 11.35±1.00 | 13.93±2.20 |
| *120 h* | 45.37±0.80 | 41.54±1.90 | 23.16±1.20 | 17.02±1.00 | 4.15±0.20 | 4.53±0.50 | 8.12±0.90 | 11.06±0.80 |
| **Side** | | | | | | | | |
| *1 h* | 18.48±0.70 | 17.75±1.00 | 13.05±0.50 | 11.30±0.70 | 10.18±0.70 | 10.60±1.10 | 14.42±0.90 | 16.64±2.40 |
| *72 h* | 25.45±1.40 | 23.17±1.50 | 14.92±0.50 | 13.22±1.10 | 7.39±0.60 | 8.12±0.70 | 12.61±0.60 | 14.23±1.20 |
| *120 h* | 65.22±1.90 | 59.24±2.00 | 34.68±2.00 | 28.79±1.80 | 2.88±0.40 | 3.18±0.20 | 5.42±0.40 | 6.53±0.60 |

### *3.2.3. The intergranular corrosion*

The intergranular corrosion (IGC) test was carried out to investigate the morphology and severity of the corrosion attacks in the SZ of the FSPed L-PBF-AlSi10Mg sample as compared to the as-printed Top and Side samples. The exposed surfaces of the SZ, Top, and Side samples after the IGC testing are shown in Figure 5.8. The FESEM micrograph in Figure 5.8a exhibits that the non-processed BM (Top sample) is more vulnerable to the pitting corrosion attack than the FSPed side, as evidenced by the noticeably higher number of corrosion pits on the BM side compared to the SZ, which further supports the polarization and EIS results. Interestingly, the FSP had a remarkable impact on the resistance of the L-PBF AlSi10Mg against the intergranular corrosion, and only minor localized IGC attacks was detected in the SZ (see Figure 5.8b), which can be associated with the ultra-fine grain structure and uniform distribution of the Si particles within the α-Al matrix in the SZ of the FSPed sample as opposed to the larger grain size as well as coarser and higher concentration of Si phase precipitated along the melt pool boundaries of the as-printed samples [45]. On the other hand, Figures 5.8c-5.8f revealed that the Top and Side samples behaved differently and showed a selective corrosion attack primarily along the melt pools' boundaries (indicated by the arrows). The selective corrosion attack along the melt pool borders of L-PBF-AlSi10Mg is a common corrosion type that has been reported frequently in other works [3,29]. This is ascribed to the breakage, coarsening, and enrichment of Si particles in the HAZ, causing the increased driving force for micro-galvanic corrosion between the Al matrix as the anodic site and Si particles (the cathodic sites) along the melt pool boundaries. As expected, a more intensive corrosion attack after IGC testing was detected on the Side sample (see Figures 5.8e and 5.8f) due to the accumulation of higher density of the melt pool boundaries on the Side surface relative to that on the Top surface (Figures 5.8c and 5.8d).

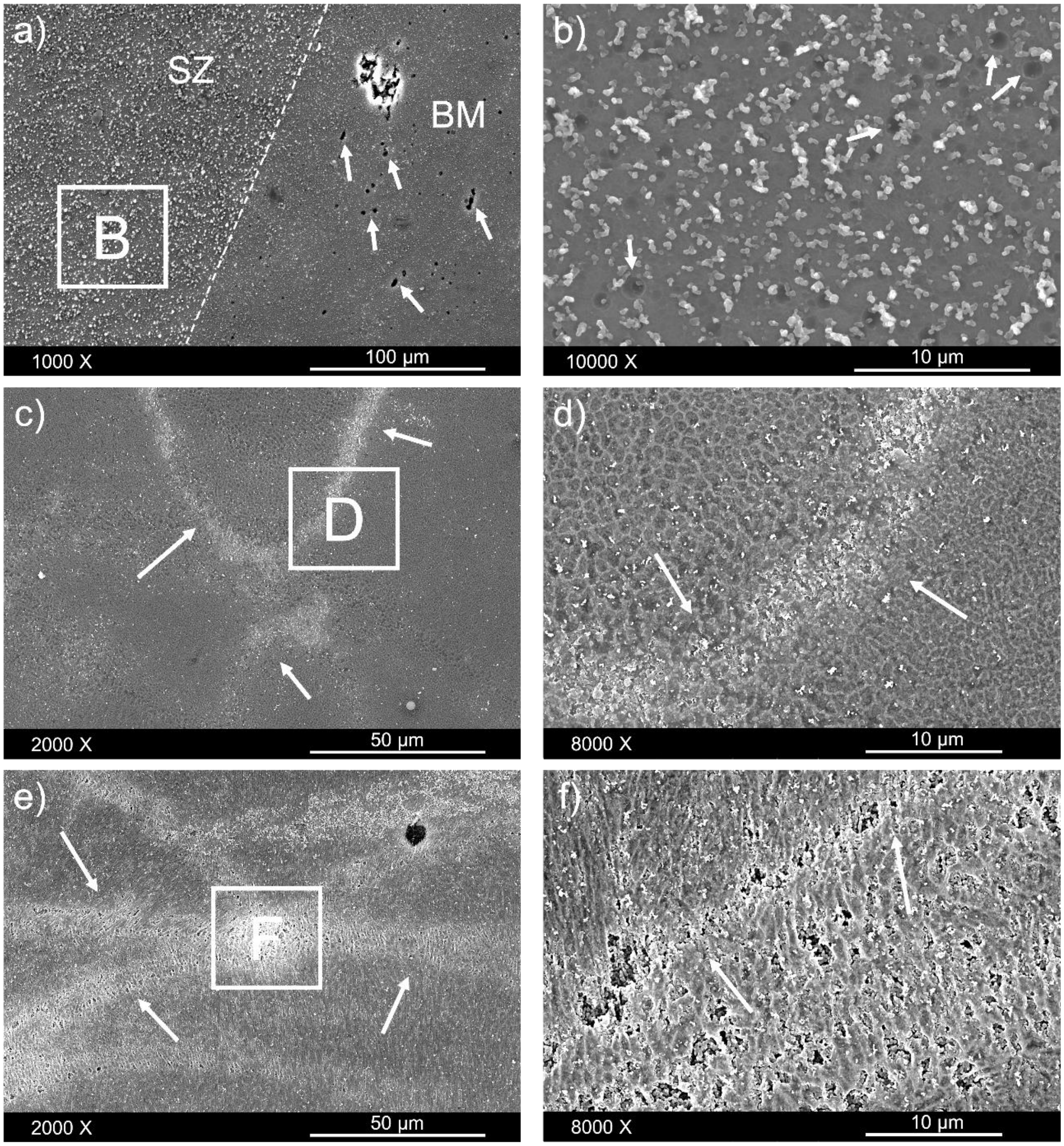

Figure 5. 8. SEM micrographs taken from the L-PBF AlSi10Mg after the intergranular corrosion testing, showing the surface of the a) SZ-BM interface, b) higher magnification of the enclosed area in (a) shown by B, c) Top sample, d) higher magnification of the enclosed area in (c) shown by D, e) Side sample, and f) higher magnification of the enclosed area in (e) shown by F.

### *3.2.4. Mott-Schottky analysis (capacitance measurements)*

The corrosion performance of Al alloys primarily depends on the characteristics of the protective passive layer on their surfaces [74], commonly showing semiconducting properties. In order to describe the semiconducting characteristics of the passive layer formed on different samples herein, Mott–Schottky analysis was performed at 1 kHz and 10 kHz in 3.5 wt.% NaCl electrolyte at room temperature. Figure 5.9a shows the obtained Mott-Schottky plots for the SZ, Top, and Side samples. Using the Mott-Schottky theory, the space charge capacitance of an n-type or p-type semiconductor can be calculated as follows [44]:

$$\frac{1}{C_{SC}^2} = \frac{2}{\varepsilon_r \varepsilon_0 e N_D}\left(E - E_{FB} - \frac{kT}{q}\right) \qquad \text{For an n-type semiconductor} \qquad \text{Eq. (13)}$$

$$\frac{1}{C_{SC}^2} = \frac{-2}{\varepsilon_r \varepsilon_0 e N_A}\left(E - E_{FB} - \frac{kT}{q}\right) \qquad \text{For a p-type semiconductor} \qquad \text{Eq. (14)}$$

where $C_{SC}$ is the space charge capacitance ($F^{-1}$ $cm^2$), $E$ is the applied potential ($V_{Ag/AgCl}$), $N_D$ and $N_A$ are the donor and acceptance density ($cm^{-3}$), respectively, and can be determined from the slope of the linear correlation between $C_{SC}^{-2}$ and $E$ ($slope = \frac{2}{\varepsilon_r \varepsilon_0 e N_D}$), $e$ is the electron charge ($1.602 \times 10^{-19}$ C), $\varepsilon_r$ is the dielectric constant for the passive (oxide) layer ($\varepsilon_r$ =10 for $Al_2O_3$ [44,75]); $\varepsilon_0$ is the vacuum permittivity ($8.854 \times 10^{-14}$ F $cm^{-1}$), $T$ is the absolute temperature, $k$ is Boltzmann's constant ($8.16 \times 10^{-5}$ eV/K), and $E_{FB}$ describes the flat band potential ($V_{Ag/AgCl}$) [44].

The type of the semiconductor (n or p) can be identified based on the negative or positive slope of the Mott-Schottky plots, indicating a p-type or an n-type semiconductor, respectively. As Figure 5.9a shows, all plots obtained at 1 kHz revealed a positive slope, suggesting the formation of a passive layer with n-type semiconducting behavior on all studied samples herein. In other words, in the formed passive layers on all L-PBF AlSi10Mg samples, regardless of the applied post-printing FSP, the interstitials defects and oxygen vacancies dominate over the cation vacancies [75].

Comparing the three samples revealed an increase in the slope of the Mott-Schottky graph from the Side sample to the Top sample, followed by the SZ sample. Figure 5.9b compares the calculated donor density of the passive films that formed on the SZ, Top, and Side samples in 3.5 wt.% NaCl solution. Considering the point defect model (PDM), the flux of oxygen vacancies and the interstitial defects (as determined by their density and diffusivity) within the passive film is a key factor that controls the kinetics of the passive film growth and its breakdown [44]. Furthermore, the adsorption and penetration of corrosive species, such as chloride ions, inside the passive layer, which is generally the initial step to pitting corrosion attack, is done through the oxygen vacancies that serve as a donor site of the electrons [75]. Therefore, a lower pitting resistance (lower breakdown potential) can be associated with the higher donor density of the passive layer.

The measured donor density values at 1 kHz were found to increase from the SZ sample to the Top and then the Side samples ($-2.03\times10^{20}$ $cm^{-3}$, $-5.1\times10^{20}$ $cm^{-3}$, and $-7.20\times10^{20}$ $cm^{-3}$, respectively), ascribed to the reduced microstructural homogeneity and increased grain size in the alloy. This can result in decreasing the resistance of the Side sample to the pitting corrosion, as evidenced by the lowest pitting potential for this sample in the anodic polarization results (Figure 5.6b).

The Mott–Schottky graphs obtained at 10 kHz (Figure 5.9c) presented a similar trend to those measured at 1 kHz, revealing an n-type semiconductor characteristic with a linear behavior for $C_{SC}^{-2}$ versus the potential with a positive slope, inversely proportional to the donors' concentration. At the higher frequency of 10 kHz, although the range of linear relationship between $C_{SC}^{-2}$ and potential is maintained, the graphs were found to be more inclined. Therefore, the n-type-semiconducting nature of the passive film has not been altered by changing the frequency. However, increasing the frequency at which the measurements were performed, resulted in an increase in the value of derivative $dC_{SC}^{-2}/dE$ measured in the linear range.

Figure 5.9d also compares the calculated donor density of the passive films that formed on the SZ, Top, and Side samples at 10 kHz. Albeit the donor density values were found to decrease by increasing the frequency from 1 kHz to 10 kHz for the SZ, Top, and Side samples ($-6.59\times10^{19}$ $cm^{-3}$, $-1.99\times10^{20}$ $cm^{-3}$, and $-3.79\times10^{20}$ $cm^{-3}$, respectively), an analogous trend between the frequencies were detected, revealing the lowest and the highest donor density values for the SZ and the Side samples, respectively.

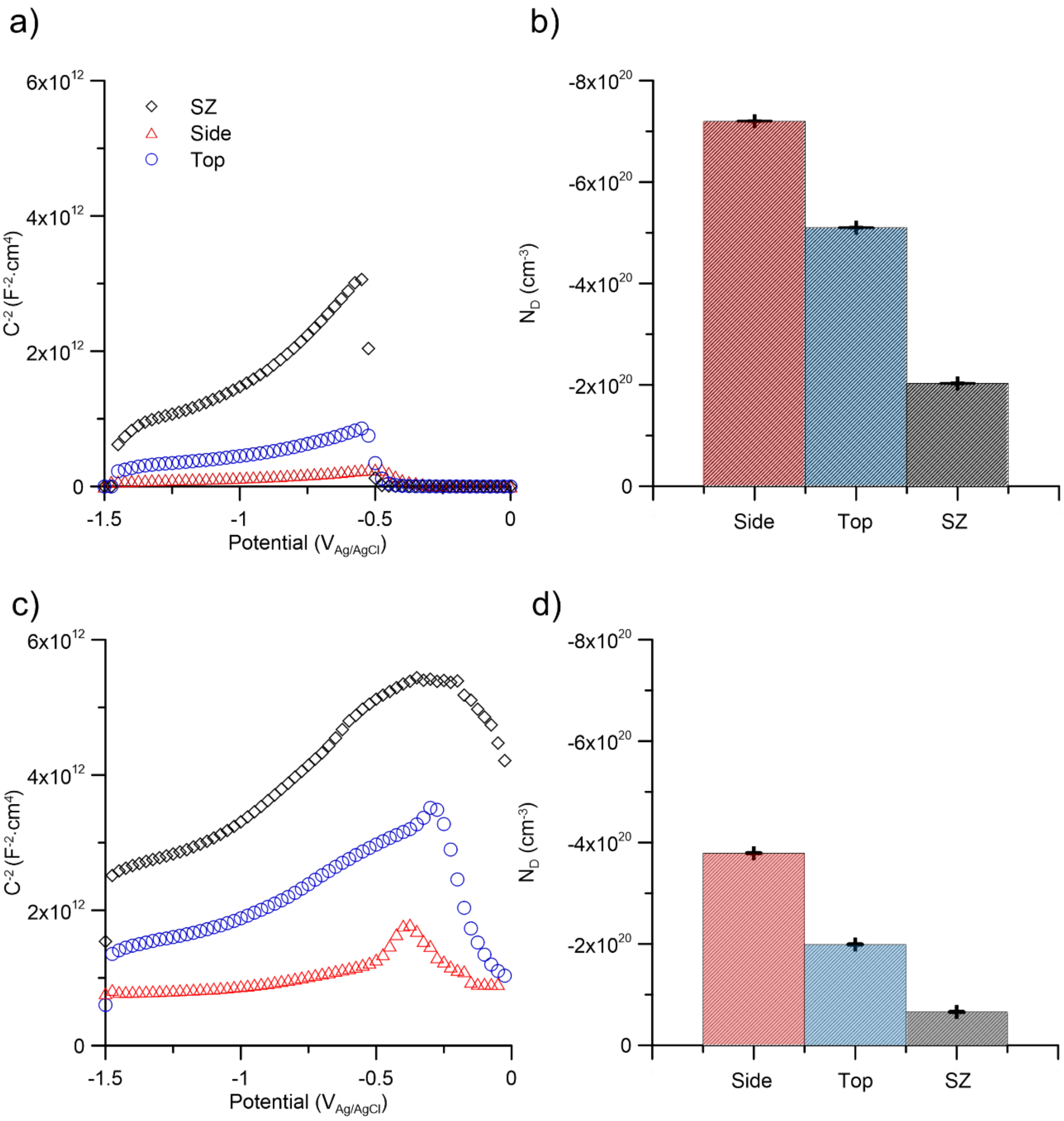

Figure 5. 9. Mott-Schottky plots and the variations of the donor density of the passive layer formed on the L-PBF AlSi10Mg alloy samples, *i.e*. the Side, Top, and SZ samples measured at the frequency of (a) and (b) 1 kHz, (c) and (d) 10 kHz.

Therefore, the non-uniformity and coarsening/enrichment of the Si phase along the melt pool boundaries of the as-printed L-AlSi10Mg sample diminish the tendency toward the formation of a slightly thicker passive/oxide layer on the sample. In a similar observation, Revilla *et al.* [40]

reported the adverse effect of the melt pool boundaries on the uniformity of the formed anodic oxide film in as-printed L-PBF-AlSi10Mg alloy. A thinner oxide layer was reported to form locally along the melt pool boundaries as compared with the center of the melt pools [40]. On the other hand, the SZ sample behaved differently and showed the lowest donor density, attributed to the microstructural uniformity of the L-PBF-AlSi10Mg sample after the FSP, characterized by the uniform distribution of the Si particles embedded in an Al matrix with an ultrafine grain structure containing a low density of LAGBs, and reduced porosity level.

## Conclusions

In this study, the impact of friction stir processing on the microstructure and the electrochemical stability of the L-PBF AlSi10Mg in aerated 3.5 wt. % NaCl electrolyte was studied. The following conclusions were drawn:

1. Applying FSP can effectively eliminate the process-induced porosities of the L-PBF AlSi10Mg alloy and result in drastic microstructural homogenization, grain refinement, and uniform dispersion of refined Si particles.
2. The FSP-induced microstructural modifications in L-PBF AlSi10Mg alloy were found to promote the formation of the significantly more stable, denser, and thicker passive layer on the alloy as compared to the as-printed condition.
3. Improvement of the corrosion performance of the FSPed sample was confirmed by the positive shift of the pitting potential and reduction in the corrosion rate and corrosion current density as compared to the as-printed samples.

4. The EIS results showed a higher passive layer resistance and charge transfer resistance for the FSPed alloy than those in the as-printed L-PBF AlSi10Mg. The calculated passive layer thickness on the FSPed region was almost three times higher than that on the as-printed Top and Side samples at different immersion times.
5. The intergranular corrosion testing revealed preferential selective attack primarily around the melt pool boundaries of the as-printed L-PBF-AlSi10Mg alloy, whilst only minor localized attack occurred in the SZ.
6. Although applying the FSP did not change the semiconducting nature of the passive layer on L-PBF AlSi10Mg (all passive layers revealed an n-type semiconducting response), the donor density of the passive layer was found to decrease after the FSP, leading to its improved resistance to pit initiation.
7. An anisotropic corrosion response was detected for the as-printed L-PBF AlSi10Mg, indicated by a higher pitting potential and lower corrosion current density for the top view sample (perpendicular to the building direction) as compared to the side view sample (parallel to the building direction), ascribed to the lower density of the melt pool boundaries formed on the top *vs* the side surface.

## Acknowledgment

The authors wish to acknowledge the support of Natural Sciences and Engineering Research Council of Canada (NSERC) [grant number RGPIN-2017-04368], Memorial University of Newfoundland, and Dalhousie University for sponsoring this work.

# References

[1] F. Robles-Hernández, J. Herrera Ramirez, R. Mackay, Al-Si Alloys: Automotive, Aeronautical, and Aerospace Applications, in: 2017: pp. E1–E1. doi:10.1007/978-3-319-58380-8_10.

[2] B.A. Fulcher, D.K. Leigh, T.J. Watt, Comparison of AlSi10Mg and Al 6061 processed through DMLS, in: Proc. Solid Free. Fabr. Symp. Austin, TX, USA, 2014.

[3] M. Rafieazad, M. Mohammadi, A. Nasiri, On Microstructure and Early Stage Corrosion Performance of Heat Treated Direct Metal Laser Sintered AlSi10Mg, Addit. Manuf. 28 (2019) 107–119.

[4] P. Fathi, M. Mohammadi, X. Duan, A.M. Nasiri, A Comparative Study on Corrosion and Microstructure of Direct Metal Laser Sintered AlSi10Mg_200C and Die Cast A360.1 Aluminum, J. Mater. Process. Technol. 259 (2018) 1–14. doi:https://doi.org/10.1016/j.jmatprotec.2018.04.013.

[5] S. Marola, D. Manfredi, G. Fiore, M.G. Poletti, M. Lombardi, P. Fino, L. Battezzati, A comparison of Selective Laser Melting with bulk rapid solidification of AlSi10Mg alloy, J. Alloys Compd. 742 (2018) 271–279.

[6] L. Thijs, K. Kempen, J. Kruth, J. V. Humbeeck, Fine-structured aluminium products with controllable texture by selective laser melting of pre-alloyed AlSi10Mg powder, Acta Mater. 61 (2013) 1809–1819. doi:https://doi.org/10.1016/j.actamat.2012.11.052.

[7] P. Fathi, M. Rafieazad, X. Duan, M. Mohammadi, A. Nasiri, On Microstructure and Corrosion Behaviour of AlSi10Mg Alloy with Low Surface Roughness Fabricated by Direct Metal Laser Sintering, Corros. Sci. 157 (2019) 126–145.

[8] T. Ishimoto, K. Hagihara, K. Hisamoto, S.-H. Sun, T. Nakano, Crystallographic texture control of beta-type Ti–15Mo–5Zr–3Al alloy by selective laser melting for the development of novel implants with a biocompatible low Young's modulus, Scr. Mater. 132 (2017) 34–38. doi:https://doi.org/10.1016/j.scriptamat.2016.12.038.

[9] H. Attar, S. Ehtemam-Haghighi, D. Kent, X. Wu, M.S. Dargusch, Comparative study of commercially pure titanium produced by laser engineered net shaping, selective laser melting and casting processes, Mater. Sci. Eng. A. 705 (2017) 385–393. doi:https://doi.org/10.1016/j.msea.2017.08.103.

[10] O. Scott-Emuakpor, J. Schwartz, T. George, C. Holycross, C. Cross, J. Slater, Bending fatigue life characterisation of direct metal laser sintering nickel alloy 718, Fatigue Fract. Eng. Mater. Struct. 38 (2015) 1105–1117. doi:10.1111/ffe.12286.

[11] S. Saedi, N.S. Moghaddam, A. Amerinatanzi, M. Elahinia, H.E. Karaca, On the effects of selective laser melting process parameters on microstructure and thermomechanical response of Ni-rich NiTi, Acta Mater. 144 (2018) 552–560. doi:https://doi.org/10.1016/j.actamat.2017.10.072.

[12] E.E. Covarrubias, M. Eshraghi, Effect of Build Angle on Surface Properties of Nickel Superalloys Processed by Selective Laser Melting, JOM. 70 (2018) 336–342. doi:10.1007/s11837-017-2706-y.

[13] T.-T. Ikeshoji, K. Nakamura, M. Yonehara, K. Imai, H. Kyogoku, Selective Laser Melting of Pure Copper, JOM. 70 (2018) 396–400. doi:10.1007/s11837-017-2695-x.

[14] A.P. Ventura, C.A. Wade, G. Pawlikowski, M. Bayes, M. Watanabe, W.Z. Misiolek, Mechanical Properties and Microstructural Characterization of Cu-4.3 Pct Sn Fabricated by Selective Laser Melting, Metall. Mater. Trans. A. 48 (2017) 178–187. doi:10.1007/s11661-

016-3779-x.

[15] D.S. D'Antuono, J. Gaies, W. Golumbfskie, M.L. Taheri, Grain boundary misorientation dependence of β phase precipitation in an Al–Mg alloy, Scr. Mater. 76 (2014) 81–84. doi:https://doi.org/10.1016/j.scriptamat.2014.01.003.

[16] M. Ghaffari, A. Vahedi Nemani, M. Rafieazad, A. Nasiri, Effect of Solidification Defects and HAZ Softening on the Anisotropic Mechanical Properties of a Wire Arc Additive-Manufactured Low-Carbon Low-Alloy Steel Part, JOM. 71 (2019) 4215–4224. doi:10.1007/s11837-019-03773-5.

[17] M. Rafieazad, M. Ghaffari, A. Vahedi Nemani, A. Nasiri, Microstructural evolution and mechanical properties of a low-carbon low-alloy steel produced by wire arc additive manufacturing, Int. J. Adv. Manuf. Technol. (2019) 1–14. doi:10.1007/s00170-019-04393-8.

[18] M. Kazemipour, M. Mohammadi, E. Mfoumou, A.M. Nasiri, Microstructure and Corrosion Characteristics of Selective Laser-Melted 316L Stainless Steel: The Impact of Process-Induced Porosities, JOM. 71 (2019) 3230–3240. doi:10.1007/s11837-019-03647-w.

[19] S. Shakerin, A. Hadadzadeh, B.S. Amirkhiz, S. Shamsdini, J. Li, M. Mohammadi, Additive manufacturing of maraging steel-H13 bimetals using laser powder bed fusion technique, Addit. Manuf. 29 (2019) 100797. doi:https://doi.org/10.1016/j.addma.2019.100797.

[20] P. Fathi, M. Mohammadi, X. Duan, A. Nasiri, Effects of Surface Finishing Procedures on Corrosion Behavior of DMLS-AlSi10Mg_200C Alloy Versus Die-Cast A360.1 Aluminum, JOM. (2019) 1–12. doi:10.1007/s11837-019-03344-8.

[21] M. Rafieazad, A. Chatterjee, A.M. Nasiri, Effects of Recycled Powder on Solidification Defects, Microstructure, and Corrosion Properties of DMLS Fabricated AlSi10Mg, JOM. 71 (2019) 3241–3252. doi:10.1007/s11837-019-03552-2.

[22] M. Shiomi, K. Osakada, K. Nakamura, T. Yamashita, F. Abe, Residual Stress within Metallic Model Made by Selective Laser Melting Process, CIRP Ann. 53 (2004) 195–198. doi:https://doi.org/10.1016/S0007-8506(07)60677-5.

[23] B.A. Szost, S. Terzi, F. Martina, D. Boisselier, A. Prytuliak, T. Pirling, M. Hofmann, D.J. Jarvis, A comparative study of additive manufacturing techniques: Residual stress and microstructural analysis of CLAD and WAAM printed Ti-6Al-4V components, Mater. Des. 89 (2016) 559–567. doi:10.1016/j.matdes.2015.09.115.

[24] H. Asgari, C. Baxter, K. Hosseinkhani, M. Mohammadi, On microstructure and mechanical properties of additively manufactured AlSi10Mg_200C using recycled powder, Mater. Sci. Eng. A. 707 (2017) 148–158. doi:10.1016/J.MSEA.2017.09.041.

[25] M. Mohammadi, H. Asgari, Achieving low surface roughness AlSi10Mg_200C parts using direct metal laser sintering, Addit. Manuf. 20 (2018) 23–32. doi:https://doi.org/10.1016/j.addma.2017.12.012.

[26] L. Zhou, A. Mehta, E. Schulz, B. McWilliams, K. Cho, Y. Sohn, Microstructure, precipitates and hardness of selectively laser melted AlSi10Mg alloy before and after heat treatment, Mater. Charact. (2018). doi:https://doi.org/10.1016/j.matchar.2018.04.022.

[27] N.T. Aboulkhair, C. Tuck, I. Ashcroft, I. Maskery, N. Everitt, On the Precipitation Hardening of Selective Laser Melted AlSi10Mg, Metall. Mater. Trans. A. 46 (2015) 3337–3341. doi:10.1007/s11661-015-2980-7.

[28] P. Ma, K.G. Prashanth, S. Scudino, Y. Jia, H. Wang, C. Zou, Z. Wei, J. Eckert, Influence of Annealing on Mechanical Properties of Al-20Si Processed by Selective Laser Melting, Metals (Basel). 4 (2014) 28–36. doi:10.3390/met4010028.

[29] M. Cabrini, F. Calignano, P. Fino, S. Lorenzi, M. Lorusso, D. Manfredi, C. Testa, T. Pastore, Corrosion Behavior of Heat-Treated AlSi10Mg Manufactured by Laser Powder Bed Fusion, Materials (Basel). 11 (2018). doi:10.3390/ma11071051.

[30] M. Cabrini, S. Lorenzi, T. Pastore, S. Pellegrini, E.P. Ambrosio, F. Calignano, D. Manfredi, M. Pavese, P. Fino, Effect of heat treatment on corrosion resistance of DMLS AlSi10Mg alloy, Electrochim. Acta. 206 (2016) 346–355. doi:https://doi.org/10.1016/j.electacta.2016.04.157.

[31] T. Rubben, R.I. Revilla, I. De Graeve, Influence of heat treatments on the corrosion mechanism of additive manufactured AlSi10Mg, Corros. Sci. (2018). doi:https://doi.org/10.1016/j.corsci.2018.11.038.

[32] A. Hadadzadeh, C. Baxter, B.S. Amirkhiz, M. Mohammadi, Strengthening mechanisms in direct metal laser sintered AlSi10Mg: Comparison between virgin and recycled powders, Addit. Manuf. 23 (2018) 108–120. doi:https://doi.org/10.1016/j.addma.2018.07.014.

[33] A.H. Maamoun, M. Elbestawi, G.K. Dosbaeva, S.C. Veldhuis, Thermal post-processing of AlSi10Mg parts produced by Selective Laser Melting using recycled powder, Addit. Manuf. 21 (2018) 234–247. doi:https://doi.org/10.1016/j.addma.2018.03.014.

[34] F. Calignano, D. Manfredi, E.P. Ambrosio, L. Iuliano, P. Fino, Influence of process parameters on surface roughness of aluminum parts produced by DMLS, Int. J. Adv. Manuf. Technol. 67 (2013) 2743–2751. doi:10.1007/s00170-012-4688-9.

[35] M. Krishnan, E. Atzeni, R. Canali, F. Calignano, D. Manfredi, E.P. Ambrosio, L. Iuliano, On the effect of process parameters on properties of AlSi10Mg parts produced by DMLS, Rapid Prototyp. J. 20 (2014) 449–458. doi:10.1108/RPJ-03-2013-0028.

[36] T. Rubben, R.I. Revilla, I. De Graeve, Effect of Heat Treatments on the Anodizing Behavior of Additive Manufactured AlSi10Mg, J. Electrochem. Soc. 166 (2019) C42--C48.

[37] Z.Y. Ma, S.R. Sharma, R.S. Mishra, Microstructural modification of as-cast Al-Si-Mg alloy by friction stir processing, Metall. Mater. Trans. A. 37 (2006) 3323–3336. doi:10.1007/BF02586167.

[38] T. Hirata, T. Kimura, T. Nakamoto, Effects of hot isostatic pressing and internal porosity on the performance of selective laser melted AlSi10Mg alloys, Mater. Sci. Eng. A. (2019) 138713. doi:https://doi.org/10.1016/j.msea.2019.138713.

[39] U. Tradowsky, J. White, R.M. Ward, N. Read, W. Reimers, M.M. Attallah, Selective laser melting of AlSi10Mg: Influence of post-processing on the microstructural and tensile properties development, Mater. Des. 105 (2016) 212–222. doi:https://doi.org/10.1016/j.matdes.2016.05.066.

[40] R.I. Revilla, Y. Rojas, I. De Graeve, On the Impact of Si Content and Porosity Artifacts on the Anodizing Behavior of Additive Manufactured Al-Si Alloys, J. Electrochem. Soc. . 166 (2019) C530–C537. http://jes.ecsdl.org/content/166/14/C530.abstract.

[41] T. Yang, K. Wang, W. Wang, P. Peng, L. Huang, K. Qiao, Y. Jin, Effect of Friction Stir Processing on Microstructure and Mechanical Properties of AlSi10Mg Aluminum Alloy Produced by Selective Laser Melting, JOM. 71 (2019). doi:10.1007/s11837-019-03343-9.

[42] J.G.S. Macías, C. Elangeswaran, L. Zhao, B. Van Hooreweder, J. Adrien, E. Maire, J.-Y. Buffière, W. Ludwig, P.J. Jacques, A. Simar, Ductilisation and fatigue life enhancement of selective laser melted AlSi10Mg by friction stir processing, Scr. Mater. 170 (2019) 124–128. doi:https://doi.org/10.1016/j.scriptamat.2019.05.044.

[43] A.H. Maamoun, S.C. Veldhuis, M. Elbestawi, Friction stir processing of AlSi10Mg parts produced by selective laser melting, J. Mater. Process. Technol. 263 (2019) 308–320.

doi:https://doi.org/10.1016/j.jmatprotec.2018.08.030.

[44] A.G. Rao, V.A. Katkar, G. Gunasekaran, V.P. Deshmukh, N. Prabhu, B.P. Kashyap, Effect of multipass friction stir processing on corrosion resistance of hypereutectic Al–30Si alloy, Corros. Sci. 83 (2014) 198–208. doi:https://doi.org/10.1016/j.corsci.2014.02.013.

[45] A.S. El-Amoush, Intergranular corrosion behavior of the 7075-T6 aluminum alloy under different annealing conditions, Mater. Chem. Phys. 126 (2011) 607–613. doi:https://doi.org/10.1016/j.matchemphys.2011.01.010.

[46] J.J. Pang, F.C. Liu, J. Liu, M.J. Tan, D.J. Blackwood, Friction stir processing of aluminium alloy AA7075: Microstructure, surface chemistry and corrosion resistance, Corros. Sci. 106 (2016) 217–228. doi:https://doi.org/10.1016/j.corsci.2016.02.006.

[47] A. Hadadzadeh, B. Shalchi Amirkhiz, S. Shakerin, J. Kelly, J. Li, M. Mohammadi, Microstructural investigation and mechanical behavior of a two-material component fabricated through selective laser melting of AlSi10Mg on an Al-Cu-Ni-Fe-Mg cast alloy substrate, (2019) 100937. doi:10.1016/j.addma.2019.100937.

[48] T.M. Moore, The Total Release Method for FIB In-Situ TEM Sample Preparation, Micros. Today. 13 (2005) 40–43. doi:10.1017/S1551929500053657.

[49] A.S. Materials, ASTM G5-14: Standard Reference Test Method for Making Potentiodynamic Anodic Polarization Measurements, ASTM, 2014. https://books.google.ca/books?id=tWpcswEACAAJ.

[50] M. Cornejo, T. Hentschel, D. Koschel, C. Matthies, L. Peguet, M. Rosefort, C. Schnatterer, E. Szala, D. Zander, Intergranular corrosion testing of 6000 aluminum alloys, Mater. Corros. 69 (2018) 626–633. doi:10.1002/maco.201709813.

[51] K.D. Ralston, N. Birbilis, C.H.J. Davies, Revealing the relationship between grain size and corrosion rate of metals, Scr. Mater. 63 (2010) 1201–1204. doi:https://doi.org/10.1016/j.scriptamat.2010.08.035.

[52] F.J. Humphreys, M. Hatherly, Chapter 15 - Control of Recrystallization, in: F.J. Humphreys, M. Hatherly (Eds.), Recryst. Relat. Annealing Phenom. (Second Ed., Second Edi, Elsevier, Oxford, 2004: pp. 469–505. doi:https://doi.org/10.1016/B978-008044164-1/50019-0.

[53] A. Hadadzadeh, B.S. Amirkhiz, J. Li, M. Mohammadi, Columnar to equiaxed transition during direct metal laser sintering of AlSi10Mg alloy: Effect of building direction, Addit. Manuf. 23 (2018) 121–131. doi:https://doi.org/10.1016/j.addma.2018.08.001.

[54] A. Hadadzadeh, B.S. Amirkhiz, A. Odeshi, J. Li, M. Mohammadi, Role of hierarchical microstructure of additively manufactured AlSi10Mg on dynamic loading behavior, Addit. Manuf. 28 (2019) 1–13. doi:https://doi.org/10.1016/j.addma.2019.04.012.

[55] A. Momeni, G.R. Ebrahimi, M. Jahazi, P. Bocher, Microstructure evolution at the onset of discontinuous dynamic recrystallization: A physics-based model of subgrain critical size, J. Alloys Compd. 587 (2014) 199–210. doi:https://doi.org/10.1016/j.jallcom.2013.10.180.

[56] R.I. Revilla, J. Liang, S. Godet, I. De Graeve, Local Corrosion Behavior of Additive Manufactured AlSiMg Alloy Assessed by SEM and SKPFM, J. Electrochem. Soc. . 164 (2017) C27–C35. doi:10.1149/2.0461702jes.

[57] M. Cabrini, S. Lorenzi, T. Pastore, S. Pellegrini, D. Manfredi, P. Fino, S. Biamino, C. Badini, Evaluation of corrosion resistance of Al–10Si–Mg alloy obtained by means of Direct Metal Laser Sintering, J. Mater. Process. Technol. 231 (2016) 326–335. doi:https://doi.org/10.1016/j.jmatprotec.2015.12.033.

[58] D. Song, A. Ma, J. Jiang, P. Lin, D. Yang, J. Fan, Corrosion behavior of equal-channel-angular-pressed pure magnesium in NaCl aqueous solution, Corros. Sci. 52 (2010) 481–

490. doi:https://doi.org/10.1016/j.corsci.2009.10.004.

[59] N. Birbilis, K.D. Ralston, S. Virtanen, H.L. Fraser, C.H.J. Davies, Grain character influences on corrosion of ECAPed pure magnesium, Corros. Eng. Sci. Technol. 45 (2010) 224–230. doi:10.1179/147842209X12559428167805.

[60] C. op't Hoog, N. Birbilis, Y. Estrin, Corrosion of Pure Mg as a Function of Grain Size and Processing Route, Adv. Eng. Mater. 10 (2008) 579–582. doi:10.1002/adem.200800046.

[61] S. Lee, H.S. White, Dissolution of the Native Oxide Film on Polycrystalline and Single-Crystal Aluminum in NaCl Solutions, J. Electrochem. Soc. . 151 (2004) B479–B483. http://jes.ecsdl.org/content/151/8/B479.abstract.

[62] G.R. Argade, S.K. Panigrahi, R.S. Mishra, Effects of grain size on the corrosion resistance of wrought magnesium alloys containing neodymium, Corros. Sci. 58 (2012) 145–151. doi:https://doi.org/10.1016/j.corsci.2012.01.021.

[63] A. Balyanov, J. Kutnyakova, N.A. Amirkhanova, V. V Stolyarov, R.Z. Valiev, X.Z. Liao, Y.H. Zhao, Y.B. Jiang, H.F. Xu, T.C. Lowe, Y.T. Zhu, Corrosion resistance of ultra fine-grained Ti, Scr. Mater. 51 (2004) 225–229. doi:https://doi.org/10.1016/j.scriptamat.2004.04.011.

[64] M.E. Orazem, I. Frateur, B. Tribollet, V. Vivier, S. Marcelin, N. Pébère, A.L. Bunge, E.A. White, D.P. Riemer, M. Musiani, Dielectric Properties of Materials Showing Constant-Phase-Element (CPE) Impedance Response, J. Electrochem. Soc. 160 (2013) C215--C225. doi:10.1149/2.033306jes.

[65] B. Hirschorn, M.E. Orazem, B. Tribollet, V. Vivier, I. Frateur, M. Musiani, Determination of effective capacitance and film thickness from constant-phase-element parameters, Electrochim. Acta. 55 (2010) 6218–6227. doi:https://doi.org/10.1016/j.electacta.2009.10.065.

[66] C.H. Hsu, F. Mansfeld, Technical Note: Concerning the Conversion of the Constant Phase Element Parameter Y0 into a Capacitance, CORROSION. 57 (2001) 747–748. doi:10.5006/1.3280607.

[67] G.J. Brug, A.L.G. [van den Eeden], M. Sluyters-Rehbach, J.H. Sluyters, The analysis of electrode impedances complicated by the presence of a constant phase element, J. Electroanal. Chem. Interfacial Electrochem. 176 (1984) 275–295. doi:https://doi.org/10.1016/S0022-0728(84)80324-1.

[68] L. Hamadou, L. Aïnouche, A. Kadri, S.A.A. Yahia, N. Benbrahim, Electrochemical impedance spectroscopy study of thermally grown oxides exhibiting constant phase element behaviour, Electrochim. Acta. 113 (2013) 99–108. doi:https://doi.org/10.1016/j.electacta.2013.09.054.

[69] B. Hirschorn, M.E. Orazem, B. Tribollet, V. Vivier, I. Frateur, M. Musiani, Constant-Phase-Element Behavior Caused by Resistivity Distributions in Films, J. Electrochem. Soc. 157 (2010) C452. doi:10.1149/1.3499564.

[70] A.B.M. [Mujibur Rahman, S. Kumar, A.R. Gerson, The speciation of Si and other alloying elements in the oxide surface film of galvanically corroded weld fusion zone of laser welded AA6061 aluminium alloy, Corros. Sci. 50 (2008) 1267–1273. doi:https://doi.org/10.1016/j.corsci.2007.11.035.

[71] M. Digne, P. Sautet, P. Raybaud, H. Toulhoat, E. Artacho, Structure and Stability of Aluminum Hydroxides: A Theoretical Study, J. Phys. Chem. B. 106 (2002) 5155–5162. doi:10.1021/jp014182a.

[72] D. [de la Fuente], E. Otero-Huerta, M. Morcillo, Studies of long-term weathering of

aluminium in the atmosphere, Corros. Sci. 49 (2007) 3134–3148. doi:https://doi.org/10.1016/j.corsci.2007.01.006.

[73] R.D. Armstrong, K. Edmondson, The impedance of metals in the passive and transpassive regions, Electrochim. Acta. 18 (1973) 937–943. doi:https://doi.org/10.1016/0013-4686(73)87025-2.

[74] Z. Szklarska-Smialowska, Mechanism of pit nucleation by electrical breakdown of the passive film, Corros. Sci. 44 (2002) 1143–1149. doi:https://doi.org/10.1016/S0010-938X(01)00113-5.

[75] S. Gashti, A. Fattah-alhosseini, Effect of Chloride Ions Concentration on the Semiconducting Behaviors of 1050 and 6061 Al Alloys, Anal. Bioanal. Electrochem. 6 (2014) 535–544.

# Chapter 6

# Summary, Recommendations, and Future works

## 6.1. Summary

In this thesis, the feasibility of the four objectives of post-printing heat-treatment, using different size and morphology of the feedstock powder, optimization of the process parameters, and post-printing surface treatment, as solutions for the elimination of the process-induced imperfection of L-PBF AlSi10Mg alloy was investigated.

First of all, the impacts of post-printing heat-treatment on microstructural modification, mechanical properties, and corrosion performance of L-PBF AlSi10Mg were studied. Microstructural characterization results revealed that an increase in the heat-treatment temperature from 200 °C to 350 °C promotes the interruption of the intercellular Si network. Moreover, increasing the heat-treatment temperature contributes to the microstructural uniformity in terms of the Si phase's size and distribution in the α-Aluminum matrix. The electrochemical analysis confirmed the improved corrosion performance of the heat-treated samples in the range of 200 °C to 300 °C, by decreasing susceptibility to penetrating selective attack at early-stage immersion time in the electrolyte.

Secondly, the impacts of adopting AlSi10Mg recycled powder with different size and morphology on the final microstructure, and corrosion properties of the L-PBF-AlSi10Mg sample were studied. Microstructural analysis results confirmed that using larger size and irregular shape of the feedstock powders results in a reduced thermal conductivity between the powders and consequently decreased the cooling rate during fabrication. This can lead to the formation of a higher level of internal defects and discontinuities, and coarsening of the Si-network phase within the final microstructure. The electrochemical measurements showed that the Si network coarsening along the melt pool boundaries deteriorated the corrosion performance of the L-PBF AlSi10Mg sample.

Thirdly, the effects of L-PBF process parameters on the microstructure and the resultant corrosion properties of the L-PBF AlSi10Mg were studied. Microstructural characterization confirmed that the sample that underwent the fastest cooling rate during the solidification revealed a finer eutectic Si phase with a more uniform grain distribution. Such L-PBF-induced microstructural modifications led to the improved corrosion properties and electrochemical stability of the sample, which experienced a faster cooling/solidification rate, attributed to the reduced driving force for galvanic corrosion between Al and Si phases due to the formation of a finer Al-Si eutectic structure along its large melt pools boundaries.

Finally, the effect of FSP on the microstructural characteristics and the corrosion properties of the L-PBF AlSi10Mg was investigated. Microstructure characterization results showed that the implementation of FSP could eliminate the internal porosities of the L-PBF AlSi10Mg alloy. Moreover, the final microstructure was significantly more homogenous with a fine grain structure and uniform distribution of the Si particles. The electrochemical stability of the FSPed sample was confirmed by the formation of the denser and thicker oxide layer on its surface compared to the as-printed condition. Moreover, reduction in the corrosion current density and the positive shift of the pitting potential compared to the as-printed samples further prove for improvement of the corrosion properties after applying FSP.

## 6.2. Recommendation and future works

The following topics are suggested for future research:

I. The addition of nano-particles as inoculants to the feedstock metal powder has been recently introduced as a new approach towards refining the grain structure and enhancing the microstructural uniformity throughout the AM fabricated parts. Therefore, the impact of the addition of the grain refiners to the feedstock materials on the final microstructure and corrosion performance of the Al alloys is a subject for future study.

II. In this thesis, FSP is introduced as an effective post-printing process capable of grain refinement of the L-PBF-AlSi10Mg alloy. On the other hand, the addition of TiB2 as a strong grain refiner to Al alloys is highly effective in creating an equiaxed and uniform microstructure. Therefore, comparing these two techniques in the grain refinement and resultant performance is a subject of future study.

III. The joining of the dissimilar Al alloys is a challenging concept for many industrial applications. L-PBF technique is capable of the fabrication of the dissimilar Al alloys. However, the interface of the dissimilar sample is susceptible to micro-galvanic corrosion. Therefore, the feasibility of the dissimilar fabrication of the Al alloys using L-PBF and evaluating its electrochemical performance, particularly in the interface, demands extensive research for future study.

# Appendix I

# Microstructural Evolution and Mechanical Properties of a Low Carbon Low Alloy Steel Produced by Wire Arc Additive Manufacturing [8]

## Preface

A version of this manuscript has been published in the International Journal of Advanced Manufacturing Technology. I am the first and corresponding author of the papers. Along with the co-authors, Mahya Ghaffari, Alireza Vahedi Nemani, and Dr. Ali Nasiri, I investigate ER70S-6 low-carbon low-alloy steel thin wall that was manufactured by WAAM method, utilizing a gas metal arc welding (GMAW) torch translated by a six-axis robotic arm. The microstructural evolution and mechanical properties of the fabricated part were investigated. I prepared methodology, experimental, formal analysis, and the first original draft of the manuscript and subsequently revised the manuscript based on the coauthors' feedback and also the peer review process. The co-authors, Mahya Ghaffari and Alireza Vahedi Nemani helped in the experimental procedure and writing the initial draft. Moreover, Dr. Ali Nasiri helped in conceptualization, design, project administration, and supervision, review & editing of the manuscript.

---

[8] M. Rafieazad, M. Ghaffari, A. Vahedi Nemani, A. Nasiri, Microstructural evolution and mechanical properties of a low-carbon low-alloy steel produced by wire arc additive manufacturing, Int. J. Adv. Manuf. Technol. (2019) 1–14. doi:10.1007/s00170-019-04393-8.(IPF=2.633)

## Abstract

The emerging technology of wire arc additive manufacturing (WAAM) has been enthusiastically embraced in recent years mainly by the welding community to fabricate various grades of structural materials. In this study, ER70S-6 low-carbon-low-alloy steel wall was manufactured by WAAM method, utilizing a gas metal arc welding (GMAW) torch translated by a six-axis robotic arm, and employing advanced surface tension transfer (STT) mode. The dominant microstructure of the fabricated part contained randomly oriented fine polygonal ferrite and a low volume fraction of lamellar pearlite as the primary micro-constituents. Additionally, a small content of bainite and acicular ferrite were also detected along the melt pool boundaries, where the material undergoes a faster cooling rate during solidification in comparison with the center of the melt pool. Mechanical properties of the part, studied at different orientations relative to the building direction, revealed a comparable tensile strength along the deposition (horizontal) direction and the building (vertical) direction of the fabricated part (~400 MPa and ~500 MPa for the yield and ultimate tensile strengths, respectively). However, the obtained plastic tensile strain at failure along the horizontal direction was nearly three times higher than that of the vertical direction, implying some extent of anisotropy in ductility. The reduced ductility of the part along the building direction was associated with the higher density of the interpass regions and the melt pool boundaries in the vertical direction, containing heat affected zones with coarser grain structure, brittle martensite-austenite constituent, and possibly a higher density of discontinuities.

**Keywords:** Additive Manufacturing (AM); Wire Arc Additive Manufacturing (WAAM); Low-Carbon-Low-Alloy Steel; Microstructure; Mechanical Properties.

## 1. Introduction

Additive manufacturing (AM) is a novel manufacturing technology in which a component is fabricated by depositing the feedstock material layer-by-layer to build a fully functional, dense, and 3D shaped component [1–3]. A wide range of different metals, composites, and polymers can be used as the feedstock material employing various AM techniques.

The additive manufacturing of metallic components can be classified based on the adopted feedstock materials into three main categories, *i.e*. powder bed processes, such as selective laser melting (SLM) or direct metal laser sintering (DMLS), powder feed processes, such as laser metal deposition (LMD), also known as direct laser fabrication (DLF), and wire feed processes, such as wire arc additive manufacturing (WAAM) [4,5]. WAAM is an AM technology that usually benefits from a robotic arm, carrying an arc welding torch as the energy source to fabricate metallic parts additively in the form of weld beads overlaid on previously deposited layers [6,7]. In WAAM, all the consumable wire is continuously fed into the adopted electric arc or plasma and entirely melted [8,9], leading to extremely high deposition rates associated with this process (3-8 kg/h), which is drastically higher than that in -of the powder bed/feed AM systems (0.1-0.6 kg/h) [4]. Therefore, it is mostly suited for fabrication of large-scale engineering components with more simple geometries and less complexity in design [9–11].

The most commonly used welding processes integrated with the WAAM technology are gas tungsten arc (GTA) and gas metal arc (GMA) welding processes [12]. In recent years, in multiple studies [12–14], the capabilities of the GMAW-based WAAM in terms of technological issues and metallurgical properties for different alloys have been widely explored. For instance, the microstructure and tensile properties of 316L austenitic stainless steel fabricated by GMA-AM [12], the feasibility of depositing steel parts by means of double electrode GMAW-based AM system [14], and the effect of the main deposition process parameters on the surface roughness of low-carbon steel parts fabricated using GMAW-based additive manufacturing [13] have been investigated.

From the fabrication perspective, there are many similarities between conventional GMAW and wire arc additive manufacturing methods, leading to analogous challenges and difficulties associated with both processes. For instance, the strength–ductility combinations in steels can be affected adversely from the thermal cycles experienced during layer-by-layer deposition of WAAM, correlated to either the heat affected zone (HAZ) softening [15–17] and/or formation of localized brittle zones (LBZs) along the interpass regions, commonly observed in the multi-pass welding processes [18,19]. Therefore, adopting an arc welding process with a low heat input transfer mode seems to be favorable for the purpose of WAAM.

Another complexity associated with the WAAM of ferrous alloys is that depending on the carbon content, alloying elements, and cooling rate of the steel, the manufactured component in the as-printed condition may possess a blend of different microstructures, *e.g.* ferrite, Widmanstätten ferrite, bainite, martensite, or acicular ferrite [20]. Thus, to obtain a desired microstructure with adequate strength and toughness in a WAAM part, the GMAW process essential parameters should be carefully selected [21].

In a recent study, Liberini *et al*. [1] characterized the microstructure of a wall-shape product obtained by the successive deposition of weld beads using an ER70S-6 steel wire through GMA-AM. The authors reported microstructural inhomogeneity across the deposited wall in the sequence of a bainitic lamellar structure at the upper zone of the wall, equiaxed grains of ferrite in the middle, and a ferritic structure with thin strips of pearlite at the lower zone [1]. Consequently, it was concluded that different thermal cycles associated with the layer-by-layer deposition nature of the

WAAM can result in various microstructures from the top to the bottom of the manufactured walls [1]. Whilst the mechanical properties of the fabricated walls were not reported in their study [1], such microstructural non-uniformity across the building direction could lead to anisotropic mechanical properties.

It is reported in multiple studies [22–25] that the high cooling rate and temperature gradient experienced throughout the components during the AM fabrication process dictate the grain growth direction and morphology, yielding heterogeneous microstructures and anisotropic mechanical properties. However, lower thermal input WAAM-based processes, such as WAAM-cold metal transfer (CMT) technique, can result in a more uniform microstructure and homogenous hardness profile [26]. Wang *et al*. [27] also showed that in a 304L austenitic stainless steel wall produced by directed energy deposition additive manufacturing, applying lower heat inputs resulted in a finer microstructure, and therefore, higher yield and tensile strengths than those in the wall fabricated using a higher heat input. They also reported that at a specific heat input, the coarser microstructure at the top of the walls compared to the bottom of the components resulted in a lower yield and tensile strengths due to a lower cooling rate at the top areas of the wall [27].

Wilson-Heid *et al*. [22] studied the relationship between the microstructure and the anisotropy in ductility of an additively fabricated Ti-6Al-4V and concluded that the elongation percentage in the transverse direction is higher than that of the longitudinal direction. Wang *et al*. [28] also reported the anisotropic mechanical properties in a WAAM Ti-6Al-4V alloy, showing a higher strength and lower ductility in the horizontal direction compared to the building (vertical) direction. The authors correlated such properties to the existence of different crystallographic textures along the deposition direction versus the building direction developed from the directional columnar growth of Ti grains during solidification. On the other hand, Haden *et al*. [29] observed no obvious anisotropy in mechanical properties such as yield and tensile strength in a low carbon low alloy steel (ER70S-6) produced via WAAM. However, in their study, the reported mechanical properties were not clearly correlated to the microstructure of the additively manufactured wall. In a recent study by Sridharan *et al*. [20], a GTA welding system was used to additively manufacture the low carbon low alloy steel ER70S-6 along the X-, Y- and Z-directions followed by a detailed mechanical properties investigation. A significant scatter in the elongation with respect to the sample directions was reported and correlated to the differences in the level of porosities and discontinuities and the localized variations of the microstructural features in each sample.

In addition to all the experimental research on the advancement of the WAAM technology and its accelerated adoption in manufacturing of various engineering materials, the simulation and modelling of various aspects of the process have been also the focus of several studies. For example, the thermal history of the process [30], the deposition path [4,11], and the dynamics of metal transfer [31] during the fabrication process have been modeled in previous studies. In a study by Fachinotti *et al.* [30], a thermal-microstructural model capable of describing the thermal history of the WAAM process during the fabrication of Ti-6Al-4V alloy wall was developed. The proposed model was also capable of predicting important microstructural features in the fabricated part based on the predicted thermal history of the process [30]. In another study, the metal transfer dynamics of a wire feeding-based 3D printing process was extensively investigated, and a correlation model between the process parameters, such as heat input and scanning strategy, and the deposited bead geometry was developed [31].

It is well established that high heat input welding processes can lead to coarsening of the ferrite grains in steels due to recrystallization or abnormal phase transformation from Austenite [32,33]. The result can be a significant HAZ softening and a noticeable reduction in HAZ toughness. This issue is even more critical in the WAAM process due to the multi-pass nature of the process. Therefore, adopting a fast cooling version of the GMAW/GTAW process would plausibly favor the HAZ toughness of the WAAM fabricated steels.

Surface tension transfer (STT) is an advanced current controlled short circuit metal transfer mode in the GMAW process developed by the Lincoln Electric Company [34]. The unique feature of the STT transfer mode is that it offers a combined reduction in energy and improved energy control through droplet by droplet control of the fusion zone, which can be beneficial in minimizing the extent of HAZ softening and can achieve a smooth bead profile and improved bead geometry [34,35]. The heat input associated with the STT-GMAW process can be as low as 20% of that in conventional spray or pulsed-GMAW processes [34]. Hence, a fast cooling process, such as STT-GMAW, can dramatically enhance the HAZ toughness of high strength low alloy steels. The capabilities of this particular transfer mode for the WAAM of metallic components are hitherto unreported.

In the context of WAAM, a large number of studies to date have been carried out on the fabrication of Ti-6Al-4V, but not so much on steels, which are the most commonly used materials in modern industry with an unlimited number of applications in various industrial sectors [29,31,36]. Therefore, this study aims at fabricating a low-carbon-low-alloy steel (ER70S-6) using wire arc additive manufacturing technique. For the first time herein, the surface tension transfer (STT) waveform control technology was adopted in wire arc additive manufacturing of the part. The used feedstock wire is commonly utilized for the welding of high-strength-low-alloy steels owning moderate amounts of scale or rust with widespread applications including structural steels, auto bodies, pipes, fittings, castings, and forgings [37]. This article presents a detailed study of the microstructure and mechanical properties of the WAAM thin-wall parts. Additionally, the influence of the manufacturing process on the anisotropy of the mechanical properties was investigated, utilizing tensile testing and fractography techniques along both vertical and horizontal directions.

## 2. Experimental Procedure

### 2.1. Materials and Fabrication Process

The used robotic WAAM platform, the fabricated wall, and its graphical representation are shown in Figure A1.1. Each deposited layer on the x-y plane was comprised of six beads with a length of 135 mm and the total height of about 150 mm, containing 50 consecutive layers. The layers have a 3 mm center-to-center overlap, leading to the total width of 22 mm for the wall and the resulting beads for each layer have a height of around 3 mm. The base plate was ASTM A36 mild steel with 12 mm thickness, which was thoroughly cleaned using stainless steel wire brushing and degreased by acetone prior to the WAAM to avoid porosity formation during the fabrication process. As drawn in Figure A1.1b, a y-scanning strategy with alternating directions, and 3 mm overlap along the x-axis between the successive passes on each x-y layer was used (y-axis is aligned with the longer dimension of the base plate). The adopted alternating direction scanning strategy was found to contribute to the uniformity of the deposited beads' profile at both ends of the y-axis, resulted in fabricating a straight wall. Moreover, the presented patterns on the front face (y-z plane) of the schematic in Figure A1.1b show the locations where vertical and horizontal tensile test samples were machined from the fabricated wall. Also, the squares labeled as the top, middle top, middle bottom, and the bottom on the front face show the location of the samples that were subjected to the microstructure and phase characterization analysis. Figure A1.1c is the side overview of the fabricated wall herein.

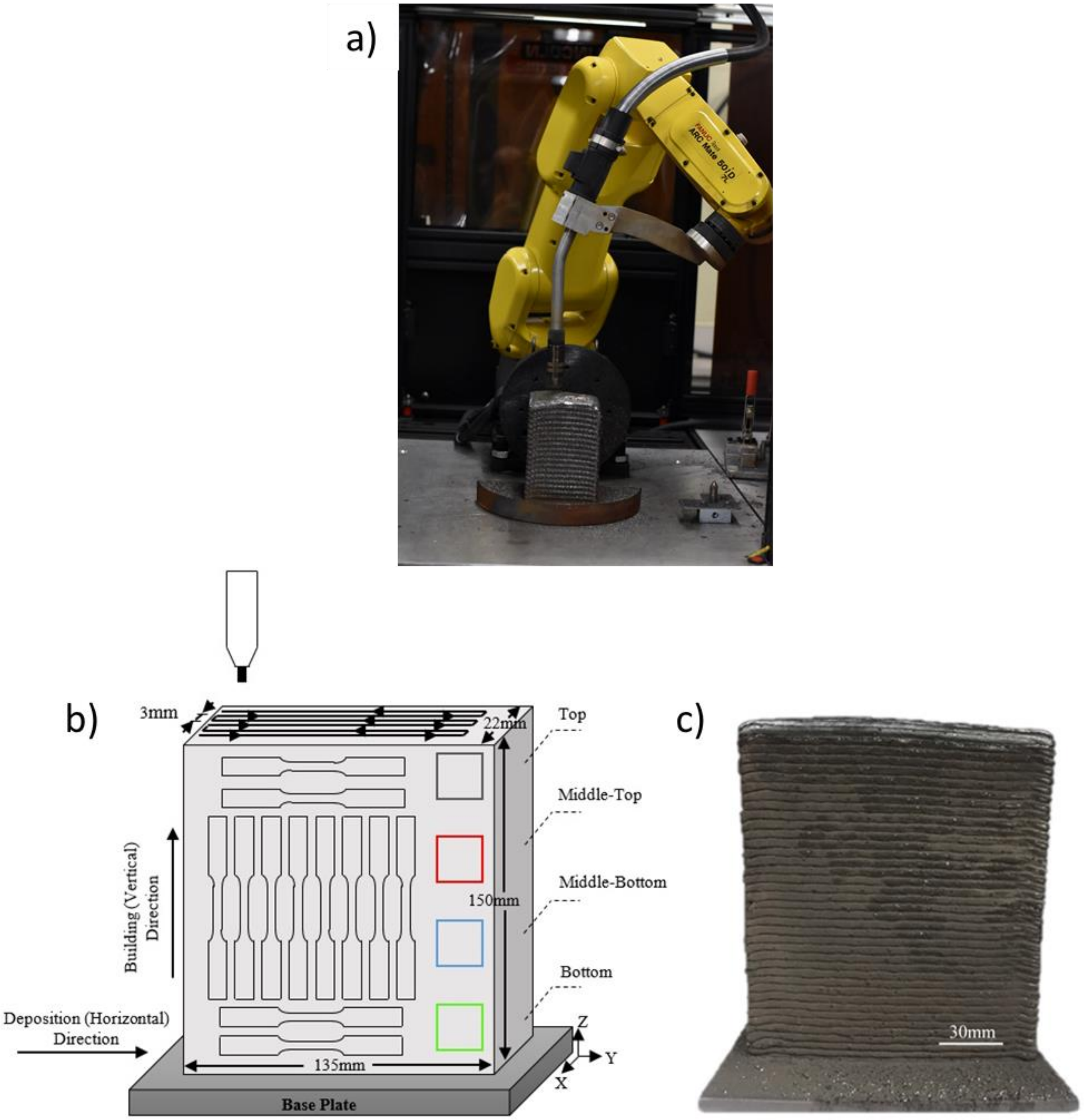

Figure A1. 1. (a) The used robotic WAAM platform, (b) schematic illustration of the WAAM-ER70S-6 steel wall, and (c) the manufactured wall using WAAM method.

The ER70S-6 wire with 0.889 mm (0.035 inches) diameter was used as the feedstock material with the chemical composition given in Table 1. A Lincoln Electric GMAW machine with a torch mounted on a 6-axis Fanuc robot was employed as the power source of the process (Figure A1.1a).

The process was carried out using the following parameters: an arc current of 320 A, an arc voltage of 28 V, a wire feeding rate of 104 mm/s (245 inches/min), a scan rate of 5 mm/s (12 inches/min), and pure argon as the shielding gas with the flow rate of 45 L/min. Additionally, advanced STT current controlled short circuit transfer process was used herein to minimize the heat input of the process and reduce the surface irregularities, the generated fume and spattering during the fabrication process. To further minimize the effects of consecutive thermal cycles on the microstructure of the previously deposited layers, a 10 min interlayer dwell time was implemented in the fabrication program after the completion of each x-y layer. The selected time interval allowed each layer to be cooled to a temperature below 165 °C (325 °F) [38] before each new layer was deposited. Consequently, a steady-state deposition and a more homogenous microstructure in all layers of the wall along the building direction would be expected due to the similarity of the thermal cycle associated with the solidification of each layer.

Following the fabrication process, the base plate was cut off and separated from the fabricated portion prior to the microstructure and mechanical properties characterization to eliminate any effect resulted from the dilution at the bottom side of the component.

Table A1. 1. The nominal chemical composition of the ER70S-6 feedstock wire (wt. %)

| ***C*** | ***Mn*** | ***Si*** | ***Cr*** | ***Ni*** | ***Mo*** | ***S*** | ***V*** | ***Cu*** | ***P*** | ***Fe*** |
|---|---|---|---|---|---|---|---|---|---|---|
| ***0.06-0.15*** | *1.40-1.85* | *0.80-1.15* | *0.15 max* | *0.15 max* | *0.15 max* | *0.04 max* | *0.03 max* | *0.50 max* | *0.03 max* | *Bal.* |

## 2.2. Microstructure Characterization

To perform microstructural characterization and investigate possible microstructural anisotropy in the printed wall, four samples from different locations of the wall, including the bottom, middle-bottom, middle-top, and the top were sectioned along both the deposition direction and the building direction (illustrated in Figure A1.1b). Standard steel grinding and polishing procedures were applied utilizing a Tegramin-30 Struers auto-grinder/polisher followed by etching using 5% Nital as the reagent. The microstructure of all specimens was examined using an optical microscope (Nikon Eclipse 50i) and a field emission scanning electron microscope (FEI MLA 650F). Phase characterization was carried out by means of a Rigaku Ultimate IV X-ray diffraction (XRD) with Cu-$K_\alpha$ source at 40 kV and 44 mA at the diffraction angle range of 5°-90° with a step size of 0.02°. Electron backscatter diffraction (EBSD) analysis was also conducted over an area of 600 × 600 $\mu m^2$ on polished samples with a step size of 1.4 μm and a tilt angle of 70°, using Nordlys II HKL EBSD detector, Oxford Instruments. To post-process the obtained EBSD data, the HKL Inc. software, known as Channel 5, was employed.

## 2.3. Mechanical Properties Measurement

Vickers microhardness testing was conducted on different areas of the wall including the bottom, middle-bottom, middle-top and the top (see Figure A1.1a), utilizing a Buehler Micromet hardness test machine at a load of 3 N and the loading time of 45 s. It should be noted that the reported microhardness test results for each sample in this study are the average value of 5 different indentation points on polished surfaces. The tensile test samples were prepared based on the ASTM E8m-04 standard subsize specimen [39] with 5 mm thickness, 25 mm gauge length, and 100 mm total length. Tensile properties were measured using an Instron load frame with a crosshead speed of 8 mm/min. It is also notable that the strain data was recorded using an extensometer. The horizontal specimens were machined from both the top and bottom zones of the wall, and the vertical tensile specimens were selected from the middle part of the wall, shown schematically in Figure A1.1b. In order to avoid the effect of endings, where the scanning direction is reversed and the arc experiences some degree of unstability, and also to eliminate the dilution effect of the base plate, the microstructural characterization and mechanical testing herein were only conducted on an effective area 15 mm away from both ends and 10 mm above the base plate. Repeatability of the results was measured by testing at least five samples under the same conditions to obtain a reliable average value. The fractured surfaces of the tensile test samples from both vertical and horizontal directions were also studied using the SEM. For each direction, three fractured samples were analyzed to ensure the consistency of the reported features between the samples from the same direction.

## 3. Results and Discussion

### 3.1. Microstructure Characterization

Figure A1.2a demonstrates the overall microstructure of the ER70S-6 steel wall at different regions, showing the variation of the microstructure from an area in the vicinity of a fusion line towards the center of the melt pool (top left corner of the image). Figures A1.2b and 2d depict the dominant microstructure of each melt pool center composed of the typical fine polygonal ferrite (F) as the primary phase and a low volume fraction of the lamellar pearlite (P) phase, which has primarily formed along the ferrite grain boundaries. Similar microstructural features were reported in a previous study for a WAAM fabricated ER70S-6 wall [29]. In addition, a closer look at the microstructure along the melt pool boundaries (Figures A1.2c and A1.2e) confirmed the formation of acicular ferrite along with bainite regions (AF + B) adjacent to the melt pool boundary. This transition in microstructure is developed because of the overlapping scanning lines and solidification of individual melt pools, resulting in different thermal histories from the center of each melt pool to the boundaries of its adjacent melt pools [40]. Since the fusion boundaries experience a higher cooling rate during solidification process compared to the center of the melt pools, the formation of some non-equilibrium AF + B phases was detected adjacent to the fusion lines. In a past study, Haselhuhn *et al.* [41] analogously reported the transition of polygonal ferrite to acicular ferrite from the melt pool center to the melt pool boundary in a WAAM-ER70S-6 wall due to faster cooling rates that the material experiences during solidification along the fusion line.

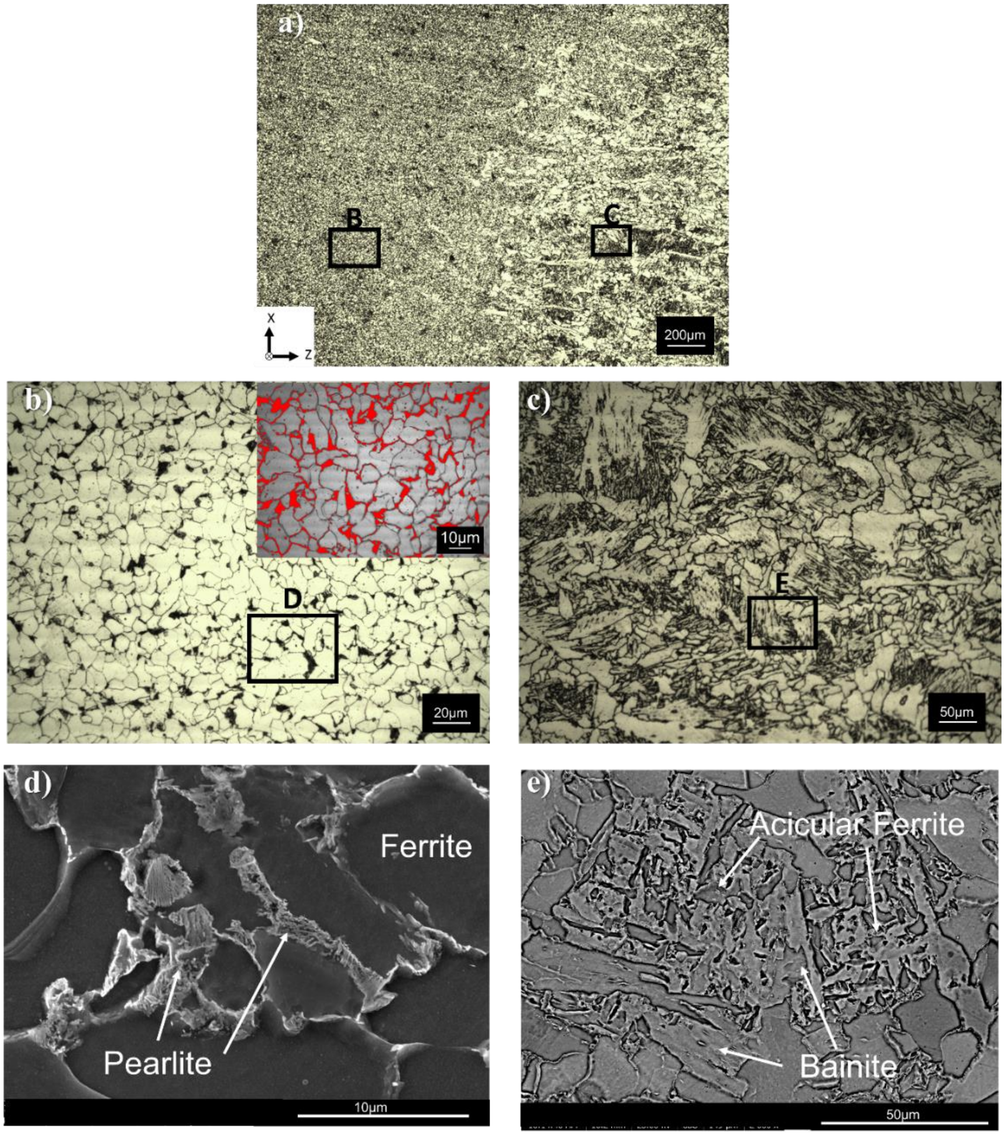

Figure A1. 2. Optical micrographs taken from (a) the WAAM-ER70S-6 steel wall at the fusion line and center of the melt pool, (b) higher magnification of the enclosed area in (a) shown by B, and the inserted image shows an example of a phase fraction analysis micrograph, presenting the distribution of the pearlite phase (in red) along the ferrite grain boundaries, (c) the enclosed area in (a) shown by C. SEM micrographs from (d) the enclosed area in (b) shown by D, and (e) the enclosed area in (c) shown by E.

To quantify the volume fraction of the pearlite phase formed along the ferrite grain boundaries, a detailed image analysis of the microstructure taken from various locations of the sample was performed using the ImageJ software (an example is shown in the inserted image in Figure A1.2b, in which the red phase corresponds to the pearlite). Due to the low carbon content of the feedstock wire (0.06-0.15%), the volume fraction of the pearlite phase was approximated to be only 12.54 ± 0.56 % of the total microstructure (the red highlighted phase shown in Figure A1.2b).

As compared to the ferrite and pearlite phases, the volume fraction of the acicular ferrite and bainite phases that formed predominantly along the fusion boundaries were negligible (as evident from the micrographs in Figure A1.2). The presence of a small volume fraction of bainite and acicular ferrite has been also reported in the microstructure of API-X70 pipeline steel, which is commonly being welded using ER70S-6 filler wire [42]. In particular, bainite offers a higher strength and toughness due to its smaller grain size and higher dislocation density as a result of providing obstacles to dislocation movement as compared to the polygonal ferrite [42]. In the context of the microstructural modifications of the as-printed additively manufactured components, implementing a post-printing heat treatment would be an alternative to modify and refine the microstructure and ultimately improve the mechanical performance of the printed sample, which is the subject of a future study by the authors.

It should be noted that the aforementioned microstructural features were observed throughout all layers of the component from the bottom to the top zones of the wall. Therefore, a uniform microstructure could be obtained in different zones of the WAAM manufactured part, albeit with some degree of inhomogeneity was detected in each deposited bead from the melt pool center towards its boundary. Such uniformity in the microstructure along the building direction of the wall could be attributed to the sequence of the layer deposition and the adopted interlayer dwell period. It is well established that in metal additive manufacturing processes, the existence of multiple and complex thermal cycles is the primary factor leading to the non-uniformity of microstructure along the building direction [20,43]. However, as stated in the experimental procedure section, a 10 min interval between each layer can minimize the effect of heat accumulation and avoid microstructural variations in different layers across the z-direction. Therefore, all layers have experienced approximately consistent heating and cooling cycles, resulting in a uniform microstructure along the building direction.

As a complement to the SEM analysis, an EBSD analysis was performed to obtain more information on crystallographic texture and orientation features of the printed sample. The EBSD inverse pole figure (IPF-z) map of the as-printed sample along the building direction (z-axis) is demonstrated in Figure A1.3a. The IPF-z map illustrates comprehensive information on the grains' orientation/misorientation, their size, and aspect ratio. To quantify the detailed information of the grains, the IPF maps were evaluated through statistical analysis of the grain area, misorientation angle, and grains' aspect ratio, shown in Figures A1.3b, A1.3c, and A1.3d, respectively.

The IPF map and the statistical distribution of the grain area and the aspect ratio show that the wall is mainly composed of randomly oriented equiaxed grains (aspect ratio < 3) with an average grain size of ~7.30 µm. The grain size is considered as one of the most prominent microstructural characteristics that affects the mechanical properties. The grain coarsening in the HAZ of the previously deposited track is clearly visible in the IPF map, denoted by the coarse grain region with an average grain size of 15.76 ± 2.34 µm, whereas the area inside the melt pool revealed a noticeably smaller grain size (4.94 ± 1.26 µm). Considering the nature of layer-by-layer deposition associated with the WAAM method, each deposited layer reheats the previous one. The resulting high temperature in the previously solidified track would facilitate the grain boundaries migration and consequently causes grain growth in the vicinity of each melt pool boundary. Such microstructural inhomogeneities in the structure of the printed component can adversely impact the mechanical properties of the part and contribute to anisotropic mechanical properties. As depicted in the grain area distribution plot (Figure A1.3b), the majority of the grains (approximately 80%) have an area smaller than 100 $\mu m^2$, representing an overall fine grain structure for the as-printed WAAM-ER70S-6 part. The misorientation distribution graph (Figure A1.3c) confirms that the misorientation angle of the grains is mostly distributed between 0-4 degree, corresponding to a uniform orientation of the cubic structure [44].

The statistical distribution of the grain shape aspect ratio is plotted in Figure A1.3d. The grain shape aspect ratio can be used as a criterion to differentiate the equiaxed grains from the columnar grains. A grain would be considered an equiaxed grain when its shape aspect ratio is smaller than 3, whereas columnar grains possess aspect ratios of $\geq 3$ [45,46]. As revealed by the grains’ aspect ratio distribution graph (Figure A1.3d), more than 90% of the grains possess an equiaxed shape and only a small portion of the grains (<6%) were characterized by a columnar shape.

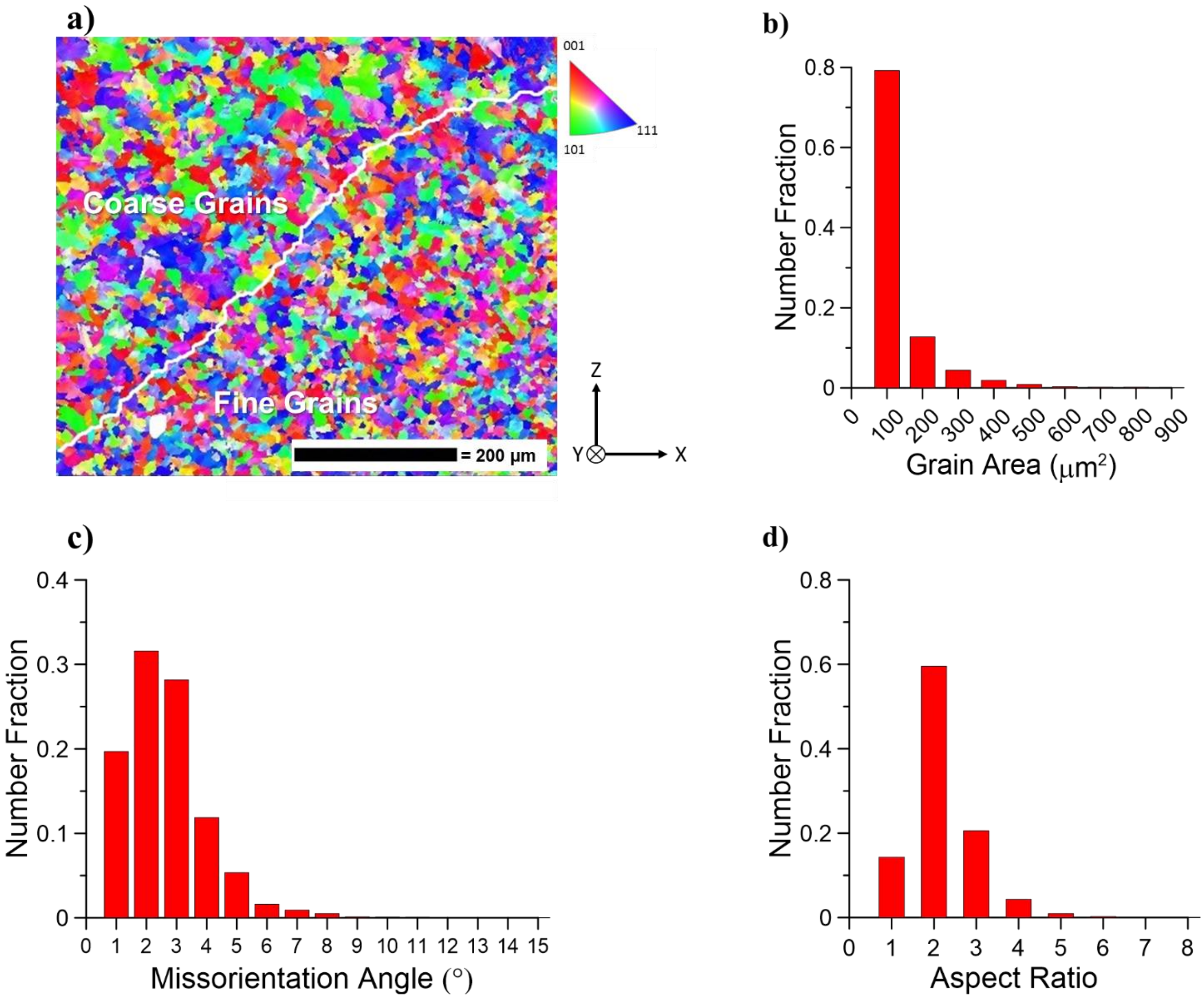

Figure A1. 3. (a) EBSD inverse pole figure map of the as-printed WAAM-ER70S-6 sample, statistical distribution plots showing the distribution of (b) grain area, (c) misorientation angle, and (d) grain shape aspect ratio.

The pole figures (PFs) from the EBSD map shown in Figure A1.3a were determined to investigate the texture distribution produced by the manufacturing process of the sample, and the result is demonstrated in Figure A1.4. The {100}, {110}, and {111} pole figures of the WAAM-ER70S-6 sample are illustrated in Figure A1.4. The X and Y directions are shown on the {100} pole figure, and the Z-axis is normal to the plane of the pole figure. The PF maps revealed a weak texture, representing a random texture with a maximum intensity of 3.08 above the random background.

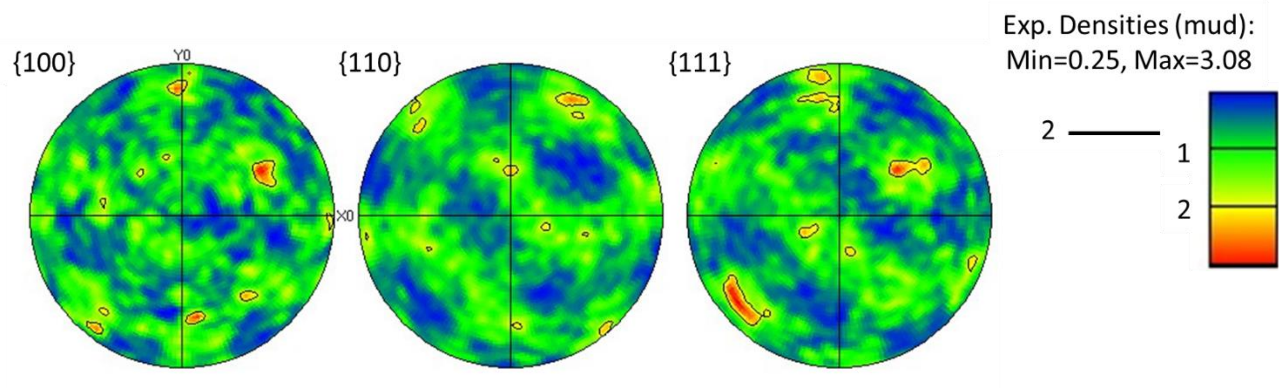

Figure A1. 4. Pole figures from the WAAM-ER70S-6 wall.

The XRD analysis of the WAAM-ER70S-6 wall was conducted for phase identification on the samples extracted from different heights along the building direction (shown in Figure A1.1b), and the obtained spectras are presented in Figure A1.5. As clearly revealed, the as-printed wall predominantly contains an α-Iron (BCC, Ferrite) phase as the main constituent, in which the α-Iron peaks are located at 2θ of approximately 44.55°, 64.85°, and 82.11° according to the JCPDS patterns of 98-000-9982. The XRD measurements also revealed the absence of an austenite (Iron-FCC) phase, confirming that either the retained austenite has not formed in the as-printed sample or its volume fraction is too low, below the detection limit of the XRD. The precipitated cementite phase (in the form of lamellae in the pearlite phase) was also not detected on the XRD spectra due to its drastically lower volume fraction as compared to the ferrite phase. The identical XRD patterns obtained from different locations across the building direction (shown in Figure A1.5) is another compelling piece of evidence for the uniformity and homogeneity of the microstructure along the building direction of the wall.

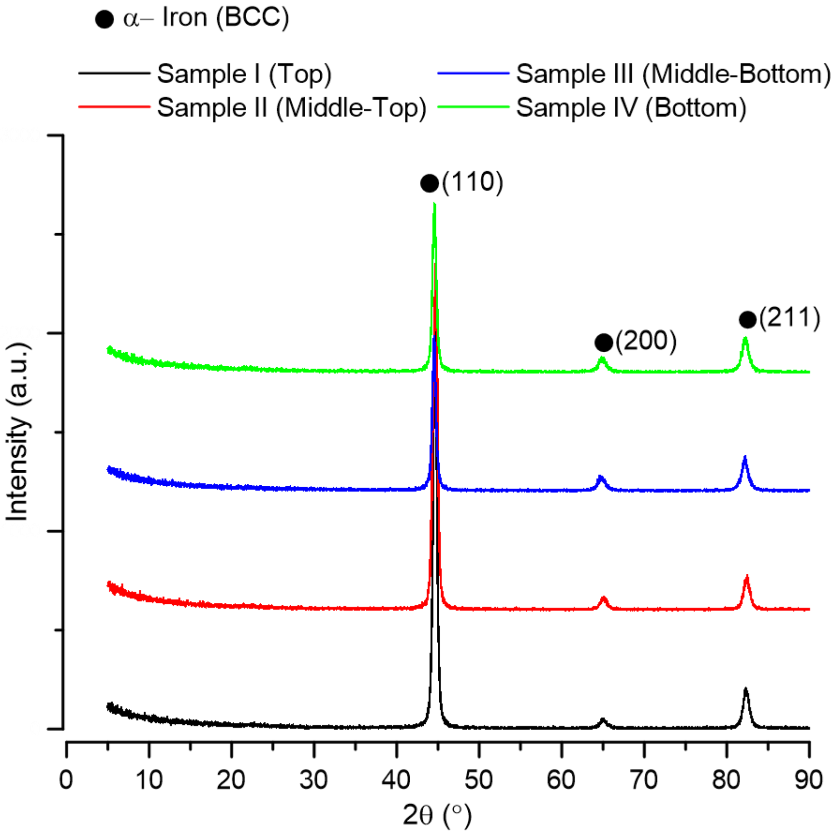

Figure A1. 5. XRD pattern of the WAAM-ER70S-6 samples taken from different locations along the building direction.

### 3.2. Mechanical Properties

Figure A1.6 presents the overall Vickers microhardness variation of the as-printed component along the building (vertical) direction from the bottom to the top of the wall with 10 mm margin from the bottom and top of the wall to eliminate the effects of both dilution and the last deposited layer. The microhardness testing results (Figure A1.6a) revealed that the overall average microhardness of the sample was 160 ± 7 HV throughout the whole sample, indicating a uniform hardness distribution across the building direction due to the consistency of the microstructure along the building direction. A uniform microhardness profile is generally favored as it represents more homogeneous and isotropic micro-mechanical properties in the fabricated part [20]. The evenly distributed microhardness values have a minor deviation (± 7 HV) from the average microhardness value (160 HV), attributed to the presence of various micro-constituents with different volume fractions within the melt pool boundaries, the center of the melt pool, versus the HAZ, as described in the microstructure characterization section. Vickers microindentation on different microstructures (Figure A1.6b) confirmed that the highest value of microhardness (~175 ± 2 HV) corresponded to the acicular ferrite and bainite (AF + B) regions at the melt pool boundaries and the lowest value (~150 ± 1 HV) belonged to the coarse polygonal ferrite plus pearlite region in the heat affected zone $(F+P)_{HAZ}$. It should also be noted that the dominant microstructure of the sample, including the fine ferrite grains with the pearlite lamellae (F + P) formed at the ferrite boundaries, showed the average microhardness of 160 ± 2 HV.

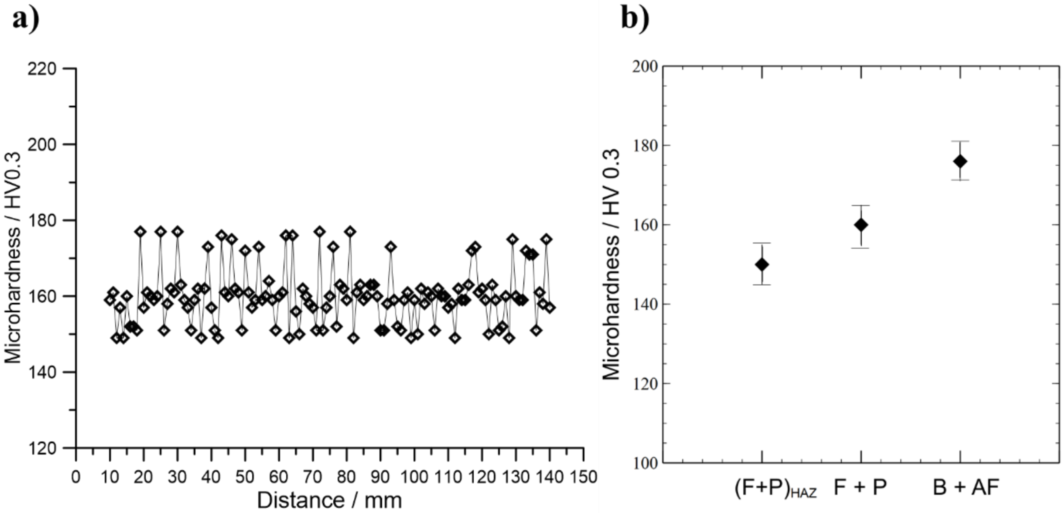

Figure A1. 6. Vickers micro-hardness distribution on (a) different points on the surface along the building (vertical) direction from the bottom to the top of the wall, and (b) the measured microhardness values of different existing constituents in the structure.

The standard stress versus strain diagrams measured from the WAAM-ER70S-6 samples along both the deposition (horizontal) direction and the building (vertical) direction at room temperature are shown in Figure A1.7. Also, the bar chart enclosed in Figure A1.7 summarizes the extracted tensile properties, including the yield strength (YS) and ultimate tensile strength (UTS) of the WAAM-ER70S-6 wall along both the deposition and building directions. The average values of UTS and YS of the horizontal and vertical samples confirmed that the additively manufactured wall had approximately similar yield strength and ultimate tensile strength values in both directions (396 ± 26 MPa and 503 ± 21 MPa, respectively), indicating isotropic tensile properties. Analogously, a few recent studies have also reported isotropic tensile strengths for the WAAM fabricated ferrous parts [20,29,47]. However, as clearly visible in Figure A1.7, the vertical specimens show a significantly lower elongation than that of the horizontal samples (12 ± 3% and 35 ± 2%, respectively), confirming the prominence of anisotropy in ductility. Such mechanical anisotropy in ductility and toughness commonly occurs in additively manufactured parts and has been reported in many studies for various metals and alloys [48–50].

The consistency in the tensile strength of the vertical and horizontal samples is mostly attributed to the uniformity and homogeneity of the microstructure, as confirmed by the evenly distributed microhardness values in all deposited layers from the bottom to the top of the WAAM manufactured wall. On the other hand, the drastic reduction in the ductility value from the horizontal sample to the vertical one can plausibly be rationalized by either (*i*) the presence of manufacturing discontinuities and defects, such as lack of fusion or porosity accumulated in the interlayer regions, (*ii*) the grain coarsening along the HAZ, and/or (*iii*) the formation of brittle martensite-austenite (MA) constituent within the bainite lamellar structures. Such a constituent with a brittle nature could potentially fracture during tensile loading of the sample prior to other constituents (F or B), leading to the onset and propagation of internal micro-cracks in early stages of the loading and ultimately failure at significantly lower strain values. Further elucidation of these phenomena is discussed in the following sections.

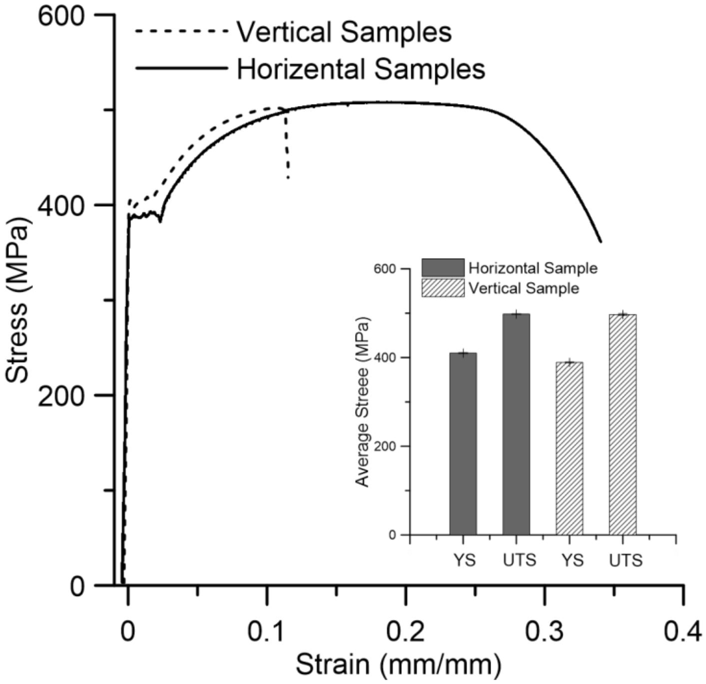

Figure A1. 7. The stress-strain curves and their corresponding tensile properties for the vertical and horizontal samples.

Figure A1.8 shows the fractured samples after conducting uniaxial tensile testing herein. Collectively, all vertical tensile samples (Figure A1.8a) revealed the development of some transverse cracks, perpendicular to the building direction (or loading direction), formed equidistant from each other during the tensile test. Ultimately, one of those cracks propagated more than the others and resulted in the failure of the sample. Formation of similar cracks with constant intervals justifies the supposition that their formation is dictated by the same reason(s). As displayed clearly in Figure A1.8b, the onset and propagation of the cracks were detected mainly in the HAZ, which was characterized by grain coarsening due to the high temperature that the material experiences in this region during the solidification of the adjacent bead. The presence of coarse grains in the HAZ deteriorates the mechanical properties, especially the ductility herein, implying that the grain coarsening around HAZ could be one of the main weakening mechanisms in the WAAM-ER70S-6 alloy along the building direction. Therefore, the cracks could potentially nucleate and propagate preferentially along the heat affected zones leading to a premature failure through the HAZ.

The impact of the grain size on the strength of the material can be described mathematically using the well-known Hall-Petch equation shown below,

$$\sigma_y = \sigma_0 + Kd^{-1/2} \qquad \text{(Eq. 1)}$$

where $\sigma_y$ is the yield strength of the material, $d$ is the average grain diameter, and $\sigma_0$ and $K$ are the material constants, representing the lattice resistance to the dislocation motion and strengthening coefficient, respectively [51]. Therefore, the HAZ can potentially yield prior to the rest of the structure during the tensile loading test. On the contrary, the horizontal samples (Figure A1.8a), which were machined primarily from the bulk of each weld bead along the deposition direction, contained the lowest possible HAZ structure incorporated in their gauge length. These samples did not reveal formation of multiple equidistant cracks on their gauge length during tensile testing. Such behavior could be ascribed to the grain size uniformity in this direction.

It should also be noted that fusion boundaries are commonly prone to interpass defects, such as lack of fusion, entrapped gas, and porosity [52,53]. Although these defects were not detected visually on the as-printed tensile samples or on the polished samples, their existence in the structure is still plausible. Such defects can readily facilitate the brittle fracture by providing potential sites for crack initiation and growth since they can act as strong stress concentrators during tensile loading [54]. Among such defects, the lack of fusion is of particular interest and highly probable to form during multi-pass deposition based processes, such as WAAM, resulting from the special heat transfer condition between the layers in the sample along the building direction [20]. It is reported that the high heat removal capacity from the interpass regions between the layers can potentially be attributed to a greater portion of the lack of fusion regions within the adjacent beads [20]. The formation of interpass defects can further be investigated by performing non-destructive testing (NDT) methods capable of detecting defects that are not open to the surface, *i.e.*, radiography or ultrasonic testing, which is the subject of a future study.

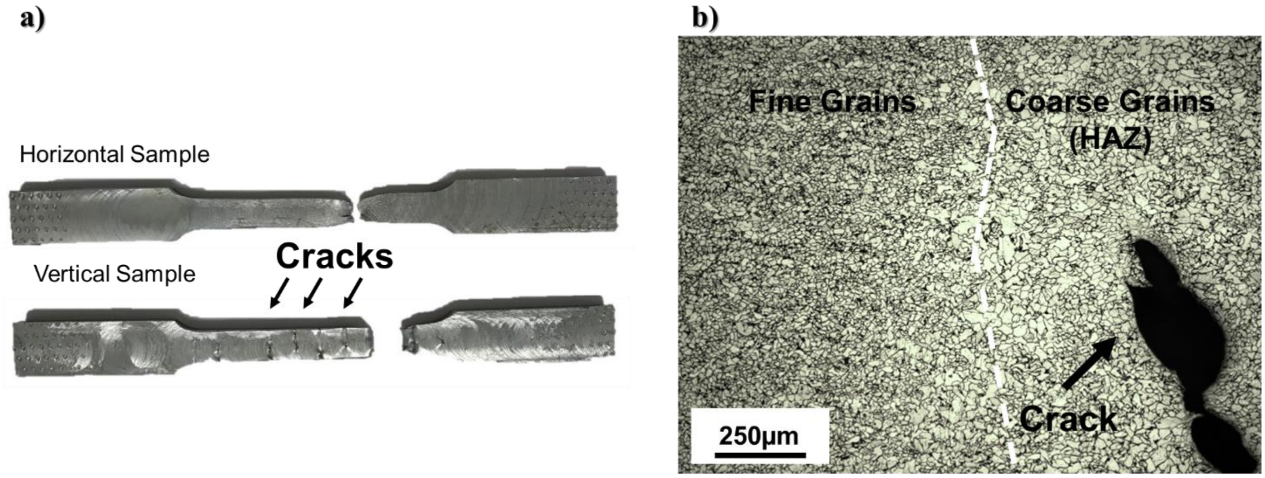

Figure A1. 8. (a) Tensile samples after fracture and (b) an optical micrograph taken from the cross section of one of the equidistant cracks (shown by the arrows in (a)) formed during tensile testing on the vertical sample.

Another scenario can be defined that could further contribute to the observed lower mechanical integrity of the WAAM sample along the building direction. It is well established that in multi-pass welding of steels, due to increasing the temperature of the interpass regions into the ferrite + austenite phase stability zone between $Ac_1$ and $Ac_3$ temperatures, a region so-called the inter-critical heat affected zone (ICHAZ) adjacent to each melt pool in the previously deposited pass forms [55,56]. In this region, the austenite phase could potentially nucleate along the bainite lath boundaries or prior austenite grain boundaries. By further diffusion of carbon atoms from the matrix (F + B) into the nucleated austenite phase due to significantly high solid solubility of carbon in austenite phase, the austenite phase can slightly grow, even though the carbon concentration of the ER70S-6 feedstock wire is low. Upon fast cooling of this region, if the carbon content is low, or there are no sufficient austenite stabilizing alloying elements to stabilize the austenite at room temperature (the case of ER70S-6), the reverted austenite phase transforms to the martensite-austenite (MA) constituent, forming localized brittle zones (LBZs) in the ICHAZ [57]. Consequently, these LBZs potentially degrade the toughness of the low alloy steels by cracking of MA constituent and its detachment from the matrix [18]. As shown in Figure A1.9, a closer look at the HAZ of the WAAM-ER70S-6 sample revealed the formation of some of those LBZs. As Figure A1.9 reveals, the new MA constituent is nucleated within the bainite lamellar structure. Although the amount of this phase was very minor as compared to the other constituents in the microstructure, it is known that the formation of martensite-austenite promotes the crack nucleation under tensile loading due to the brittle nature of this phase [58], the induced residual tensile stress on the matrix resulted from the martensitic transformation [58], the incoherency of the MA-ferrite interface that leads to the MA-ferrite interfacial cracking [59], and finally the slip localization in the ferritic matrix around the hard MA phase that could potentially lead to the localized cleavage of the matrix [20]. Therefore, the formation of the MA constituent in the ICHAZ can further contribute to the de-bonding and fracture concentration between the consecutive layers.

Due to the geometry of the vertical samples relative to the building direction, these samples accommodate a high density of melt-pool boundaries and ICHAZs. Therefore, the content of MA phase formed in these samples is significantly higher than that in the horizontal samples. Such microstructural variation between the vertical and horizontal samples can be partially responsible for not only the measured lower ductility of the vertical samples than that of the horizontal samples, but also the formation of the equidistance macro-cracks on the vertical samples during the tensile testing.

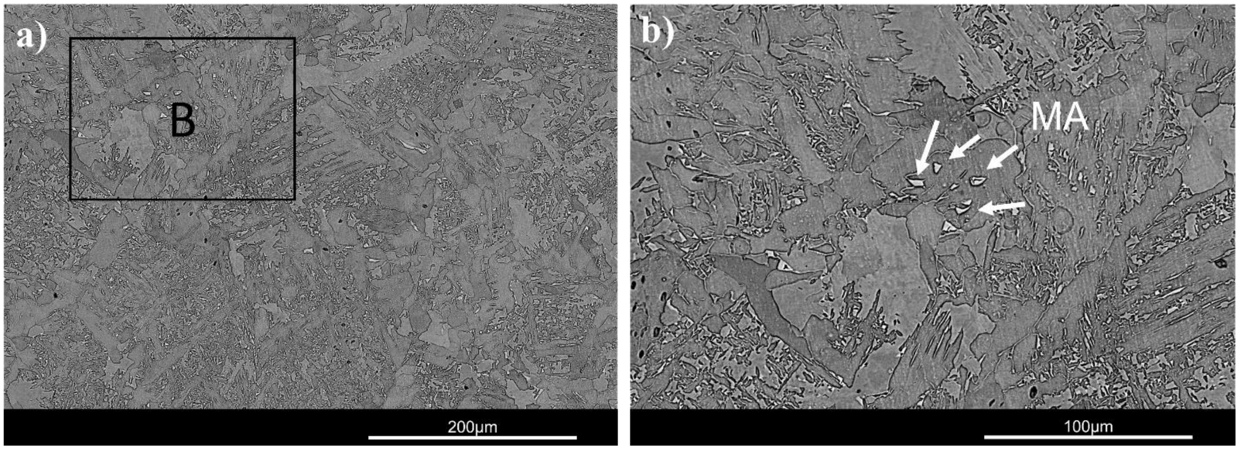

Figure A1. 9. SEM micrograph taken from (a) the HAZ of the as-printed WAAM-ER70S-6 and (b) the higher magnification of the enclosed area in (a) shown by B, demonstrating the formation of MA phase between coarse bainite lamellas.

To further study the fracture behavior of the samples, the representative SEM fractographs of the horizontal and vertical samples were also analyzed and are depicted in Figure A1.10. The fracture surface of the horizontal sample was predominantly comprised of large and deep cuplike depressions and conical dimples with relatively uniform size, indicating occurrence of an extensive plastic deformation and ductile behavior during tensile testing [60]. It confirmed that the fracture is dominated and controlled by microvoids nucleation at regions of localized strain discontinuity, followed by the coalescence of microvoids, leading to a cup and cone-shaped failure surface with the shear lip of around 45° [61].

A different fracture surface for the vertical sample is clearly distinguishable from the micrographs shown in Figures A1.10c and A1.10d. It was revealed that the degree of plastic deformation for the vertical sample was not as severe as that in the horizontal sample. Although dimples can be observed on the fractured surfaces of both vertical and horizontal samples, the morphology of the dimples was found to be different, corresponding to the variation of mechanical behaviour and fracture mechanism of the samples during tensile testing [60]. A comparison between dimples formed on the fracture surface of the vertical and horizontal tensile samples at higher magnification (Figure A1.10b and A1.10d) reveals that their size is smaller and shallower in the vertical sample, implying that a lower plastic strain was retained by the sample prior to its failure [62,63]. Moreover, there are some nearly flat areas, including micro-cracks (marked by white arrows in Figure A1.10c), in the vertical samples, a compelling evidence for the occurrence of a relatively fast cleavage fracture due to the crack propagation [61]. Therefore, the observed morphological features of the fractured surfaces of both horizontal and vertical samples were found to be in good agreement with their tensile test results, confirming a lower ductility for the vertical samples than the horizontal ones, albeit the tensile strength remained approximately constant.

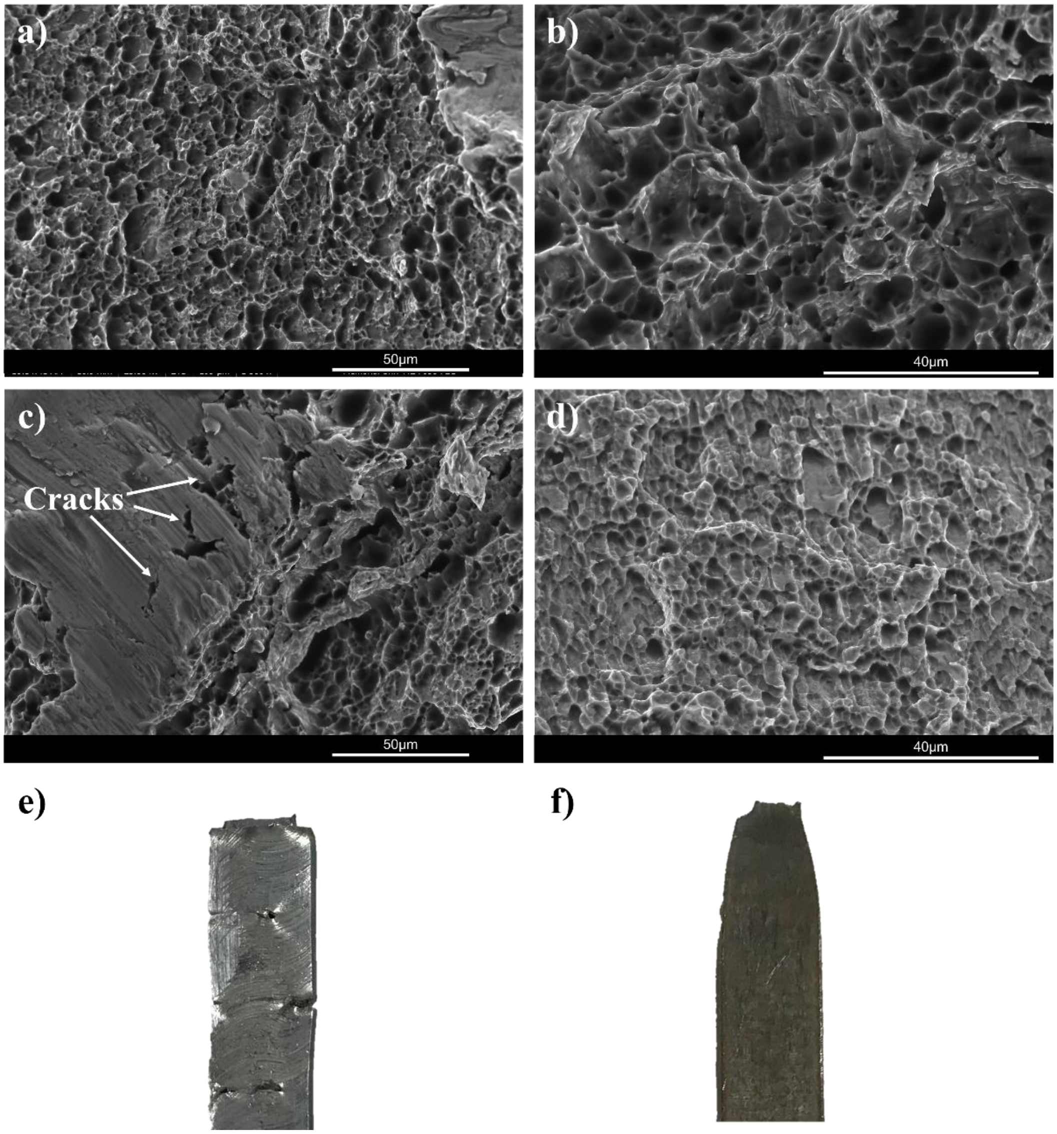

Figure A1. 10. SE-SEM micrographs taken from the fractured surfaces after uniaxial tensile testing: (a) and (b) the horizontal sample, (c) and (d) the vertical sample. The side view image from the gauge of the fractured (e) vertical sample and (f) horizontal sample.

Likewise, the side view of the fractured samples after uniaxial tensile testing (Figures A1.10e and 10f) confirmed that there is no sign of extensive plastic deformation and necking in vertical samples. On the other hand, an almost homogenous deformation has occurred in the necking area of the horizontal sample, consistent with the results of tensile testing. Hence, it can be concluded that the horizontal samples showed a ductile failure during tensile testing, while vertical samples exhibited a mix ductile-brittle fracture. Due to the similarity of the WAAM process to the conventional welding processes, such as GMAW or GTAW, it was expected that the fabricated wall using WAAM might provoke anisotropy in tensile properties. Depending on the sources of non-uniformity herein, *i.e*. HAZ grain coarsening, interpass discontinuities, or formation of LBZs, authors may need to come up with various innovative strategies to suppress the measured anisotropy in mechanical properties through optimizing the process parameters, deposition strategy, and/or conducting post-printing heat treatment, which all are subjected to future studies.

## 4. Conclusions

In this study, ER70S-6 low-carbon-low-alloy steel walls were additively manufactured utilizing WAAM technique. Microstructure and mechanical properties of the manufactured component were characterized in different zones and directions. The following conclusions can be drawn:

1. The microstructure of the fabricated wall included two distinct regions across the melt pools, *i.e*., a wide region composed of fine polygonal ferrite and lamellar pearlite phases as the predominant microstructure of each melt pool, and a confined region at the melt pool boundaries containing acicular ferrite along with bainite constituents. Formation of different regions with disparate microstructure in the fabricated part is primarily due to the existence of different temperature gradients and solidification rates from the center of each melt pool towards the boundaries of its adjacent solidified tracks.
2. The printed microstructure was primarily comprised of randomly oriented equiaxed grains possessing a weak cubic texture.

3. The specific fabrication methodology in this study, utilizing advanced STT mode for the material’s deposition and the adopted y-scanning strategy with alternating directions and 3 mm overlap along the x-axis between the successive passes, along with the implemented cooling intervals between the consecutive layers, contributed to the formation of a similar microstructure in all layers of the wall along the vertical direction. This further contributed to the consistency of the localized mechanical properties along the building direction.
4. The average microhardness of the WAAM fabricated component was 160 ± 7 HV, which was roughly consistent along the building direction of the component. However, the Vickers microindentation revealed that at the fusion boundaries, where some fraction of acicular ferrite and bainite micro-constituents were detected, the highest microhardness value was reached (~175 ± 2 HV), whereas the heat affected zone containing coarse ferrite grains revealed the lowest microhardness (~150 ± 1 HV).
5. According to the tensile testing results, comparable yield and ultimate tensile strengths were obtained along the building (vertical) direction and deposition (horizontal) direction of the fabricated WAAM-ER70S-6 part. However, the ductility along the horizontal direction was approximately three times higher than that of the vertical direction. The significantly lower ductility in the building direction was primarily ascribed to the higher density of the interpass regions and the melt pool boundaries in the vertical direction, where a coarse grain structure in the HAZ, formation of localized brittle zones (MA constituent), and plausibly a higher density of interpass discontinuities exist.
6. The fracture surfaces of both vertical and horizontal samples showed a dimple structure characteristic of microvoid coalescence. However, dimples were found to be larger and deeper

on the fracture surface of the horizontal samples, confirming the substantial plastic deformation of the part along the deposition direction as compared to the building direction.

## Acknowledgments

The authors would like to thank the support of Natural Sciences and Engineering Research Council of Canada (NSERC) [grant number RGPIN-2017-04368] for sponsoring this work.

# References

[1] M. Liberini, A. Astarita, G. Campatelli, A. Scippa, F. Montevecchi, G. Venturini, M. Durante, L. Boccarusso, F.M.C. Minutolo, A. Squillace, Selection of optimal process parameters for wire arc additive manufacturing, Procedia CIRP. 62 (2017) 470–474. doi:10.1016/j.procir.2016.06.124.

[2] J. Xiong, G. Zhang, Adaptive control of deposited height in GMAW-based layer additive manufacturing, J. Mater. Process. Technol. 214 (2014) 962–968. doi:10.1016/j.jmatprotec.2013.11.014.

[3] A.C.M. Bekker, J.C. Verlinden, Life cycle assessment of wire + arc additive manufacturing compared to green sand casting and CNC milling in stainless steel DC Power Electrode wire Nozzle Shielding gas Arc Weld pool Workpiece Substrate, J. Clean. Prod. 177 (2018) 438–447. doi:10.1016/j.jclepro.2017.12.148.

[4] D. Ding, Z. Pan, D. Cuiuri, H. Li, A multi-bead overlapping model for robotic wire and arc additive manufacturing (WAAM), Robot. Comput. Integr. Manuf. 31 (2015) 101–110. doi:10.1016/j.rcim.2014.08.008.

[5] C. Shen, Z. Pan, D. Cuiuri, B. Dong, H. Li, In-depth study of the mechanical properties for Fe3Al based iron aluminide fabricated using the wire-arc additive manufacturing process, Mater. Sci. Eng. A. 669 (2016) 118–126. doi:10.1016/j.msea.2016.05.047.

[6] W.E. Frazier, Metal Additive Manufacturing: A Review, J. Mater. Eng. Perform. 23 (2014) 1917–1928. doi:10.1007/s11665-014-0958-z.

[7] S. Das, D.L. Bourell, S.S. Babu, Metallic materials for 3D printing, MRS Bull. 41 (2016) 729–741.

[8] J. Xiong, Z. Yin, W. Zhang, Closed-loop control of variable layer width for thin-walled parts in wire and arc additive manufacturing, J. Mater. Process. Technol. 233 (2016) 100–106. doi:10.1016/j.jmatprotec.2016.02.021.

[9] J. Xiong, Y. Lei, H. Chen, G. Zhang, Fabrication of inclined thin-walled parts in multi-layer single-pass GMAW-based additive manufacturing with flat position deposition, J. Mater. Process. Technol. 240 (2017) 397–403. doi:10.1016/j.jmatprotec.2016.10.019.

[10] N. Shamsaei, A. Yadollahi, L. Bian, S.M. Thompson, An overview of Direct Laser Deposition for additive manufacturing; Part II: Mechanical behavior, process parameter optimization and control, Addit. Manuf. 8 (2015) 12–35. doi:10.1016/j.addma.2015.07.002.

[11] Y. Li, Y. Sun, Q. Han, G. Zhang, I. Horváth, Enhanced beads overlapping model for wire and arc additive manufacturing of multi-layer multi-bead metallic parts, J. Mater. Process. Technol. 252 (2018) 838–848. doi:10.1016/j.jmatprotec.2017.10.017.

[12] X. Chen, J. Li, X. Cheng, B. He, H. Wang, Z. Huang, Microstructure and mechanical properties of the austenitic stainless steel 316L fabricated by gas metal arc additive manufacturing, Mater. Sci. Eng. A. 703 (2017) 567–577. doi:https://doi.org/10.1016/j.msea.2017.05.024.

[13] J. Xiong, Y. Li, R. Li, Z. Yin, In fl uences of process parameters on surface roughness of multi-layer single- pass thin-walled parts in GMAW-based additive manufacturing, J. Mater. Process. Tech. 252 (2018) 128–136. doi:10.1016/j.jmatprotec.2017.09.020.

[14] D. Yang, C. He, G. Zhang, Forming characteristics of thin-wall steel parts by double electrode GMAW based additive manufacturing, J. Mater. Process. Technol. 227 (2016) 153–160. doi:10.1016/j.jmatprotec.2015.08.021.

[15] T. Mohandas, G.M. Reddy, B.S. Kumar, Heat-affected zone softening in high-strength low-

alloy steels, J. Mater. Process. Technol. 88 (1999) 284–294.
[16] C. Zhang, X. Song, P. Lu, X. Hu, Effect of microstructure on mechanical properties in weld-repaired high strength low alloy steel, Mater. Des. 36 (2012) 233–242. doi:10.1016/j.matdes.2011.11.016.
[17] J.R. Joshi, M. Potta, K. Adepu, M.R. Gankidi, R.K. Katta, Influence of Welding Techniques on Heat Affected Zone Softening of Dissimilar Metal Maraging Steel and High Strength Low Alloy Steel Gas Tungsten Arc Weldments, Trans. Indian Inst. Met. 70 (2017) 69–81.
[18] X. Li, X. Ma, S. V Subramanian, C. Shang, R.D.K. Misra, Influence of prior austenite grain size on martensite–austenite constituent and toughness in the heat affected zone of 700MPa high strength linepipe steel, Mater. Sci. Eng. A. 616 (2014) 141–147. doi:https://doi.org/10.1016/j.msea.2014.07.100.
[19] C.L. Davis, J.E. King, Cleavage initiation in the intercritically reheated coarse-grained heat-affected zone: Part I. Fractographic evidence, Metall. Mater. Trans. A. 25 (1994) 563–573. doi:10.1007/BF02651598.
[20] N. Sridharan, M.W. Noakes, A. Nycz, L.J. Love, R.R. Dehoff, S.S. Babu, On the toughness scatter in low alloy C-Mn steel samples fabricated using wire arc additive manufacturing, Mater. Sci. Eng. A. 713 (2018) 18–27. doi:https://doi.org/10.1016/j.msea.2017.11.101.
[21] W. Ou, T. Mukherjee, G.L. Knapp, Y. Wei, T. DebRoy, Fusion zone geometries, cooling rates and solidification parameters during wire arc additive manufacturing, Int. J. Heat Mass Transf. 127 (2018) 1084–1094. doi:https://doi.org/10.1016/j.ijheatmasstransfer.2018.08.111.
[22] A.E. Wilson-Heid, Z. Wang, B. McCornac, A.M. Beese, Quantitative relationship between anisotropic strain to failure and grain morphology in additively manufactured Ti-6Al-4V, Mater. Sci. Eng. A. 706 (2017) 287–294. doi:10.1016/j.msea.2017.09.017.
[23] D. Yang, G. Wang, G. Zhang, Thermal analysis for single-pass multi-layer GMAW based additive manufacturing using infrared thermography, J. Mater. Process. Technol. 244 (2017) 215–224. doi:10.1016/j.jmatprotec.2017.01.024.
[24] M.H. Farshidianfar, A. Khajepour, A. Gerlich, Real-time control of microstructure in laser additive manufacturing, (2016) 1173–1186. doi:10.1007/s00170-015-7423-5.
[25] T. Wang, Y. Zhang, Z. Wu, C. Shi, Microstructure and properties of die steel fabricated by WAAM using H13 wire, Vaccum. 149 (2018) 185–189. doi:10.1016/j.vacuum.2017.12.034.
[26] J.L. Prado-Cerqueira, A.M. Camacho, J.L. Diéguez, Á. Rodríguez-Prieto, A.M. Aragón, C. Lorenzo-Martín, Á. Yanguas-Gil, Analysis of Favorable Process Conditions for the Manufacturing of Thin-Wall Pieces of Mild Steel Obtained by Wire and Arc Additive Manufacturing (WAAM), Mater. (Basel, Switzerland). 11 (2018) 1449. doi:10.3390/ma11081449.
[27] Z. Wang, T.A. Palmer, A.M. Beese, Effect of processing parameters on microstructure and tensile properties of austenitic stainless steel 304L made by directed energy deposition additive manufacturing, Acta Mater. 110 (2016) 226–235. doi:10.1016/j.actamat.2016.03.019.
[28] F. Wang, S. Williams, P. Colegrove, A.A. Antonysamy, Microstructure and Mechanical Properties of Wire and Arc Additive Manufactured Ti-6Al-4V, (n.d.). doi:10.1007/s11661-012-1444-6.
[29] C. V Haden, G. Zeng, F.M. Carter, C. Ruhl, B.A. Krick, D.G. Harlow, Wire and arc additive manufactured steel: Tensile and wear properties, Addit. Manuf. 16 (2017) 115–123.

doi:https://doi.org/10.1016/j.addma.2017.05.010.

[30] V.D. Fachinotti, A. Cardona, B. Baufeld, O. Van der Biest, Finite-element modelling of heat transfer in shaped metal deposition and experimental validation, Acta Mater. 60 (2012) 6621–6630. doi:https://doi.org/10.1016/j.actamat.2012.08.031.

[31] R. Hu, X. Chen, G. Yang, S. Gong, S. Pang, Metal transfer in wire feeding-based electron beam 3D printing: Modes, dynamics, and transition criterion, Int. J. Heat Mass Transf. 126 (2018) 877–887. doi:https://doi.org/10.1016/j.ijheatmasstransfer.2018.06.033.

[32] S. Gook, A. Gumenyuk, M. Rethmeier, Hybrid laser arc welding of X80 and X120 steel grade, Sci. Technol. Weld. Join. 19 (2014) 15–24.

[33] R. Alagesan, T.S. Kumar, Optimization of welding cycle time by establishing full GMAW process (STT and P-GMAW) through a newly designed semi-automatic welding positioner, Int. J. Res. Eng. Technol. 3 (2014).

[34] B.D. DeRuntz, Assessing the benefits of surface tension transfer welding to industry, J. Ind. Technol. 19 (2003) 55–62.

[35] E.K. Stava, The surface tension transfer power source, A new, low-spatter arc welding machine, Weldit-Journal. 1 (1993) 25–29.

[36] W.E. Frazier, Metal Additive Manufacturing: A Review, J. Mater. Eng. Perform. 23 (2014) 1917–1928. doi:10.1007/s11665-014-0958-z.

[37] American Welding Society, Specification for Carbon Steel Electrodes and Rods for Gas Shielded Arc Welding, Am. Weld. Soc. 2005 (2005) 44. doi:978-0-87171-530-2.

[38] A.W.S.A. 28/A5. 28M, Specification for Low Alloy Steel Electrodes and Rods for Gas Shielded Arc Welding, (2005).

[39] ASTM Int., Standard Test Methods for Tension Testing of Metallic Materials 1, Astm. i (2015) 1–27. doi:10.1520/E0008.

[40] P.A. Colegrove, H.E. Coules, J. Fairman, F. Martina, T. Kashoob, H. Mamash, L.D. Cozzolino, Microstructure and residual stress improvement in wire and arc additively manufactured parts through high-pressure rolling, J. Mater. Process. Technol. 213 (2013) 1782–1791. doi:10.1016/j.jmatprotec.2013.04.012.

[41] A.S. Haselhuhn, B. Wijnen, G.C. Anzalone, P.G. Sanders, J.M. Pearce, In situ formation of substrate release mechanisms for gas metal arc weld metal 3-D printing, J. Mater. Process. Technol. 226 (2015) 50–59. doi:10.1016/j.jmatprotec.2015.06.038.

[42] L.B. Godefroid, L.C. Cândido, R.V.B. Toffolo, L.H.S. Barbosa, Microstructure and mechanical properties of two API steels for iron ore pipelines, Mater. Res. 17 (2014) 114–120. doi:10.1590/S1516-14392014005000068.

[43] J.H. Tweed, J.F. Knott, Effect of reheating on microstructure and toughness of C–Mn weld metal, Met. Sci. 17 (1983) 45–54. doi:10.1179/030634583790427603.

[44] C. Zhang, Y. Li, M. Gao, X. Zeng, Wire arc additive manufacturing of Al-6Mg alloy using variable polarity cold metal transfer arc as power source, Mater. Sci. Eng. A. 711 (2018) 415–423. doi:10.1016/j.msea.2017.11.084.

[45] K. V Yang, Y. Shi, F. Palm, X. Wu, P. Rometsch, Columnar to equiaxed transition in Al-Mg(-Sc)-Zr alloys produced by selective laser melting, Scr. Mater. 145 (2018) 113–117. doi:https://doi.org/10.1016/j.scriptamat.2017.10.021.

[46] V.B. Biscuola, M.A. Martorano, Mechanical Blocking Mechanism for the Columnar to Equiaxed Transition, Metall. Mater. Trans. A. 39 (2008) 2885–2895. doi:10.1007/s11661-008-9643-x.

[47] S. Suryakumar, K.P. Karunakaran, U. Chandrasekhar, M.A. Somashekara, A study of the

mechanical properties of objects built through weld-deposition, Proc. Inst. Mech. Eng. Part B J. Eng. Manuf. 227 (2013) 1138–1147. doi:10.1177/0954405413482122.

[48] B.E. Carroll, T.A. Palmer, A.M. Beese, Anisotropic tensile behavior of Ti-6Al-4V components fabricated with directed energy deposition additive manufacturing, Acta Mater. 87 (2015) 309–320. doi:10.1016/j.actamat.2014.12.054.

[49] L. Thijs, M.L.M. Sistiaga, R. Wauthle, Q. Xie, J.-P. Kruth, J. Van Humbeeck, Strong morphological and crystallographic texture and resulting yield strength anisotropy in selective laser melted tantalum, Acta Mater. 61 (2013) 4657–4668.

[50] Q. Zhang, J. Chen, Z. Zhao, H. Tan, X. Lin, W. Huang, Microstructure and anisotropic tensile behavior of laser additive manufactured TC21 titanium alloy, Mater. Sci. Eng. A. 673 (2016) 204–212. doi:10.1016/j.msea.2016.07.040.

[51] E.O. Hall, The Deformation and Ageing of Mild Steel: III Discussion of Results, Proc. Phys. Soc. Sect. B. 64 (1951) 747–753. doi:10.1088/0370-1301/64/9/303.

[52] A. Lopez, R. Bacelar, I. Pires, T.G. Santos, J.P. Sousa, L. Quintino, Non-destructive testing application of radiography and ultrasound for wire and arc additive manufacturing, Addit. Manuf. 21 (2018) 298–306. doi:https://doi.org/10.1016/j.addma.2018.03.020.

[53] B.A. Szost, S. Terzi, F. Martina, D. Boisselier, A. Prytuliak, T. Pirling, M. Hofmann, D.J. Jarvis, A comparative study of additive manufacturing techniques: Residual stress and microstructural analysis of CLAD and WAAM printed Ti-6Al-4V components, Mater. Des. 89 (2016) 559–567. doi:10.1016/j.matdes.2015.09.115.

[54] A. Kudzal, B. McWilliams, C. Hofmeister, F. Kellogg, J. Yu, J. Taggart-Scarff, J. Liang, Effect of scan pattern on the microstructure and mechanical properties of Powder Bed Fusion additive manufactured 17-4 stainless steel, Mater. Des. 133 (2017) 205–215. doi:10.1016/j.matdes.2017.07.047.

[55] B.C. Kim, S. Lee, N.J. Kim, D.Y. Lee, Microstructure and local brittle zone phenomena in high-strength low-alloy steel welds, Metall. Trans. A. 22 (1991) 139–149. doi:10.1007/BF03350956.

[56] O.M. Akselsen, Ø. Grong, J.K. Solberg, Structure–property relationships in intercritical heat affected zone of low-carbon microalloyed steels, Mater. Sci. Technol. 3 (1987) 649–655. doi:10.1179/mst.1987.3.8.649.

[57] Y. Li, T.N. Baker, Effect of morphology of martensite–austenite phase on fracture of weld heat affected zone in vanadium and niobium microalloyed steels, Mater. Sci. Technol. 26 (2010) 1029–1040. doi:10.1179/026708309X12512744154360.

[58] A. Lambert, A. Lambert, J. Drillet, A.F. Gourgues, T. Sturel, A. Pineau, Microstructure of martensite–austenite constituents in heat affected zones of high strength low alloy steel welds in relation to toughness properties, Sci. Technol. Weld. Join. 5 (2000) 168–173. doi:10.1179/136217100101538164.

[59] N. Huda, A.R.H. Midawi, J. Gianetto, R. Lazor, A.P. Gerlich, Influence of martensite-austenite (MA) on impact toughness of X80 line pipe steels, Mater. Sci. Eng. A. 662 (2016) 481–491. doi:https://doi.org/10.1016/j.msea.2016.03.095.

[60] X. Shi, S. Ma, C. Liu, Q. Wu, J. Lu, Y. Liu, W. Shi, Selective laser melting-wire arc additive manufacturing hybrid fabrication of Ti-6Al-4V alloy: Microstructure and mechanical properties, Mater. Sci. Eng. A. 684 (2017) 196–204. doi:10.1016/j.msea.2016.12.065.

[61] X. Xu, S. Ganguly, J. Ding, S. Guo, S. Williams, F. Martina, Microstructural evolution and mechanical properties of maraging steel produced by wire+arc additive manufacture process, Mater. Charact. (2017). doi:10.1016/j.matchar.2017.12.002.

[62] L.E. Murr, S.A. Quinones, S.M. Gaytan, M.I. Lopez, A. Rodela, E.Y. Martinez, D.H. Hernandez, E.Y. Martinez, F. Medina, R.B. Wicker, Microstructure and mechanical behavior of Ti–6Al–4V produced by rapid-layer manufacturing, for biomedical applications, J. Mech. Behav. Biomed. Mater. 2 (2009) 20–32. doi:10.1016/j.jmbbm.2008.05.004.

[63] L.E. Murr, E. V. Esquivel, S.A. Quinones, S.M. Gaytan, M.I. Lopez, E.Y. Martinez, F. Medina, D.H. Hernandez, E.Y. Martinez, J.L. Martinez, S.W. Stafford, D.K. Brown, T. Hoppe, W. Meyers, U. Lindhe, R.B. Wicker, Microstructures and mechanical properties of electron beam-rapid manufactured Ti–6Al–4V biomedical prototypes compared to wrought Ti–6Al–4V, Mater. Charact. 60 (2009) 96–105. doi:10.1016/j.matchar.2008.07.006.

# Appendix II

# On Microstructure and Mechanical Properties of a Low-Carbon Low-Alloy Steel Block Fabricated by Wire Arc Additive Manufacturing[9]

## Preface

A version of this manuscript has been submitted in the Journal of the Materials Engineering and Performance, 2020. I am the first and corresponding author of the papers. Along with the co-authors, Mahya Ghaffari, Alireza Vahedi Nemani, and Dr. Ali Nasiri, I investigate ER70S-6 low-carbon low-alloy steel block was manufactured by WAAM method, utilizing a gas metal arc welding (GMAW) torch translated by a six-axis robotic arm. The microstructure and mechanical anisotropy of the fabricated part were investigated and compared with the thin wall fabricated sample in the previous chapter. I prepared methodology, experimental, formal analysis, and the first original draft of the manuscript and subsequently revised the manuscript based on the coauthors' feedback and also the peer review process. The co-authors, Mahya Ghaffari and Alireza Vahedi Nemani helped in the experimental procedure and writing the initial draft. Moreover, Dr. Ali Nasiri helped in conceptualization, design, project administration, and supervision, review & editing of the manuscript.

---

[9] M. Rafieazad, A. Vahedi Nemani, M. Ghaffari, A. Nasiri, On Microstructure and Mechanical Properties of a Low-Carbon Low-Alloy Steel Block Fabricated by Wire Arc Additive Manufacturing, the journal of the Materials Engineering and Performance, 2020, https://doi.org/10.1007/s11665-021-05568-9 (IPF=1.652)

## Abstract

In this study, wire arc additive manufacturing process is employed to fabricate a low-carbon low-alloy steel block, using an ER70S-6 solid wire. Three sets of samples with different orientations, including perpendicular (Vertical), parallel (Horizontal), and 45° (45-degree) relative to the deposition plane, were prepared in order to investigate the anisotropy in mechanical properties and microstructure of the fabricated part. Both Horizontal and 45-degree samples showed a uniform microstructure containing mostly ferritic grains with a small volume fraction of pearlite at their grain boundaries. Differently, a periodic microstructure was detected in the Vertical sample, consisting of a combination of acicular ferrite, bainite, and allotriomorphic ferrite formed in the interlayer regions in addition to polygonal ferrite within the melt pools' center. Moreover, the uniaxial tensile and Charpy impact results exhibited isotropic tensile, yield, elongation, and impact properties for both Horizontal and 45-degree samples; however, the Vertical sample showed a lower mechanical performance. The improved mechanical properties of the Horizontal and 45-degree samples were correlated to their uniform ferritic microstructure.

**Keywords:** Additive Manufacturing (AM); Wire Arc Additive Manufacturing (WAAM); Low-Carbon Low-Alloy Steel; Microstructure; Mechanical Properties.

## 1. Introduction

Additive Manufacturing (AM) is a rapidly developing technology by which 3D components are produced through layer-by-layer deposition of the metallic, polymeric, or even ceramic materials using feedstock powder particles or solid wires [1]. The metal AM process can be categorized based on the implemented heating source into two main categories, *i.e.*, beam-based methods, such as selective laser ,melting (SLM) or electron beam melting (EBM), and arc-based technologies such as wire arc additive manufacturing (WAAM) [2]. Although the WAAM technology has not been completely industrialized yet, it has gained substantial attention in different industries, including aerospace, marine, and oil and gas for the fabrication of meter-scale metallic components for structural applications [2]. As compared to other AM technologies, WAAM is mainly identified by its low capital cost, unlimited build envelope, and significantly high deposition rate (3-8 kg/h), leading to substantial reduction in the fabrication time [2]. The common WAAM processes implement either a gas metal arc (GMA), gas tungsten arc (GTA), or plasma arc (PA) as the heat source [3–5]. Cold metal transfer (CMT) is also a new variation of GMA technology and widely adopted as the heat source to produce WAAM components [6].

Despite the cost-saving advantage of WAAM technology in fabrication of large-scale components from a wide range of materials, the high heat input and nonuniform solidification rate associated with the process lead to microstructural inhomogeneity and the anisotropy of the mechanical properties [3,7]. Wu *et al.* [8] reported a highly anisotropic tensile strength for a thin wall 316 L stainless steel fabricated by GMA-WAAM. It has been reported that the high temperature gradient, fast cooling rate, and sequential heating and cooling cycles experienced by components during WAAM can impact the final microstructure, leading to a heterogeneous grain structure and anisotropic mechanical properties [9–11]. Even reducing the heat input by implementing the CMT-WAAM technology for the fabrication of a Cr-Mn type steel was not found to be an effective approach to hinder the anisotropy in mechanical properties [12]. It is well accepted that the WAAM processing parameters directly impact the in-situ thermal history during solidification of the part, determining the final microstructure and ultimately the part's mechanical performance [13,14]. As one of the less studied processing parameters, scanning or deposition pattern is an important factor that affects the thermal history, microstructural characteristics, and mechanical performance of AM components [15]. In the WAAM technology, processing parameters, such as heat input [16], post-printing thermal treatment [17], and size of the deposited wire [18] have been widely studied to tailor the microstructure and mechanical properties of the fabricated part. However, only limited research in the literature has attempted to investigate the deposition strategy's impact on the microstructural modification and mechanical properties, especially for low-carbon low-alloy steels with broad applications for the pipeline, casting, and forgings [19]. Focusing on investigating the impact of deposition strategy on the microstructural modifications and the resultant mechanical properties, the present study has adopted a stripe scanning strategy with 90° rotation between consecutive layers to fabricate an ER70S-6 block using WAAM technology as compared to all-y scanning strategy commonly reported in the literature. The impact of the adopted deposition strategy on anisotropy in mechanical properties was investigated, utilizing tensile testing, impact testing, and fractography at different orientations of the fabricated block, *i.e.*, vertical, horizontal, and 45° relative to the sample's building plane.

## 2. Experimental Procedure

### 2.1. Materials and fabrication procedures

A cuboid block of ER70S-6 alloy (Figure A2.1b) was fabricated following a stripe strategy with a 90° rotation between successive layers using a robotic-controlled WAAM platform as shown in Figure A2.1a, equipped with a GMA torch. In order to minimize the surface irregularities and heat input during the process, an advanced surface tension transfer (STT) mode was employed. Each deposited layer in X-Y plane contains 40 individual beads with a length of 120 mm and a 3 mm center-to-center overlap, leading to the overall width of 120 mm. The total height of the part is 200 mm, comprising 40 consecutive layers with an average height of ~5 mm for each deposited layer. To control the impacts of complex thermal cycles associated with the WAAM process on the microstructure of the previously deposited layers, after each X-Y layer deposition, a 10-min interlayer dwell time was applied during the fabrication. Moreover, the presented schematic pattern in Figure A2.1c shows the positions where Horizontal, Vertical, and 45-degree tensile and impact test samples were machined from the WAAM fabricated block. A 0.035 in. diameter ER70S-6 wire (0.06–0.15 wt.% C, 1.40–1.85 wt.% Mn, 0.80–1.15 wt.% Si, and Bal. Fe) was utilized as the feedstock material. The detailed process parameters can be found in the previous authors' publication [7].

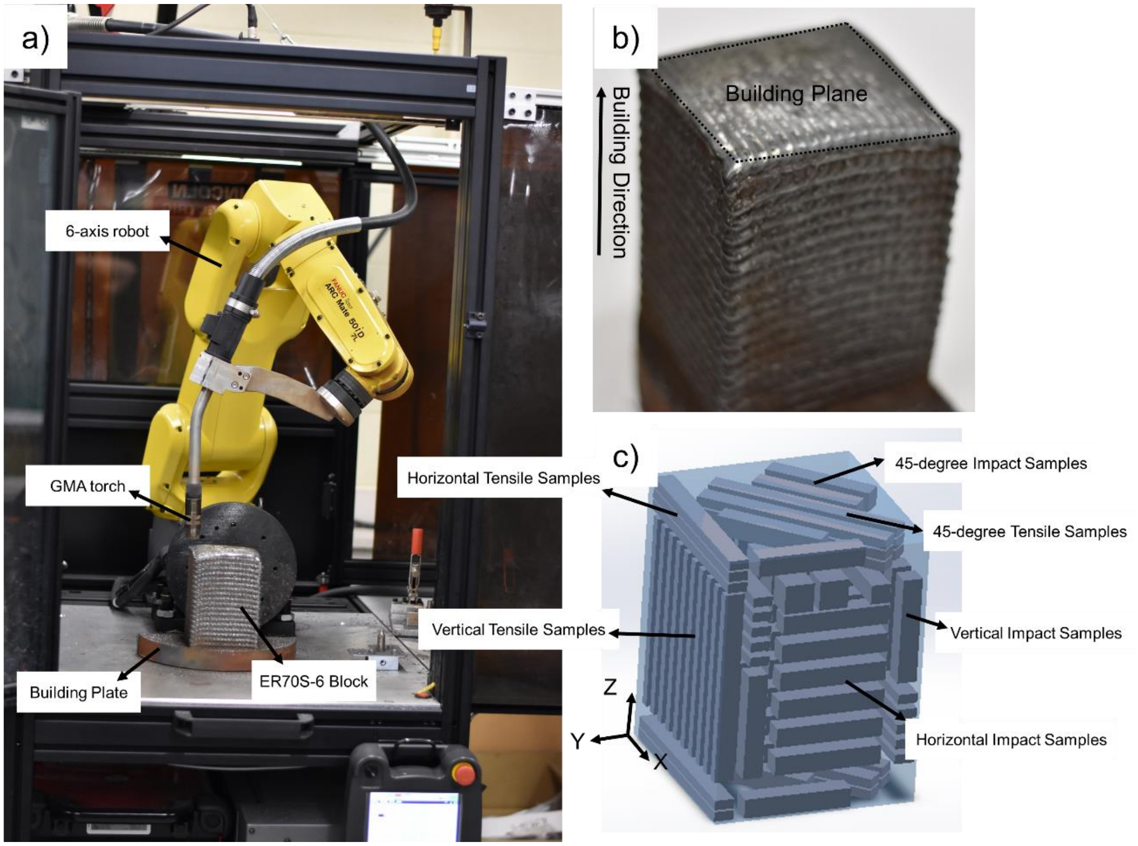

Figure A2. 1. (a) The robotic WAAM platform, (b) the fabricated block using WAAM method, (c) schematic drawing of the WAAM-ER70S-6 steel block showing the position of tensile and impact testing samples.

## 2.2. Microstructural Characterization and Mechanical Properties

The microstructural characterization and investigation of possible formed microstructural inhomogeneity in the fabricated component were carried out on three samples prepared from different orientations of parallel, perpendicular, and 45° with respect to the deposition plane (X-Y), denoted by Horizontal, Vertical, and 45-degree samples, respectively. Standard grinding and polishing procedures for steels were implemented using a Tegramin-30 Struers auto-grinder/polisher. In order to reveal the microstructure, the polished samples were etched using 5% Nital as the etchant. The microstructure of all samples was investigated using an optical microscope (Nikon Eclipse 50i), and a field emission scanning electron microscope (SEM) (FEI MLA 650FEG). Electron backscatter diffraction (EBSD) analysis was also performed over a large area of 4000 × 600 $\mu m^2$ with a step size of 1.5 μm and a tilt angle of 70°, using a Nordlys II HKL EBSD detector, Oxford Instruments. The tensile test samples were made based on the ASTM E8m-04 standard sub-size specimen [20] and tested using an Instron load frame at the crosshead speed of 8 mm/min, and an extensometer to record strain data. The samples for the Charpy impact tests were made according to ASTM E23–18 [21]. The absorbed energy by each sample during fracture was obtained at six different temperatures, *i.e.* -146 °C, -100 °C, -20 °C, 0 °C, 23 °C (room temperature), and 98 °C using an automatic impact testing apparatus (a JBS-300 machine) with the maximum capacity of 300 J. The fractured surfaces of both tensile and impact test samples from all three directions were also analyzed using the SEM.

## 3. Results and Discussion

### 3.1. Microstructural Characterization

Figure A2.2 shows the cross-sectional overview of the WAAM-ER70S-6 steel block taken from different orientations (from prepared gauge length of the tensile samples prior to testing), revealing the microstructural variations resulting from the implemented 90° rotation deposition strategy. Optical micrographs in Horizontal and 45-degree directions (Figure A2.2a and b) illustrate a uniform microstructure with almost no imperfection, such as pores and cracks, within the entire cross-section, indicating the formation of a sound and defect-free AM part on the X-Y plane with a clear metallurgical bonding between the neighboring tracks. The microstructures of the Horizontal and 45-degree samples were characterized with a relatively uniform microstructure without a significant grains morphology alternation between the tracks, attributed to the high interlayer temperature and consequently the lower interpass cooling rates, resulted from the center-to-center overlap of the tracks in the deposition (X-Y) plane. However, the Vertical sample (Figure A2.2c) shows a periodic nonuniform microstructure containing a variety of interlayer discontinuities, such as lack of fusion and porosities, formed particularly along the inter-layers' regions perpendicular to the building direction. A banded structure comprised of polygonal ferrite and a mixture of acicular ferrite (AF), bainite (B), and allotriomorphic ferrite (α) (as shown in Figure A2.3) was found to form between consecutive layers, resulting from the nonuniform cooling rate of each melt pool in the areas near to its boundaries as compared to the center. Moreover, the Vertical sample has experienced a 10 min dwelling time between deposition of successive layers along the Z-direction, resulting in the nonhomogeneous energy input and consequently the formation of the periodic microstructure as shown in Figure A2.2c. Similar observations were reported in a previous study by Ge *et al*. [22] for a WAAM-2Cr13 thin wall fabricated with a long dwelling time (210 s), which was characterized by a periodic microstructure composed of martensite laths in a ferritic matrix. Differently, adopting a short dwelling time (30 s) during fabrication was reported to create a uniform ferritic microstructure [22]. It is notable that the height of the banded microstructures is similar to the height of each deposited layer (~3 mm).

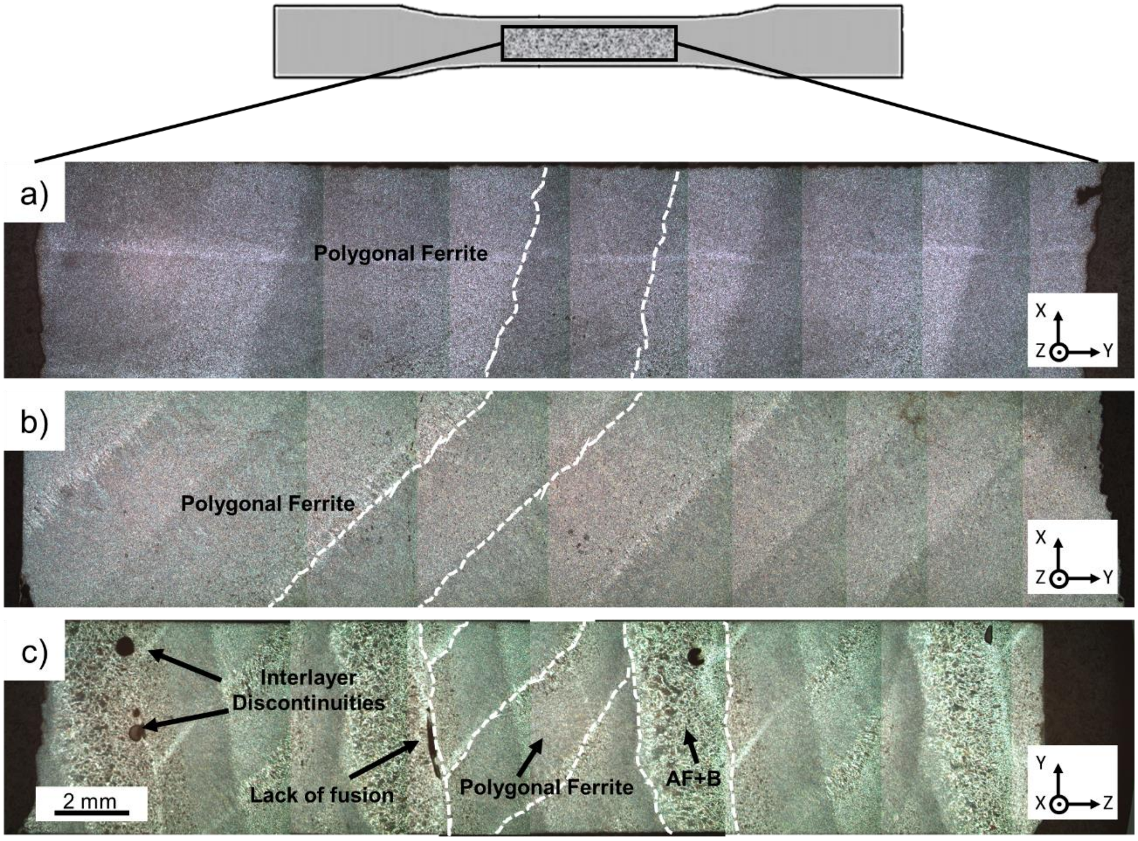

Figure A2. 2. Optical micrographs taken from the overall cross-sectional overview of the (a) Horizontal, (b) 45-degree, and (c) Vertical samples.

Figure A2.3a schematically represents two consecutive deposited beads along the Z-direction, showing three distinguishable regions with distinct microstructures, *i.e.*, melt pool center, melt pool boundary, and a heat affected zone (HAZ) in the previously deposited layer (Bead 1). Figure A2.3b shows the overall microstructure of the Vertical sample in the vicinity of a melt pool' boundary, in which two successive beads and their corresponding HAZ are noticeable, revealing the variation of microstructure from an area adjacent to a fusion line (Figure A2.3d) towards the middle of the melt pool (Figure A2.3e). The microstructural transition from a uniform and fine polygonal ferritic (F) structure at the center of the melt pool to a combination of acicular ferrite (AF), bainite (B), and allotriomorphic ferrite (shaded areas in Figure A2.3d) microstructure in the melt pool boundary (Figures A2.3c and A2.3d) is evident. Moving closer to the fusion line in the melt pool boundary areas revealed columnar grains of acicular ferrite, bainite, and allotriomorphic ferrite, elongated along the heat dissipation direction (the red arrow in Figure A2.3d) during solidification. However, the dominant microstructure of each melt pool is fine polygonal ferrite with a slight volume fraction of pearlite on the grain boundaries (Figure A2.3e).

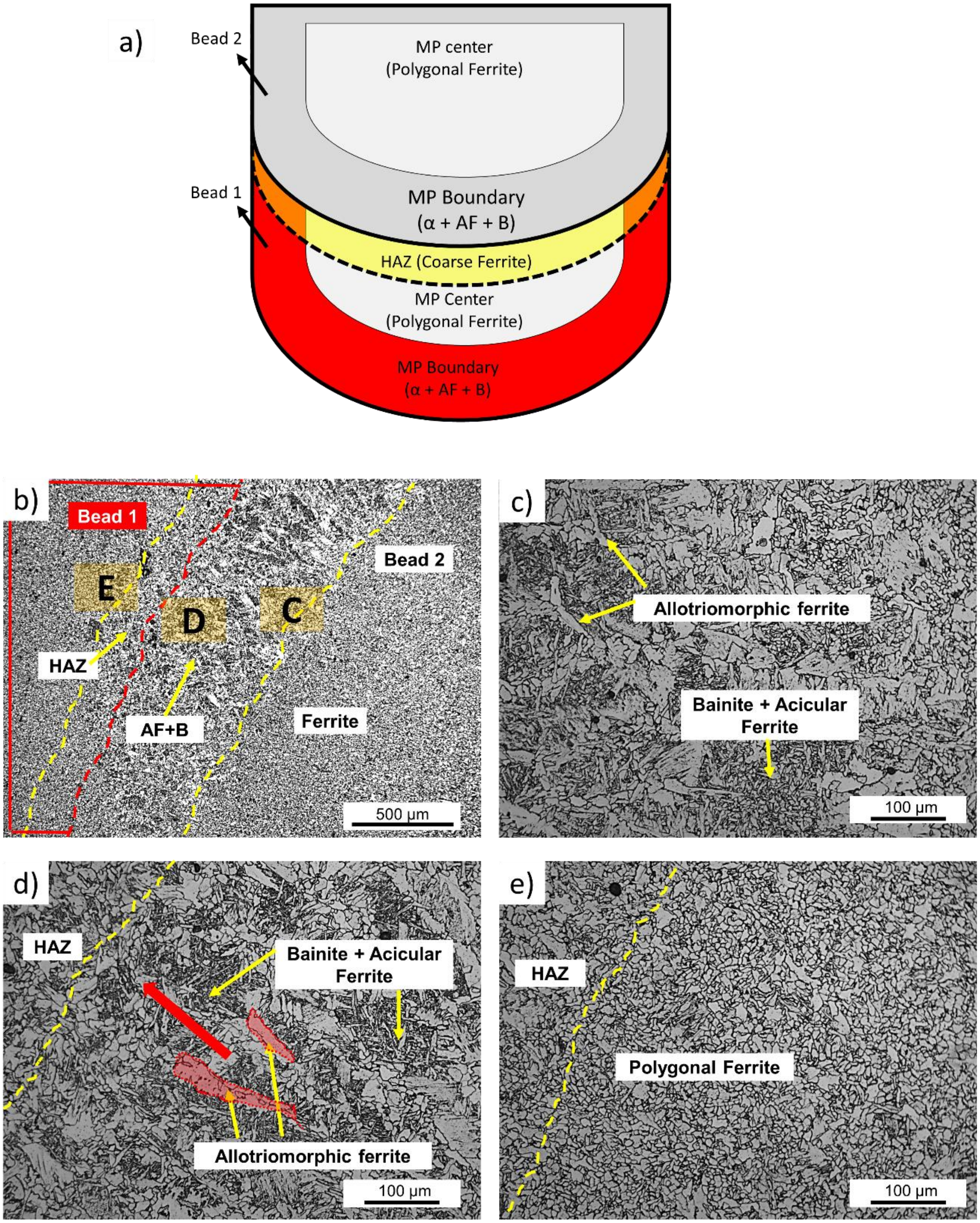

Figure A2. 3. (a) Schematic representation of two consecutive deposited beads, Optical micrographs taken from (b) the fusion line and center of the melt pool, and higher magnification of the (c) melt pool boundary shown as C in (b), (d) fusion line shown as D in (b), and (e) melt pool center shown as E in (b).

In complementary to the performed optical microscopy investigation, SEM and EBSD analysis were also carried out (Figure A2.4) for detailed microstructural characterization of the samples. The EBSD inverse pole figure (IPF) map from the entire microstructure between two adjacent layers along the building direction (Z-axis) (Figure A2.4a) shows the overall grains' orientation/misorientation, size, and aspect ratio. The variation of the grain size and morphology can be clearly seen along the entire cross section in the Vertical sample. In Figure A2.4a, there are regions (region B) with coarser grain structure with the average grain size of 38.88±1.54 µm located at the melt pool boundaries (Figure A2.4b). The SEM micrographs from the same area (Figure A2.4$b_1$) revealed the formation of the nonequilibrium AF + B constituents adjacent to the melt pool boundary, resulted from the faster cooling rate of the fusion zone at the melt pool boundaries as compared to the center of the melt pool. Differently, the melt pool's center was characterized by equiaxed (aspect ratio < 3) and randomly oriented ferritic grain structure with the average grain size of 7.23±0.34 µm (Figure A2.4d). The SEM micrograph from the melt pool center (Figure A2.4$d_1$) confirmed the formation of the PF grains with a very small volume fraction of lamellar pearlite (P) (11.44 ± 0.47%) formed at the grain boundaries, which is the predominant microstructure over the entire fabricated block. The grain structure in HAZ (Figures A2.4c and A2.4$c_1$) consists of coarser ferrite grains (10.86±0.25 µm) as compared to the center of the melt pool, which is a direct consequence of the grain boundaries migration in the previously deposited bead, triggered by the significantly high temperature from deposition of a new layer [23].

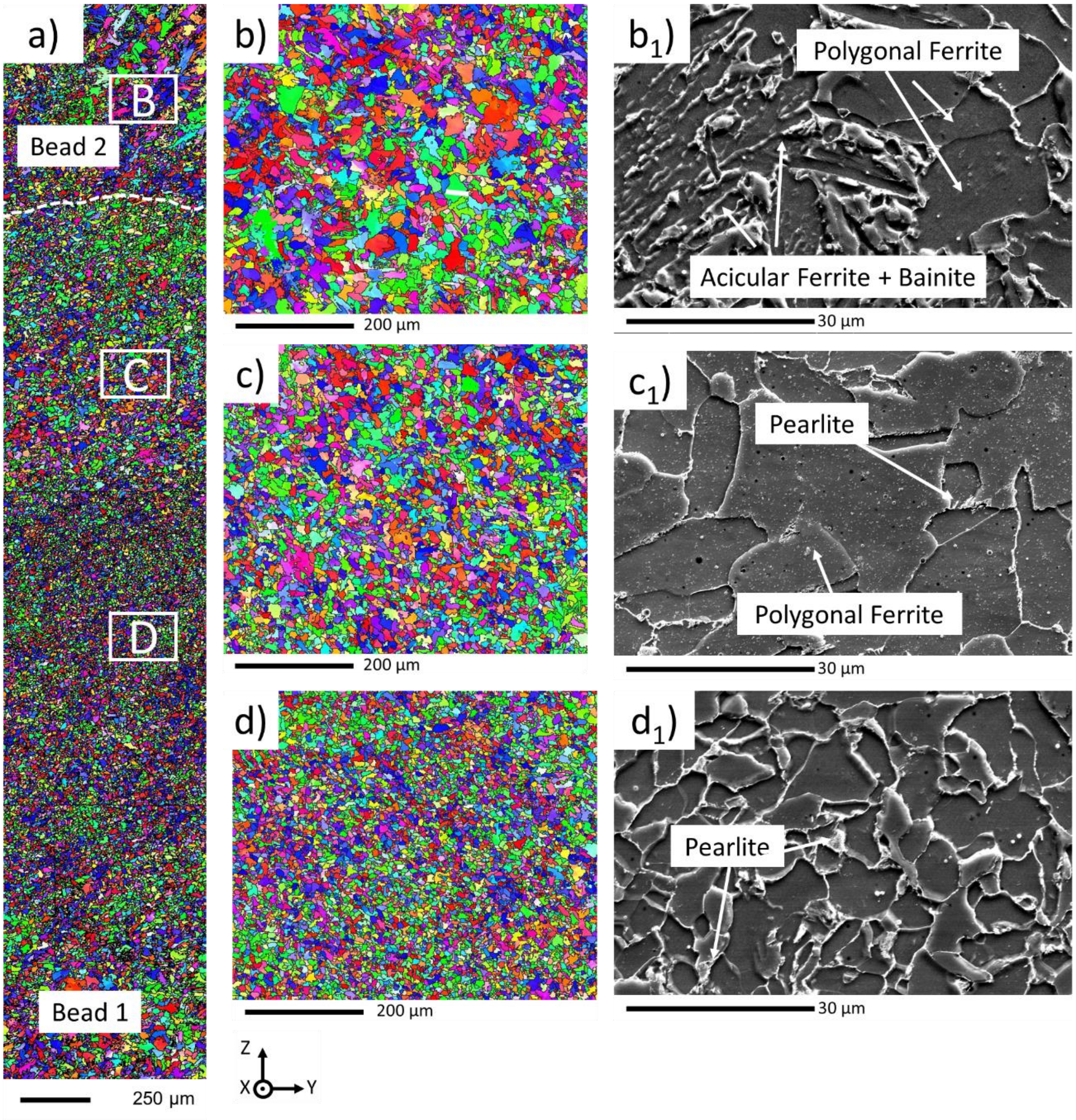

Figure A2. 4. The EBSD inverse pole figure maps taken from (a) the entire cross-sectional overview along building direction of the WAAM-ER70SR-6 sample, (b) the higher magnification of the enclosed area in (a) noted by B, (b1) the SEM image from the same area of the (b), (c) the higher magnification of the enclosed area in (a) noted by C, (c1) the SEM image from the same area of the (c), (d) the higher magnification of the enclosed area in (a) noted by D, (d1) the SEM image from the same area of the (d).

### 3.2. Mechanical Properties

The orientation of tensile and impact testing samples in the horizontal, vertical, and 45° directions in the fabricated block is presented in Figure A2.1c. Figure A2.5a shows the engineering tensile stress-strain graphs for the Vertical, Horizontal, and 45-degree samples. At each orientation, at least five samples were tested to ensure reproducibility of the results.

The majority of the tensile graphs displayed the common yield point phenomenon frequently seen in low-carbon and mild steels [24,25]. A similar discontinuous yielding characteristic has been reported for other WAAM fabricated ER70S-6 parts as well [3,7,25]. Along the deposition plane, the Horizontal and 45-degree samples showed a uniform deformation with a similar ductile failure during tensile testing. Moreover, as shown in Figure A2.2a and A2.2b, since the Horizontal and 45-degree samples have a uniform microstructure, variation of MP boundaries orientation with respect to the tensile direction (90° and 45° for Horizontal and 45-degree sample, respectively) has not affected the ultimate tensile strength (UTS), yield strength (YS), and elongation of the samples. As a result, similar average UTS, YS, and elongation values (406 ± 23 MPa, 524 ± 13 MPa, and 37 ± 3%, respectively) were obtained for both samples, confirming the isotropic mechanical performance of the fabricated block on its X-Y plane. On the other hand, the average UTS, YS, and elongation values of the Vertical samples were found to be lower than those of the other two samples (386 ± 26 MPa, 405 ± 22 MPa, and 10 ± 2%, respectively), confirming the anisotropic tensile properties of the WAAM manufactured block. The lower tensile strength and elongation properties of the Vertical sample can be correlated to either microstructural variations across the building direction or pre-existing interlayer imperfections, which are, in turn, associated with the heat dissipation characteristics and the implemented interlayer dwelling time during manufacturing of the part, consistent with the previous studies [3,7,9,22].

The Charpy V-notch impact results for the Horizontal, 45-degree, and Vertical samples performed at six different temperatures of -146 °C, -100 °C, -20 °C, 0 °C, 23 °C (room temperature), and 98 °C are given in Fig 5b. The fitted curves to the obtained experimental data points represent cubic functions with the error parameter value ($R^2$) above 0.90, featuring a Ductile to Brittle Transition Temperature (DBTT) for the fabricated alloy at ~ −20 °C. The results also confirm that the DBTT is constant and independent from the samples' orientations. The average values of the absorbed energy for the Horizontal and 45-degree samples at all seven temperatures are higher than those of the Vertical sample, ascribed to their uniform ferritic and defect-free structure. The formation of uniform and smaller ferritic grains in Horizontal and 45-degree samples promotes both yield strength and tensile strength and further improves ductile fracture mechanisms, while the Vertical sample with periodic microstructure of acicular ferrite and bainitic are expected to have a more brittle nature and be more susceptible to crack propagation [26,27].

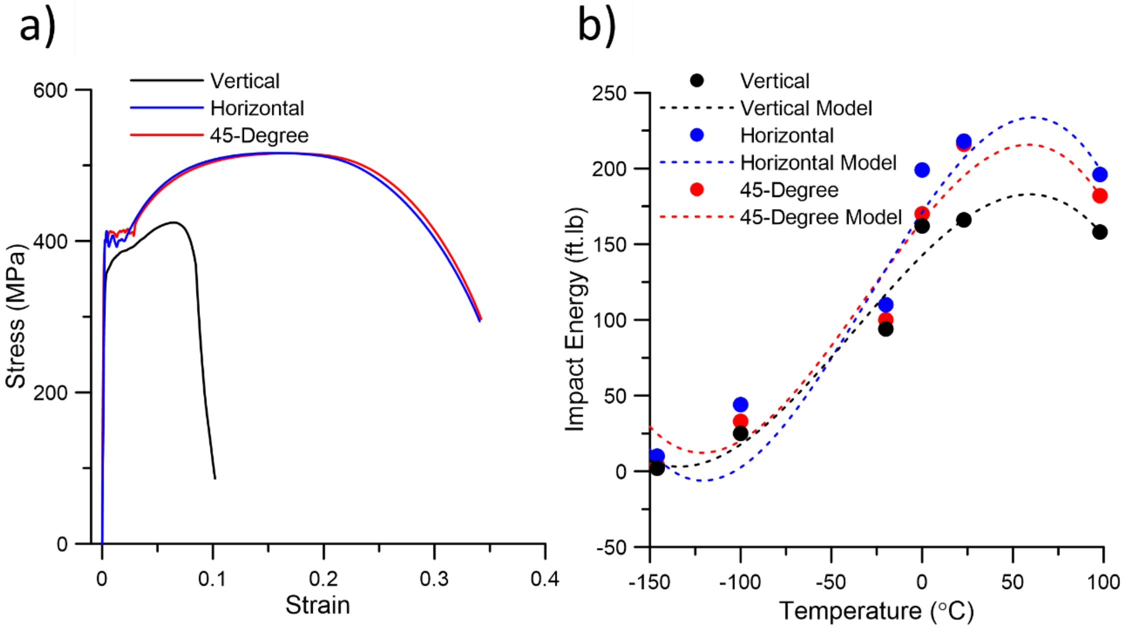

Figure A2. 5. (a) the stress-strain curves and (b) the absorbed impact energy for the Horizontal, Vertical, and 45-degree samples

To further investigate the fracture performance of the fabricated samples, the fracture surfaces of all samples after uniaxial tensile and impact testing were analyzed and shown in Figure A2.6. The SEM fractographs of the Horizontal and 45-degree samples (Figure A2.6a and b) mainly showed the characteristics of dimple-like fracture, confirming an extended plastic deformation and ductile fracture. Differently, the Vertical sample (Figure A2.6c) showed inclusions combined with smaller and shallower dimples, indicating that it experienced a lower degree of plastic strain before failure. Using Energy Dispersive-X-ray Spectroscopy (EDS), the inclusions were characterized to be mainly composed of $MnO$-$SiO_2$, commonly reported to form in ferrous alloys weld metals [28]. These inclusions in the Vertical sample can be formed due to the slag entrapment between successive layers. A comparison between the fracture surfaces after the impact test at room temperature revealed some nearly flat surfaces in the Vertical samples (Figure A2.6f), representing relatively fast crack propagation and occurrence of a rapid cleavage fracture [29]. However, the Horizontal and 45-degree samples (Figures A2.6d and e) showed no cleavage on their fractured surfaces. Another noticeable high absorbed energy feature on the fracture surfaces of the Horizontal and 45-degree samples is the secondary cracks, resulted from energy dissipation in the material during the dislocations movements [30].

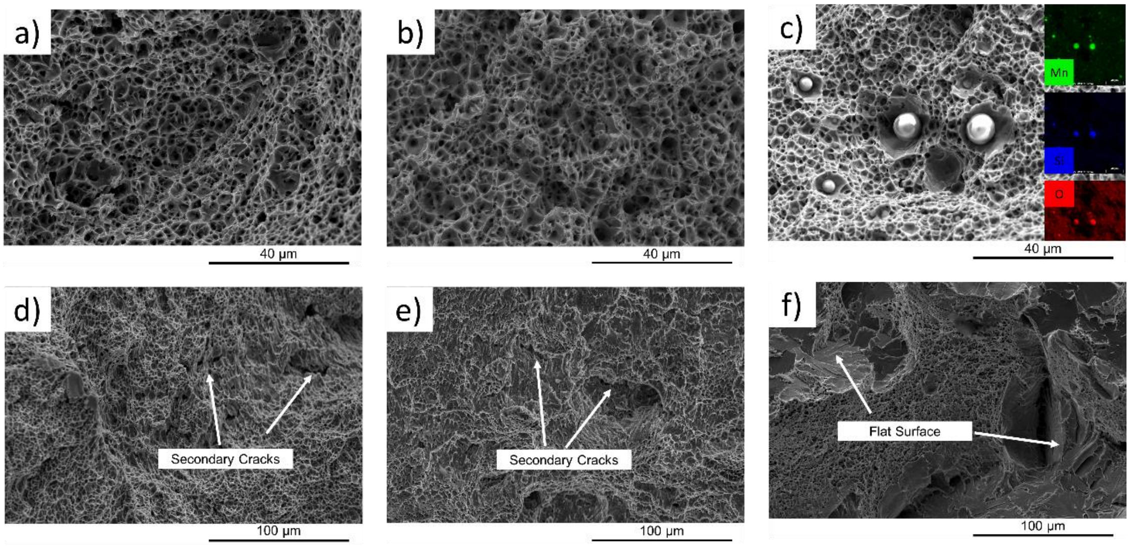

Figure A2. 6. SEM micrographs taken from the fractured surfaces after uniaxial tensile testing of (a) Horizontal, (b) 45-degree, and (c) Vertical samples and after impact testing of (d) Horizontal, (e) 45-degree, and (f) Vertical samples at room temperature (23 °C).

### 3.3. Comparisons with the WAAM-ER70S-6 thin-wall fabricated using all-y scanning strategy

To better understand the impact of deposition strategy and sample size on the microstructure and mechanical properties of the fabricated block, comparisons were made between the microstructure and mechanical properties of the block fabricated with a 90° deposition strategy studied herein and a thin-wall fabricated by all-y scanning strategy studied in the authors' previous works [3,7].

The formation of the AF+B microstructure near the melt pool boundaries and fine polygonal ferrite with small amount of pearlite in its grain boundaries as a primary microstructure of the melt pool center have been also observed in a WAAM-ER70S thin-wall fabricated using all-y scanning strategy [3,7]. However, using a 90° deposition strategy led to the formation of the periodic microstructure along the building direction, which was not detected in the thin-wall fabricated sample [3,7]. Moreover, the grain size variations for the extreme fine and coarse regions of the thin-wall sample were reported to be in the range of ~4.94 µm to ~15.76 µm, respectively.

The thin-wall sample with 22 mm width has experienced significantly lower heat accumulation and a faster cooling rate as compared to the block sample with 120 mm width. Therefore, in the thin-wall sample, all the deposited layers have faced almost the same thermal cycles, giving rise to a finer and more uniform microstructure than the block sample.

Furthermore, the anisotropy in mechanical properties of the Horizontal and Vertical samples detected for the block sample was also detected in the thin-wall sample. The reported average values of UTS, YS, and elongation for Horizontal and Vertical samples were 396 ± 26 MPa, 503 ± 21 MPa, 35 ± 2%, 402 ± 23 MPa, 502 ± 19 MPa, 12 ± 3%, respectively [3,7]. The measured lower UTS and YS values for the Vertical sample in the block part than those in the thin-wall sample can be attributed to the formation of the periodic microstructure with sharp boundaries between the deposited layer and also the formation of substantial interpass defects in the vertical direction of the block sample. Moreover, the formation of the martensite–austenite (MA) constituent within the bainite lamellar structures was reported as a contributing factor to the improved tensile strength and degradation of the toughness in the thin-wall sample [3,7]. However, in this study, larger geometrical features of the fabricated block create higher heat accumulation, leading to its slower cooling rate during solidification, which would consequently impact the final microstructure, level of interpass discontinuities, and suppress the MA micro-constituent formation [31,32].

## 4. Conclusions

In this study, a block of ER70S-6 low-carbon low-alloy steel was fabricated utilizing the WAAM technique with deposition strategy of 90° rotation between successive layers. Microstructure and mechanical characteristics of the fabricated part were measured at different orientations with respect to the deposition plane and compared with the thin-wall sample of the same alloy fabricated using all-y scanning strategy. The following conclusions can be drawn:

1. The microstructure of the Horizontal and 45-degree samples contained mainly ferrite grains with a small volume fraction of pearlite formed at the grain boundaries. However, a more heterogeneous microstructure was detected in the Vertical sample, composed of three distinct regions of fine polygonal ferritic grains formed in melt pools' centers, a combination of allotriomorphic ferrite and acicular ferrite and bainite in the melt pools' boundaries, and coarse polygonal ferritic grains in HAZ. The microstructure of the thin-wall sample was reported to be finer, more uniform and equiaxed than the block sample, resulted from higher cooling rate of the thin-wall sample during fabrication.

2. The EBSD results revealed that the overall microstructure was predominantly composed of randomly oriented equiaxed grains across the entire building direction. The slower cooling rate during solidification in the block sample resulted in coarsening of the average grain size by 60% as compared to the thin-wall sample.

3. The tensile test results of the Horizontal and 45-degree samples showed the isotropic YS, UTS, and elongation properties along with the building plane of the fabricated WAAM-ER70S-6 block. However, the mechanical performance was dropped in the Vertical sample, associated with the existence of the discontinuities in the interpass regions and heterogeneity of the microstructure along the vertical direction. The reduced UTS and YS along the building direction of the block versus the thin-wall sample were ascribed to the formation of the periodic microstructure, interpass discontinuities, and suppressing of the MA micro-constituent formation.

4. The average impact resistance of the Horizontal and 45-degree samples at different temperatures were similar and higher than that of the Vertical samples, dictated by the microstructural variations between the samples.

5. The fracture surfaces of Horizontal and 45-degree samples at room temperature revealed dimpled rupture characteristics and secondary cracks, suggesting a pure ductile fracture. However, the fracture surface of the Vertical sample showed smaller and shallower dimples, inclusions and some flat regions, confirming the reduced toughness of the fabricated sample along the building direction as compared to the building plane.

## Acknowledgments

The authors acknowledge the support of Natural Sciences and Engineering Research Council of Canada (NSERC), Canada Research Chair (CRC) program, Memorial University of Newfoundland, and Dalhousie University for sponsoring this work.

## References

[1] W.E. Frazier, Metal Additive Manufacturing: A Review, J. Mater. Eng. Perform. 23 (2014) 1917–1928. doi:10.1007/s11665-014-0958-z.

[2] A. Taşdemir, S. Nohut, An overview of wire arc additive manufacturing (WAAM) in shipbuilding industry, Ships Offshore Struct. 0 (2020) 1–18. doi:10.1080/17445302.2020.1786232.

[3] M. Ghaffari, A. Vahedi Nemani, M. Rafieazad, A. Nasiri, Effect of Solidification Defects and HAZ Softening on the Anisotropic Mechanical Properties of a Wire Arc Additive-Manufactured Low-Carbon Low-Alloy Steel Part, JOM. 71 (2019) 4215–4224. doi:10.1007/s11837-019-03773-5.

[4] J.P. Oliveira, B. Crispim, Z. Zeng, T. Omori, F.M. Braz Fernandes, R.M. Miranda, Microstructure and mechanical properties of gas tungsten arc welded Cu-Al-Mn shape memory alloy rods, J. Mater. Process. Technol. 271 (2019) 93–100. doi:https://doi.org/10.1016/j.jmatprotec.2019.03.020.

[5] F. Martina, J. Mehnen, S.W. Williams, P. Colegrove, F. Wang, Investigation of the benefits of plasma deposition for the additive layer manufacture of Ti–6Al–4V, J. Mater. Process. Technol. 212 (2012) 1377–1386. doi:https://doi.org/10.1016/j.jmatprotec.2012.02.002.

[6] P.P. Nikam, D. Arun, K.D. Ramkumar, N. Sivashanmugam, Microstructure characterization and tensile properties of CMT-based wire plus arc additive manufactured ER2594, Mater. Charact. 169 (2020) 110671. doi:https://doi.org/10.1016/j.matchar.2020.110671.

[7] M. Rafieazad, M. Ghaffari, A. Vahedi Nemani, A. Nasiri, Microstructural evolution and mechanical properties of a low-carbon low-alloy steel produced by wire arc additive manufacturing, Int. J. Adv. Manuf. Technol. (2019) 1–14. doi:10.1007/s00170-019-04393-8.

[8] W. Wu, J. Xue, L. Wang, Z. Zhang, Y. Hu, C. Dong, Forming Process, Microstructure, and Mechanical Properties of Thin-Walled 316L Stainless Steel Using Speed-Cold-Welding Additive Manufacturing, Metals (Basel). 9 (2019). doi:10.3390/met9010109.

[9] A. [Vahedi Nemani], M. Ghaffari, A. Nasiri, Comparison of microstructural characteristics and mechanical properties of shipbuilding steel plates fabricated by conventional rolling versus wire arc additive manufacturing, Addit. Manuf. 32 (2020) 101086. doi:https://doi.org/10.1016/j.addma.2020.101086.

[10] M. Ghaffari, A.V. Nemani, A. Nasiri, Interfacial bonding between a wire arc additive manufactured 420 martensitic stainless steel part and its wrought base plate, Mater. Chem. Phys. 251 (2020) 123199. doi:https://doi.org/10.1016/j.matchemphys.2020.123199.

[11] A. Vahedi Nemani, M. Ghaffari, A. Nasiri, On the Post-Printing Heat Treatment of a Wire Arc Additively Manufactured ER70S Part, Materials (Basel). 13 (2020). doi:10.3390/ma13122795.

[12] X. Zhang, Q. Zhou, K. Wang, Y. Peng, J. Ding, J. Kong, S. Williams, Study on microstructure and tensile properties of high nitrogen Cr-Mn steel processed by CMT wire and arc additive manufacturing, Mater. Des. 166 (2019) 107611. doi:https://doi.org/10.1016/j.matdes.2019.107611.

[13] J.P. Oliveira, A.D. LaLonde, J. Ma, Processing parameters in laser powder bed fusion metal additive manufacturing, Mater. Des. 193 (2020) 108762.

doi:https://doi.org/10.1016/j.matdes.2020.108762.

[14] J.P. Oliveira, T.G. Santos, R.M. Miranda, Revisiting fundamental welding concepts to improve additive manufacturing: From theory to practice, Prog. Mater. Sci. 107 (2020) 100590. doi:https://doi.org/10.1016/j.pmatsci.2019.100590.

[15] L.N. Carter, C. Martin, P.J. Withers, M.M. Attallah, The influence of the laser scan strategy on grain structure and cracking behaviour in SLM powder-bed fabricated nickel superalloy, J. Alloys Compd. 615 (2014) 338–347. doi:https://doi.org/10.1016/j.jallcom.2014.06.172.

[16] D. Wen, P. Long, J. Li, L. Huang, Z. Zheng, Effects of linear heat input on microstructure and corrosion behavior of an austenitic stainless steel processed by wire arc additive manufacturing, Vacuum. 173 (2020) 109131. doi:https://doi.org/10.1016/j.vacuum.2019.109131.

[17] X. Fang, H. Li, X. Li, K. Huang, L. Zhang, B. Lu, Effect of post heat treatment on the microstructure and mechanical properties of wire-arc additively manufactured A357 alloy components, Mater. Lett. 269 (2020) 127674. doi:https://doi.org/10.1016/j.matlet.2020.127674.

[18] C. Wang, W. Suder, J. Ding, S. Williams, The effect of wire size on high deposition rate wire and plasma arc additive manufacture of Ti-6Al-4V, J. Mater. Process. Technol. 288 (2021) 116842. doi:https://doi.org/10.1016/j.jmatprotec.2020.116842.

[19] Q. Xue, D. Benson, M.A. Meyers, V.F. Nesterenko, E.A. Olevsky, Constitutive response of welded HSLA 100 steel, Mater. Sci. Eng. A. 354 (2003) 166–179. doi:https://doi.org/10.1016/S0921-5093(03)00007-8.

[20] ASTM E8M-04, Standard Test Methods for Tension Testing of Metallic Materials [Metric], ASTM International, West Conshohocken, PA, 2008. doi:10.1520/E0008M-04.

[21] A. E23-18, Standard Test Methods for Notched Bar Impact Testing of Metallic Materials, ASTM Int. (2018). www.astm.org.

[22] J. Ge, J. Lin, H. Fu, Y. Lei, R. Xiao, Tailoring microstructural features of wire arc additive manufacturing 2Cr13 part via varying inter-layer dwelling time, Mater. Lett. 232 (2018) 11–13. doi:https://doi.org/10.1016/j.matlet.2018.08.037.

[23] Y. Zhang, Y. Chen, P. Li, A.T. Male, Weld deposition-based rapid prototyping : a preliminary study, 135 (2003) 347–357.

[24] N. Sridharan, M.W. Noakes, A. Nycz, L.J. Love, R.R. Dehoff, S.S. Babu, On the toughness scatter in low alloy C-Mn steel samples fabricated using wire arc additive manufacturing, Mater. Sci. Eng. A. 713 (2018) 18–27. doi:https://doi.org/10.1016/j.msea.2017.11.101.

[25] B. Shassere, A. Nycz, M.W. Noakes, C. Masuo, N. Sridharan, Correlation of Microstructure and Mechanical Properties of Metal Big Area Additive Manufacturing, Appl. Sci. 9 (2019). doi:10.3390/app9040787.

[26] A. Waqas, X. Qin, J. Xiong, C. Zheng, H. Wang, Analysis of Ductile Fracture Obtained by Charpy Impact Test of a Steel Structure Created by Robot-Assisted GMAW-Based Additive Manufacturing, Metals (Basel). 9 (2019). doi:10.3390/met9111208.

[27] Y. Zhao, X. Tong, X.H. Wei, S.S. Xu, S. Lan, X.-L. Wang, Z.W. Zhang, Effects of microstructure on crack resistance and low-temperature toughness of ultra-low carbon high strength steel, Int. J. Plast. 116 (2019) 203–215. doi:https://doi.org/10.1016/j.ijplas.2019.01.004.

[28] K.C. Hsieh, S.S. Babu, J.M. Vitek, S.A. David, Calculation of inclusion formation in low-alloy-steel welds, Mater. Sci. Eng. A. 215 (1996) 84–91. doi:https://doi.org/10.1016/0921-5093(96)10370-1.

[29] X. Xu, S. Ganguly, J. Ding, S. Guo, S. Williams, F. Martina, Microstructural evolution and mechanical properties of maraging steel produced by wire+arc additive manufacture process, Mater. Charact. (2017). doi:10.1016/j.matchar.2017.12.002.

[30] J.W. Kysar, Energy dissipation mechanisms in ductile fracture, J. Mech. Phys. Solids. 51 (2003) 795–824. doi:https://doi.org/10.1016/S0022-5096(02)00141-2.

[31] N. Huda, A.R.H. Midawi, J. Gianetto, R. Lazor, A.P. Gerlich, Influence of martensite-austenite (MA) on impact toughness of X80 line pipe steels, Mater. Sci. Eng. A. 662 (2016) 481–491. doi:https://doi.org/10.1016/j.msea.2016.03.095.

[32] C.L. Davis, J.E. King, Effect of cooling rate on intercritically reheated microstructure and toughness in high strength low alloy steel, Mater. Sci. Technol. 9 (1993) 8–15. doi:10.1179/mst.1993.9.1.8.

# Appendix III

# Nanosecond laser fabrication of hydrophobic stainless-steel surfaces: the impact on microstructure and corrosion resistance[10]

## Preface

A version of this manuscript has been submitted in the Journal of the Materials. I am the first and corresponding author of the papers. Along with the co-authors, Jaffer Alkarim Jaffer, Cong Cui, Dr. Xili Duan, and Dr. Ali Nasiri, I investigate the capability of nanosecond fiber laser surface texturing followed by a low energy coating in the fabrication of hydrophobic 17-4 PH stainless steel surfaces as an alternative to the ultrashort lasers previously utilized for hydrophobic surfaces production. I prepared methodology, experimental, formal analysis, and the first original draft of the manuscript and subsequently revised the manuscript based on the coauthors' feedback and also the peer review process. The co-authors Jaffer Alkarim Jaffer and Cong Cui helped in the experimental procedure and writing the initial draft. Moreover, Dr. Xili Duan and Dr. Ali Nasiri helped in conceptualization, design, project administration, and supervision, review & editing of the manuscript.

---

[10] M. Rafieazad, J.A. Jaffer, C. Cui, X. Duan, A. Nasiri, Nanosecond Laser Fabrication of Hydrophobic Stainless Steel Surfaces: The Impact on Microstructure and Corrosion Resistance, Materials (Basel). 11 (2018) 1577. https://doi.org/10.3390/ma11091577 (IPF=3.057)

## Abstract

Creation of hydrophobic and super-hydrophobic surfaces has attracted broad attention as a promising solution for protection of the metal surfaces from corrosive environments. This work investigates the capability of nanosecond fiber laser surface texturing followed by a low energy coating in the fabrication of hydrophobic 17-4PH stainless steel surfaces as an alternative to ultrashort lasers previously utilized for hydrophobic surfaces production. Laser texturing of the surface followed by applying the hydrophobic coating resulted in steady-state contact angles of up to 145°, while the non-textured coated base metal exhibited the contact angle of 121°. The microstructure and compositional analysis results confirmed that the laser texturing process neither affects the microstructure of the base metal nor causes elemental loss from the melted regions during the ultrafast melting process. However, the electrochemical measurements demonstrated that the water-repelling property of the surface did not contribute to the anticorrosion capability of the substrate. The resultant higher corrosion current density, lower corrosion potential, and higher corrosion rate of the laser textured surfaces were ascribed to the size of fabricated surface micro-grooves, which cannot retain the entrapped air inside the hierarchical structure when fully immersed in a corrosive medium, thus degrading the material's corrosion performance.

**Keywords:** Hydrophobicity; 17-4 PH Stainless Steel; Nanosecond Laser; Contact Angle; Corrosion Resistance.

## 1. Introduction

Corrosion is an irreversible oxidation reaction on material due to its interaction with an immediate environment [1]. It is a common problem especially in highly aggressive environments [2], degrading the integrity and lifetime of metal surfaces and causing problems both economically and operationally in engineering applications. External factors such as salinity [3], temperature [4], pH [2], and pollutants [5] influence the rate of corrosion of materials. Fabrication processes such as welding [6] and heat treatment [7] can also affect the corrosion resistance of the metal.

One form of corrosion protection that has been recently gaining significant interests among the research community is the application of hydrophobic properties on materials. Combining corrosion protection with other benefits of hydrophobicity such as anti-icing [8], control of bio-fouling [2], self-cleaning [2], water repellency [9], reduction of turbulent flow resistance [10] makes this property extremely beneficial for applications in harsh or highly humid environments, such as pipelines, wellhead platforms, or power transmission lines.

In nature, there are a variety of hydrophobic and super-hydrophobic surfaces such as plants' leaf [11] and living creatures [12]. A surface with so-called hydrophobic property has a wet contact angle greater than 90°, while super-hydrophobic surfaces have remarkably higher water repellency with a wet contact angle greater than 150° [2,11]. Previous studies have discussed two major controlling factors that dictate the hydrophobicity of the surface, i.e., surface roughness and surface energy [2,13]. It should be noted that surface energy is the main factor to achieve hydrophobicity, which primarily is controlled by the surface's chemical composition [2]. However, the superhydrophobicity cannot be obtained only by minimizing the surface energy. It also requires tailoring the surface roughness [10]. As an example, Nishino et al. [13] reported the lowest surface free energy of any solid to be 6.7 $mJ/m^2$ obtained by covering the surface of a glass with regular aligned closest hexagonal packed −CF3 groups, but the best-achieved contact angle was reported to be only 119°, which is far from super-hydrophobicity [13]. Therefore, hierarchical surface features are crucial requirements to achieve superhydrophobicity [10]. These hierarchical surfaces are composed of micro hills and valleys similar to the surface of a lotus leaf or insect bodies [10,11].

A wide variety of materials have been used so far to create hydrophobic and super-hydrophobic properties on their surfaces, including both organic materials, which are commonly hydrophobic by nature and inorganic materials, such as metals with hydrophilic nature [2]. Also, various processes and techniques have been utilized to fabricate hydrophobic surfaces, such as photolithography [14], laser/plasma treatment [15], chemical etching [16], and layer by layer deposition [17], among others. In general, metals due to their better physical, mechanical, chemical, and thermal properties, and laser treatment technique due to its relatively shorter processing time and being highly reproducible have attracted more interests for fabrication of hydrophobic and superhydrophobic surfaces [18,19].

Superhydrophobic surfaces are also evident to provide corrosion resistance improvement to different types of metallic substrates. Boinovich et al. [20] reported that nanosecond laser treatment of the Al surfaces induces hydrophobicity, which in turn enhances resistivity to pitting corrosion in sodium chloride solutions. Yuan et al. [18] similarly analyzed the corrosion characteristics of fluoropolymer films on copper substrates in NaCl medium. It was noted that polymeric films due to the chelating action and formation of insoluble diffusion barriers could protect the substrates from corrosion [19], resulting in 12 times lower corrosion current density for the coated samples than that of the base metal after 21 days of exposure in NaCl corrosive environment [19].

Corrosion resistance evaluation of superhydrophobic stainless steel surfaces has also been investigated in some studies. Latthe et al. [21] studied the corrosion resistance of a chemically etched super hydrophobic 430 stainless steel substrate immersed in 5 wt.% NaCl aqueous solution and described the resultant superhydrophobic surface as a “physical barrier between the metal and the environment.” In a similar experiment, Park et al. [22] used 304 stainless steel substrate immersed in 3.5 wt.% NaCl aqueous solution to compare superhydrophobic and superhydrophilic variations of the substrate and found that the superhydrophobic surfaces showed a higher resistance to corrosion. A different approach, based on the application of three different superhydrophobic membranes on 080M46 steel, was taken by Wang et al. [23] to fabricate hydrophobic steel surfaces. Similarly, they reported that the corrosion resistivity of all three membranes was far superior to the base metal [23]. Trdan et al. [24] also reported a direct relation between wettability and corrosion behavior by showing the effect of the transition from superhydrophilicity to superhydrophobicity on corrosion behavior of AISI 316L stainless steel using nanosecond laser treatment. All the above studies indicate that there might be correlations between corrosion resistance and the wettability of metallic surfaces.

As reported by Mohamed et al. [2], in all previous studies the mechanism behind the corrosion resistance improvement of the metallic surfaces due to their hydrophobic and superhydrophobic properties was claimed to be the retention of the air pocket layer on the surface of the metal, acting as a barrier and preventing the corrosion process from taking place. Air trapping on the surface can enhance the hydrophobicity since air is an extremely hydrophobic compound with a contact angle of 180° [25].

Although a few studies have been carried out on the correlation between hydrophobicity and corrosion resistance of stainless steel alloys [6,7,26], 17-4 PH stainless steel with broad applications in marine, chemical, petrochemical, food processing, and aerospace industries has never been the focus of such studies. Furthermore, in most of the past studies, highly expensive ultrashort pulse lasers, also known as ultrafast lasers, such as femtosecond and picosecond lasers, have been utilized to fabricate hydrophobic surfaces with prolonged processing time (scanning speed of 1 mm/s) [23]. Very limited information is available on laser fabrication of hydrophobic surfaces and its effectiveness using nanosecond fiber lasers with fast processing time [23]. These lasers would be highly beneficial for surface texturing of materials for real industrial applications and should be considered as a cost-effective alternative to expensive ultrashort lasers. Therefore, the purpose of this study is to evaluate the effectiveness of hydrophobic 17-4 PH stainless steel surfaces fabricated through nanosecond fiber laser surface texturing combined with applying a hydrophobic coating and to analyze its impact on the microstructure and corrosion resistance of the surface.

## 2. Materials and Methods

### 2.1. Material

Martensitic type 17-4 PH stainless steel (SS 630-H1025) with a size of 20 × 10 × 3 mm was used as the base metal coupons for laser surface texturing. The H1025 heat treatment designation indicates that the alloy has been precipitation hardened at 551±15°C for 4 hrs, followed by air cooling. The measured chemical composition of the base metal before laser treatment is given in the Table 1.

Table A3. 1**.** The measured chemical composition of 17-4 PH stainless steel before laser treatment (all in wt. %)

| **Elements** | **Cr** | **Ni** | **Cu** | **Si** | **Mn** | **Fe** |
|---|---|---|---|---|---|---|
| 17-4 PH | 16.70±0.05 | 3.70±0.06 | 2.91±0.07 | 0.26±0.08 | 0.46±0.01 | Bal. |

## 2.2. Preparation of Hydrophobic Surfaces

To prepare the hydrophobic surfaces, a combination of laser surface texturing followed by applying a 2-4 nm thick optically clear hydrophobic dip coating, to roughen the surface and lower the surface energy, respectively, were used. The nanoscale thickness of the used hydrophobic coating is reported by the supplier [27]. The surface of the base metal was subjected to mechanical grinding using 600 grit SiC abrasive paper prior to the surface texturing. For the surface texturing, a BMF20A/B fiber laser machine with the wavelength of 1060 nm, laser power of 12 W, the frequency of 20 kHz, scanning speed of 600 mm/s, and the pulse width of 60 ns on a substrate surface of 20 × 10 mm in an argon atmosphere was employed. The chemical composition of the hydrophobic coating was 50-52% Ethanol, mixture of 42-46% 2-(difluoromethoxymethyl)-1,1,1,2,3,3,3-heptafluoropropane and 4-methoxy-1,1,1,2,2,3,3,4,4-nona-fluorobutan, 2-3% 2 propanol, and 2-3% Methanol (Metal Repellency Treatment from Aculon Performance Surface Solutions [27]). To remove oil and other contaminants from the specimens' surfaces, the stainless steel samples were first cleaned ultrasonically in acetone. After this procedure, three variations of hydrophobic surfaces were produced. The first group of samples was simply coated with the hydrophobic coating (referred to as "coated base"), while the other two variations were textured with the laser first using two different topographical designs as shown in Figure A3.1 and then were coated using the hydrophobic coating (referred to as "coated channeled" and "coated varied channeled").

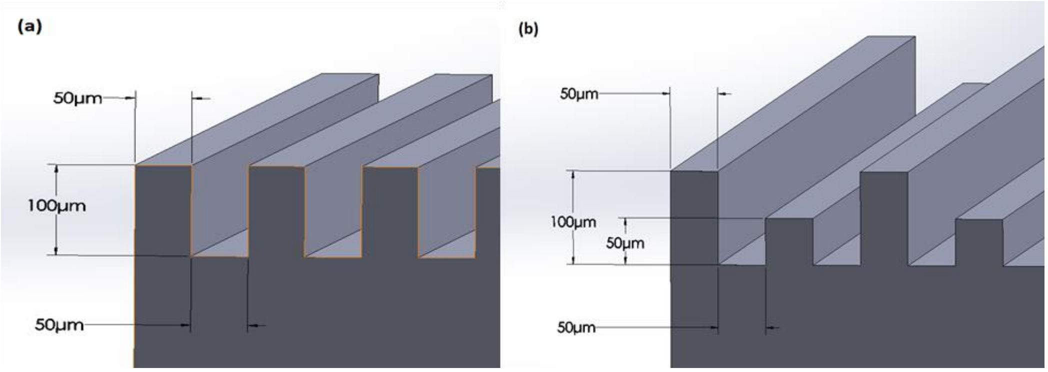

Figure A3. 1. Desired designs of (a) the channeled structure, and (b) the varied channeled structure.

## 2.3. Characterization

The surface structures, morphologies, and microstructures of the prepared samples were studied using an optical microscope (Nikon Eclipse 50i) and a scanning electron microscope (SEM) (FEI MLA 650F) equipped with high throughput Bruker energy dispersive X-ray (EDX) analytical system, which was used to investigate compositional inhomogeneity and possible alloying elements loss from the regions that encounter superficial melting followed by solidification during the laser surface texturing process. To prepare the samples for microscopic analysis, the samples were mounted in an epoxy resin followed by standard grinding and polishing sample preparation procedures for stainless steels. The polished specimens were then etched using Nital 5% reagent (5 vol. % $HNO_3$, and 95 vol. % Methanol) to reveal the microstructure.

## 2.4. Wettability Measurements

Contact angle measurements were performed using an optical-based contact angle measuring system (OCA 15) consisting of an adjustable sample support unit, a light source, a dosing syringe, camera, and lens under the clean experimental condition to eliminate the contamination of the surfaces via air-born organics. The system’s software captures and analyzes the drop shape and measures the static contact angle. The sample was laid flat on a smooth and clean surface, in line with the camera at a distance of approximately 10 cm. The camera's focus and light source were adjusted for optimal clarity and brightness of images. A water droplet of 10 µl was dosed using the software at a dispense rate of 2 µl/s. The given diameter of the sessile drop is about 1.4 mm. All analyses were carried out at room temperature.

### 2.5. Electrochemical Measurements

Electrochemical corrosion measurements were performed on the treated surfaces using an IVIUM CompactStat™ Potentiostat controlled by the software from the same manufacturer. Using a conventional three-electrode set-up, the samples were exposed to aerated 3.5 wt. % NaCl solution to mimic the seawater environment at the temperature of 25 °C. A graphite rod was used as the counter electrode (CE), and saturated silver/silver chloride (Ag/AgCl) was used as the reference electrode (RE). The samples were connected as an electrode using copper wire and conductive tape. The exposed area of the base metal and coated base metal samples was 2 $cm^2$, and for channeled and varied channeled samples was 5.96 $cm^2$ and 4.97 $cm^2$, respectively. The rest of the sample was covered with polyester resin to isolate the surfaces not required for testing. Potentiodynamic polarization analysis was conducted by scanning from −0.3 V to +0.3 V about the open circuit potential (OCP) with a scanning rate of 0.125 mV/s. The repeatability of the corrosion test results was measured by testing at least three samples.

## 3. Results

### 3.1. Surface Morphology

The desired surface topographies for this study have been shown in Figure A3.1, while the SEM images from the surfaces of the actual fabricated samples from side and top views are presented in Figure A3.2. The tips are thinner in Figures A3.2a and A3.2c due to the ablation of material by the laser. The shorter tips in Figure A3.2b, and 2d show the effect of prolonged laser exposure and how the top has flattened due to melting and evaporation of material. There is also evidence of superficial melting followed by solidification (indicated in Figure A3.2b) of some of the material on the structured surface.

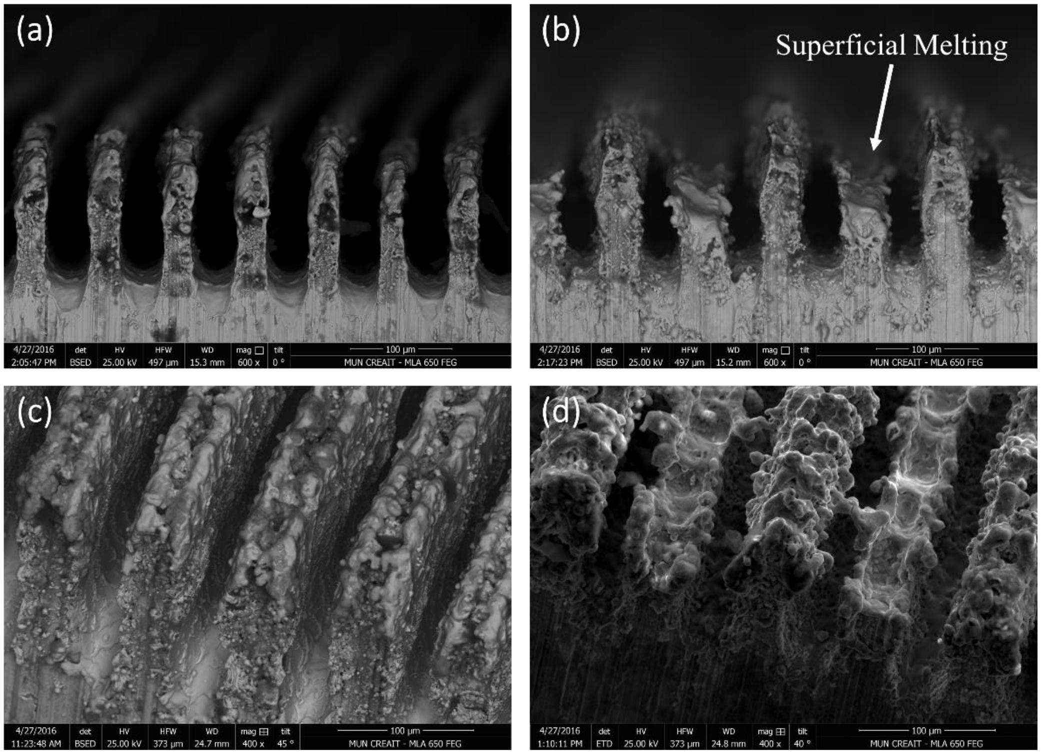

Figure A3. 2/ SEM images of (a) the channeled structure-side view, (b) the varied channeled structure- side view, (c) the channeled structure-top view, and (d) the varied channeled structure-top view.

## 3.2. Microstructure

Figure A3.3 demonstrates the optical and SEM micrographs of the 17-4 PH stainless steel materials used in this study composed of martensite and δ-ferrite phases. The parallel groups of lath martensite as the matrix and elongated δ-ferrite phase in different directions along the primary austenite grain boundaries form the microstructure of the base metal.

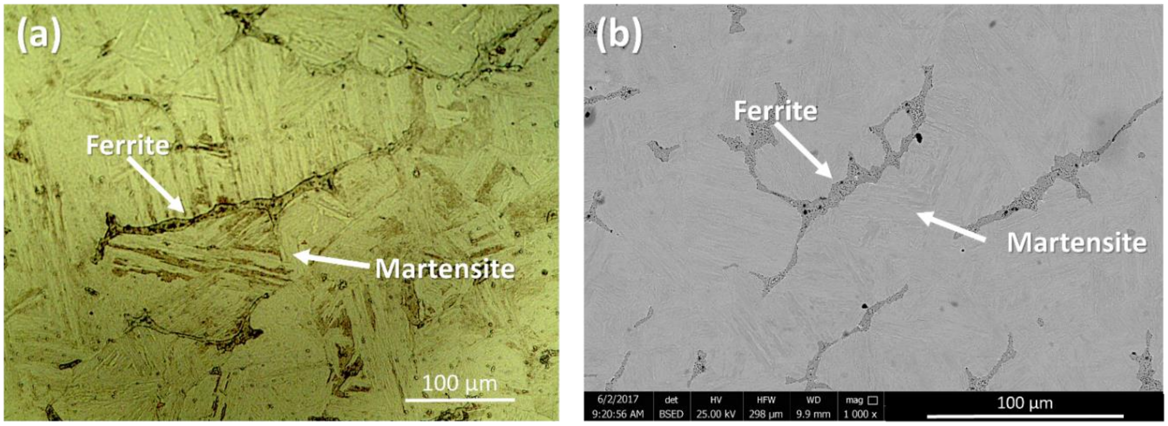

Figure A3. 3**.** (a) Optical microscope image and (b) SEM micrograph of the 17-4 PH stainless steel base material.

As shown in Figure A3.3, the ferrite phase encompasses very fine precipitates, which were detected exclusively on the ferrite phase. Although no evidence of secondary phase formation from the martensitic phase was detected under SEM, the applied H1025 heat treatment should have triggered formation of coherent nano-precipitates, i.e. Cu-rich precipitates (CRPs), from the martensite phase [28,29].

The EDX concentration maps of the ferrite phases in Figure A3. 4 indicate a higher concentration of Cr in spherical precipitates within the δ-ferrite region [30]. Park et al. [31] reported that Cr-enriched phases deteriorate the corrosion resistivity of the alloy. As shown by the white arrows in the Cu map concentration, a few irregulars shaped Cu-enriched particles (CRPs) within the ferrite phase also present. In comparison, the martensite phase showed uniform concentration of Cr and Cu elements. Table 2 shows EDX compositional analysis results of the major micro-constituents of the sample, including both ferrite and martensite phases.

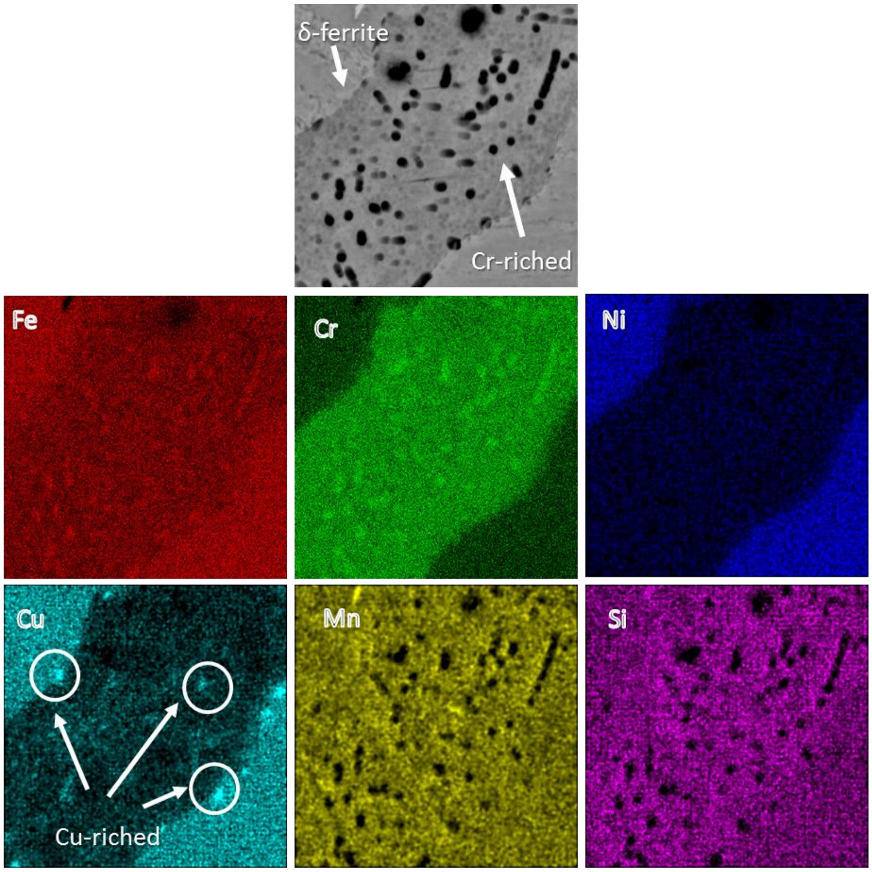

Figure A3. **4.** EDX concentration maps of the δ-ferrite phase.

Table A3. 2**.** The measured chemical composition of 17-4 PH stainless steel micro-constituents (all in wt. %)

| **Phase** | **Cr** | **Ni** | **Cu** | **Si** | **Mn** | **Fe** |
|---|---|---|---|---|---|---|
| δ-Ferrite | 22.3±0.2 | 1.6±0.1 | 1.2±0.2 | 0.4±0.1 | 0.1±0.1 | Bal. |
| Martesite | 16.5±0.1 | 3.7±0.1 | 2.9±0.1 | 0.3±0.1 | 0.1±0.9 | Bal. |

### 3.3. Wetting Behavior

The static contact angles for the fabricated surfaces are shown in Figure A3.5. As expected, the base metal surface has the lowest contact angle (see Figure A3.5a). The coated base sample shows an increase of 48° contact angle compared to the base metal indicating a hydrophobic surface. The channeled and varied channeled structures (Figures A3.5c and A3.5e) show higher hydrophobicity (~ 4° and 9° increase, respectively, from the coated base sample) primarily due to the surface micro-roughness that was fabricated on the surface using the laser texturing process. After applying the hydrophobic coating on the textured surfaces, the channeled and varied channeled surfaces exhibited more hydrophobic behavior with contact angles of 138°±5° and 145°±4°, respectively. Therefore, the combined effects of surface micro-roughness and the coating have resulted in a hydrophobic surface with contact angles just below the required contact angle for superhydrophobicity (150°).

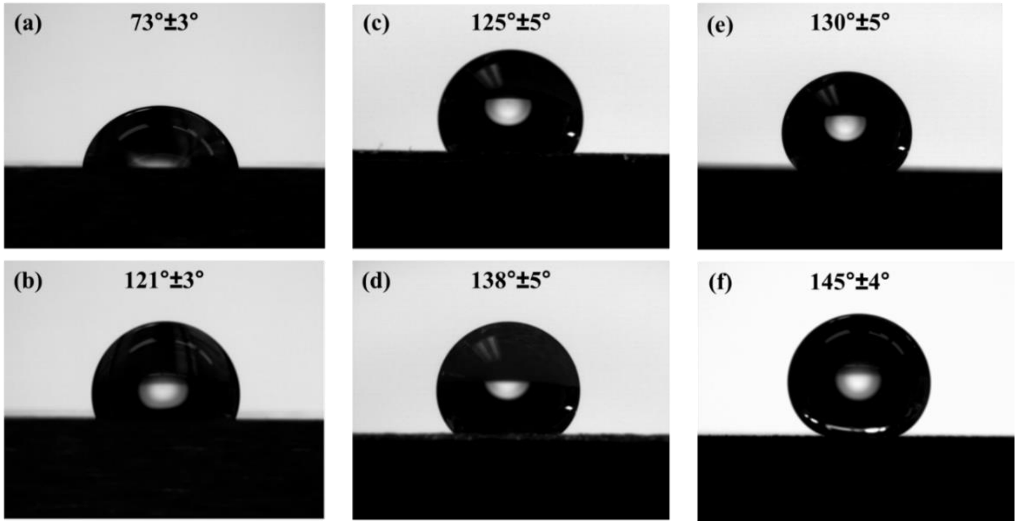

Figure A3. 5**.** Contact angle measurements of the (a) base without coating, (b) coated base, (c) channeled without coating, (d) coated channeled, (e) varied channeled without coating, (f) coated varied channeled.

As evidenced by Figure A3.5, the varied channeled sample with or without coating shows a higher contact angle than its channeled counterpart. To fabricate the varied channeled samples, the laser beam was directly interacting with the surface of the channels to adjust the height of the channels relative to each other. This has resulted in the superficial melting of the tips followed by their rapid cooling and solidification leading to the formation of solidified regions on the tips of the channels (shown in Figures A3.2d and A3.6). These regions provide multimodal roughness on the fabricated surface, contributing to further improvement of the hydrophobicity. Similar phenomena were reported in previous studies [23]. When additional smaller sized surface features are added to the existing surface structure, the water repellency and the contact angle can be increased [23]. However, in the channeled sample, channels' tips do not experience melting and solidification, and less additional surface features were generated, resulting in a lower contact angle than the varied channeled sample.

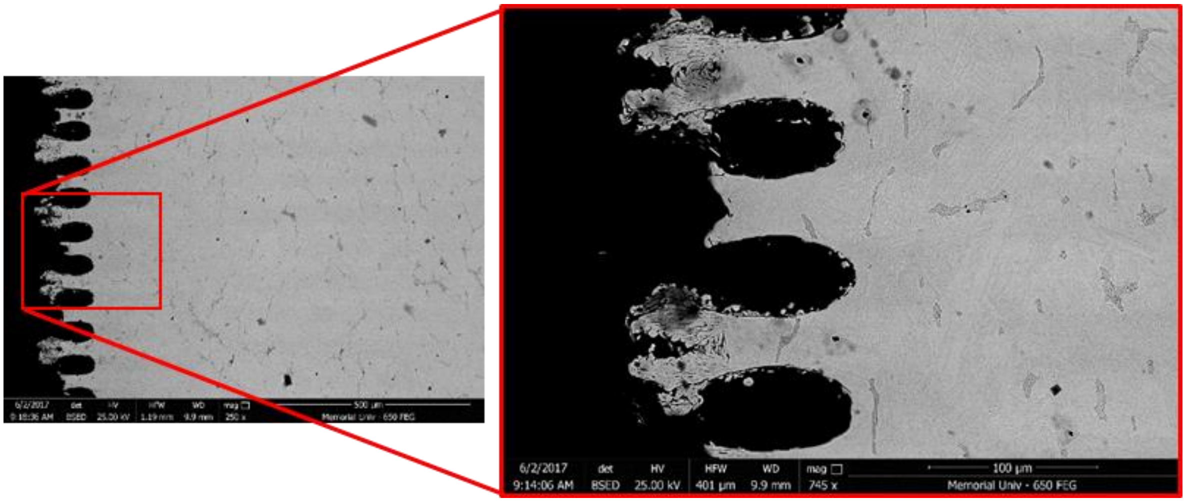

Figure A3. 6**.** Surface features of the sample with varied channeled morphology.

In the context of surface wettability, there are two models capable of describing the correlation between surface roughness and hydrophobicity. The first one proposed by Wenzel [32] assumes that liquid droplet is in contact with the absolute area of the rough surface by,

$$\cos \theta = r \cos \theta_0 \quad (1)$$

where θ shows the contact angle on the rough surface, $\theta_0$ represents the equilibrium contact angle on an ideal smooth surface, and r defines the non-dimensional surface roughness ratio, also known as topography factor [32] When this model is applied to rough surfaces, it predicts an increase of the apparent contact angle (θ) for hydrophobic surfaces and decrease of the contact angle for hydrophilic surfaces by increasing the surface roughness (r-value). Because the laser surface texturing in this study changed the wettability of the surface from a hydrophilic surface ($\theta = 73° \pm 3$) to a hydrophobic surface ($\theta > 90°$), the Wenzel model is not expected to be able to describe the behavior of the fabricated laser textured surfaces.

The other model is Cassie-Baxter model [33], in which it is assumed that droplets do not wet the rough surfaces completely due to the existing air packs that are trapped within the interstices of the rough surface. The apparent contact angle ($\theta_r^C$) with this model is calculated by [26]:

$$\cos\theta_r^C = f(\cos\theta_e + 1) - 1 \tag{2}$$

where f is the fraction of the surface in contact with the liquid and $\theta_e$ is the intrinsic contact angle for a smooth surface. Applying this model to both hydrophobic and hydrophilic surfaces confirms that apparent contact angle on rough surfaces is always higher than that of the smooth surfaces [34]. Therefore, the measured contact angles in this study are expected to fit the Cassie-Baxter model than the Wenzel model.

### 3.4. Corrosion Behavior

Figure A3.7 shows the polarization characteristics (Tafel plots) of all samples comparing the base metal with the hydrophobic surface variants. As a general trend, better corrosion resistance is shown by an increase in corrosion potential and a decrease in corrosion current density. Hence, the preliminary observation of the graph shows that the base metal and coated base metal show higher corrosion resistance than the more hydrophobic textured samples.

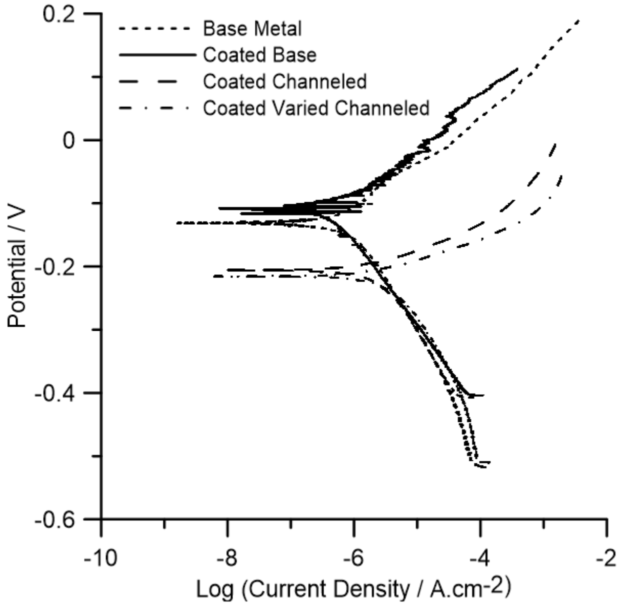

Figure A3. 7**.** Tafel plot comparison between (a) base metal, (b) coated base, (c) coated channeled, and (d) coated varied channeled.

From the graph, each plot can be considered to calculate and quantify the corrosion rate. The anodic slope ($\beta_A$) and the cathodic slope ($\beta_C$) can thus be obtained for each plot. The intersection between the two slopes indicates the corrosion current ($I_{CORR}$) and the corrosion potential ($E_{CORR}$) versus the reference electrode. However, this can also be calculated (in SI units) from the following formula:

$$I_{CORR} = (\beta_A \, \beta_C)/(2.3 \times R_p \times (\beta_A + \beta_C)) \qquad (3)$$

where $R_p$ is the polarization resistance (in ohms.cm$^{-2}$) measured by the potentiostat software. The corrosion current can then be used to calculate the corrosion rate (in mm/year) from the following formula:

$$\text{Corrosion Rate} = (3.27 \times 10^3 \times \mathrm{I}_{\mathrm{CORR.}} \times \mathrm{E.W.})/(\mathrm{A} \times \rho) \quad (4)$$

where E.W. stands for the equivalent weight of the alloy (in grams), A is the surface area (in $cm^2$) exposed to the electrolyte, and ρ is the density of the sample (in $g/cm^3$).

Table 3 shows the corrosion potential, corrosion current, corrosion current density, and the corrosion rate of each of the samples calculated from the formulas above. The corrosion rate of the base metal shows an evident decrease from 0.012 mm/year to 0.005 mm/year with applying the hydrophobic coating, representing an almost 50% increase in its uniform corrosion resistance, which is ascribed to the protective nature of the coating on the substrate. On the other hand, the corrosion rate of the coated channeled and coated varied channeled was increased to 0.032 mm/year and 0.043 mm/year, respectively, representing a loss of corrosion resistance by a factor of ~ 3 to 4, even though the coated textured surfaces were more hydrophobic, as evidenced by showing higher contact angles (Figure A3.5). As shown in Table 3, the corrosion current density values (ICORR) of the hydrophobic laser textured surfaces follow the same trend as the corrosion rate data since ICORR is directly related to the corrosion rate (see equation 4). However, the corrosion potential values (ECORR), correlating to the thermodynamic tendency for corrosion, show a pronounced negative shift to less noble values for the laser textured surfaces as compared to those of the base metal representing a higher corrosion tendency. Therefore, coated laser textured surfaces displayed both an increased corrosion rate and corrosion tendency, meaning water repellency unexpectedly was not found effective towards protection of the surface against uniform corrosion attack in this study.

Table A3. 3**.** Results obtained and calculated from the Tafel plots shown in Figure A3.7.

| **Surface type** | **Corrosion potential ($V_{Ag/AgCl}$)** | **Corrosion current (A)** | **Corrosion current density ($A.cm^{-2}$)** | **Corrosion Rate (mm/y)** |
|---|---|---|---|---|
| Base metal | -0.136 | $2.070\times10^{-6}$ | $1.035\times10^{-6}$ | 0.012 |
| Coated base metal | -0.110 | $8.036\times10^{-7}$ | $4.018\times10^{-7}$ | 0.005 |
| Coated channeled | -0.209 | $1.657\times10^{-5}$ | $2.776\times10^{-6}$ | 0.032 |
| Coated varied channeled | -0.205 | $1.878\times10^{-5}$ | $3.799\times10^{-6}$ | 0.043 |

Contact angle measurements after the corrosion tests were also performed to check if the coating was compromised during the corrosion test. Figure A3.8 shows that although surfaces are still hydrophobic, there is a slight decrease in the contact angle values, which is more pronounced for the coated base metal. After fully immersion of the samples in the corrosive electrolyte and performing the potentiodynamic polarization testing, the hydrophobic coating might have been locally peeled off from the surface resulting in a decrease in the contact angle.

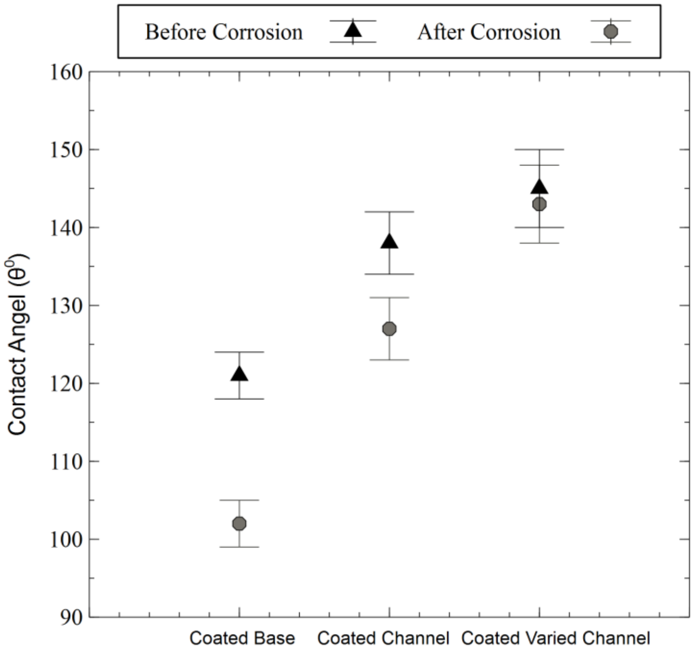

Figure A3. 8**.** Contact angle (in degrees) comparison before and after the potentiodynamic polarization tests.

As mentioned above, hydrophobicity and the resultant corrosion resistivity enhancement are primarily controlled by two main factors, i.e., surface morphology and surface energy, and the inferior is controlled by surface chemical composition [2]. During the laser surface texturing, the interaction of the laser with the surface and the resultant high temperature on the surface melts and ablates materials, which can also cause undesirable volatile alloying elements loss from the superficial melted regions, and consequently, the metallurgical properties of the surface including its electrochemical resistance can change. To investigate the impact of the laser surface texturing on chemical composition inhomogeneity and possible loss of volatile elements from the melted regions (Figure A3.9a), SEM-EDX composition line scan analysis of the melted regions was performed. As Figure A3.9b shows, there is no elemental deficiency in the melted region adjacent to the surface relative to the base metal, especially Chromium and Nickel elements, which are primarily responsible for corrosion resistivity of the alloy [35]. This confirms that the performed laser surface texturing had no detrimental effect on the chemical composition of the material after melting followed by solidification, which will be in contact with the corrosive medium. Therefore, the reduction of corrosion resistivity of the laser textured specimens is not due to the elemental loss from the superficial melted regions or any change in the substrate's chemical composition.

As shown in Figure A3.9b, two peaks were detected across the Cr line scan, in the same positions as another two valleys across the Ni and Cu lines, in which their positions correspond to the δ-ferrite phase containing higher Cr content and lower concentration of Ni and Cu relative to the martensitic matrix. Delta ferrite phase has been shown to have a higher solubility for Cr, since Cr is a ferrite stabilizing element, and lower solid solubility for Ni and Cu elements [36].

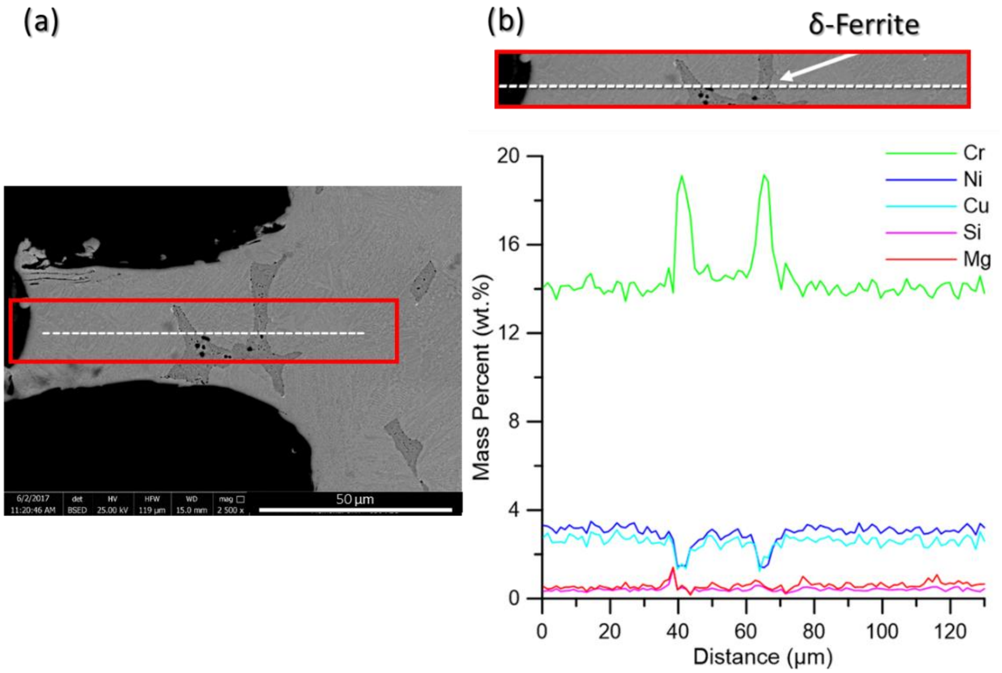

Figure A3. 9**.** (a) SEM image taken from one surface feature of the sample with varied channeled morphology showing the position of the EDX-line scan using a dashed-line in the enclosed area, and (b) the corresponding EDX composition line scans indicating scans of Cr, Ni, Cu, Si, and Mg.

The other controlling factor to be investigated is the surface morphology. The mechanism behind the improved corrosion resistivity of superhydrophobic stainless steels surfaces in previous studies [37] has been reported to be the trapped air (air-packs) within the micro/nano-structures that hinders the solution penetration into the surface (as proposed by the Cassie-Baxter's model [33]), resulting in a reduced contact area between the surface and the corrosive medium, leading to the improved corrosion resistivity of the surface. Therefore, for the case of superhydrophobic surfaces, the surface features are small enough to retain the trapped air on the surface even after full immersion of the sample in the corrosive medium during electrochemical testing. This requires careful optimization of the size of grooves and surface protuberances. Luo et al. [38] reported that although having microfeatures can generate hydrophobic properties, superhydrophobicity can be achieved only if the feature's ratio is optimum. They noted that if the width of features decreases from 250 µm to 10 µm, the contact angle will be increased from 60° to 129° [38].

The presented results in this study demonstrated that when the laser textured stainless steel surface is only hydrophobic, the surface features are not small enough to maintain the protective air-packs between the surface and the solution. Therefore, all the trapped air might have escaped from the surface as soon as the surface is immersed in the corrosive medium. Consequently, all the surface micro-grooves will act as a channel for microfluidic, resulting in an increased area of solid-liquid interface and enhanced corrosion rate. Similar corrosion resistance degradation was reported by Trdan et al. [24] for the laser surface textured 316L stainless steel when the surface is not superhydrophobic. They observed a significant directional corrosion attack propagated inside the channels [24]. Contrarily, this effect is entirely annihilated, when the surface becomes super hydrophobic [24].

Although the applied hydrophobic coating contributed to water-repelling property of the surface and a slight improvement in corrosion performance of the base metal, the size of the nanosecond laser fabricated micro-grooves was found to be the primary factor in dictating corrosion performance of the hydrophobic surfaces. Therefore, nanosecond fiber laser surface texturing will be an effective replacement for slow and highly expensive ultrashort laser texturing, only if the size of micro-groove features is carefully optimized, resulting in superhydrophobic property, which allows the air-packs to remain on the surface inside the hierarchical structure in fully immersed condition. Otherwise, the resultant corrosion loss compromises the effectiveness of this technique.

## 4. Conclusions

Hydrophobic 17-4 PH stainless steel surfaces were successfully fabricated using a fast and cost-effective nanosecond laser surface texturing technique followed by applying a hydrophobic coating to the surfaces. This processing technique facilitates fabrication of large-scale hydrophobic metallic surfaces proper for various industrial applications. The samples showed hydrophobic properties directly after the fabrication process. The obtained hydrophobic property can be ascribed to the combined effects of the laser-induced roughness and low surface energy resulted from the coating. The coating could only increase the steady state contact angle of water on the non-textured base metal up to 121°; however, by laser texturing of the surface, the contact angle was increased up to 145° without undesirable loss of volatile elements from the melted zones.

The resultant hydrophobicity did not render the desired corrosion protection capability to the stainless steel substrate. The lowest corrosion potential with the highest corrosion current density leading to the highest corrosion rate was measured on the laser textured hydrophobic samples. Therefore, the water repelling property of the 17-4 PH stainless steel was not found effective in preventing the aggressive chloride ions from approaching the substrate. This can be attributed to the large size of the fabricated micro-grooves on the surface, meaning the surface features are not capable of retaining the entrapped air inside the hierarchical structure in fully immersed condition in the corrosive medium, resulting in an increased contact area between water and the solid substrate and degradation of corrosion property. Nonetheless, the hydrophobicity of the fabricated samples was maintained even after electrochemical corrosion testing. Therefore, further optimization of the size of the micro-grooves is required to create a superhydrophobic surface with enhanced corrosion property.

## Acknowledgments

The authors would like to thank the support of Petroleum Research Newfoundland and Labrador [grant number C15-03], the Newfoundland and Labrador Innovation Council [grant number 5404.1891.102], and the Memorial University of Newfoundland for sponsoring this work.

## References

[1] D. Thirumoolan, T. Siva, K. Vetrivel, S. Sathiyanarayanan, K.A. Basha, Corrosion resistant performance of hydrophobic poly(N-vinyl imidazole-co-ethyl methacrylate) coating on mild steel, Prog. Org. Coatings. 89 (2015) 181–191. doi:10.1016/j.porgcoat.2015.09.014.

[2] A.M.A. Mohamed, A.M. Abdullah, N.A. Younan, Corrosion Behavior of Superhydrophobic Surfaces: A Review, Arab. J. Chem. 8 (2015) 749–765. doi:10.1016/j.arabjc.2014.03.006.

[3] K. Zakowski, M. Narozny, M. Szocinski, K. Darowicki, Influence of water salinity on corrosion risk - the case of the southern Baltic Sea coast, Environ. Monit. Assess. 186 (2014) 4871–4879. doi:10.1007/s10661-014-3744-3.

[4] G.W. Ladan Khaksar, J. Shirokoff, Electrochemical and Microstructural Analysis of FeS Films from Acidic Chemical Bath at Varying Temperatures, pH, and Immersion Time, Int. J. Corros. 2016 (2016) 9. doi:10.1155/2016/1025261.

[5] X.T. Wang, B.R. Hou, Effect of sulphide pollutants on mild steel corrosion in 3·5% NaCl solutions, Corros. Eng. Sci. Technol. 45 (2010) 57–60. doi:10.1179/147842209X12476568584188.

[6] J. Xiong, M.Y. Tan, M. Forsyth, The corrosion behaviors of stainless steel weldments in sodium chloride solution observed using a novel electrochemical measurement approach, Desalination. 327 (2013) 39–45. doi:10.1016/j.desal.2013.08.006.

[7] R.K. Gupta, N. Parvathavarthini, A. Vinod Kumar, R.K. Dayal, Influence of Inclusion and Specimen Orientations on Intergranular Corrosion Testing of AISI 316LN Stainless Steel, Trans. Indian Inst. Met. 64 (2011) 365–375. doi:10.1007/s12666-011-0088-3.

[8] S. Farhadi, M. Farzaneh, S.A. Kulinich, Anti-icing performance of superhydrophobic surfaces, Appl. Surf. Sci. 257 (2011) 6264–6269. doi:https://doi.org/10.1016/j.apsusc.2011.02.057.

[9] S. Khorsand, K. Raeissi, F. Ashrafizadeh, Corrosion Resistance and Long-term Durability of Super-hydrophobic Nickel Film Prepared by Electrodeposition Process, Appl. Surf. Sci. 305 (2014) 498–505. doi:10.1016/j.apsusc.2014.03.123.

[10] Z. Ahmad, A.U. Khan, R. Farooq, N.R. Mastoi, T. Saif, Hydrophobicity A Green Technique for Enhancing Corrosion Resistance of Alloys, in: New Trends Alloy Dev. Charact. Appl., InTech, 2015.

[11] W. Barthlott, C. Neinhuis, Purity of the Sacred Lotus, or Escape from Contamination in Biological Surfaces, Planta. 202 (1997) 1–8. doi:10.1007/s004250050096.

[12] R. Hensel, R. Helbig, S. Aland, A. Voigt, C. Neinhuis, C. Werner, Tunable nano-replication to explore the omniphobic characteristics of springtail skin, NPG Asia Mater. 5 (2013) e37. http://dx.doi.org/10.1038/am.2012.66.

[13] T. Nishino, M. Meguro, K. Nakamae, M. Matsushita, Y. Ueda, The Lowest Surface Free Energy Based on -CF3 Alignment, Langmuir. 15 (1999) 4321–4323. doi:10.1021/la981727s.

[14] T. Limongi, R. Schipani, A. Di Vito, A. Giugni, M. Francardi, B. Torre, M. Allione, E. Miele, N. Malara, S. Alrasheed, R. Raimondo, P. Candeloro, V. Mollace, E. Di Fabrizio, Photolithography and Micromolding Techniques for the Realization of 3D Polycaprolactone Scaffolds for Tissue Engineering Applications, Microelectron. Eng. 141 (2015) 135–139. doi:10.1016/j.mee.2015.02.030.

[15] A. Rodriguez, M. Echeverría, M. Ellman, N. Perez, Y.K. Verevkin, C.S. Peng, T. Berthou, Z. Wang, I. Ayerdi, J. Savall, S.M. Olaizola, Laser Interference Lithography for Nanoscale Structuring of Materials: From Laboratory to Industry, Microelectron. Eng. 86 (2009) 937–940. doi:10.1016/j.mee.2008.12.043.

[16] Y. Liu, X. Yin, J. Zhang, Y. Wang, Z. Han, L. Ren, Biomimetic Hydrophobic Surface Fabricated by Chemical Etching Method from Hierarchically Structured Magnesium Alloy Substrate, Appl. Surf. Sci. 280 (2013) 845–849. doi:10.1016/j.apsusc.2013.05.072.

[17] D.J. Abson, R.J. Pargeter, Factors Influencing As-deposited Strength, Microstructure, and Toughness of Manual Metal Arc Welds Suitable for C-Mn Steel Fabrications, Int. Mater. Rev. 31 (1986) 141–196. doi:10.1179/095066086790324302.

[18] S. Yuan, S.O. Pehkonen, B. Liang, Y.P. Ting, K.G. Neoh, E.T. Kang, Superhydrophobic Fluoropolymer-modified Copper Surface via Surface Graft Polymerisation for Corrosion Protection, Corros. Sci. 53 (2011) 2738–2747. doi:10.1016/j.corsci.2011.05.008.

[19] E. Geler, D.S. Azambuja, Corrosion Inhibition of Copper in Chloride Solutions by Pyrazole, Corros. Sci. 42 (2000) 631–643. doi:http://dx.doi.org/10.1016/S0010-938X(99)00080-3.

[20] L.B. Boinovich, A.M. Emelyanenko, A.D. Modestov, A.G. Domantovsky, K.A. Emelyanenko, Synergistic Effect of Superhydrophobicity and Oxidized Layers on Corrosion Resistance of Aluminum Alloy Surface Textured by Nanosecond Laser Treatment., ACS Appl. Mater. Interfaces. 7 (2015) 19500–19508. doi:10.1021/acsami.5b06217.

[21] S.S. Latthe, P. Sudhagar, A. Devadoss, A.M. Kumar, S. Liu, C. Terashima, K. Nakata, A. Fujishima, A Mechanically Bendable Superhydrophobic Steel Surface with Self-cleaning and Corrosion-Resistant Properties, J. Mater. Chem. A. 3 (2015) 14263–14271. doi:10.1039/C5TA02604K.

[22] B. Park, W. Hwang, A facile Fabrication Method for Corrosion-resistant Micro/Nanostructures on Stainless Steel Surfaces with Tunable Wettability, Scr. Mater. 113 (2016) 118–121. doi:10.1016/j.scriptamat.2015.10.018.

[23] N. Wang, D. Xiong, Superhydrophobic Membranes on Metal Substrate and their Corrosion Protection in Different Corrosive Media, Appl. Surf. Sci. 305 (2014) 603–608. doi:10.1016/j.apsusc.2014.03.142.

[24] U. Trdan, M. Hočevar, P. Gregorčič, Transition from Superhydrophilic to Superhydrophobic State of Laser Textured Stainless Steel Surface and its Effect on Corrosion Resistance, Corros. Sci. 123 (2017) 21–26. doi:10.1016/j.corsci.2017.04.005.

[25] H. Ogihara, J. Xie, T. Saji, Factors Determining Wettability of Superhydrophobic Paper Prepared by Spraying Nanoparticle Suspensions, Colloids Surfaces A Physicochem. Eng. Asp. 434 (2013) 35–41. doi:https://doi.org/10.1016/j.colsurfa.2013.05.034.

[26] B. Wu, M. Zhou, J. Li, X. Ye, G. Li, L. Cai, Superhydrophobic surfaces fabricated by microstructuring of stainless steel using a femtosecond laser, Appl. Surf. Sci. 256 (2009) 61–66. doi:10.1016/j.apsusc.2009.07.061.

[27] Aculon, Aculon Performance Surface Solution, Aculon. (n.d.). http://www.aculon.com/multisurfacehydrophobic.php (accessed April 20, 2017).

[28] Z. Wang, H. Li, Q. Shen, W. Liu, Z. Wang, Nano-precipitates evolution and their effects on mechanical properties of 17-4 precipitation-hardening stainless steel, Acta Mater. 156 (2018) 158–171. doi:https://doi.org/10.1016/j.actamat.2018.06.031.

[29] M. Murayama, K. Hono, Y. Katayama, Microstructural evolution in a 17-4 PH stainless steel after aging at 400C, Metall. Mater. Trans. A. 30 (1999) 345–353. doi:10.1007/s11661-

999-0323-2.

[30] K.T. Youn, Y.M. Rhyim, W. Do Yoo, J.H. Lee, Study on the Microstructure and Mechanical Properties of 17-4 PH Stainless Steel Depending on Heat Treatment and Aging Time, in: Heat Treat. Mater., Trans Tech Publications, 2006: pp. 15–20. doi:10.4028/www.scientific.net/SSP.118.15.

[31] S.H.C. Park, Y.S. Sato, H. Kokawa, K. Okamoto, S. Hirano, M. Inagaki, Corrosion resistance of friction stir welded 304 stainless steel, Scr. Mater. 51 (2004) 101–105. doi:https://doi.org/10.1016/j.scriptamat.2004.04.001.

[32] R.N. Wenzel, Surface roughness and contact angle., J. Phys. Chem. 53 (1949) 1466–1467.

[33] A.B.D. Cassie, S. Baxter, Wettability of Porous Surfaces, Trans. Faraday Soc. 40 (1944) 546–551. http://dx.doi.org/10.1039/tf9444000546.

[34] Y.C. Jung, B. Bhushan, Contact angle, adhesion and friction properties of micro-and nanopatterned polymers for superhydrophobicity, Nanotechnology. 17 (2006) 4970. http://stacks.iop.org/0957-4484/17/i=19/a=033.

[35] T. Ogawa, T. Koseki, Effect of composition profiles on metallurgy and corrosion behavior of duplex stainless steel weld metals, Weld. J. 68 (1989) 181.

[36] Q. Gao, Y. Zhang, H. Zhang, H. Li, F. Qu, J. Han, C. Lu, B. Wu, Y. Lu, Y. Ma, Precipitates and Particles Coarsening of 9Cr–1.7W–0.4Mo–Co Ferritic Heat-Resistant Steel after Isothermal Aging, Sci. Rep. 7 (2017) 5859. doi:10.1038/s41598-017-06191-2.

[37] D.-M. Chun, C.-V. Ngo, K.-M. Lee, Fast fabrication of superhydrophobic metallic surface using nanosecond laser texturing and low-temperature annealing, CIRP Ann. - Manuf. Technol. 65 (2016) 519–522. doi:https://doi.org/10.1016/j.cirp.2016.04.019.

[38] A. Leon, E. Aghion, Effect of surface roughness on corrosion fatigue performance of AlSi10Mg alloy produced by Selective Laser Melting (SLM), Mater. Charact. 131 (2017) 188–194. doi:https://doi.org/10.1016/j.matchar.2017.06.029.